12-2020

HYPERPOLARIZED CARBON-13 MAGNETIC RESONANCE MEASUREMENTS OF TISSUE PERFUSION AND METABOLISM

Keith Michel

HYPERPOLARIZED CARBON-13 MAGNETIC RESONANCE MEASUREMENTS OF TISSUE PERFUSION AND METABOLISM

by

Keith Andrew Michel, B.S.

APPROVED:

_____
James A. Bankson, Ph.D.
Advisory Professor

_____
John D. Hazle, Ph.D.

_____
R. Jason Stafford, Ph.D.

Aradhana M. Venkatesan, M.D.

_____
Aradhana M. Venkatesan, M.D.

Arvind Rao

_____
Arvind Rao, Ph.D.

APPROVED:

_____
Dean, The University of Texas
MD Anderson Cancer Center UTHealth Graduate School of Biomedical Sciences

HYPERPOLARIZED CARBON-13 MAGNETIC RESONANCE MEASUREMENTS OF TISSUE PERFUSION AND METABOLISM

A

DISSERTATION

Presented to the Faculty of

The University of Texas

MD Anderson Cancer Center UTHealth

Graduate School of Biomedical Sciences

in Partial Fulfillment

of the Requirements

for the Degree of

DOCTOR OF PHILOSOPHY

by

Keith Andrew Michel, B.S.

Houston, Texas

December 2020

To my parents, Kristina and Gary Michel.

I am forever grateful for all your love and support.

Acknowledgements

There are so many colleagues, friends and family who deserve my gratitude for their help and support that any set of acknowledgements will fail to give full credit to all of those who are entitled to it. But here goes.

I am very grateful to my advisor, James Bankson, for his thoughtful mentorship throughout my time working at MD Anderson. Ever since I was first hired as a technician in the Small Animal Imaging Facility (SAIF) nearly a decade ago, he has always encouraged and challenged me to grow and learn. I would not be where I am now without his guidance, and I look forward to continuing our research together as I move to the next stage of my career. I would also like to thank my advisory committee for their helpful input during my time as a graduate student. Our discussions have always helped to contextualize my results and make clear the next steps that were needed.

I have been very fortunate to work with many extraordinary colleagues and collaborators, and without their aid the work covered in this dissertation would never have been possible. Everyone who works in SAIF deserves my thanks for their assistance with rodent imaging experiments, particularly Charles Kingsley and Jorge de la Cerda. Additionally, I am very grateful for the often unseen efforts of John Hazle and James Bankson that have made this facility possible. I am also indebted to Matthew Merritt and Mukundan Ragavan from the University of Florida for helping me appreciate the complexities of the biochemistry involved in the metabolism of HP agents. I hope that I have at least partially repaid that debt through my contributions to our collaboration in imaging these agents. My colleagues in the MD Anderson Magnetic

Resonance Systems Laboratory have always been gracious in devoting their time and efforts to assist me with experiments and data analyses. Among these colleagues, I am especially grateful to Chris Walker, Zhan Xu and Collin Harlan both for their experimental assistance and for the camaraderie we have shared during my time as a graduate student.

Lastly, I want to thank the family and friends who have made this a journey worth taking. My old friend, Zach Averyt, and his wife Amelia deserve special mention for their support in the last mile of my graduate career. I never would have imagined when we ran into one another by chance in December 2019 that I would later rely on them for my physical and emotional well-being in the midst of a global pandemic, but restoring our friendship has been one of the few bright spots in this miserable year. I am also grateful to the many friends I have made in the Medical Physics program throughout my time at MD Anderson. I look forward to the day when we are able to properly celebrate our achievements in person, once it is safe and responsible to do so.

HYPERPOLARIZED CARBON-13 MAGNETIC RESONANCE MEASUREMENTS
OF TISSUE PERFUSION AND METABOLISM

Keith Andrew Michel, B.S.

Advisory Professor: James A. Bankson, Ph.D.

Hyperpolarized Magnetic Resonance Imaging (HP MRI) is an emerging modality that enables non-invasive interrogation of cells and tissues with unprecedented biochemical detail. This technology provides rapid imaging measurements of the activity of a small quantity of molecules with a strongly polarized nuclear magnetic moment. This polarization is created in a polarizer separate from the imaging magnet, and decays continuously towards a non-detectable thermal equilibrium once the imaging agent is removed from the polarizer and administered by intravenous injection. Specialized imaging strategies are therefore needed to extract as much information as possible from the HP signal during its limited lifetime.

In this work, we present innovative strategies for measurement of tissue perfusion and metabolism with HP MRI. These techniques include the capacity to sensitize the imaging signal to the diffusive motion of HP molecules, providing improved accuracy and reproducibility for assessment of agent uptake in tissue. The proposed methods were evaluated in numerical simulations, implemented on a preclinical MRI system and demonstrated *in vivo* in rodents through imaging of HP ^{13}C urea. Using the simulation and imaging infrastructure developed in this work, established methods for encoding HP chemical signals were compared quantitatively. Lastly, our method was adapted for imaging of [2-^{13}C]dihydroxyacetone, a novel HP agent that probes enzymatic flux through multiple biochemical pathways *in vivo*.

Our results demonstrate the capacity of HP MRI to measure tissue perfusion and metabolism in ways not possible with the imaging modalities currently available in the clinic. As the use of HP MRI advances in clinical investigations of human disease, these imaging measurements can offer real-time and individualized information on disease states for early detection and therapeutic guidance.

Contents

List of Figures

List of Tables

List of Abbreviations

2-DG – 2-deoxy-D-glucose

β**HB** – Beta-hydroxybutyrate

ALT – Alanine Transaminase

ATP – Adenosine Triphosphate

AUC – Area Under the Curve

CA – Carbonic Anhydrase

CSI – Chemical Shift Imaging

DCE – Dynamic Contrast Enhancement

DHA(P) – Dihydroxyacetone (Phosphate)

DMSO – Dimethyl Sulfoxide

dDNP – Dissolution Dynamic Nuclear Polarization

DNP – Dynamic Nuclear Polarization

DSC – Dynamic Susceptibility Contrast

EP(S)I – Echo Planar (Spectroscopic) Imaging

EPR – Electron Paramagnetic Resonance

FDG – 2-deoxy-2-[^{18}F]fluoro-D-glucose

FID – Free Induction Decay

FIR – Finite Impulse Response

FOV – Field of View

FT – Fourier Transform

FWHM – Full Width at Half-Maximum

G3P – Glycerol-3-phosphate

GA3P – Glyceraldehyde-3-phosphate

GBM – Glioblastoma

H&E – Hematoxylin and Eosin

HP – Hyperpolarized

(i)DFT – (Inverse) Discrete Fourier Transform

IDEAL – Iterative Decomposition of Chemical Shifts with Echo Asymmetry and Least Squares Estimation

IVIM – Intravoxel Incoherent Motion

LDH(A) – Lactate Dehydrogenase (A)

NAD(H/$^+$) – (Reduced / Oxidized) Nicotinamide Adenine Dinucleotide

NAFLD – Non-Alcoholic Fatty Liver Disease

NRMSE – Normalized Root Mean Square Error

NSA – Effective Number of Signal Averages

MRI – Magnetic Resonance Imaging

NMR – Nuclear Magnetic Resonance

PDH – Pyruvate Dehydrogenase

PEP – Phosphoenolpyruvate

PET – Positron Emission Tomography

PHIP – Parahydrogen Induced Polarization

QC – Quality Control

RARE – Rapid Acquisition with Relaxation Enhancement

ROI – Region of Interest

SEOP – Spin Exchange Optical Pumping

SLR – Shinnar Le-Roux

SNR – Signal to Noise Ratio

TCA – Tricarboxylic Acid

TE – Echo Time

TR – Repetition Time

VIF – Vascular Input Function

Chapter 1

Introduction

Cancer is a class of diseases arising from the unrestrained proliferation of a population of cells [1]. Despite advances in our understanding of these diseases and significant investments in the development of more effective therapies, cancer remains a leading cause of mortality in the United States and worldwide [2]. As our comprehension of cancer biology has grown in the past two decades, it is increasingly understood as a disease in which the accumulation of genetic mutations drive a phenotypic transformation supported by dysregulation of metabolism and interactions with the tissue microenvironment [3].

In the progression of tumorigenesis, mutated cells continually reshape their environment by recruiting new blood vessels, inflammatory immune cells and growth factors. These environmental changes can in turn promote the genetic instability and aberrant cellular signaling that drive continued cellular proliferation. Notably, every cancer is unique in the series of genetic mutations and environmental transformations it undergoes. Even within a single tumor, expansion of cellular populations accumulating different mutations and subject to disparate environmental signals results in significant genomic and phenotypic heterogeneity [4]. This heterogeneity represents a tremendous impediment to the selection of appropriate therapies and to the assessment of their efficacy. In recent years, these considerations have led to a significant paradigm shift in oncology away from standardized treatments and towards individualized precision medicine [5].

The importance of imaging to these precision medicine initiatives cannot be overstated. The most widely used clinical imaging methods provide anatomical detail suitable for assessing tumor size. Treatment response in solid tumors is still most commonly assessed by tracking this radiological tumor size over time [6]. However, there is much greater potential for precisely quantifying disease state and treatment response through functional and molecular imaging modalities [7]. While these molecular imaging methods often lack significant morphological detail, they provide direct pathophysiological insights into individual tumors that are more sensitive to the diversity of cellular conditions present.

New molecular imaging methods that expand the clinical capability to measure the physiological and biochemical state of tissues in a rapid and reproducible manner will be a critical component of precision medicine for cancer. One such emerging molecular imaging modality is hyperpolarized (HP) ^{13}C MRI [8]. In this technique, a small quantity of ^{13}C labeled molecules are subjected to conditions that generate a large nuclear magnetic polarization. The polarization process takes place in a polarizer separate from the MRI system used for imaging. Once removed from the polarizer the HP agent is quickly administered by intravenous injection, and imaging can provide direct and quantitative measurements of perfusion, uptake and metabolism *in vivo*. Clinical trials are currently underway at several sites worldwide investigating HP MRI in cancer and other diseases [9, 10].

HP MRI has tremendous potential to detect short-term changes in tumor metabolism and to provide non-invasive measurements of treatment response, but standardized methods for image acquisition and analysis have not been established. Robust HP MRI acquisition strategies are difficult to formulate due to the transient nature of the HP signal. Outside of the polarizer the HP agent depolarizes continuously, and a portion of the HP signal is depleted by each imaging measurement. In addition to these magnetization loss mechanisms, the evolution of HP signals *in vivo* is further complicated by the effects of capillary delivery of the HP agent to tissues of interest. In most cases, analysis of HP MRI data is very challenging since a significant but unknown proportion of the signal arises from blood rather than the cellular and extracellular

spaces that are often of primary interest. To derive quantitative biomarkers of tissue function, these effects must be considered in the design of HP imaging experiments and properly accounted for in the analysis methods, for example via pharmacokinetic modeling [11] and numerical simulation [12]. Additional challenges arise when formulating imaging strategies for novel HP agents, which can create signals very difficult to image *in vivo* due to their very brief lifetimes and the ranges of resonant frequencies they exhibit.

In this work, we develop a framework for acquisition and analysis of preclinical HP imaging data. This framework includes extensive infrastructure for numerical simulation of HP imaging experiments, both for the purpose of experimental design and for pharmacokinetic analysis of HP agent perfusion and uptake in tissue. The acquisition methods presented here provide a high degree of flexibility in the strategy of chemical and spatial encoding, and also permit the application of a novel method for preferentially suppressing the vascular component of HP signals *in vivo*. The feasibility of this novel HP signal suppression strategy is demonstrated via imaging of HP ^{13}C urea in rodents. Furthermore, an investigation of the hepatic metabolism of the novel imaging agent, [2-^{13}C]dihydroxyacetone, exemplifies the flexibility of our imaging framework and the significant potential of HP MRI to improve our basic understanding of the biochemical foundations of many diseases.

1.1 Specific Aims

The overall goal of this work is to improve measurements of the physiological fate of HP agents *in vivo*. Such measurements are challenging due to both the transient nature of HP signals and their dynamic evolution by perfusion, capillary extravasation and interaction with target biology. If these effects are properly accounted for in the acquisition and analysis of HP images, quantitative biomarkers of tissue perfusion and metabolism can be obtained [11]. Such biomarkers hold tremendous potential in the rapid assessment of disease state, for example in the context of early treatment response [13–19].

This project has developed an imaging method capable of resolving the signals observed in HP MRI experiments with ^{13}C urea, [1-^{13}C]pyruvate and [2-^{13}C]dihydroxyacetone (DHA). Our central hypothesis is that *an optimized image acquisition and analysis protocol will permit characterization of the physiological fate of HP agents with chemical, spatial and functional resolution*. This hypothesis has been tested with the following aims:

Aim 1: *Implement a MR imaging method for flexible dynamic preclinical imaging of HP agents.* We will create a pulse sequence for our preclinical MRI system capable of implementing multiple methods for encoding k-space and chemical shift. Selectivity for dynamic imaging of individual chemical shifts will be enabled through two of the most widely used methods in HP MRI: spectral-spatial excitation pulses [20] and constrained phase-sensitive decomposition of echo-time shifted readouts (IDEAL) [21, 22]. The SNR performance of chemical shift encoding via spectral-spatial excitation and IDEAL imaging will be compared in both numerical simulations and ^{13}C-enriched thermal phantom experiments. For simulations, the pulse sequence parameters usable on our preclinical MRI system will be used in order to match the results obtained in phantom experiments. These results will guide the selection of an acquisition strategy that provides optimal image quality for *in vivo* HP imaging.

Aim 2: *Evaluate perfusion and permeability effects by imaging HP ^{13}C urea in the rat liver with and without motion sensitization.* Dynamic imaging of HP urea will

probe vascular perfusion in the liver, measuring the representative blood volume fraction for hepatic tissue and the permeability of liver microvasculature to a low molecular weight imaging agent. Diffusion preparation gradients can be applied in an interleaved fashion during the dynamic experiment to suppress moving signals from flowing blood, preferentially weighting the HP signal to urea within the extravascular space and improving the accuracy of this measurement. The diffusion gradient magnitude and timing, as well as other sequence parameters such as repetition time and excitation angle, will be chosen based on simulation experiments quantifying the accuracy and reproducibility of pharmacokinetic modeling of HP urea uptake in tissue. While urea is not itself a metabolic agent, these results will demonstrate the capability of our imaging method to resolve HP signals arising from the metabolically distinct vascular and tissue spaces.

Aim 3: *Acquire spectroscopic images of HP DHA metabolites in vivo.* Imaging of HP DHA and its downstream metabolites in the rat liver will be conducted with the sequence developed in Aim 1. Since the signal intensities of many of these metabolites is quite weak *in vivo*, sequence parameters will be chosen carefully to maximize SNR. Imaging of these metabolic signals is particularly challenging due to their very wide chemical shift separation ($>$150 ppm) and rapid relaxation in tissue. Despite these obstacles, HP DHA imaging can probe the biochemical flux into multiple metabolic pathways, including glycolysis, gluconeogenesis and ketogenesis. This agent therefore provides a wealth of information on the metabolic state of the liver and mammalian body as a whole.

Chapter 2

MRI Physics

Magnetic Resonance Imaging is unique amongst medical imaging modalities in the physics of its signal generation and detection. Most medical imaging is based on the measurement of radiative energy passing through tissue from internal or external sources. In contrast, MRI maps the volume density and relaxation properties of nuclear spins using static and time-varying magnetic fields. The fundamental physics underpinning MRI are the same as Nuclear Magnetic Resonance (NMR) spectroscopy, which is widely used in a variety of disciplines including chemistry and materials science.

In this chapter we will review the basis of NMR signals, techniques for strengthening these signals via hyperpolarization, relaxation and contrast mechanisms, and Fourier methods for spectroscopy and imaging.

2.1   NMR Signal

In a standard NMR experiment a sample is placed in a strong, uniform magnetic field. By virtue of the elementary particles that make up individual nuclei, they possess quantized values of angular momentum called spin. Nuclear spin can take on half-integer or integer values depending on the number of protons and neutrons a nucleus contains. The nuclei most commonly used in NMR and MRI, and most relevant to this work, have a spin quantum number of ½. A nucleus with non-zero spin possesses

a magnetic moment and experiences a torque given by the cross-product of the individual nuclear magnetic moment vector and the magnetic field it experiences. This torque causes the nuclear moment to precess at the Larmor frequency [23], which is proportional to the magnetic field strength ($\vec{B_0}$) and nuclear gyromagnetic ratio (γ):

$$\omega_0 = 2\pi f_0 = -\gamma \vec{B_0} \tag{2.1}$$

Here the negative sign indicates a left-handed direction of precession relative to the direction of $\vec{B_0}$. The quantity ω is used throughout this chapter to denote angular frequency (in radians per unit time), while f denotes cyclic frequency (in cycles per unit time). A convenient way to express the gyromagnetic ratio in the latter case is $\frac{\gamma}{2\pi}$, typically in units of megahertz per Tesla.

A nucleus with a spin of I can inhabit $2I + 1$ energy levels within a magnetic field, referred to as spin states. These nuclear spin states correspond to differing angles between the precessing nuclear magnetic moment and $\vec{B_0}$. For an isolated spin ½ nucleus, the directional axis of its Larmor precession is either parallel (+) or antiparallel (-) to $\vec{B_0}$ [24]. At equilibrium, the ratio of the number of nuclei in the antiparallel alignment state to those in the parallel state follows a Boltzmann distribution [25]:

$$\frac{N_-}{N_+} = e^{-\frac{\gamma \hbar B_0}{kT}} \tag{2.2}$$

Here $\hbar$ and k denote the reduced Planck's constant and Boltzmann constant, respectively, while T is temperature. The number of nuclear moments in the state with lower potential energy, aligned parallel to $\vec{B_0}$, is greater than the number aligned antiparallel at equilibrium. This excess of nuclei in the lower energy alignment state gives rise to an aggregate magnetic moment ($\vec{M}$) in the sample. At equilibrium, $\vec{M}$ is aligned with $\vec{B_0}$ and not detectable. However, when a time-varying magnetic field ($\vec{B_1}$) is applied to the sample at the Larmor frequency and perpendicular to $\vec{B_0}$, $\vec{M}$ is progressively nutated out of alignment with $\vec{B_0}$. For the values of $\vec{B_0}$ used in NMR and MRI, f_0 is in the Radio Frequency (RF) range and $\vec{B_1}$ is therefore referred to as a RF pulse. After the application of this RF pulse, the portion of $\vec{M}$ perpendicular to $\vec{B_0}$ is transiently detectable in the form of a voltage induced in conductive coils of the NMR system [26, 27].
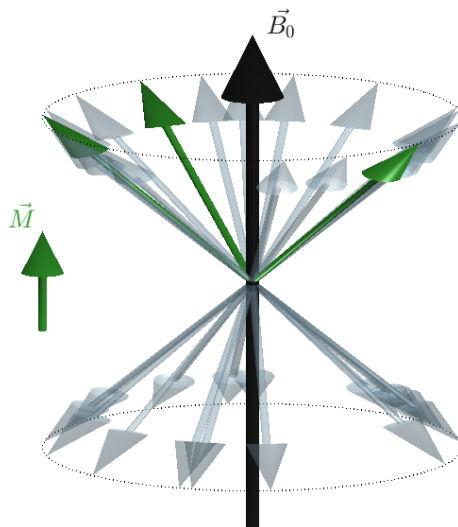
Figure 2.1: For spin ½ nuclides at thermal equilibrium, individual magnetic moments in an applied magnetic field ($\vec{B}_0$) precess at the Larmor frequency with the axis of precession aligned with or against $\vec{B}_0$. A slightly greater number of nuclear moments align with $\vec{B}_0$, which generates a small net magnetic moment ($\vec{M}$) as shown here in green. The population difference between spin states in this illustration is much larger than typically observed in thermally polarized spin systems.

The signal recorded in a MRI examination is therefore an ensemble measurement arising from the bulk magnetic polarization of a small fraction of the NMR-active nuclei present. The most common isotope employed in magnetic resonance experiments is protium (hydrogen-1, ^{1}H), which is the most abundant isotope in the universe and ubiquitous in living tissue. Other isotopes of nuclei common in biological systems, such as carbon-13 (^{13}C), are useful in biochemical and medical research. However, these applications are often limited by low isotopic abundance and low nuclear gyromagnetic ratio, both of which result in poor sensitivity. From equation 2.2, the fraction of nuclear moments in the lower energy state can be derived:

$$P = \frac{N_+ - N_-}{N_+ + N_-} = \tanh \frac{\gamma \hbar B_0}{2kT} \tag{2.3}$$

A larger NMR signal can therefore be achieved through a greater nuclear polarization fraction at greater static magnetic field strengths or lower temperatures. However, neither $\vec{B}_0$ or T can be easily manipulated to directly improve MRI sensitivity in clinical practice. Plots of polarization fraction for the two nuclides of greatest interest in this work are shown in figure 2.2. Even at 7 T, the strongest $\vec{B}_0$ currently available for

clinical MRI, the thermal polarization fraction of excess ^{13}C nuclear moments aligned with $\vec{B}_0$ is approximately 6 ppm at room temperature.
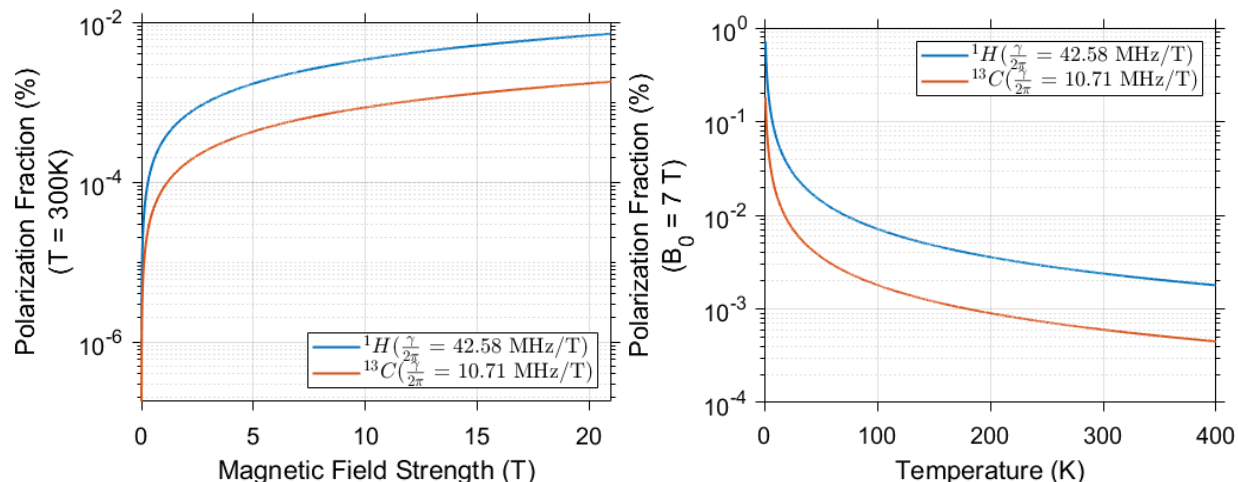
Figure 2.2: The thermal equilibrium spin polarization fractions for ^{1}H and ^{13}C plotted semi-logarithmically against magnetic field strength (B_0 in units of Tesla) and temperature (T on the Kelvin scale) show larger polarizations for lower T or for greater B_0 or γ.

2.2 Hyperpolarization Techniques

A variety of techniques have been developed to transiently overpopulate the nuclear alignment state parallel to $\vec{B}_0$ and provide dramatic enhancements in NMR detection sensitivity. The simplest such hyperpolarization method exposes the NMR sample to a high magnetic field at low temperature [28]. This technique is known as brute-force polarization, and does not provide as large sample polarizations as other hyperpolarization methods that rely on the transfer of spin state polarization to the NMR-active nuclei of interest from electrons or molecular hydrogen.

When the NMR nuclei are in the gaseous state, hyperpolarization is most easily achieved via spin-exchange optical pumping (SEOP). In this technique, most commonly used for polarizing xenon-129 (^{129}Xe) and helium-3 (^{3}He), circularly polarized infrared light is used to polarize the electrons of an alkali metal [29]. The polarized electrons then transfer their spin polarization to the NMR nuclei via atomic collisions. Polarization fractions of $>50\%$ can be achieved with SEOP for ^{129}Xe [30] and the hyper-

polarized (HP) gas produced has enabled exciting new MRI methods *in vivo*, primarily for imaging lung function. Since SEOP relies on molecular collisions for polarization transfer it is most feasible in the gaseous state which limits its utility in polarizing the NMR isotopes and molecules most useful for probing biochemistry *in vivo*.
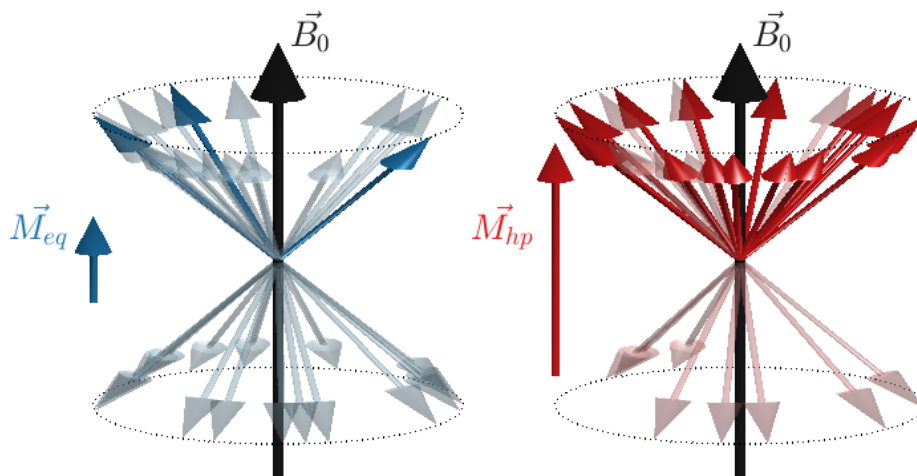
Figure 2.3: In spin systems at thermal equilibrium, the number of excess nuclear moments aligned with $\vec{B}_0$ is very small, which can result in poor detection sensitivity for the net moment ($\vec{M}_{eq}$, left). This poor sensitivity is particularly problematic for NMR studies of low gyromagnetic ratio nuclei such as ^{13}C. Hyperpolarization techniques create spin populations containing a much larger proportion of nuclear moments aligned with $\vec{B}_0$, producing a greater aggregate magnetic moment ($\vec{M}_{hp}$, right).

In an alternative hyperpolarization method, the spin order of molecular hydrogen is transferred to molecules of interest through chemical couplings. In the first step of this process, called parahydrogen induced polarization (PHIP), molecular hydrogen (H_2) is exposed to a catalyst at cryogenic temperatures. These conditions enrich the parahydrogen isomer (pH_2) in which the magnetic moments of the individual ^{1}H nuclei are oriented in opposite directions [31]. The pH_2-enriched spin system therefore has a uniformity of ^{1}H spin state that is much greater than a population of thermally polarized ^{1}H nuclei, and this spin order persists when the H_2 is warmed to ambient temperatures. The spin order can then be transferred to other molecules via chemical hydrogenation reactions or via simultaneous interaction of both pH_2 and the molecule of interest with a catalyst. Using an appropriate catalyst or polarization transfer methods in an NMR system, the pH_2 spin order can be used ultimately to enrich the

parallel spin state of ^{13}C or ^{15}N nuclei in organic molecules [32]. Unlike other hyperpolarization methods, PHIP requires a chemical interaction of H_2 with the substrate that is to be polarized, which is generally a less efficient polarization transfer method than direct interaction of nuclei with strongly polarized electrons. Additionally, the catalysts used in this process can be toxic and difficult to remove from solution in the timeframe necessary to utilize the HP solution *in vivo*. As a result, PHIP methods have been limited to *in vitro* and preclinical applications.

The hyperpolarization technology employed in this work, Dynamic Nuclear Polarization (DNP), differs from the methods described above in that it relies on the transfer of spin polarization from electron to nucleus in the solid state via hyperfine coupling [33]. DNP, specifically the more recently developed dissolution DNP method that allows very large polarization fractions to be achieved for ^{13}C in the liquid state, will be discussed in greater detail in the following chapter.

2.3 Relaxation and Contrast Mechanisms

A distinguishing factor of MRI compared to other medical imaging modalities is the variety of contrast mechanisms that affect the imaging signal. For the ^{1}H imaging routinely performed clinically, these mechanisms provide exquisite soft tissue contrast and permit imaging of tissue function in ways not possible via other modalities. In HP MRI, they must be accounted for in quantifying imaging signals in order to derive parameters reflective of tissue function.

Spin-Lattice (T_1) Relaxation and Radio Frequency Excitation

Regardless of whether the bulk magnetization is derived from thermal polarization or hyperpolarization methods, $\vec{M}$ will relax over time towards thermal equilibrium. A variety of mechanisms contribute to this relaxation process, however they are in general mediated by the transfer of energy from individual nuclear magnetic moments to their surrounding environment. For this reason, this relaxation process is often called spin-lattice relaxation. By convention, the direction of $\vec{B}_0$ is assigned the longitudinal

or z-axis in 3D space, leading to the alternative term, longitudinal relaxation. For a sample with initial z-axis magnetization M_{init}, the z-component of $\vec{M}$ will change over time to approach the thermal equilibrium magnetic moment of M_0. The rate of this change is directly proportional to the displacement of M_z from this equilibrium value, resulting in exponential growth or decay towards M_0 with a time constant of T_1 [25, 34].

$$M_z(t) = M_{init}e^{-\frac{t}{T_1}} + M_0\left(1 - e^{-\frac{t}{T_1}}\right) \tag{2.4}$$

Note that without application of any RF pulse, M_{init} will be $\gg M_0$ for HP experiments. If $t = 0$ denotes the moment at the end of a RF pulse applied to a thermally polarized spin system, M_{init} will be $< M_0$. For a RF pulse that is brief in duration, the nutation angle (θ) will determine the redistribution of $\vec{M}$ into the x-, y- and z-components by simple trigonometry. For short RF pulses applied at the Larmor frequency, this excitation angle can be calculated from the nuclear gyromagnetic ratio and the time integral of $\vec{B}_1$ [35].

$$\theta = \gamma \int_0^T \vec{B}_1(\tau)d\tau \tag{2.5}$$

where T is the duration of the RF pulse.

Immediately after a RF pulse, $\vec{M}$ will precess about the z-axis at the Larmor frequency. It is therefore useful to consider a coordinate system, distinct from the true laboratory reference frame, in which the x-y plane is rotating about the z-axis at this frequency. In such a rotating frame of reference, $\vec{B}_1$ appears as a vector along a single direction in the transverse (x'-y') plane for a simple RF pulse. If an RF pulse is applied in the x' direction, $\vec{M}$ is nutated about $\vec{B}_1$ leading to components in the y' and z directions. Immediately after the RF pulse is applied to a spin system with $\vec{M}$ initially along the z-axis these components are determined by the excitation angle [34]:

$$M_{y'} = M\sin\theta$$
$$M_z = M\cos\theta \tag{2.6}$$

In this case, the quantity $M_{y'}$ represents the detectable component of the aggregate magnetization at the end of the RF pulse, after which M_z recovers or decays towards M_0 as defined in equation 2.4.

In studies using thermally polarized spin populations, a shorter T_1 is generally favorable from a signal to noise perspective. A shorter T_1 allows the thermal spin system to return to equilibrium more quickly allowing repeated application of RF pulses and averaging of multiple measurements in a brief timeframe. For HP spin systems, however, the level of thermal polarization is typically negligible and undetectable *in vivo*. T_1 therefore represents a decay process that limits the overall lifetime of the HP signal. Longer T_1 time constants are therefore preferable in HP MRI, particularly when the HP nuclei rely on relatively slow physiological processes such as systemic blood flow to enter the tissues of interest. For the same reason, small excitation angles are often used in HP experiments so as not to deplete the HP magnetization before the nuclei can experience uptake and/or chemical transformation.

A comprehensive review of the mechanisms contributing to spin-lattice relaxation is beyond the scope of this discussion, however the most dominant effect in ^{1}H NMR is dipole-dipole relaxation. In this relaxation mechanism, the translational, rotational and intramolecular motion of molecules carrying magnetic moments cause them to impress time-varying magnetic fields on the detectable nuclear moments. When these local fields oscillate close to the Larmor frequency, they can cause nutation of nearby magnetic moments towards the z-axis [36]. Notably, both dipoles in dipole-dipole relaxation do not need to be NMR-active nuclei. Paramagnetic electrons — found in (triplet) molecular oxygen, deoxygenated hemoglobin and gadolinium-based contrast agents — are also magnetic dipoles that can mediate this form of relaxation. These effects are fairly well characterized for ^{1}H MRI, however their impact on relaxation of HP ^{13}C *in vivo* warrant further study. In particular, the effect of blood oxygenation state on the T_1 of common HP ^{13}C agents has not been as fully characterized at clinical field strengths, which could be an important consideration since these agents are nearly always administered intravenously.

One spin-lattice effect, chemical shift anisotropy, is worth special mention because of its significance in HP ^{13}C imaging and spectroscopy. This effect is most impactful when the ^{13}C label resides in a molecule with anisotropic molecular structure and when the labeled molecule is not able to move freely in solution [37]. Both of these

situations are common for metabolically active HP ^{13}C agents, which are frequently ^{13}C-labeled on highly anisotropic carboxyl groups and bind to proteins that mediate transport and metabolism *in vivo*. The strength of this chemical shift anisotropy effect scales with B_0^2. This effect can result in a decreasing T_1 with increasing magnetic field strength for many ^{13}C agents, which is the opposite of the trend typically observed in ^{1}H NMR.

Spin-Spin (T_2 and T_2^*) Relaxation

Prior to application of the RF pulse, $\vec{M}$ is oriented along the z-axis due to the partial coherence of the individual nuclear magnetic moment vectors in this direction. Upon being nutated into the transverse plane, $\vec{M}$ maintains this phase coherence in the direction along which it is oriented at the end of the RF pulse. However, this phase coherence is not permanently maintained due to variations in the local magnetic field experienced by the vast number of nuclei in every milliliter of fluid or tissue. As described in the previous section, these localized magnetic non-uniformities can result from the superposition of $\vec{B}_0$ and the magnetic moments of nearby nuclei, electrons and molecules. The distribution of local magnetic fields experienced by individual nuclei causes a matching distribution in precessional frequency, as indicated in equation 2.1. This spread of frequencies in the sample volume appears over time as a progressive loss of phase coherence for the component of $\vec{M}$ in the transverse plane, M_{xy}. As individual nuclear magnetic moments fall out of phase with one other, the magnitude of the detectable signal induced by M_{xy} in a NMR signal reception coil decreases exponentially with a time constant T_2^* [25, 34]. If the component of $\vec{M}$ in the transverse plane is M_{init} at $t = 0$ then in the rotating reference frame,

$$M_{xy}(t) = M_{init} e^{-\frac{t}{T_2^{(*)}}} \tag{2.7}$$

where $T_2^{(*)}$ can be either T_2^* or T_2 depending on the type of MR scan used. When viewed in the rotating frame of reference, M_{xy} behaves as described in this equation. However, in the laboratory frame the exponential decay described here corresponds to the envelope of a damped sinusoid that oscillates at the Larmor frequency. This damped

sinusoidal signal is the induced voltage directly recorded in a MR study, and is often called the Free Induction Decay (FID).

Since this relaxation mechanism refers to the loss of partial phase coherence for the ensemble of spin angular moments that generate detectable magnetization in the transverse plane, it is often called spin-spin or transverse relaxation. In reality, additional mechanisms account for the observed M_{xy} relaxation rate, including chemical exchange, direct transfer of spin state polarization between pairs of nuclei and the mechanisms that mediate spin-lattice relaxation [25]. Conservation of angular momentum dictates that the loss of transverse spin coherence described in equation 2.7 must occur at least as fast as the change in longitudinal spin coherence expressed in equation 2.4. In other words, $T_2 \leq T_1$. As discussed in the previous paragraph, the assumption of a perfectly uniform $\vec{B}_0$ field is violated for even small NMR and MRI sampling volumes. In addition to the microscopic mechanisms described above, $\vec{B}_0$ non-uniformities arise from the presence of paramagnetic substances, mismatches in magnetic susceptibility at air-tissue interfaces, and both fundamental and practical limitations in MRI hardware. For the signal recorded immediately following a single RF pulse, the decay time constant encapsulates all of these effects and is referred to as T_2^*. If spins experiencing these inhomogeneities are subjected to two RF pulses in quick succession, the second pulse will cause a reversal of precessional frequency for some nuclei and refocus a portion of the dephased M_{xy}. After a delay equal to the time separation of the two RF pulses, the maximal amount of refocusing occurs and a signal called a spin echo is generated [38]. The greatest spin-echo amplitude occurs for a refocusing RF pulse nutation angle of 180 degrees. Even when a perfect 180 degree refocusing pulse is applied, not all mechanisms of spin-spin relaxation are fully reversed. The spin echo signal will therefore possess a decreased amplitude relative to the signal present immediately after the first RF pulse. Multiple spin echoes can be generated by applying multiple refocusing pulses, and T_2 is the time constant in equation 2.7 describing the decreasing amplitudes of these subsequent spin echoes with time.

T_2^* accounts for mechanisms of spin coherence loss that are not captured by T_2.

The rate of T_2^* decay is therefore always faster than T_2 decay, and the T_2^* rate can be expressed as the sum of the T_2 rate and a rate that accounts for these additional effects (T_2') [25].

$$\frac{1}{T_2^*} = \frac{1}{T_2} + \frac{1}{T_2'} \tag{2.8}$$

Small values of T_2' occur most often in ^{1}H MRI for sampling volumes with poor $\vec{B}_0$ homogeneity or containing paramagnetic molecules, leading to substantial differences between T_2 and T_2^*. When imaging many of the most commonly used HP ^{13}C substrates, there is also a large difference between T_2 and T_2^* due in part to the large sampling volumes in which excellent $\vec{B}_0$ uniformity is difficult to achieve. Although this makes spin echo experiments appealing for HP ^{13}C MRI from a signal to noise perspective, the effects of refocusing pulses on HP spin systems need to be handled carefully in order to avoid extinguishing the large and non-recoverable z-axis magnetization. For this reason, double spin echo methods with two refocusing pulses have been used for HP imaging [39]. If both refocusing pulses have a 180° nutation angle and occur close to one another in time, the second pulse will mostly reverse the effects of the first pulse on the z-axis magnetization and preserve HP signal for imaging over time.

The Bloch Equations

The Bloch equations are a set of equations describing the behavior of the aggregate NMR magnetization over time. These equations are named for Felix Bloch, who first introduced in 1946 such a set of equations accounting for the RF excitation and relaxation effect described in the preceding sections. They can be derived as solutions to the following vector-valued differential equation [25, 34].

$$\frac{d\vec{M}}{dt} = \gamma \vec{M} \times \vec{B} + \frac{1}{T_1}\left(\vec{M}_0 - \vec{M}_z\right) - \frac{1}{T_2}\vec{M}_{xy} \tag{2.9}$$

Here all vector variables are composed of three values describing the corresponding magnetic fields in each direction. $\vec{B}$ describes all external magnetic fields acting on the subject, including $\vec{B}_0$, the magnetic component of RF fields ($\vec{B}_1$), and — as we shall discuss in section 2.5 — magnetic field gradients. The cross product in the first term may be conceptualized as a torque applied to $\vec{M}$ when its direction does not coincide

perfectly with $\vec{B}$, which contains non-zero values in the x and/or y direction when an RF pulse is active. When no RF pulse affects the magnetization, solutions to this differential equation are found in equations 2.4 and 2.7. Following a 90° pulse, the tip of $\vec{M}$ can be visualized as tracing out a damped helix over time as shown in figure 2.4.
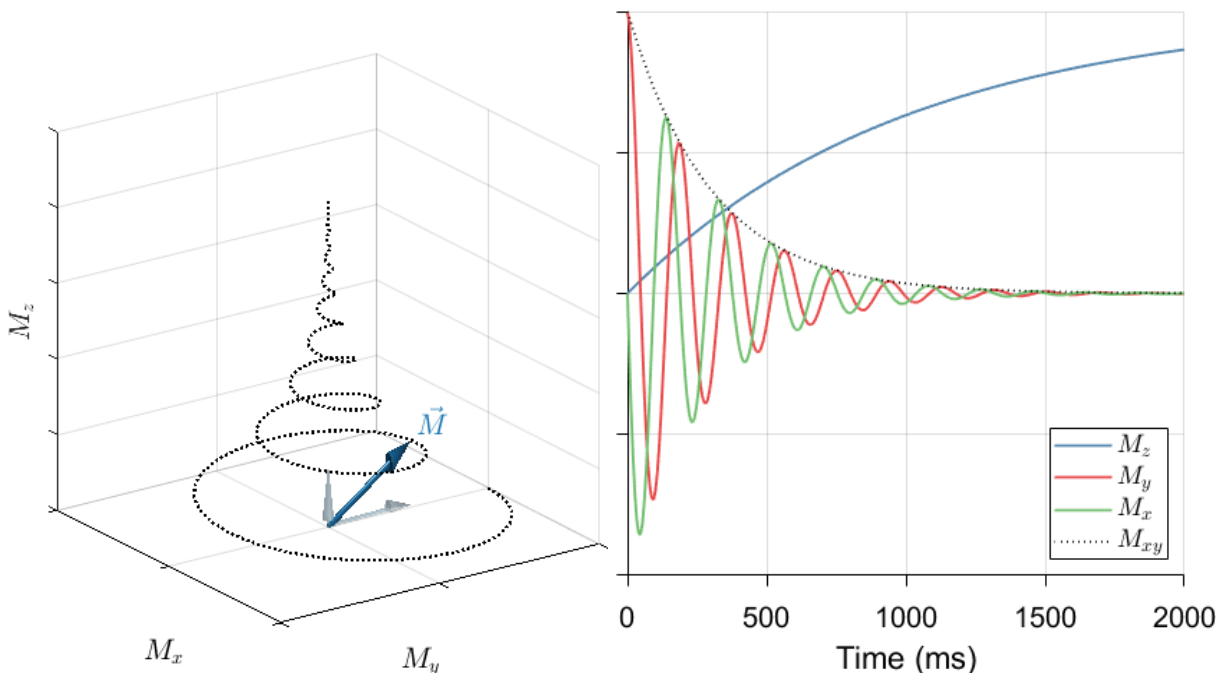
Figure 2.4: After the application of a 90° RF excitation pulse to a thermally polarized spin system at equilibrium, the net magnetization vector ($\vec{M}$) is displaced into the transverse plane. Without any further perturbation, relaxation effects cause this vector to follow a damped helical trajectory as it returns to equilibrium (left). The component of $\vec{M}$ in the transverse plane exhibits sinusoidal oscillation at the Larmor frequency and decays exponentially over time with a rate of $\frac{1}{T_2}$, inducing a characteristic FID signal in an appropriately positioned receiving coil.

Solving equation 2.9 in a more generalized case is difficult due to the cross product in the first term. This non-linear differential equation may also be modified to account for additional effects not described in this form. Some examples of such modifications are the Bloch-Torrey equations [40], which describe effects of molecular diffusion, and the Bloch-McConnell equations [41], which describe the effects of chemical exchange. Application of these equations provide invaluable insight into NMR and MRI experiments, especially for HP MRI in which $\vec{M}$ represents a non-renewable signal source [12].

2.4 NMR Fourier Spectroscopy

Chemical Shift

The transient NMR signal provides detailed information on the chemical environment of the population of polarized nuclei. This effect arises from the diamagnetism of moving orbital electrons, which create a small local magnetic field that opposes $\vec{B}_0$. Nuclei in molecular environments with a greater density of orbital electrons therefore experience a reduced magnetic field due to this diamagnetic shielding. The resulting difference in the impressed magnetic field results in a proportional shift in the precessional frequency of the nuclear magnetic moment, called a chemical shift [42]. For a nucleus experiencing an effective magnetic field ($\vec{B}_{eff}$) that is the combination of $\vec{B}_0$ and the diamagnetic electron field (B_e), equation 2.1 can be rewritten:

$$f = -\frac{\gamma}{2\pi}\vec{B}_{eff} = -\frac{\gamma}{2\pi}(\vec{B}_0 - \vec{B}_e) = f_e - f_0 \tag{2.10}$$

Here, f_e denotes the relative chemical shift frequency, which is the frequency of the signal observed upon demodulation of the NMR system frequency, f_0, from the directly measured FID. This relative frequency is typically determined empirically for a given chemical environment relative to a reference chemical shift that is assigned a chemical shift of zero for each NMR nucleus. For ^{1}H and ^{13}C spectroscopy this reference shift corresponds to the resonances of these nuclei in tetramethylsilane [43]. The frequency of a chemical shift may be expressed relative to the nuclear reference shift in units of Hz or ppm, with the latter having the advantage of being independent of $\vec{B}_0$. If the reference chemical shift (in Hz) for a given nuclide is f_{ref}, then the chemical shift at any frequency in ppm is given by:

$$\delta = \frac{f - f_{ref}}{f_{ref}} \times 10^6 \tag{2.11}$$

The convention of expressing this quantity in ppm derives from the fact that the numerator of this equation is typically expressed in Hz while the denominator is on the order of MHz for most modern NMR and MRI systems. By convention, the chemical shift axis is usually presented with decreasing values from left to right. This orientation places signal from nuclides experiencing less diamagnetic electronic shielding

on the left side of graphs and those experiencing more shielding on the right side. Chemical shifts observed in ^{1}H spectroscopy are typically in the 0 to 12 ppm range, or an approximately 3.6 kHz bandwidth at 7 T. Due to the greater diversity of molecular bonding for carbon, a much wider range of shifts is observed in ^{13}C spectroscopy that extends from 0 to >200 ppm (>15 kHz at 7 T).

Since chemical shift is an effect determined by the intramolecular environment of nuclear magnetic moments, it is distinct from the effects of the distribution of localized precessional frequencies that mediate the relaxation effects discussed in the previous sections. For an identical $\vec{B}_{eff}$, all chemically identical nuclides (e.g. the protiums in water or in the methyl group of a specific type of fat molecule) would ideally resonate at precisely the same frequency. In reality, each set of chemically equivalent nuclear moments is observed to have a distribution of frequencies due to the differing microscopic magnetic fields produced by molecular moments and local $\vec{B}_0$ inhomogeneities in the vicinity of the individual nuclides. The width of this frequency distribution observed for each chemical shift is therefore related directly to the rate of spin-spin relaxation that determines the lifetime of the FID. If contributions to spin-spin relaxation from effects other than localized variations in magnetic field are negligible, the width of the frequency distribution about a chemical shift at half of its maximum amplitude is [34]:

$$\Delta f_{\frac{1}{2}} = \frac{1}{\pi T_2^*} \qquad (2.12)$$

Under ideal conditions, this equation describes the width of a Lorentzian peak for each chemical shift in a properly processed NMR spectrum.

The FID signal generated by the NMR sample or MRI subject is a time-varying voltage produced in a conductive coil via electromagnetic induction. This coil is oriented spatially to intercept the component of the aggregate magnetization vector that lies in the transverse plane, M_{xy}. In the laboratory reference frame, this voltage measured from a sample containing a single chemical shift will be observed to oscillate at the frequency f defined in equation 2.10 and decay over time as specified in equation 2.7. A rough rule of thumb for the lifetime of the FID following an RF pulse is $5 \times T_2^*$. When the FID is demodulated by the NMR system frequency, f_0, the rate of its oscil-

lation becomes f_e and the signal represents M_{xy} in the rotating reference frame. In practice the FID is sampled in quadrature, by mixing the signal from receiving coils with two sinusoids that oscillate at f_0 but possess a 90 degree phase shift relative to one another. This form of sampling produces two components, referred to as In-phase (I) and Quadrature (Q), which are conveniently represented as the real and imaginary parts of a complex-valued signal. If a single chemical shift is present resonating at the angular frequency $\omega = 2\pi f$, the observed in-phase, quadrature and complex signals will be

$$I(t) = M_x(t) = M_{xy}(t)\sin(\omega t)$$

$$Q(t) = M_y(t) = M_{xy}(t)\cos(\omega t) \tag{2.13}$$

$$S(t) = I(t) + iQ(t) = M_{xy}(t)(\sin(\omega t) + i\cos(\omega t)) = M_{xy}(t)e^{i\omega t}$$

where i denotes the imaginary unit and $M_{xy}(t)$ decays with time constant T_2^* as described in equation 2.7. As indicated in this last equation, the complex signal values can be represented either as real and imaginary components or as a complex exponential, which is also called phasor notation. In phasor form, each complex value is specified by its magnitude ($M_{xy}(t)$) and a phase (ωt, with units of radians) that is the product of time and angular frequency. When multiple chemical shifts contribute to the NMR signal, the FID is — in the simplest case — the sum of the individual time domain signals across all species present. The fundamental challenge of NMR spectroscopy lies in extracting the phasor magnitudes ($M_{xy}(t=0)$) and frequencies (f) for these chemical shifts given the observed FID signal ($S(t)$).

Fourier Spectroscopy

The Fourier Transform (FT) provides the frequency content of a time domain signal by decomposing it into a series of sinusoids with varying frequency, phase and amplitude. The FT is defined as the integral of the product of a function, $g(t)$, and a unit phasor [44].

$$\mathcal{F}\{g(t)\} = G(f) = \int_{-\infty}^{\infty} g(t)e^{-i2\pi ft}dt \tag{2.14}$$

Just as the human auditory system interprets pressure applied to the eardrum over time as a series of tones, the FT converts a finite time domain signal into a spectrum

depicting the amplitudes and phases of its constituent frequencies. Applying the FT to the FID recorded in a NMR experiment therefore provides a spectrum representing the magnitudes and precessional frequencies of the aggregate magnetic moments for the chemical shifts present [45].

In practice, the continuous FT given in equation 2.14 is not directly applicable to the FID since this signal is sampled digitally at discrete time points. Instead the Discrete Fourier Transform (DFT) is used, which can be defined for a series of function values ($g(\tau)$) sampled at N equally spaced points as [44]:

$$\mathbb{F}\{g(\tau)\} = G(\nu) = \frac{1}{N} \sum_{\tau=0}^{N-1} g(\tau)e^{-\frac{i2\pi\nu\tau}{N}} \tag{2.15}$$

In the context of NMR and MRI studies, an increment of τ represents the time delay elapsed between subsequent digital samples, called the dwell time (t_D). Intuitively, it is easy to comprehend that high frequency signals must be sampled with a small t_D in order to be measured accurately. After applying of the DFT, a complex-valued NMR spectrum of N discrete frequencies (denoted by ν) is obtained. The total frequency bandwidth is equal to the FID sampling frequency ($1/t_D$). The FID is typically band-pass filtered during the data acquisition process so that frequencies outside of this spectral bandwidth are removed. The RF pulse shape imparts an additional frequency selectivity separate from the bandwidth defined by sampling and the acquisition filter. For a conventional RF pulse, the excitation profile in the frequency domain is approximated by the FT of $\vec{B}_1(t)$ in the rotating reference frame [35]. Using shaped RF pulses therefore provides a straightforward way to modulate the frequency content of the NMR signal, for example in MR Spectroscopic Imaging (MRSI). When a uniform excitation profile is desirable, as in routine NMR spectroscopy, a very short duration rectangular pulse is often used.

In NMR spectroscopy, the Fourier transformed spectrum is usually processed so that the real component depicts the frequency distribution of chemical shifts in the sample. This is accomplished by applying phase corrections to the complex Fourier transformed spectrum that compensate for delays between RF excitation and signal readout, and for variations in effective nutation angle for different chemical shifts
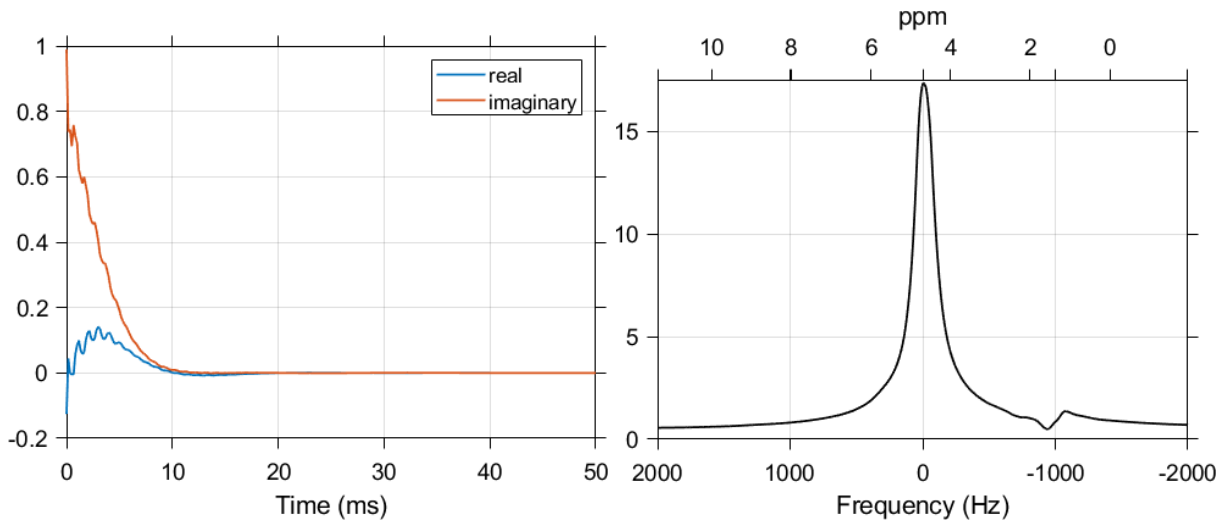
Figure 2.5: ^{1}H FID (left) and magnitude spectrum (right) of a 1.6 cm slab covering a healthy rat liver measured at 7 T. Without any signal suppression strategies, the dominant signals in this spectrum are water and fat at 4.7 and ≈ 1.5 ppm, respectively.

[45]. Once phase-corrected, the real NMR spectrum exhibits chemical shift peaks with linewidths narrower than in a corresponding magnitude spectrum. If relaxation effects are consistent across all chemical shifts observed in a spectrum, the area under the curve measured at a specific fractional peak width for each peak provides a quantitative measure of the relative number of nuclides in that molecular environment.

Noise in NMR Data

NMR data possess notable noise properties due to the complex values they take and the physics underlying signal generation. The noise measured from the receiving coils of a NMR or MRI system in the absence of any RF nutation of the net magnetic moment is ideally zero-mean white noise, without any correlation between coils or between real and imaginary components of the complex-valued data. This noise arises both from the thermal electronic noise in the receiving chain instrumentation and from the motion of molecular moments and charged particles within the sensitive volume of a NMR coil [46]. In general noise with greater variance is produced by larger or more electronically resistive RF coils, or by samples with greater electrical conductivity. Figure 2.6 depicts the distribution of raw (not Fourier transformed) noise acquired using a ^{13}C imaging setup on a preclinical 7 T MRI system, which is employed throughout

this work. The real and imaginary channels each demonstrate a zero-mean Gaussian noise distribution.
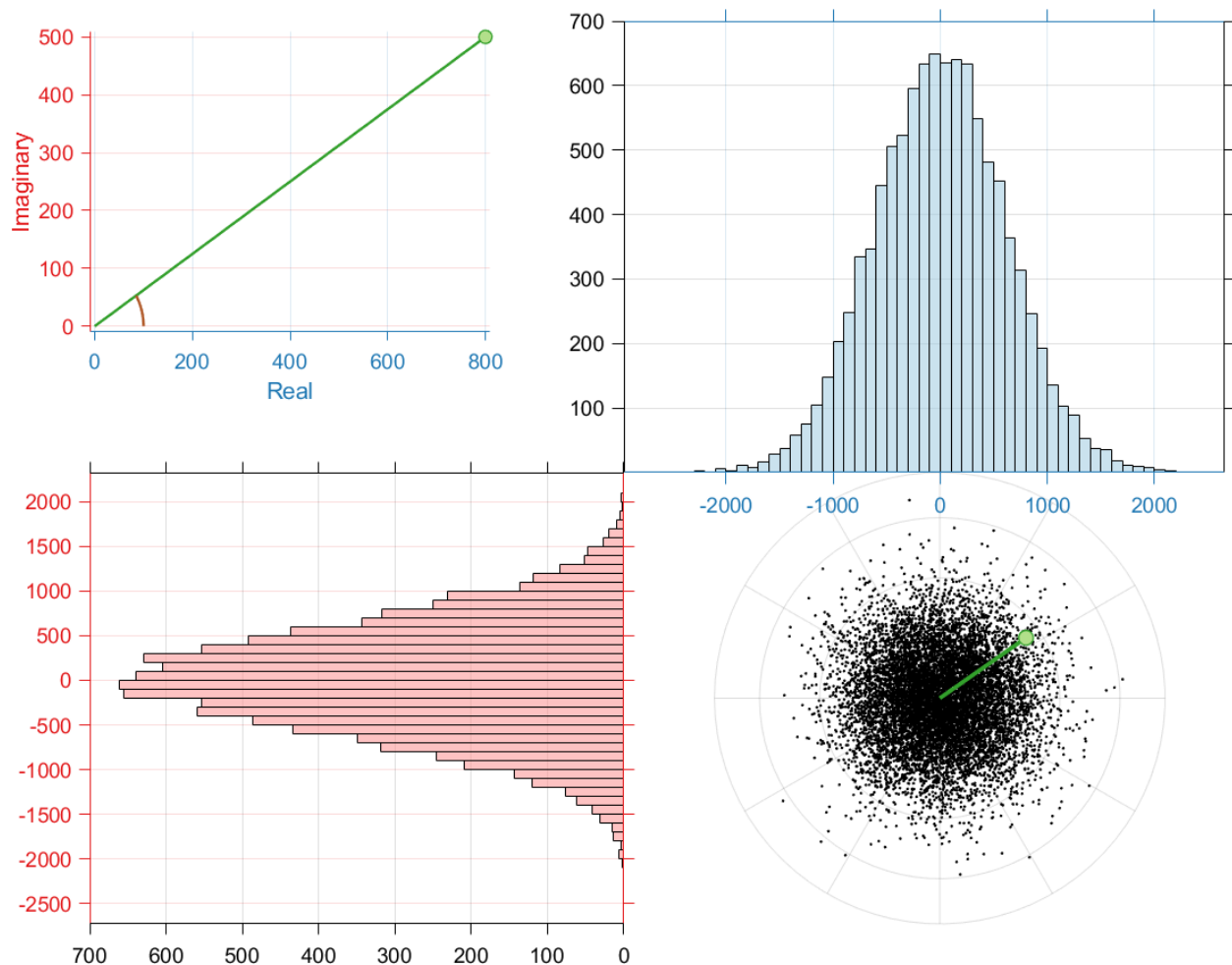
Figure 2.6: MR data take complex values, which can be represented either as real and imaginary Cartesian coordinates (red and blue) or as magnitude and phase polar coordinates (green and brown). The histograms and scatter plot in this figure show the distribution of raw complex noise acquired on a Bruker 7 T preclinical MRI system. These data were measured using a 48 µs dwell time from a 2 cm diameter ^{13}C surface coil. The real and imaginary components of ideal MR noise follow a zero-mean bivariate normal distribution.

For phase-corrected real NMR spectra, the noise seen in regions devoid of signal would ideally exhibit a zero-mean Gaussian distribution similar to that observed in the raw real and imaginary noise, but with a variance scaled by the number of points in the applied DFT. Given a real MR signal amplitude S and noise variance σ^2, the

signal to noise ratio is simply the ratio of the signal to the noise standard deviation.

$$SNR_{real} = \frac{S}{\sigma} \tag{2.16}$$

In MRI, however, images are most often viewed and analyzed in magnitude mode, which presents values corresponding to the radial distance from the origin to a point in the complex plane. The magnitude of complex valued zero-mean Gaussian noise follows a Rayleigh distribution, which is characterized by a standard deviation of $\sqrt{2 - \frac{\pi}{2}}$ times the standard deviation of the underlying complex noise distribution [47, 48]. Accurate estimation of magnitude image SNR therefore requires the application of a correction factor to the noise standard deviation estimate obtained from magnitude images.

$$SNR_{mag} = \sqrt{2 - \frac{\pi}{2}} \frac{S}{\sigma_{mag}} \approx 0.655 \frac{S}{\sigma_{mag}} \tag{2.17}$$

An estimate of σ_{mag} can be made by reconstructing a magnitude image acquired with RF pulse power set to zero, or by specifying a region of a magnitude image that is devoid of signal [49]. In this latter approach, care must be taken to exclude spurious signal created by image artifacts.

The Rayleigh distribution describing pure magnitude noise in MR images is a special case of the more general Rician distribution that is followed by noisy magnitude MR data [50]. For complex signal magnitudes above $\approx 3\sigma$, the Rician distribution exhibits a normal probability density function. At the high SNRs routinely seen in ^{1}H MRI, a Gaussian distribution can therefore be assumed for voxels within a uniform high-signal region of the image. If such a uniform high-signal region is present, its standard deviation may be used as an estimate of σ to calculate SNR using equation 2.16. In HP ^{13}C imaging, however, low SNRs are often observed and coarse image matrices make the calculation of standard deviation within a uniform signal region very difficult. For these reasons, SNR values reported for ^{13}C images in this work are calculated using equation 2.17, with σ_{mag} measured from an image reconstructed from pure acquisition noise.
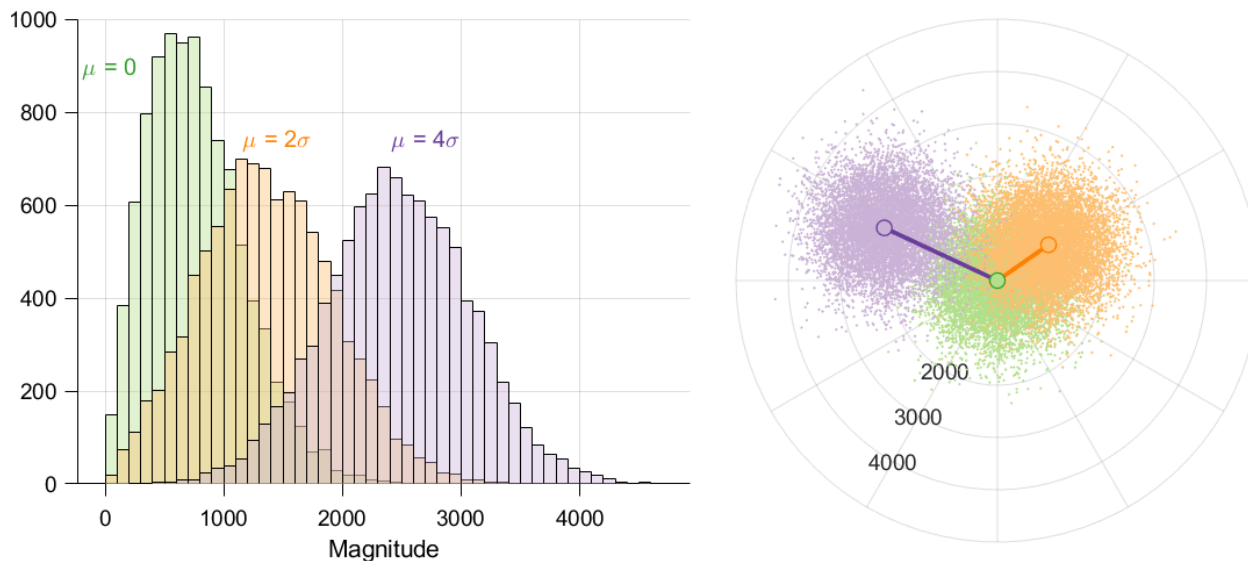
Figure 2.7: Data from figure 2.6 were used to generate magnitude distributions with means (μ) of 0, 2 and 4 times the standard deviation of the underlying complex noise distribution (σ). Magnitude MR data in the presence of ideal noise follows a distribution that is Rician, which is equivalent to the Rayleigh distribution at $\mu = 0$ and approximately equivalent to a normal distribution for $\mu > 3\sigma$.

2.5   Magnetic Resonance Imaging

The Fourier transform is the fundamental mathematical transformation that enables modern NMR spectroscopy. Applying the DFT to a digitized FID provides the signal frequency content in the form of a NMR spectrum from which the chemical content of the interrogated sample may be identified. Importantly, the DFT is a linear and invertible transformation [44]. By applying the inverse DFT (iDFT) to a signal representing a NMR frequency spectrum, the time domain signal (FID) is obtained. If the input signal represents spatial rather than temporal frequency, the iDFT provides a spatial profile of the corresponding subject. Due to the linearity of the iDFT, signals representing spatial frequencies sampled in two or three orthogonal directions can be transformed separately in each direction. This process provides a set of images, and is the mathematical basis for Magnetic Resonance Imaging.

In order to encode spatial frequencies for imaging, linear magnetic field gradients are typically applied [51]. These gradient fields are magnetic fields directed along the same axis as $\vec{B}_0$, with amplitudes that vary linearly along each spatial direction. In
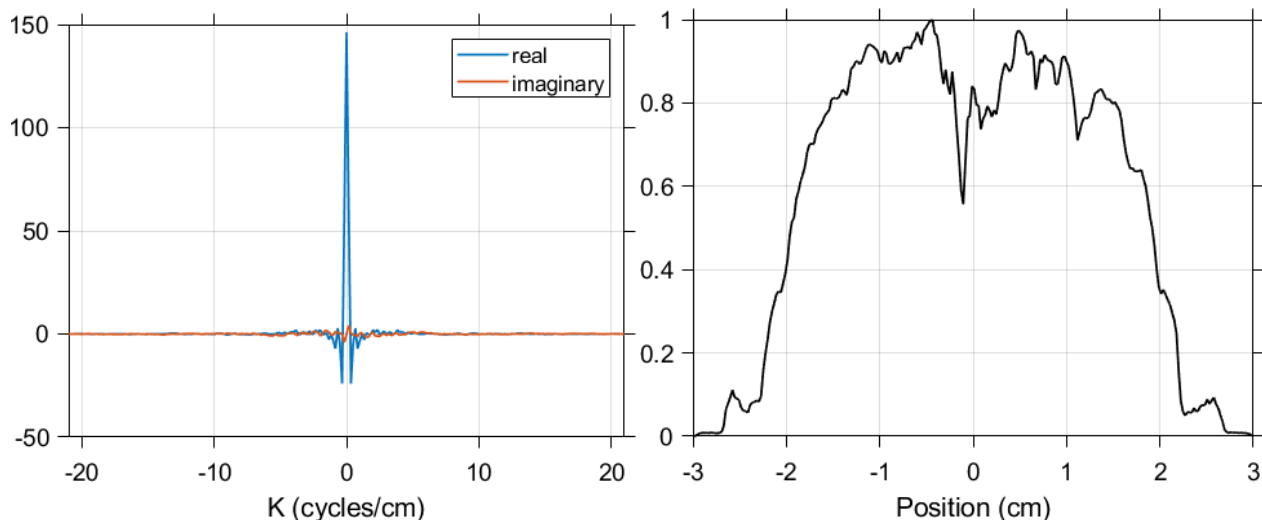
Figure 2.8: The iDFT converts a measured set of spatial frequencies (left) to a spatial projection along the physical direction of the encoding gradient (right). For clarity, only the magnitude spatial profile is shown.

MRI systems, gradients in the x, y and z directions can be used in combination to create an effective linear field gradient in any direction. By applying these gradients for a brief duration of time following an RF pulse, the precessional frequencies of individual nuclear magnetic moments are modulated linearly with position along the corresponding spatial axis.

$$\omega(x) = -\gamma(B_0 + G_x x) \tag{2.18}$$

Sets of nuclear moments that behave identically when manipulated via RF excitation and field gradients are often called isochromats. This term refers to the fact that they precess at the same — or very close to the same — frequency, just as all visible light of a specific color is electromagnetic radiation with the same frequency. In imaging, this denotes a group of NMR moments that share the same frequency by virtue of position and/or chemical shift, depending on the context.

After the application of a gradient field for an increment of time, the isochromats contributing to the detectable net aggregate magnetization (M_{xy}) will possess phases that vary along the gradient axis in direct proportion to the duration of time the gradient is active, the amplitude of the gradient and the nuclear gyromagnetic ratio [52]. Ignoring relaxation effects, the signal observed at any point in time during application

of a constant amplitude linear field gradient (G_x) is proportional to the volume integral of the imaged object's nuclear spin density (ρ), modulated by the spatially varying phase the gradient imparts.

$$S(t) \propto \iiint_V \rho\left(\vec{r}\right) e^{i\omega(\vec{r})t} = \iiint_V \rho(\vec{r}) e^{-i\gamma(B_0 + G_x x)t} \tag{2.19}$$

Here, $\vec{r}$ denotes position in three dimensional space and we are assuming all spins are stationary. By sampling this signal in quadrature at the Larmor frequency as described in section 2.4, the contribution of $\vec{B}_0$ in the exponential argument is eliminated. The remaining phase term in equation 2.19 describes a wave of magnetic moment encoded in the subject along the gradient direction. This wave may be characterized by its k-number, which is the wave's spatial frequency. The k-number is equal to the reciprocal of the wavelength, often expressed in cycles per centimeter. Note that this k-number corresponds only to the spatial phase roll imparted by gradients, and not the wavelength of electromagnetic interactions between the spin system and the receiving coils. Recording the voltage signal induced in a receive coil by M_{xy} in the presence of this wave effectively samples the spatial frequency of isochromats in the subject corresponding to this k-number. The spatial frequency domain discretized by k-numbers sampled in two or three orthogonal directions is called k-space, which is the domain of direct signal detection in modern MRI. In order to encode signals for which the iDFT provides three dimensional images, the goal of a MRI experiment is to sample an extent of k-space uniformly in three directions.

$$S(k_x, k_y, k_z) \propto \iiint_V \rho(\vec{r}) e^{-i(k_x x + k_y y + k_z z)} \tag{2.20}$$

In reality, field gradients cannot be switched on and off instantaneously. Most often they are ramped up and down linearly with time, resulting in trapezoidal gradient pulses. The k-number encoded over time by a gradient pulse of any shape or direction is

$$\vec{k}(t) = \gamma \int_0^t \vec{G}(\tau) d\tau \tag{2.21}$$

where $\vec{G}$ is the gradient amplitude. Sampling of k-space in MRI can be performed in two ways, typically called phase encoding and frequency encoding. Phase encoding
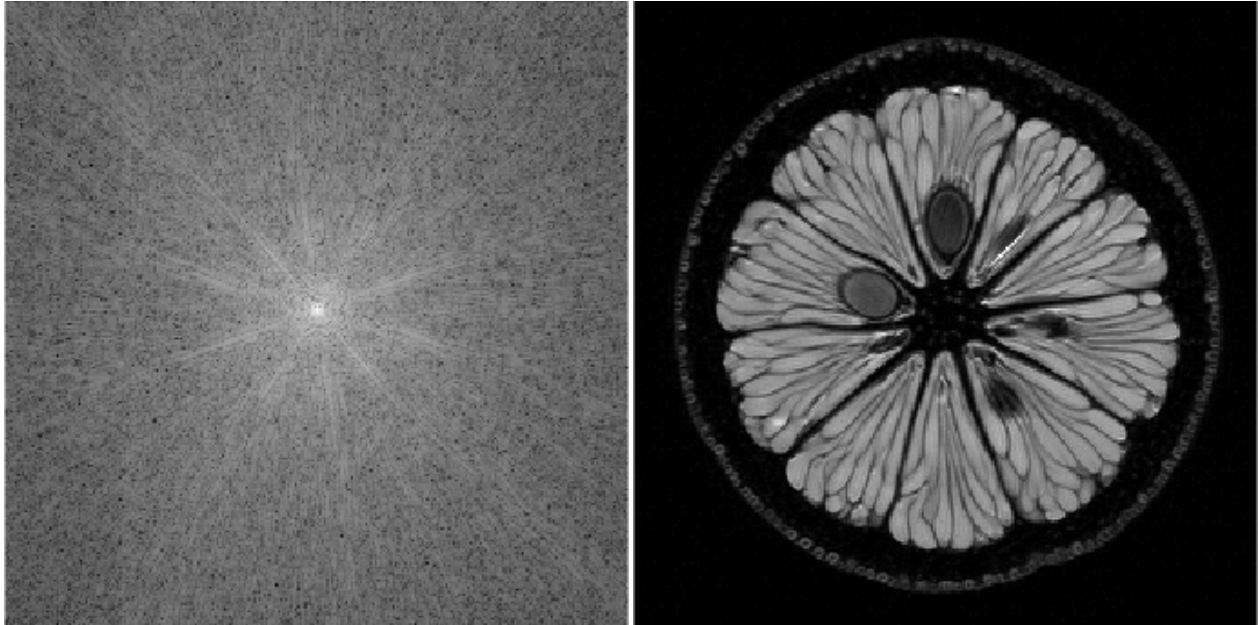
Figure 2.9: The iDFT converts a measured set of two-dimensional spatial frequencies (k-space, left) to an image (right). For clarity, only the magnitude data are shown, and k-space is displayed on a logarithmic scale.

refers to a strategy in which a gradient pulse is applied briefly to encode a single k-number in a specific direction. By iterating through a series of gradient amplitudes and directions, k-space can be sampled point-wise in one, two or three dimensions [53]. Phase encoding alone is a very inefficient method in terms of scan time, since it records only a single k-space point per gradient pulse amplitude and direction. Frequency encoding, in contrast, encodes k-numbers continuously over time by sampling M_{xy} periodically during a gradient pulse. In the case of a constant frequency encoding gradient amplitude, the product of the sampling dwell time, gradient amplitude and gyromagnetic ratio determine the increment of k-number between samples.

In most MRI scans, constant amplitude frequency encoding is used in one direction to acquire rectilinear lines of k-space, and phase encoding is used for encoding one or two directions orthogonal to the frequency encoded direction [35]. In the simplest case, a full line of frequency encoded k-numbers at a single phase encoded k-number is sampled following each RF pulse. In order to sample k-space symmetrically about the origin, the frequency encoding gradient must be preceded by a preparation gradient of opposite polarity in the same direction. In this context, as the readout frequency

gradient progressively unwinds the phase imparted by the preparation gradient, the recorded signal oscillates with increasing amplitude, reaching a maximum at $k = 0$ and diminishing thereafter. Since this signal is produced solely by the spatial phase refocusing influence of the readout gradient, it is called a gradient echo (or, by some authors, a gradient recalled echo). As described in section 2.3, spin echoes are generated by the application of two RF pulses with a separation in time that is short relative to the rate of spin-spin relaxation (T_2). These spin echoes may be encoded to represent image spatial frequencies in the same manner described here for gradient echoes. Since a spin echo without any spatial gradient encoding evolves over time in a manner controlled primarily by the chemical shifts present, image artifacts can occur in spin echo imaging if the centers of the spin and gradient echoes do not coincide. This chemical shift offset is exploited in some approaches to spin echo chemical shift imaging [54]. In general, gradient echo imaging methods are more useful for rapid or dynamic imaging, or for encoding images with signal intensities weighted according to T_2^*. Since $T_2 > T_2^*$, spin echo imaging methods generally offer more time for MR signal encoding and are typically more useful for higher resolution anatomical imaging, including T_2-weighted imaging.

The composite sequence of RF and gradient pulses arranged in time for MR imaging and spectroscopy is called a pulse sequence. A very wide variety of pulse sequences are used to achieve different contrasts and to accelerate the acquisition of k-space data. Generalizations about MRI methods without exceptions are difficult to make, however there are a handful of scan parameters that affect all pulse sequences in a mostly consistent manner. From an image contrast perspective, the three most important parameters that can be defined for any pulse sequence are the RF pulse excitation angle (θ), repetition time (TR) and echo time (TE). The RF excitation angle controls the redistribution of longitudinal and transverse magnetization as described in equation 2.6. The repetition time denotes the time elapsed between subsequent RF excitation pulses that nutate a given set of isochromats, and therefore in general refers to the duration of time that is allowed for spin-lattice relaxation. Note that in spin echo type sequences the RF excitation pulses are distinct from the refocusing pulses, and both

excitation and refocusing pulses will control the time allowed for T_1 relaxation. Most spin echo sequences use a nominal 90 degree excitation and 180 degree refocusing pulse since these settings provide the maximum spin echo signal amplitude. For the purpose of the following discussion of image contrast, the maximum excitation angle will be considered to be 90 degrees.

Most pulse sequences are designed to operate on a steady-state longitudinal magnetization (M_z). This steady-state level is determined for isochromats within the subject by their spin-lattice relaxation rate, the repetition time and the excitation angle. In general, greater T_1 weighting of MR signals is achieved by using shorter repetition times or — particularly for gradient echo sequences — larger excitation angles. These changes to a given pulse sequence will decrease the magnitude of the steady-state M_z it establishes, allowing isochromats with shorter T_1 relaxation times to establish steady-state levels of M_z that are greater than isochromats with longer T_1 relaxation times. Greater $T_2^{(*)}$ weighting is achieved for a given pulse sequence by extending the echo time, which is defined as the time elapsed between RF excitation and the moment at which $k = 0$ is sampled (i.e. the peak of the gradient echo). This increase in TE incurs a reduction in imaging signal magnitude due to the greater amount of $T_2^{(*)}$ decay occurring before signal readout, however the image contrast that is attained is often very useful for differentiating diseased tissues *in vivo* [55]. When neither T_1 nor $T_2^{(*)}$ contrast is desirable, spin-density weighted imaging signals can be encoded using a short TE and long TR to minimize spin-spin signal decay and maximize spin-lattice recovery.

For routine MRI sequences that operate on thermally polarized spin systems, the choice of image weighting depends on the desired visibility and contrast of tissues in the resulting images. Special considerations must be given to a pulse sequence used for HP imaging. As discussed in section 2.3, for the HP case T_1 is the time constant of M_z decay, usually towards an undetectable equilibrium value. Furthermore, each RF pulse depletes a portion of the non-recoverable M_z. If a conventional gradient echo imaging method were used for HP MRI, apodization of the encoded spatial frequency signals over time would impart a filtering effect that can lead to severely

blurred and non-quantifiable images. This effect is simulated in figure 2.10 by applying an HP signal apodization filter to the raw ^{1}H MR imaging data of a lemon. Also, since the nuclear moments that provide the HP signal are exogenous and typically delivered by perfusion, the dynamics of signal evolution *in vivo* complicate HP imaging experiments. Imaging approaches for HP MRI are generally designed either to sample the temporal dynamics of the HP imaging signal or to encode high quality spectroscopic images of a specific set of chemical shifts that are averaged over time. For the latter approach, precise timing can be difficult since many HP agents depolarize completely within a few minutes of being removed from the polarizer. These single time point data can also only be quantified with simple frequency integration or ratiometric approaches. Imaging data acquired dynamically over time can be expected to exhibit lower image quality — either in terms of SNR, spatial resolution or both — but are required in some form for pharmacokinetic modeling of HP agent uptake and metabolism.
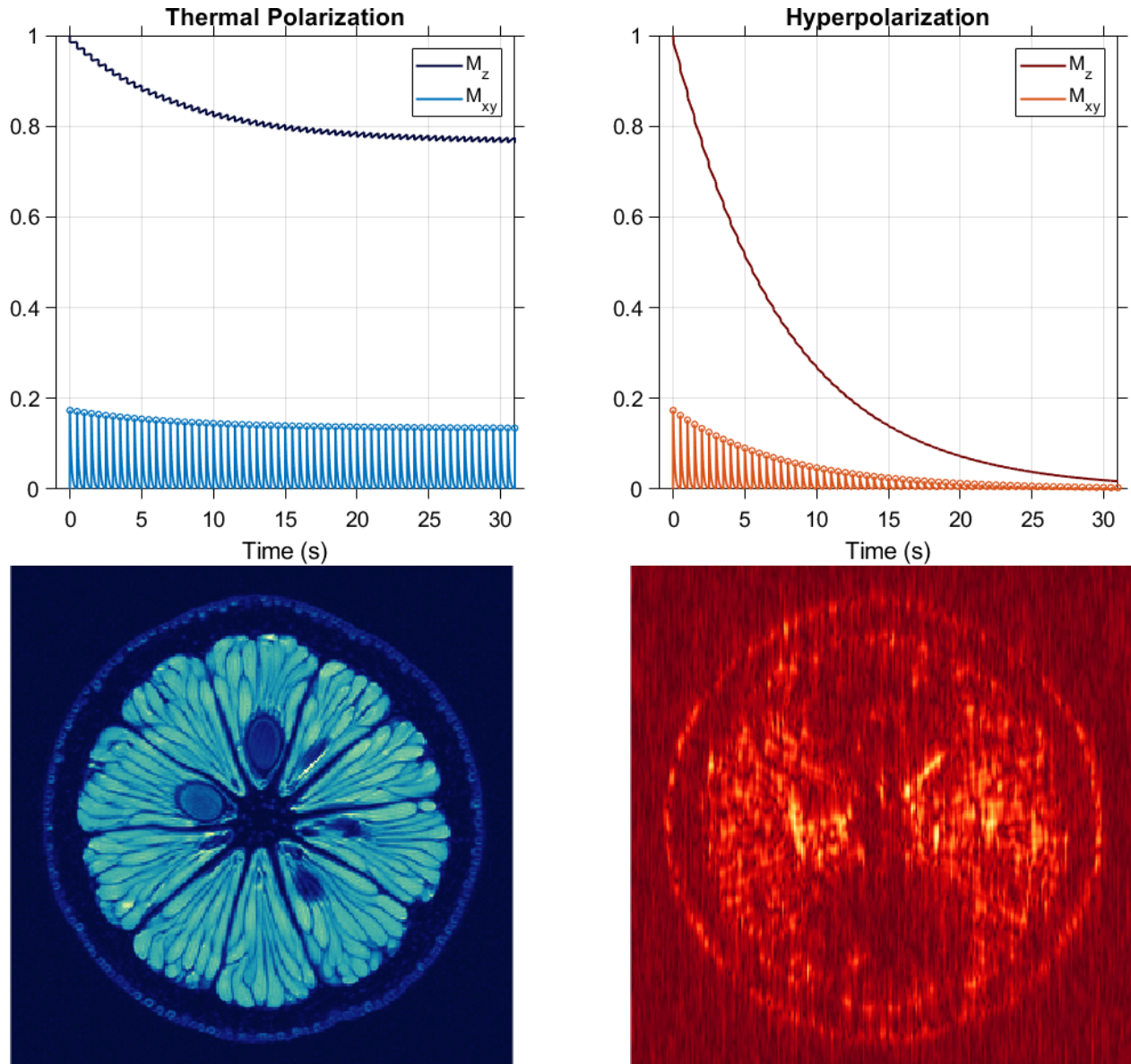
Figure 2.10: In conventional gradient echo imaging of thermally polarized subjects, the periodic application of RF pulses establishes a steady-state level of longitudinal magnetization (M_z) determined by the pulse nutation angle and the rate of M_z recovery ($\frac{1}{T_1}$). Once established, this steady-state M_z produces a consistent amount of transverse magnetization (M_{xy}) with each excitation prior to encoding of the image spatial frequencies. In HP imaging, each RF pulse depletes a portion of the non-recoverable HP M_Z, which also decays continuously with time constant T_1. If the same gradient echo imaging method were applied to a HP spin system, the depletion of M_Z would have an undesirable filtering effect on the encoded image spatial frequencies, resulting in severe image blurring. Because of this filtering effect, as well as the effects of vascular delivery for HP ^{13}C agents *in vivo* (not accounted for in this figure), specialized imaging techniques are needed for HP MRI.

Chapter 3

Hyperpolarized ^{13}C MRI

In its most basic sense, NMR hyperpolarization is the production of a sample containing a net nuclear moment much greater than would occur at thermal equilibrium. Such a technique was theorized by Felix Bloch in the same 1946 paper in which he introduced his eponymous equations.

> As to the nuclear induction effect, there exists the interesting possibility of first establishing the equilibrium in a strong magnetic field under conditions of relatively short relaxation time (by evaporation into an oxygen atmosphere, addition of a paramagnetic catalyst, heating, etc.), thereupon considerably lengthening the relaxation time (by recondensation, removal of the catalyst, cooling, etc.), and thus preserving the high field polarization for a considerable time, even when the sample is removed from the high field. A subsequent nuclear induction experiment, carried out under suitable conditions, can then exhibit either a moment, pertaining to the field in which it was originally established, or indicate that the relaxation time was comparable or short, compared to the time which has elapsed since removal. [34]

Although these precise physical methods for polarizing nuclear spins better describe brute-force polarization, temporarily establishing a large aggregate magnetic moment in conditions separate from those in which the MR experiment is carried out is the fundamental idea underlying the hyperpolarization method discussed in this chapter. As reviewed briefly in section 2.2, methods by which high nuclear spin polarizations may be attained include polarization transfer from metal electrons via optical pumping and

from parahydrogen via chemical interactions. A more recently developed hyperpolarization method, dissolution dynamic nuclear polarization (dDNP), is the focus of this work.

In this chapter, the process and implementation of hyperpolarization by dDNP will be reviewed. This discussion will cover the production of the HP sample, its use in spectroscopic and imaging experiments with living systems, and an overview of some important ^{13}C labeled HP agents. At the close of this chapter, a recent study applying this method to the measurement of the effect of a metabolic intervention in a mouse model of brain cancer is presented.

3.1 Dissolution Dynamic Nuclear Polarization

Dissolution DNP was demonstrated first in the seminal work of Jan Henrik Ardenkjær-Larsen [56]. This technology can produce biocompatible solutions containing ^{13}C labeled molecules with spin polarizations far exceeding what had been reported previously in the liquid state.

DNP refers to a class of hyperpolarization techniques that exploit electron paramagnetic resonance (EPR) effects to create large nuclear spin polarization fractions. This process is most efficient at high magnetic field and low temperature (typically $\vec{B}_0 > 3$ T and $T < 2$ K) in the solid state. In these conditions, the paramagnetic electrons achieve a spin polarization fraction that approaches 100% due to their large gyromagnetic ratio ($\frac{\gamma_e}{2\pi}$ = -28,025 MHz/T), while the equilibrium nuclear polarization remains <1%. The transfer of electron spin polarization to nuclei can be accomplished in a variety of ways that will not be fully covered here, including magic angle spinning [57] and photochemical reactions [58]. For the purpose of dDNP, polarization transfer is induced by narrow-band saturation of an EPR line using a time-varying magnetic field with a frequency that is the difference between the EPR and NMR Larmor frequencies. At the field strengths used in DNP, this saturation frequency usually falls

within the microwave range of the electromagnetic spectrum. In an amorphous solid irradiated at the appropriate microwave frequency, hyperfine coupling and thermal mixing of the electron and nuclear spins permit cross-relaxation mechanisms that strongly favor the accumulation of nuclear moment alignment in the direction of $\vec{B}_0$. This DNP process is a well-established NMR technique used in high energy physics research and for the investigation of solid state molecular structures, having been first proposed theoretically [33] and demonstrated experimentally [59] in the 1950s. The pivotal innovation in Ardenkjær-Larsen's work was the rapid dissolution of the solid DNP sample in a superheated solution, yielding HP solutions that are useful for interrogation of biochemistry and physiology *in vivo*. Using a suitable radical, DNP can be used to attain large solid state polarization fractions for any NMR nuclide, however dDNP has been applied primarily to ^{13}C labeled molecules.

The dDNP process is usually performed on a highly ^{13}C-enriched solution. A high concentration of ^{13}C nuclei not only increases the absolute level of net magnetic moment attainable, but also enhances the efficiency of the DNP process, which depends on physical proximity of nuclear and radical electron magnetic moments. This solution is prepared with a glassing agent and a triarylmethyl (trityl) radical, then loaded into a specially-built dDNP polarizer. The polarizer consists of a superconducting magnet equipped with a specialized insert designed to provide an extremely low temperature and pressure environment using a vacuum-pumped liquid helium bath. Once loaded into this insert within the polarizer, the DNP sample is cooled to <2 K. Microwave irradiation at a narrow frequency band catalyzes polarization transfer from electrons to ^{13}C nuclei, however this build up of solid state polarization proceeds slowly due to several factors, including the relatively low likelihood of cross-relaxation mechanisms in the solid state [60]. The electron T_1 is relatively short in the solid state (≈ 1 s), but at a lower polarizer field strength (e.g. 3.35 T) it can be reduced significantly via doping with small quantities of gadolinium or other lanthanide ions [61]. In these conditions,

the doped DNP sample polarizes more quickly and attains a greater maximum level of polarization [62]. A NMR coil tuned to the ^{13}C frequency may be used to monitor the build-up of the solid state nuclear polarization via low excitation angle RF pulses. This build-up curve follows the same shape as a traditional T_1 exponential recovery curve in MRI, due to solid state spin-lattice effects in the coupled electron and ^{13}C spin systems. Depending on the polarizer field strength and the chemical properties of both the radical and the ^{13}C molecule being polarized, continuous microwave irradiation must be applied for an hour or more to attain maximal nuclear polarization levels.

In order to facilitate transfer of polarization from radical electrons to ^{13}C nuclei, the molecules in the DNP sample must form an amorphous glass matrix when rapidly chilled to cryogenic temperatures. The crystalline lattice formed by most aqueous solutions when frozen inhibits thermal mixing of the radical electrons and ^{13}C nuclei, which is a critical mechanism of angular momentum transfer in the solid state [60]. With some notable exceptions, a glassing agent must be added to the DNP sample to prevent crystal formation and allow thermal mixing at low temperature. The DNP solution described in Ardenkjær-Larsen's initial publication consisted of ^{13}C urea dissolved in glycerol, which functioned as a glassing agent. For aqueous dDNP solutions, common glassing agents include dimethyl sulfoxide (DMSO), dimethyl acetamide and ethanol. The amount of glassing agent used represents a trade-off between the efficacy of glass formation and the dilution of ^{13}C nuclei, which impart competing effects for the DNP process. Additionally, the presence of the glassing agent in the final HP solution can pose an added impediment to its use *in vivo*. If a pharmaceutical grade glassing agent cannot be employed, or the glassing agent concentration after dissolution is too high, the HP solution cannot be administered in human subjects and may not be usable in animal studies.

Once sufficiently high spin polarization is achieved for ^{13}C nuclei in the solid state,

a dissolution is performed. A dissolution buffer is loaded into a heating chamber outside of the DNP insert. Within this chamber, the liquid buffer is heated to ≈200° C and pressurized to ≈10 bar using helium gas. The DNP sample is then raised out of the liquid helium bath and the superheated buffer is forced through the sample chamber by the pressurized helium gas, melting the sample and ejecting it from the polarizer in liquid form within seconds. The polarization of the ^{13}C compound is retained through this dissolution process, providing a HP solution with a transient NMR signal four orders of magnitude greater than the equilibrium conditions attainable in a typical MRI or NMR instrument. The dissolution buffer is typically formulated chemically and heated to an appropriate temperature such that it produces a biocompatible solution when combined with the frozen DNP sample. This is critical for studies in living systems, both *in vitro* and *in vivo*, since a non-physiological pH and temperature in the HP solution could significantly perturb the biological processes under investigation.

Currently, the most widely used preclinical polarizer is the Oxford Instruments HyperSense, which is largely based on Ardenkjær-Larsen's original design. This polarizer operates at 3.35 T using an open and reusable sample cup that is loaded with a DNP sample and inserted directly into the liquid helium bath. Upon dissolution, the buffer is forced through the sample cup via a stick that lowers into the DNP insert and connects tightly around the cup opening, preventing direct contact between the superheated liquid and cryogenic helium. This design is advantageous in that samples are easy to prepare and it uses no disposable parts, however there is a risk that a cup could be displaced in the DNP insert. If a dissolution is attempted with a displaced sample cup, superheated buffer is sprayed directly into the liquid helium bath and flash frozen. This catastrophic event results in significant downtime for the polarizer as the DNP insert must be warmed and flushed with helium gas to clear away the frozen buffer.

Apart from this risk of a major dissolution failure, the reusable nature of the Hy-

perSense cups and fluid lines that carry liquid into and out of the DNP insert mostly preclude the possibility of producing the sterile solutions necessary for HP studies in human subjects. Additionally, this system can only polarize a single sample at a time, which limits system throughput due to the long solid state polarization build-up time. These issues were addressed in the design of the GE SPINlab. This polarizer was designed for clinical use and consists of a 5 T magnet and a multichannel DNP insert that can polarize up to 4 samples simultaneously [63]. Each sample must be prepared in a fully enclosed fluid path that can be assembled in a clean environment. This fluid path consists of a sample cup and three syringes connected with durable plastic tubing. Two syringes are loaded with components of the dissolution buffer and the third is kept empty to receive the HP solution upon dissolution. End stage sterilization is performed by forcing the HP solution through a sterile filter at the end of the fluid path connected to the receiving syringe. The sample cup is loaded with the DNP sample, sealed to the fluid path with a laser welder and the entire fluid path assembly is pressure tested before insertion into the polarizer. While this reduces the risk of a catastrophic dissolution failure, there are several epoxy and glue joints in these fluid paths that can fail. In the worst case scenario, such a failure can introduce the heated dissolution buffer into the cryogenic environment of the DNP insert, requiring polarizer downtime as described in the previous paragraph.

In addition to sterility concerns, the temperature, chemical content and polarization level of the HP solution must be verified before it is cleared by a pharmacist for administration in human subjects. For these purposes, the SPINlab can be interfaced with a Quality Control (QC) module that rapidly analyzes the concentration and pH of a small quantity of the HP agent spectrophotometrically. Additionally, the trityl radical does not have regulatory approval for injection in humans. For clinical use, the radical is therefore removed from the HP solution by forcing it through a filter integrated into the fluid line, and the residual trityl concentration is measured op-
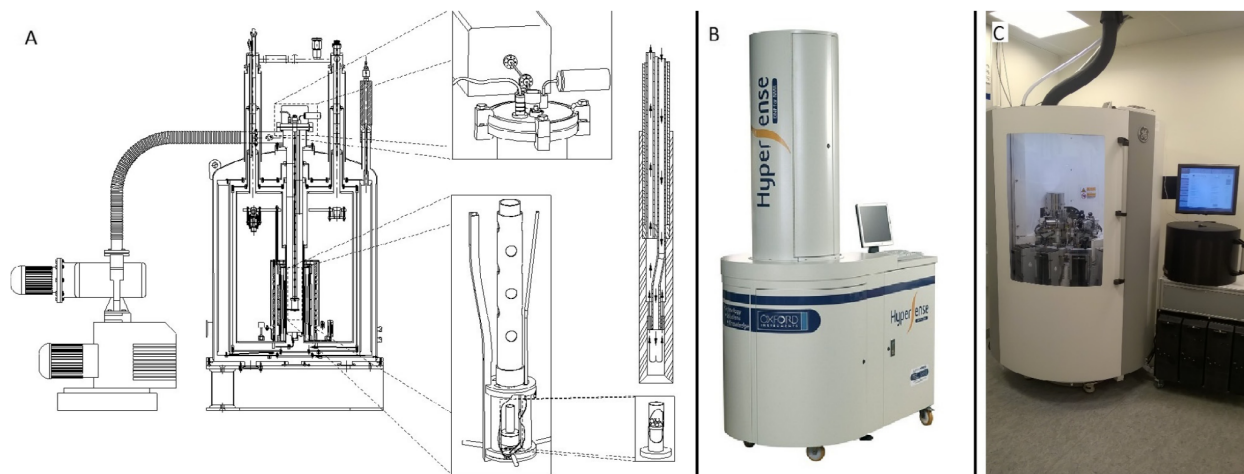
Figure 3.1: The original dDNP system created by Ardenkjær-Larsen, et al. consists of a 3.35 T magnet interfaced with a vacuum pump and DNP insert (A). Individual samples are prepared in open cups inserted manually into the DNP insert and irradiated with microwaves for ≈1 hour before dissolution. This same design was used in the Oxford Instruments HyperSense (B), with the addition of an automated dissolution system. The GE Healthcare SPINlab (C) offers an improved design, with a cryogen-free 5 T magnet and DNP insert that can polarize up to four samples simultaneously in fully enclosed fluid paths. The SPINlab can be equipped with a QC module (black cylinder below the LCD screen) for rapid analysis of the HP solution prior to administering in human subjects.
Figure reprinted from Jan Henrik Ardenkjær-Larsen. On the present and future of dissolution-DNP. *Journal of Magnetic Resonance* 2016; 264: 3-12. doi:10.1016/j.jmr.2016.01.015. with permission from Elsevier (License Number 4865461302802).

tically. The QC module also contains an infrared temperature probe and a compact NMR system for verifying the sample temperature and percent polarization. Due to the possibility of the HP product failing any of these various QC checks — or of fluid path failure — multiple fluid lines are typically loaded into the SPINlab for human studies. In the event of a dissolution or QC failure, a second dissolution can be attempted within minutes using a backup fluid path.

Upon dissolution of the DNP sample, the HP signal decays with at a rate determined by the T_1 time constant of the ^{13}C labeled molecule in the liquid state. This spin-lattice decay of the HP ^{13}C signal limits the time available for imaging to within a few minutes of dissolution. For studies in human subjects, the QC process entails

an unavoidable added delay — typically around 30 to 60 seconds — between dissolution and HP signal readout during which some polarization loss occurs. Due to these constraints, the dDNP system must be installed in close proximity to the NMR or MRI systems on which the HP agent will be used. An interesting possibility is to perform the polarization and dissolution process in separate systems. If the frozen DNP sample is extracted from the polarizer and kept in a high magnetic field and low temperature environment, polarization loss would occur at a rate determined by the ^{13}C T_1 in the solid state. This solid state T_1 is typically two orders of magnitude longer than the corresponding liquid state T_1, which could allow sufficient time for transport to a dissolution system that is sited distant from the polarizer but near a magnet prepared for HP signal readout. However, maintaining such a low temperature outside of the DNP system is extremely difficult, and the separation of the DNP and dissolution systems is currently an active area of research [64].

3.2 Hyperpolarized Imaging Agents

The capability to produce HP ^{13}C labeled solutions has opened new avenues of chemical interrogation in biology and medicine. Unlike the most commonly used gadolinium and iodine based contrast agents, the HP agent is itself a signal source for imaging that decays over time. In these respects, HP MRI is very similar to rapid dynamic imaging of short-lived radionuclides that is sometimes performed in nuclear medicine. With current instrumentation, nuclear medicine imaging is sensitive to concentrations of radionuclide with a lower bound in the nanomolar to picomolar range [65] while HP agents must be present in millimolar or micromolar concentrations for reliable detection [66]. Although inferior in sensitivity, HP MRI can provide real-time insight into biochemical reactions in ways not possible via positron or single photon emission imaging. The emission events that underlie all nuclear medicine modalities occur with equal probability over time in all nuclei of a given radioisotope. A nuclear

medicine study cannot directly distinguish the chemical environment of a radionuclide and seeks to quantify the delivery, uptake and/or retention of the radionuclide in a tissue of interest to provide insight into a physiological or biochemical process solely through the number of nuclear decay events occurring within an imaging volume over time.

While in nuclear medicine imaging discrete decay events are registered in detectors with precisely known positions and mapped to image space, the signal source in MR imaging is the net magnetization induced in a subject by an external magnetic field. As discussed in the previous chapter, this magnetization arises from a population of NMR active nuclei due to an excess of nuclei with spin state aligned parallel rather than anti-parallel to the direction of an external magnetic field. Although the signal detected in MRI always represents a large population of nuclei, sub-populations can be distinguished by virtue of slight differences in the local magnetic field they experience. As outlined in section 2.4, an important determinant of this local magnetic field is the configuration of the orbital electrons surrounding a given nucleus, which shield the nucleus from external fields and impart a resonant frequency shift specific to the chemical environment of the nuclear magnetic moment. NMR active nuclei present in different molecules therefore experience unique chemical shifts, and through this effect the precursors and products of specific chemical reactions can be distinguished.

To date, dozens of HP compounds have been developed as agents for imaging and basic science research. Many of these agents have demonstrated the capacity to resolve metabolism, perfusion and other biological functions. There are several practical considerations that affect the usability of a HP ^{13}C agent. Perhaps the most important property of these agents from a physics perspective is a slow spin-lattice relaxation rate of the ^{13}C spin system, which impacts both the ability to generate large nuclear spin polarization fractions in the solid state and the lifetime of the HP signal following dissolution. When bound directly to other NMR-active nuclei such as ^{1}H, heteronu-

clear coupling (J-coupling) of the spin system results in splitting of the ^{13}C resonance lines and rapid spin-lattice relaxation. For molecules in which undesirable heteronuclear coupling is unavoidable, isomeric substitution of the ^{13}C-bound nuclei (e.g. ^{2}H for ^{1}H, or ^{15}N for ^{14}N) can significantly prolong the lifetime of the HP signals of interest [67]. From a biological perspective, HP agents for metabolic applications must undergo rapid cellular uptake and chemical conversion in order to allow observation of the metabolic products of interest during the HP signal lifetime.

As is the case for radiopharmaceutical imaging agents, the chemical structure of a HP agent impacts the evolution of the imaging signals it creates *in vivo* and relates directly to the biological process that is to be measured. The dDNP agents that have been most thoroughly investigated are ^{13}C labeled on carbonyl functional groups, which consist of a carbon-oxygen double bond. Carbonyl groups are present in a wide variety of organic molecules that are the reactive substrates for many vital enzymes that exploit the asymmetric electronegativity of the carbon-oxygen bond. Measurement of the molecular flux through these enzymatic reactions in tissue is typically the putative goal of MR studies using metabolic HP agents. Several HP agents have also been developed for the disparate purpose of measuring perfusion and capillary permeability *in vivo*. In these agents, a molecular structure that is biochemically stable in tissue within the time frame of the HP measurement is needed, and the dispersion of the HP agent in tissue is controlled in part by the ability of the agent to cross capillary and other biological membranes. Apart from measurement of metabolism and perfusion, a third class of HP agents is intended for probing the chemical conditions of the extracellular space. These agents undergo chemical reactions that are dependent on the pH of the interstitium or the extracellular presence of enzymes which indicate necrotic cell death. In the following subsections, the HP agents most relevant to this work are introduced.

[1-^{13}C]Pyruvate

[1-^{13}C]Pyruvate is by far the most widely studied HP ^{13}C agent, to the extent that in some contexts the term hyperpolarized MRI is considered synonymous with imaging studies of this agent. Pyruvate sits at a crucial branching point in cellular metabolism, and has several biochemical properties that make it an excellent HP imaging agent [68–70]. Pyruvate is the conjugate base of pyruvic acid, a simple organic acid consisting of carboxyl, ketone and methyl groups. Neat pyruvic acid glasses when brought to cryogenic temperatures, and therefore a high purity solution for DNP can be formulated with just the addition of a suitable radical. Most often pyruvic acid for dDNP is ^{13}C labeled in the C-1 position, which corresponds to the carboxyl carbon. The ^{13}C MR signal that results is characterized by a long T_1 of around 60 seconds in solution, which allows time for QC and transport into a nearby MRI system before the HP signal fully relaxes [63]. The metabolic products observed following administration of [1-^{13}C]pyruvate in living systems create well-resolved spectral signals spanning a chemical shift range of around 24 ppm, with a minimum separation for neighboring peaks of around 2.5 ppm. At typical MRI field strengths this ^{13}C spectrum is sufficiently compact for broadband excitation and has adequate chemical shift separation for resolving the distinct metabolic signals *in vivo*. These spectral characteristics permit the application of a variety of different strategies for imaging the chemical shifts of interest.

Pyruvate is generated as the final product of glycolysis, the series of enzymatic reactions that produce the primary intermediate of cellular energy, adenosine triphosphate (ATP). When administered intravenously, pyruvate rapidly distributes in tissue and is transported into cells through monocarboxylate transporters (MCTs). In the cytosol, pyruvate may be reduced to form lactate, transaminated to form alanine, or transported into the mitochondrion where it may provide carbon fuel to the tricarboxylic acid (TCA) cycle in two ways: via decarboxylation to form acetyl coenzyme

A (acetyl-CoA) or via carboxylation to form oxaloacetate. Importantly, each of these reactions proceeds rapidly, and the corresponding enzymatic fluxes can therefore be measured via MR studies of HP pyruvate *in vivo*.

The overall reaction of glycolysis breaks the six carbon monosaccharide, glucose, into two pyruvate molecules, producing two ATP molecules and two reduced nicotinamide adenine dinucleotide (NADH) cofactors. In most eukaryotic cells pyruvate is typically present in very low concentrations since it is quickly shuttled into various divergent biochemical pathways. For differentiated mammalian cells in an adequately oxygenated environment, pyruvate is primarily imported into the mitochondria where it is decarboxylated in a reaction that produces one NADH cofactor, donates the ketone and methyl carbons to the TCA cycle through acetyl-CoA, and releases the carboxyl group as carbon dioxide (CO_2). The TCA cycle is a series of reactions that occur within the mitochondrial matrix, involving the progressive oxidation of carboxylic acids and reduction of enzymatic cofactors. These reduced cofactors, which include NADH, in turn participate in redox reactions with enzymatic complexes embedded in the mitochondrial inner membrane that pump hydrogen cations (H^+) out of the mitochondrial matrix into the intermembrane space. The resulting electrochemical gradient across the inner membrane powers ATP production via H^+ transport down the gradient through the transmembrane enzyme ATP synthase. This process is called oxidative phosphorylation, since it depends on the presence of molecular oxygen (O_2) as the terminal electron acceptor in the chain of redox reactions driving H^+ transport. The theoretical energetic yield of glycolysis, the TCA cycle and oxidative phosphorylation for a single glucose molecule is about 30 ATP, compared to the net production of 2 ATP through glycolysis alone [71].

In the absence of the oxygen necessary to drive oxidative phosphorylation, cells must rely on the relatively inefficient ATP yield of glycolysis to meet their energetic needs. Under these hypoxic conditions, the oxidized form of nicotinamide adenine din-
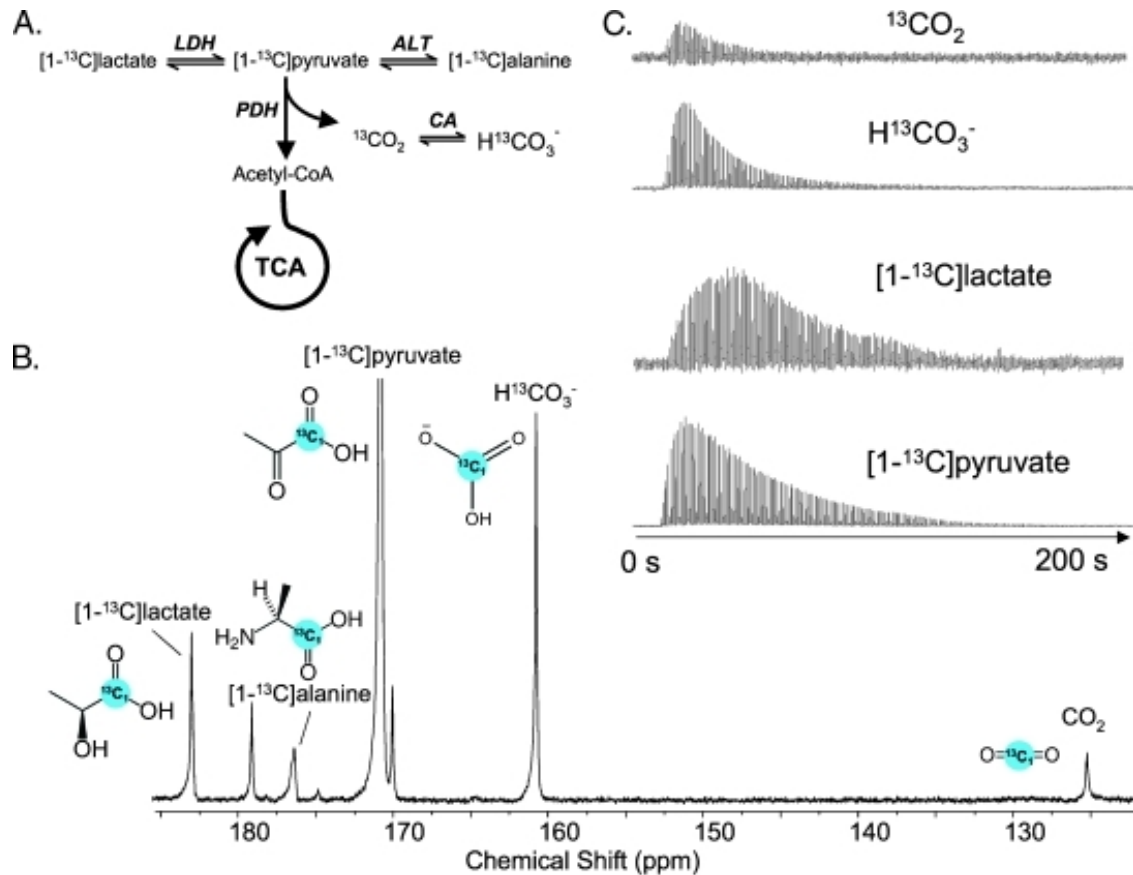
Figure 3.2: HP [1-^{13}C]pyruvate can undergo rapid enzymatic conversion *in vivo* via lactate dehydrogenase (LDH), alanine transaminase (ALT) or pyruvate dehydrogenase (PDH), as shown in diagram (A). In the decarboxylation reaction catalyzed by mitochondrial PDH, the ^{13}C label is released in carbon dioxide (CO_2), which is in rapid enzymatic equilibrium with bicarbonate (HCO_3^-) via carbonic anhydrase (CA). Measurement of $H^{13}CO_3^-$ therefore provides a marker of pyruvate flux into the TCA cycle. These metabolites are shown in a HP ^{13}C NMR spectrum of an isolated perfused rat heart (B). Apart from the metabolites labeled in this figure, HP pyruvate hydrate is observed at approximately 179 ppm. This signal arises from the spontaneous and reversible formation of a geminal diol via hydration of the ketone carbon of pyruvate. Pyruvate hydrate is not metabolically active, and therefore represents a signal that may need to be accounted for in spectroscopic imaging so as to not interfere with the metabolic signals of interest. Because of the dramatic increase in sensitivity provided by dDNP, metabolic signals can be measured over time with temporal resolution on the order of 1 second (C). Note that the data shown in this figure were acquired from an isolated organ in a high resolution NMR system, which provides spectroscopic detail difficult to match in intact animals. In particular, $^{13}CO_2$ is typically not observed for HP [1-^{13}C]pyruvate experiments *in vivo*, due in part to rapid T_1 relaxation of this resonance.

ucleotide (NAD^+) needed to drive glycolysis would become rapidly depleted if it could not be restored from NADH. Without oxidative phosphorylation, pyruvate flux into the TCA cycle provides no energetic output, and the reoxidation of NADH to NAD^+ necessary to sustain continual glycolytic flux can be realized in mammalian cells through reduction of pyruvate to lactate. This redox reaction is catalyzed by the enzyme lactate dehydrogenase (LDH), which exists in several different isoforms with differing propensities for the forward and reverse reactions. The lactate produced in cells relying on anaerobic metabolism can be exported by MCTs, then subsequently imported through MCTs into cells with adequate oxygen to metabolize lactate aerobically [72]. It is important to note that none of these metabolic pathways occur in isolation. Within any eukaryotic cell, the flux of carbon skeletons through glycolysis and the TCA cycle are linked at various points to many other biochemical pathways through which organic molecules may be siphoned off for anabolic synthesis or donated for catabolic ATP production. In order to provide the necessary biomolecular building blocks, tissues undergoing rapid cellular growth therefore exhibit a high rate of glycolytic flux, a metabolic phenotype that is similar to tissues lacking adequate oxygen for oxidative phosphorylation [73].

This observation that proliferative tissues always rely predominantly on glycolysis, even in aerobic conditions, was first observed by Otto Warburg in the 1950s and is called the Warburg effect. Warburg further hypothesized that this effect resulted from dysfunctional mitochondria and was the etiological cause of malignant cellular growth [74], however these malignancies are now understood to result from genetic mutations. The Warburg effect has profound implications in the context of cancer metabolism. A variety of therapeutic strategies have been devised targeting the aberrant metabolism of cancer[75], and diagnostic evaluation of neoplastic growths on the basis of their metabolic activity is routinely performed using ^{18}F-fluorodeoxyglucose (FDG). FDG is a radiolabeled glucose analog that is imported into the cell in the same manner as glu-

cose, but undergoes only the initial reaction of glycolysis and becomes trapped in the cytosol [65]. Highly glycolytic tissues thereby accumulate a large amount of the ^{18}F radionuclide, which can be detected with exquisite sensitivity by positron emission tomographic (PET) imaging. However, due to the lack of insight into chemical endpoints, a strong FDG-PET imaging signal is open to multiple interpretations. Such signals could be observed, for example, in tissues that rely on glycolysis due to hypoxic conditions rather than abnormal proliferation. Furthermore, FDG-PET measurements are not well suited for detecting neoplastic growths in tissues with high baseline glycolytic activity, such as the brain, or in physical proximity to organs with large FDG-PET signals, such as in the prostate which neighbors the urinary bladder. HP pyruvate can therefore provide an alternative method of metabolic imaging in these cases, as well as metabolic measurements that are complimentary to FDG-PET in other organs [9].

To date, HP pyruvate imaging has been investigated in the human prostate, heart, brain, liver, kidney, pancreas, breast and breast [10], in addition to a plethora of preclinical disease models in small and large animals. The rapid readout of tissue metabolic state provided by pyruvate imaging is particularly well suited to detecting early responses to treatments, as has been demonstrated in androgen ablation therapy for patients with prostate cancer [13] and will be shown for a glycolytic inhibitor in a mouse model of brain cancer at the end of this chapter [76]. The capability to detect non-response early and adjust the treatment a patient receives is of great importance in oncology, both in terms of limiting unnecessary toxicities and providing optimal personalized therapies. HP pyruvate imaging may also be very useful for guidance of certain biopsies in a manner that spares damage to healthy tissue, e.g. in the prostate.

It should be noted that the dosage of intravenous HP pyruvate used for these measurements is quite large compared to the trace amounts of metabolic agents used in FDG-PET and other nuclear medicine studies. This is an unavoidable aspect of these imaging studies due to the inherently low sensitivity of MR signals, even for HP

agents. At very high doses, there is a risk that the enzymatic transport or metabolic conversion reactions probed by the HP agent could be saturated as the agent concentration reaches its peak level in tissues of interest. The precise level at which these saturation effects occur is difficult to predict, and is highly dependent on the organ under investigation. Partial saturation of the conversion of HP pyruvate to lactate and bicarbonate has been observed in the heart, liver and kidney of healthy rats at injected doses as low as 0.1 mmol/kg [66]. This pyruvate dosage matches that typically used in patient studies [77–79], however these saturation effects could be expected to have less impact in human subjects due to the longer injection times and much slower blood velocities. Additionally, the observation of saturation effects in healthy tissues cannot be generalized to HP pyruvate measurements in cancer, where increased expression of MCT and LDH permit a much greater rate of pyruvate uptake and turnover [72].

^{13}C Urea

Among HP agents used for measurement of tissue perfusion, urea is unique in that it is an endogenous molecule with a well-established safety profile *in vivo*. Pharmaceutical grade ^{13}C urea with near unity isotopic enrichment is widely available and inexpensive due in part to its use in routine breath tests for common bacterial infections of the gastrointestinal tract [80]. Urea is present in mammalian blood and tissue at millimolar concentrations as a waste product of amino acid metabolism and is filtered out of the blood by the kidneys to form the primary solute constituent of urine. Large doses of urea have historically been administered intravenously as a treatment for hyponatremia without any adverse effects [81].

^{13}C urea was the first dDNP agent used in Ardenkjær-Larsen's 2003 publication introducing the technique [56], and was utilized for angiographic imaging in rodents in the same year [82]. Since it undergoes no significant chemical transformations *in vivo*, HP ^{13}C urea imaging provides a measurement of blood flow and capillary permeabil-

ity. Compared to the most commonly used gadolinium chelate MRI contrast agents, urea is a much smaller molecule and could therefore be expected to more accurately represent the delivery of vital molecular components of blood such as O_2 and glucose. Additionally, the safety profile of urea is favorable for intravenous administration in patients for whom gadolinium agents are contraindicated, e.g. due to compromised kidney function. In fact, direct measurement of HP ^{13}C urea transport in the kidney is a particular interesting application, which can provide spatially resolved and quantitative assessments of glomerular filtration rate [83]. In most tissues with continuous capillaries, HP ^{13}C urea has not been observed to collect outside of the capillary space in a significant amount [84]. However, solid tumors, as well as certain organs such as the liver and spleen, are characterized by highly permeable capillaries through which urea passes easily. Measurement of tissue perfusion and capillary permeability for these tissues using HP ^{13}C urea will be discussed further in the next chapter.

[2-^{13}C]Pyruvate

As discussed in section 3.2, the ^{13}C-labeled carboxyl carbon of [1-^{13}C]pyruvate is most often released as [13]CO_2 when this substrate enters the TCA cycle. The resulting generation of H[13]CO^{3-} is sometimes detectable *in vivo*, providing a measurement of flux through PDH into the TCA cycle. However, this H[13]CO^{3-} signal provides no insight into the ultimate chemical fate of the ketone and methyl carbons of pyruvate. For this purpose an alternate isotopologue, [2-^{13}C]pyruvic acid, may be used. With the ^{13}C label residing on the ketone carbon, HP signals can be observed from metabolites associated with the TCA cycle, such as citrate, glutamate, acetoacetate and acetylcarnitine, in addition to lactate and alanine [85]. This provides much greater detail into oxidative metabolism than can be had through [1-^{13}C]pyruvate, however the many chemical shifts that result span a very wide frequency range of >150 ppm, with some of these peaks resonating at close to the same frequency. These spectroscopic features, as well

as the relatively rapid T_1 relaxation of many of these signals, make imaging of these metabolites very difficult *in vivo*. Nevertheless, the broader insight into metabolism provided by [2-^{13}C]pyruvate may prove very useful for improving our understanding of metabolism in healthy and diseased tissues. The application of [2-^{13}C]pyruvate is particularly interesting in tissues that rely on oxidative metabolism such as the heart [86] and the brain, with a recently published work demonstrating imaging and spectroscopic data from the brains of healthy human volunteers [87].

[1,4-^{13}C]Fumarate

Fumarate is a four-carbon TCA cycle intermediate with a safety profile compatible with intravenous administration. The two carboxyl carbons on either end of the molecule are chemically equivalent and may be polarized by DNP in the conjugate acid form, [1,4-^{13}C]fumaric acid. The HP fumarate that is obtained following dissolution distributes rapidly in tissue when introduced into the blood, however cellular uptake of fumarate is slow relative to the lifetime of the HP signal. Endogenous fumarate is converted to malate in a hydration reaction catalyzed by the enzyme fumarase, which occurs both in the cytosol and the mitochondrion. Due to the slow rate of fumarate transport across the plasma membrane, interaction of HP fumarate with fumarase mainly occurs when this membrane is compromised due to necrotic cell death. The observation of fumarase activity on HP fumarate in tumors has been shown to be a sensitive indicator of necrosis occurring with 24 to 72 hours after chemotherapeutic [88] and anti-angiogenic treatment [89]. Similar to the metabolic measurements obtained through [1-^{13}C]pyruvate, necrosis imaging via [1,4-^{13}C]fumarate has great potential to evaluate early treatment efficacy in cancer, permitting changes to ineffective therapies much sooner than would be possible with established diagnostic methods.

[2-^{13}C]Dihydroxyacetone

Dihydroxyacetone (DHA) is a three-carbon ketose, the phosphate ester of which is an important glycolytic intermediate (dihydroxyacetone phosphate). Like [2-^{13}C]pyruvate, HP [2-^{13}C]dihydroxyacetone has been demonstrated to probe multiple biochemical pathways in preclinical studies, and there are similar challenges associated with imaging the diverse metabolic signals generated by DHA metabolism *in vivo* due to their wide chemical shifts and rapid relaxation rates [90]. In addition to measurements of glycolytic and TCA cycle activity, HP DHA has been used to measure hepatic glycerol metabolism and gluconeogenesis in isolated perfused mouse livers [91]. This study of isolated livers demonstrated that several of the downstream metabolic signals are sensitive to nutritional state. The spectroscopic measurement of specific metabolic products of HP DHA has more recently been shown to reflect acute changes in metabolism induced by infusion of fructose (but not glucose) in the livers of fasted rats [92]. In chapter 6, we will present the results of experiments measuring the hepatic metabolism of HP DHA *in vivo*, including the previously unreported observation of ketogenic metabolism.

3.3 Hyperpolarized Pyruvate MR Spectroscopy Depicts Glycolytic Inhibition in a Mouse Model of Glioma

Introduction

Glioblastoma (GBM) is the most commonly diagnosed primary brain tumor in adults, and has a very poor prognosis with deterioration of cognitive function and quality of life [93]. Despite considerable research investment in improved therapies, the median survival remains 12-14 months [94]. Treatment for GBM and most other gliomas typically consists of surgical resection with subsequent chemotherapy and radiotherapy.

During and after therapy, most patients undergo serial MRI scans to assess treatment response and disease recurrence. Enhancement in T1-weighted post-contrast images remains the reference standard for identification of high grade malignant tissue in the brain, but these images often depict misleading changes in patients receiving chemotherapy, radiotherapy or symptomatic therapies [93]. There is therefore a need for imaging methods capable of accurately and quantitatively measuring treatment response in glioma. As new therapies for glioma are developed to exploit the propensity of tumors to utilize glycolysis [95], new imaging approaches for monitoring the efficacy of these treatments will also be needed.

Dissolution dynamic nuclear polarization (dDNP) can enhance the MR signal of [1-^{13}C]pyruvate more than 10,000-fold compared to thermal equilibrium, enabling new insights into tumor metabolism in vivo [56]. Previous work in rodent models of glioma has demonstrated that hyperpolarized (HP) [1-^{13}C]pyruvate MR spectroscopy detects decreases in tumor lactate metabolism caused by radiation [14] and chemotherapies [16, 18, 19, 96] within a few days of treatment. Recent advances in HP ^{13}C MRI have

enabled the real-time measurement of glycolytic metabolism in patients with brain cancer [78, 97]. The hypothesis of the present study was that dynamic HP MR spectroscopy could be used in mouse models to detect an acute decrease in aerobic glycolysis following treatment with the glycolytic inhibitor, WP1122. Our purpose was to investigate the feasibility of using HP [1-^{13}C]pyruvate to probe the metabolic state of glioma as a direct readout of treatment effect with a glycolytic inhibitor.

Materials and Methods

Animals

Thirteen 6-10 weeks old female Athymic Nude mice were implanted with 5 x 10^5 U87MG cells (ATCC, Manassas, VA) expressing firefly luciferase. We administered cells by stereotactic injection into the right caudate nucleus through a transcranial plastic guide screw [98]. Five female Athymic Nude mice served as experimental healthy controls. We monitored initial tumor engraftment and early growth by bioluminescent imaging. Our Institutional Animal Care and Use Committee approved all animal experiment procedures, which were performed between October 2016 and March 2017.

Experimental Drug

2-Deoxy-D-glucose (2-DG) is a widely studied inhibitor of glycolysis; however, its therapeutic use in vivo is limited due to its rapid metabolism. WP1122 (3,6-di-O-acetyl-2-deoxy-D-glucose) is a prodrug of 2-DG that improves biodistribution and prolongs exposure. Increased levels of 2-DG were observed in the murine brain when WP1122 was used instead of 2-DG itself [99]. WP1122 was therefore expected to lead to enhanced metabolic effects in brain tumors.

MRI protocol

Approximately 40 days after implantation, mice were scanned using a 7 T small animal MRI system running ParaVision 6 and equipped with BGA-12SHP gradients and a 72 mm inner diameter ^{1}H/^{13}C volume resonator (Bruker Biospin MRI, Billerica, MA). We anesthetized each mouse using 2% isoflurane, inserted a catheter into the tail vein and secured the animal on the MRI bed with a heating pad and respiratory monitoring pillow. A 20 mm mini-flex coil (Rapid MR International, Columbus, OH) placed on the cranium was used for HP ^{13}C signal reception. [1-^{13}C]pyruvate was hyperpolarized using a HyperSense dDNP system (Oxford Instruments, Abingdon, UK), as described previously [11, 15]. 200 μL of 80 mM HP [1-^{13}C]pyruvate (approximately 60 mg/kg) was injected into the tail vein during dynamic ^{13}C MR spectroscopy. We performed baseline scans around 40 days post-implantation and repeated all MRI scans the following day, 30 minutes after administering 2.5 g/kg WP1122 by oral gavage.

In each MRI session the following scans were acquired: axial and coronal T_2-weighted RARE (TE/TR = 57/3000 ms), axial T_1-weighted RARE (TE/TR = 7.25/1000 ms), and axial slice-selective dynamic ^{13}C spectroscopy (90 repetitions, TR = 2000 ms, 20° excitation angle, 10 mm slice, 2048 complex points over 5000 Hz spectral width). The slice position for ^{13}C MR spectroscopy was centered on the tumor as visualized in T_2-weighted coronal images. T_1-weighted axial images were acquired before and after administration of 0.2 mmol/kg of gadopentetate dimeglumine (Magnevist, Bayer Healthcare, Berlin, Germany) via tail vein catheter.

Histology

After the final imaging session, the brain of each mouse was immediately excised, frozen over liquid nitrogen and stored at -80°C. Frozen sections were cut at a thickness of 10 μm, fixed with 4% paraformaldehyde and stained with hematoxylin and eosin (H&E) using standard methods [100].

Data Analysis

Dynamic HP ^{13}C spectra were analyzed using code written in-house in MATLAB R2016a (Mathworks, Natick, MA). Spectral peaks corresponding to [1-^{13}C]pyruvate and [1-^{13}C]lactate were fit with Lorentzian line shapes to obtain relative metabolite amplitudes for each time point. A simple precursor-product model of HP lactate production was fit to these metabolite time curves in order to estimate the rate of pyruvate to lactate conversion in tissue, k_{PL}. This model-based analysis assumes that all of the observed HP pyruvate is in contact with the enzymes that mediate conversion to lactate. A longitudinal relaxation time constant of 30 s was assumed for [1-^{13}C]lactate *in vivo* [101]. In addition, the normalized lactate ratio (nLac) was calculated as the sum of lactate amplitudes over time divided by the sum of pyruvate and lactate amplitudes over time.

Statistical Analysis

We made statistical comparisons of lactate metrics between mice bearing gliomas and healthy controls using the one-tailed Wilcoxon rank-sum test. Using the one-tailed Wilcoxon signed-rank test, we compared paired measurements obtained on subsequent days from the same mice before and after WP1122 treatment. We used built-in functions in MATLAB R2016a to perform all statistical tests. Differences were considered statistically significant for p-values less than 0.05.

Results

Representative MRI and H&E-stained images from a mouse bearing an orthotopic glioma are shown in Figure 3.3. Tumor volumes of 53.76 ± 36.01 mm^3 were observed on T_2-weighted imaging at the second (final) scan time point. H&E staining confirmed the presence of tumors in the right deep gray matter of mice implanted with U87MG cells.
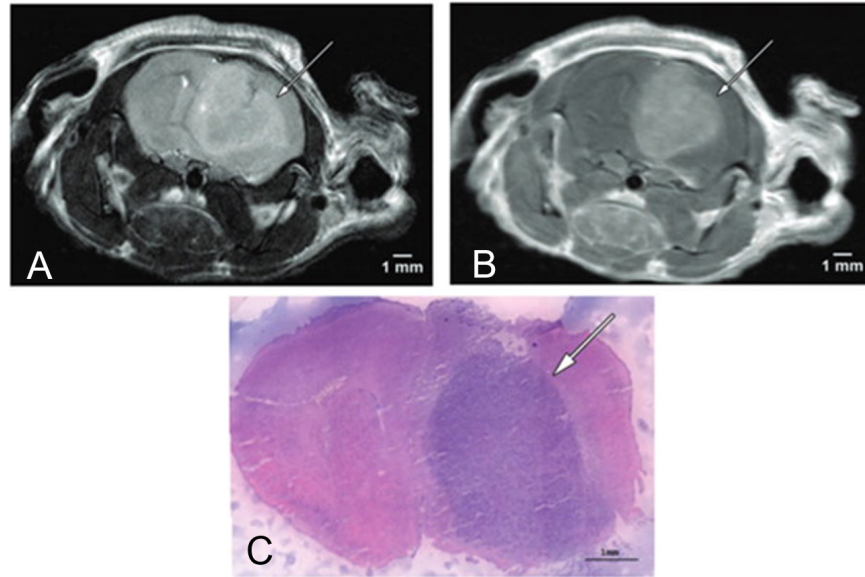
Figure 3.3: Representative images of a mouse with orthotopic glioma. Large well-vascularized tumors were present 40 days after implantation of U87MG glioma cells, as shown by the hyperintense lesion on T_2-weighted (A) and gadolinium-enhanced T_1-weighted (B) axial MRI. The corresponding slice from hematoxylin and eosin (H&E) staining (C) demonstrates a large infiltrative tumor centered in the right sided deep gray matter.

Figure 3.4A shows the typical location of the 1 cm slice used for ^{13}C MR spectroscopy. Representative ^{13}C dynamic spectra from the animal depicted in Figure 3.4A are shown as waterfall plots in Figure 3.4B and 3.4C. HP pyruvate and lactate signals were observed with high SNR following the pyruvate injection, and a reduction in the relative amount of lactate was usually seen after treatment with WP1122 for mice with orthotopic gliomas.

Table 3.1 and Figure 3.5 summarize the quantification of HP lactate from dynamic ^{13}C spectroscopy. At baseline, mice with orthotopic gliomas exhibited mean k_{PL} and nLac values of 0.027 sec^{-1} and 0.28, respectively, which were greater than those observed in healthy control mice (mean k_{PL}=0.011 sec^{-1}, nLac=0.16; p=0.001 for both). Following treatment with the glycolytic inhibitor WP1122, a decrease in k_{PL} and nLac was observed for mice bearing glioma (from baseline mean k_{PL}=0.027 sec^{-1} to post-treatment k_{PL}=0.018 sec^{-1}, p=0.01; from baseline mean nLac=0.28 to post-treatment
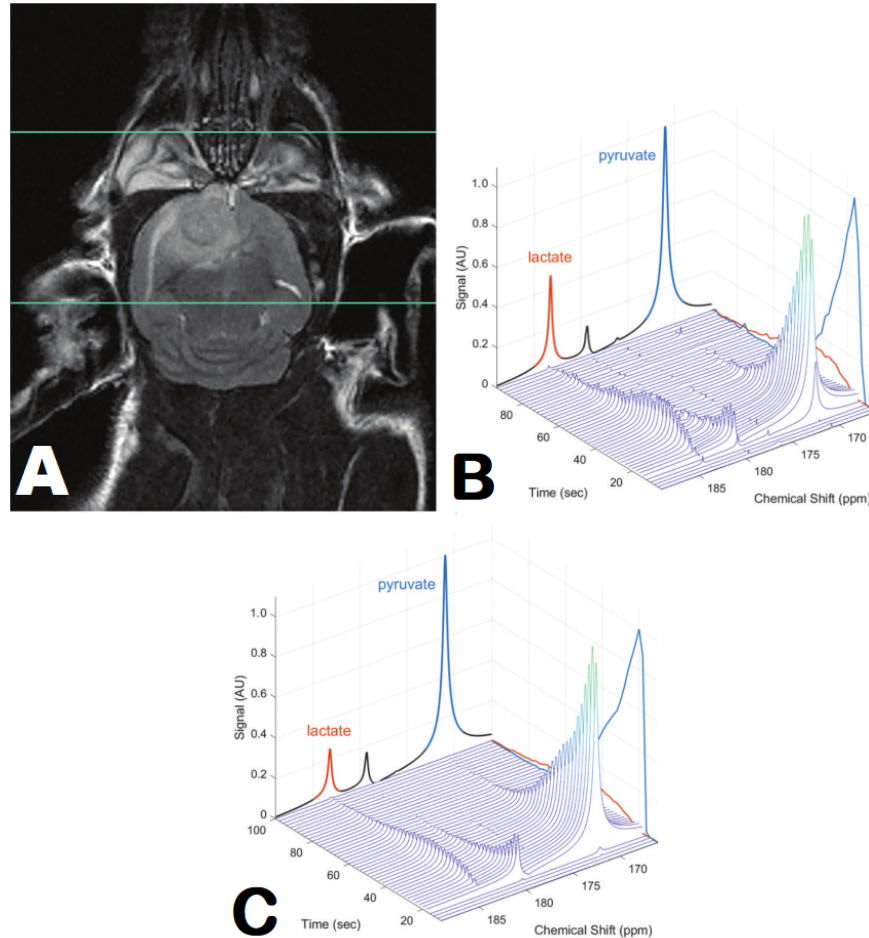
Figure 3.4: Representative hyperpolarized (HP) MR spectroscopic data from a mouse with orthotopic glioma. Pulse-acquire spectroscopy was performed for a 1 cm axial slice centered on the tumor as visualized in coronal T_2-weighted images (A) during injection of HP pyruvate through a tail-vein catheter. Waterfall plots show more lactate signal at baseline (B) than 30 minutes after treatment with the glycolytic inhibitor WP1122 (C).

nLac=0.22, p=0.01). In healthy control mice, no decrease in HP lactate was seen after WP1122 treatment (baseline mean k_{PL}=0.011 sec^{-1} to post-treatment k_{PL}=0.017 sec^{-1}, p=0.91; baseline mean nLac=0.16 to post-treatment nLac=0.21, p=0.84).

Discussion

In this study, we investigated the use of dynamic HP pyruvate MR spectroscopy to assess changes in tumor metabolism after administration of the glycolytic inhibitor
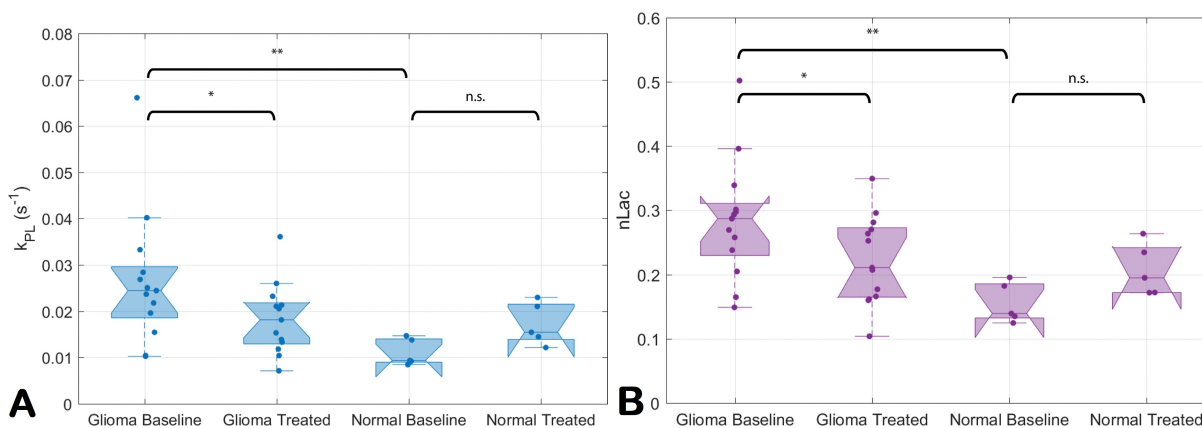
Figure 3.5: Apparent conversion rate of pyruvate to lactate (k_{PL}, left) and lactate signal normalized to sum of lactate and pyruvate signals (nLac, right) were greater in mice bearing orthotopic glioma than in healthy controls (p=0.001 for both k_{PL} and nLac, One-tailed Wilcoxon rank-sum test). After treatment with the glycolytic inhibitor WP1122, a decrease in lactate was observed for mice with glioma (p=0.01 for k_{PL} both and nLac, One-tailed paired Wilcoxon signed-rank test), but no significant decrease was seen for healthy controls (p=0.91 for k_{PL} and p=0.84 for nLac, One-tailed paired Wilcoxon signed-rank test). *, statistical significance with p<0.05; **, statistical significance with p<0.01; ns, no statistically significant difference.

Type of Mouse Brain	Baseline		WP1122 Treated	
	k_{PL} (sec^{-1})	nLac	k_{PL} (sec^{-1})	nLac
Brain with Glioma (n=13)	0.027 ± 0.015	0.28 ± 0.094	0.018 ± 0.0077	0.22 ± 0.069
Healthy Brain (n=5)	0.011 ± 0.0029	0.16 ± 0.031	0.017 ± 0.0046	0.21 ± 0.041

Table 3.1: Hyperpolarized lactate quantifications in diseased and healthy mouse brains. Values are given as means $\pm$ standard deviations of the apparent rate constants of pyruvate to lactate conversion (k_{PL}) and normalized lactate (nLac), the time-integrated ratio of lactate to combined pyruvate and lactate.

WP1122. HP lactate production was quantified at baseline and 30 minutes after oral administration of WP1122 in mice with gliomas and healthy controls, as both an apparent reaction rate (k_{PL}) and normalized lactate ratio (nLac). Both metrics of HP lactate decreased after WP1122 treatment in mice with gliomas, while no significant change was seen in healthy controls.

HP [1-^{13}C]pyruvate MR spectroscopy delivers valuable insights into tumor metabolism that are not directly obtainable through other imaging modalities. Lactate dehydrogenase A (LDHA) expression is upregulated in glioma cells, resulting in higher lactate production and maintaining the cellular reducing potential necessary to sustain glycolysis [102, 103]. Measurements of HP pyruvate and lactate specifically probe the reaction catalyzed by LDHA, delivering information on enzymatic flux that can assess treatment response and disease state in various models of malignant disease [11]. Importantly, the changes in cancer metabolism detectable by HP pyruvate MR spectroscopy reflect the real-time glycolytic state of tumors and precede morphological changes seen in T_2-weighted imaging [15, 18]. This technology therefore holds great promise to provide early indications of response in glioma [17] following treatment with radiation [14], chemotherapy [16, 19] and immunotherapy. HP pyruvate MR spectroscopy measurements are particularly well-suited for assessing the effects of emerging metabolic therapies for glioma, such as inhibitors of glycolytic and mitochondrial metabolism [104].

Recent studies have established the safety and feasibility of HP pyruvate MR in patients with brain tumors, and demonstrated higher lactate production in some tumors relative to background brain metabolism [78, 97]. The unique information offered by HP pyruvate imaging complements the advanced MRI methods often used in patients with brain tumors. Proton spectroscopy and recently introduced methods for deuterium spectroscopy [105] can interrogate the quantities of key metabolites including lactate in normal and diseased tissues; however, these are steady-state measurements

of metabolite pool size and not the direct assessments of enzymatic flux provided by HP MR spectroscopy. The combination of more established advanced MRI methods and real-time metabolic imaging with HP MR spectroscopic imaging could offer drastic improvements in evaluating glioma disease state and treatment response.

While providing detailed dynamic spectroscopic data, the acquisition method used in our study is limited by its lack of spatial resolution. Our data were acquired from the region of the brain containing the tumor, weighted by proximity to the ^{13}C surface coil used for HP signal reception. The tumors interrogated in our study were implanted at a relatively superficial depth. They were large and well-vascularized at the time of HP pyruvate MR spectroscopy. Therefore, despite the contribution of signal from normal tissue, the significant decrease in lactate in tumor-bearing animals following administration of WP1122 was greater than the modest increase in lactate observed in normal matched brain anatomy (Figure 3.5) and can be considered representative of tumor metabolism. While there are imaging methods capable of discriminating HP signals in tumors from other tissues, the application of these methods would incur diminished signal to noise ratio relative to slice selective spectroscopy [106], and with relatively coarse spatial resolution, would not eliminate partial volume averaging effects. Because of the heterogeneous distribution of tissues measured with HP MR spectroscopy and the non-uniform signal reception profile, we chose to quantify our data with a precursor-product model and an area under the curve method. More complicated and physiologically accurate models account for the transport of HP substrates between metabolically distinct physical compartments; however, they require estimation of a vascular input function and fitting of several additional unknown parameters [11]. The quantification methods used here are a compromise given the limited HP signal available from the small quantity of pyruvate that can be administered in a mouse.

Further research is needed to establish the utility of HP pyruvate measurements

in clinical decision making for patients with glioma. HP pyruvate imaging in human subjects has resolved differences in metabolism between regions within healthy brains [107], between normal brain tissue and tumor, and between subregions of large tumors [78, 97]. More thorough clinical trials must be completed to quantify the variability in standardized acquisition and analysis methods before this technology can guide treatment decisions.

Our results show that hyperpolarized MR spectroscopy with [1-^{13}C]pyruvate can assess both baseline metabolism and treatment effects, with promise for rapidly and non-invasively quantifying the metabolic state of gliomas.

Chapter 4

Quantitative Analysis of Hyperpolarized MRI

Hyperpolarized agents must be delivered quickly to the tissues of interest in order to interrogate tissue function within their signal lifetime. In most cases, HP ^{13}C agents are introduced directly to the blood via intravenous injection, although direct intra-arterial infusion may enhance agent delivery and allow HP studies of certain organs with reduced doses or short T_1 agents [108]. Once in the blood stream, the HP agent traverses the vascular tree and extravasates from downstream capillary blood into tissue. In studies using HP agents intended to measure perfusion and permeability, these rates of blood flow and capillary extravasation are of primary interest. For studies of metabolism, the rate of HP agent delivery through the blood controls the amount of agent available to undergo metabolic conversion in tissues of interest. Accounting for the delivery of the administered agent by vascular perfusion is therefore a critical factor in nearly any HP study.

In this chapter, methods for quantification of HP agent perfusion and metabolism are presented. First, a pharmacokinetic model of vascular delivery and extravasation for HP agents is presented. We then address metabolism of HP agents in extended physiological models and in quantification approaches that are not model-based. Lastly, we present novel strategies for dynamic acquisition and analysis of HP perfusion data that are designed to improve measures of vascular volume and permeability.

4.1 Perfusion Modeling

The amount of HP agent delivered to a given tissue is determined by the quantity of agent injected and the rate of delivery via perfusion. When administered to a rodent, a HP solution is typically delivered via tail vein injection and passes through the inferior vena cava into the right atrium of the heart. In human patients injection into a vein in the arm delivers the agent to the heart via the superior vena cava. After being delivered to the right atrium, the HP agent passes through the right ventricle, lungs, left atrium and left ventricle before entering systemic circulation. While the delivery of HP agent to the tip of a thin catheter placed in a vein could be modeled as a boxcar function, at each step of the vascular tree resistance to flow and mixing of the HP solution with blood smooths out the leading edge of the HP agent bolus.

VIF Modeling

When the bolus reaches the smaller arteries and arterioles supplying most tissues of the body it can often be modeled accurately as a gamma variate function. The gamma variate function is often used in nuclear medicine and dynamic susceptibility contrast (DSC) MRI, and can be derived mathematically from the dilution of a short-lived tracer via flow through multiple well-mixed chambers [109]. This function can be expressed as a function of time and two shape parameters (α, β) as

$$y(t) = At^{\alpha} \exp\left(-t/\beta\right) \tag{4.1}$$

In this form, A scales the output while α and β affect both the shape and scale of the function, making least-squares curve fitting difficult. A simplified version of the gamma variate function derived by Madsen is parameterized instead by three parameters: α, the time at which the function maximum occurs (t_{max}) and the maximum value (y_{max}) [110].

$$y(t) = y_{max} \left(\frac{t}{t_{max}}\right)^{\alpha} \exp\left(\alpha\left(1 - \frac{t}{t_{max}}\right)\right) \tag{4.2}$$

Fitting equation 4.2 to data is much simpler since the three parameters are not coupled in any way. The parameter α controls the shape of the curve, with a larger value

corresponding to a sharper rise and fall. Both t_{max} and y_{max} are easily estimated for data with reasonable SNR and affect only the location and magnitude of the function maximum. If a voxel is present in an HP imaging dataset with predominantly vascular signal that could reasonably be expected to represent the delivery of the agent to the tissue of interest, equation 4.2 can be fit to the time curve of this voxel to obtain the shape of the vascular input function (VIF).[1] Alternatives for VIF measurement for HP MRI that have been demonstrated in small animals include monitoring the signal in the left ventricle of the heart [11] and invasive sampling of blood via arterial cannula [111], however these techniques are more difficult to implement in clinical imaging.

In either form, the gamma variate function describes the concentration of HP agent in blood delivered to the capillaries of a tissue of interest over time. The inner surface of most capillaries consist of a continuous tube of endothelial cells held together in a single layer by tight junctions. Oxygen, glucose and small molecules can pass through the small gaps present at the intercellular junctions of the endothelium, and can also be transported across endothelial cells in pinocytic vesicles [71]. The outer surface of this endothelial cell layer is anchored to a thin basement membrane of connective tissue that supports the blood vessel. In the brain the outer surface of this basement membrane is tightly surrounded by the processes of astrocytes, forming the blood-brain barrier that restricts the transport of blood solutes into the brain parenchyma. Certain organs such as kidney and small intestine have fenestrated capillaries with an intact basement membrane, and are more permeable due to small openings in the endothelial cell lining of the vessels. Sinusoidal capillaries present in the liver, bone marrow and spleen are even more permeable than fenestrated capillaries due to larger openings in both the endothelium and basement membrane. In tumors, disregulation of angiogenic signaling results in leaky capillaries that are malformed with a non-uniform and porous endothelial lining that is not tightly bound to its basement membrane [112, 113]. Unlike capillaries in most normal tissues, tumor vasculature is

---

[1]In many contexts the function describing the rate of imaging contrast agent delivery to tissue is called the *arterial* input function, or AIF. Throughout this chapter we use the more general term, VIF, in part to reflect its use in organs with partially non-arterial blood supply (e.g. liver) and in small animal studies for which the low temporal resolution of dynamic HP imaging relative to the rate of blood circulation permits VIF measurement in either arterial or venous blood.

also characterized by vessels that are tortuous and highly variable in size, shape and branching. As a result, solid tumors often possess regions that are strongly perfused in addition to regions that are hypoxic or even necrotic due to inadequate perfusion.

Two-Compartment Perfusion Model

For the purposes of pharmacokinetic modeling, a volume of tissue is assumed to contain one or more compartments in which the concentration of HP agent is uniform. Most widely used HP agents are small molecules that are present natively in tissue and can pass out of the capillaries into the interstitial space. The rate of this imaging agent extravasation into the extravascular extracellular space depends on the permeability of the capillaries, the biochemical properties of the HP agent and the concentration gradient across the capillary membrane. For this discussion of perfusion and permeability modeling, we will consider the case of a HP agent that is biochemically inert and predominantly extracellular within the time frame of the imaging experiment such as ^{13}C urea [84].

In the case of such an extracellular HP perfusion agent, a convenient pharmacokinetic model for describing signal evolution *in vivo* consists of two physical compartments corresponding to the vascular and extravascular spaces with volume fractions v_b and v_e, respectively. The total HP magnetization within a voxel will be proportional to the sum of the HP agent concentrations in each compartment weighted by their corresponding volume fractions.

$$M_z(t) \propto v_b \mathbf{C_b}(t) + v_e \mathbf{C_e}(t) \tag{4.3}$$

The VIF is denoted by $\mathbf{C_b}(t)^2$. As discussed above, the VIF describing the delivery of a HP perfusion agent to tissue capillaries can be modeled using a gamma variate function fit to a voxel containing predominantly vascular signal. This approach estimates the shape of the VIF, however its absolute magnitude requires special consideration in HP MRI due to partial volume effects and non-uniformities in RF excitation and signal reception sensitivity. The currently available RF coil hardware is limited in

---

^{2}Throughout this chapter, quantities describing concentrations of HP agent are shown in bold font.

its anatomical coverage, especially for body imaging on clinical MRI systems. As a result, corrections for non-uniformities in coil receptivity (B_1^-) and often transmission field (B_1^+) may be necessary to obtain a suitable estimate of the VIF amplitude. Alternatively, the VIF amplitude may be fit to signal time curves alongside the other pharmacokinetic model parameters, however this approach can suffer from coupling of VIF amplitude with other parameters, particularly v_b.

For a brief duration of time in which the HP agent is present in tissue capillaries, molecular flux of the agent across the capillary endothelium can be described using Fick's first law. This law states that the molar flux (J, e.g. with units of mol/m^2/s) in a given direction is equal to the inverse of the concentration gradient in that direction times the molecular diffusivity (D, e.g. with units of m^2/s).

$$J = -D\frac{\partial \mathbf{C}}{\partial x} \tag{4.4}$$

Concretely, this law means that in the absence of any other effects stochastic molecular motion will act to reduce the concentration gradient of a solute. If we model the barrier separating our two compartments as a single thin membrane of thickness Δx, the concentration within this membrane space can be assumed to change linearly as a function of position.

$$\mathbf{C}_{\text{inter}}(x) = \mathbf{C}_{\mathbf{b}} + (\mathbf{C}_{\mathbf{e}} - \mathbf{C}_{\mathbf{b}})\frac{x}{\Delta x} \tag{4.5}$$

The molecular flux through the membrane can then be calculated by combining equations 4.4 and 4.5.

$$J = -D\frac{\partial \mathbf{C}_{\text{inter}}}{\partial x} = -\frac{D}{\Delta x}(\mathbf{C}_{\mathbf{e}} - \mathbf{C}_{\mathbf{b}}) = P(\mathbf{C}_{\mathbf{b}} - \mathbf{C}_{\mathbf{e}}) \tag{4.6}$$

Here we have collected the constants into a single coefficient, P, which describes the permeability of the capillary barrier. This permeability coefficient takes a value (e.g. with units of m/s) that depends on the characteristics of the capillaries, the imaging agent and the flow driving the agent through the vascular space.

Since the VIF is assumed to describe $\mathbf{C}_{\mathbf{b}}(t)$, we must formulate an equation describing how the imaging agent concentration in the extravascular compartment changes with time. If the change in extravascular concentration can be assumed to occur only

due to the transcapillary flux described in the previous paragraph, it will have a value equal to this flux (e.g. units of mol/m^2/s) times the capillary surface area (A, e.g. with units of m^2) divided by the total volume of the extravascular compartment within the volume of interest ($V v_e$, e.g. with units of m^3).

$$\frac{\partial \mathbf{C_e}}{\partial t} = J \frac{A}{V v_e} = \frac{PA}{V v_e} (\mathbf{C_b} - \mathbf{C_e}) = \frac{k_{ve}}{v_e} (\mathbf{C_b} - \mathbf{C_e}) \tag{4.7}$$

Here, we have collected all constants apart from the extravascular volume fraction into the volume transfer rate constant k_{ve}. This quantity effectively describes the proportion of imaging agent in the vascular space that is transferred into the extravascular space in a given amount of time (e.g. with units of 1/s), and therefore is considered to quantify the permeability of the microvasculature to the imaging agent.

Equation 4.7 is very similar to the differential equation that forms the basis of the extended Tofts model [114], which is widely used for analysis of dynamic contrast enhancement (DCE) MRI data. In DCE analysis, the concentration of a gadolinium chelate contrast agent measured from rapidly acquired T_1-weighted images is used to obtain volume fraction and capillary permeability measures from a pharmacokinetic model similar to our two-compartment model for HP perfusion agents. However, an important distinction is that the gadolinium chelate collects in tissue over time, accelerating spin-lattice relaxation in proportion to its concentration. HP agents, in contrast, provide a direct source of signal with an intensity proportional to the amount of HP agent in the imaging volume.

We have so far only considered the change in the extravascular concentration of a HP perfusion agent within a brief period of time during which T_1 decay of the HP agent can be neglected. Equation 4.7 can be modified to include these relaxation effects:

$$\frac{\partial \mathbf{C_e}}{\partial t} = \frac{k_{ve}}{v_e} \mathbf{C_b} - \left(\frac{k_{ve}}{v_e} + \frac{1}{T_1} \right) \mathbf{C_e} = \frac{k_{ve}}{v_e} \mathbf{C_b} - \alpha \mathbf{C_e} \tag{4.8}$$

Here we have collected the effects of reverse capillary transport (i.e. washout, which is assumed to occur at the same rate as forward capillary transport) and spin-lattice decay into a single coefficient, α. Note that T_1 in this equation refers to the apparent relaxation rate of the HP signal *in vivo*, which is usually significantly shorter than

the T_1 measured in solution and may include loss mechanisms other than true spin-lattice relaxation. Just as in the solution for the extended Tofts model, a solution to the differential equation 4.8 can be found by applying an integrating factor that describes the system response to a unit impulse of HP agent in the blood.

$$\mathbf{C_e}(t) = \mathbf{C_e}(t=0)e^{-\alpha t} + \frac{k_{ve}}{v_e}\int_0^t \mathbf{C_b}(\tau)e^{-\alpha(t-\tau)}d\tau \tag{4.9}$$

By combination of equations 4.3 and 4.9, an equation describing the longitudinal HP magnetization over time can be derived. However, such an equation is not very useful in itself since M_z is not observed directly. We must therefore consider the effects of RF excitation on the HP spin system. If the method used for HP imaging is a spoiled gradient echo pulse sequence, the transverse magnetization (M_{xy}) can be assumed to be negligible when each RF pulse is applied. Most often this assumption is met by using a repetition time for dynamic HP ^{13}C imaging that is of sufficient length that a negligible amount of transverse magnetization persists across excitations of the same set of isochromats due to spin-spin decay ($TR > 5T_2^*$). However, even if this is not the case, spoiled gradient echo sequences vary the phase of RF excitation pulses and the amplitude of gradient pulses applied after data readout to suppress the contribution of coherent transverse signal from separate excitation cycles [35]. Even when spectrally selective pulses of relatively long duration (e.g. 10 ms or more) are used, this RF pulse duration is typically very short relative to the repetition time that elapses between pulses. In this case, the effect of the RF pulse can be modeled as an instantaneous redistribution of the longitudinal and transverse net magnetic moment.

$$M_z(T_{RF}) = M_z(T_{pre})\cos(\theta) \tag{4.10}$$

Here, T_{pre} and T_{RF} denote the moments in time at the start and end of the RF pulse, respectively. The longitudinal HP magnetization in the TR interval elapsed between pulses ($T_{RF} \le t \le T_{RF} + TR$) can be described as:

$$M_z(t) \propto v_b\mathbf{C_b}(t) + v_e\mathbf{C_e}(T_{RF})e^{-\alpha(t-T_{RF})} + k_{ve}\int_{T_{RF}}^t \mathbf{C_b}(\tau)e^{-\alpha(t-\tau)}d\tau \tag{4.11}$$

The observed imaging signal is derived from the transverse magnetization, with some amount of spin-spin relaxation occurring during the encoding of k-space and/or chem-

ical shift.

$$M_{xy}(T_{RF} + TE) = M_z(T_{pre}) \sin(\theta) e^{-\frac{TE}{T_2^*}} \tag{4.12}$$

Equations 4.10-4.12 describe the behavior of the HP magnetization in the context of our two-compartment model of perfusion agent behavior in tissue. The evolution of longitudinal magnetization is modeled continuously in the TR interval using equation 4.11, with RF losses depicted discretely in time using equation 4.10. The volume transfer coefficient and the compartment volume fractions constitute the three primary physiological parameters (k_{ve}, v_b, v_e) describing the evolution of the HP signal. Given values for these model parameters, as well as a VIF and the effective relaxation time constants, simulated signal curves can be generated for any set of spoiled gradient echo imaging parameters.

As noted in the first paragraph of this section, we are assuming our imaging agent does not enter extravascular cells during the HP signal lifetime. It will therefore be the case that the two individual compartment volumes account for less than the total imaging volume ($v_b + v_e < 1$). Since the compartment volume fractions most often are unknown parameters that must be estimated via least squares curve fitting approaches, it is useful to parameterize these quantities in a way that is more amenable to this process. This can be done by describing the extravascular volume into which the HP agent can distribute as a fraction of the total extravascular volume.

$$v_e = v_{ei}(1 - v_b) \tag{4.13}$$

An optimization strategy that constrains both v_b and v_{ei} to within the open interval $(0, 1)$ can therefore provide realistic volume fractions. Apart from the cellular space, the large voxel sizes generally used in HP MRI often include subvolumes that are inaccessible to any HP agent, such as air or cortical bone, which effectively reduces v_e. Therefore, even for agents that readily diffuse into cells, this manner of formulating the volume fractions may be useful. However, the fitting of the model parameter v_{ei} in many cases would not be expected to provide much value in itself and is only necessary to precisely account for the concentration of the HP agent within the extravascular compartment. Since estimation of an additional parameter in data fitting increases

the variance of all parameters derived from this process, a common simplifying assumption when applying two-compartment modeling to real data is that $v_e = 1 - v_b$ (i.e. $v_{ei} = 1$).

In addition to the sub-compartmentalization of the extravascular space, the cellular component of blood also deserves consideration. By far the largest cellular component of whole blood is made up of erythrocytes, which typically constitute a volume fraction (hematocrit) of 40-50% [71]. If the HP agent is not able to enter this volume, the modeled vascular concentration must be corrected for the fact that this signal represents the imaging agent in the plasma volume rather than the whole blood volume, as is done for modeling of DCE-MRI data with gadolinium chelates [114]. In the case of urea [115] and pyruvate [116], the erythrocyte plasma membrane contains transport proteins that quickly equilibrate the intracellular and blood plasma concentrations, and we therefore assume a uniform HP agent concentration in the blood for the model formulated in this section. However other HP agents might need special consideration in this regard, particularly if pharmacokinetic modeling is applied to HP images in situations where the imaging subject may have an abnormally high or low hematocrit.

4.2 Metabolic Quantification of HP Pyruvate

The two-compartment pharmacokinetic model derived in the previous section is useful for modeling the evolution of HP signal in tissue for perfusion agents such as urea, but requires modification to account for the behavior of biochemically active HP agents. Such agents are primarily metabolized by enzymes present within cells, so the labeled molecules must additionally cross the plasma membrane and in some cases the mitochondrial membrane before the downstream metabolites of interest are observed. A more physiologically accurate three compartment model of vascular delivery, uptake and conversion would therefore account for each of these processes with rate constants for capillary transport, plasma membrane transport and enzymatic activity [11]. However, the use of such intricate pharmacokinetic models in the analysis of HP MRI data can be very difficult. In general, a pharmacokinetic model with more parameters may

more faithfully represent the physiological processes of interest, however when applied to a given dataset a larger number of unknowns results in greater variances for the parameter estimates derived from the data fitting process. Compared to our two-compartment perfusion model, a three-compartment metabolic model entails — at the very least — an additional volume fraction, an additional volume transfer coefficient and a rate constant describing intracellular metabolic conversion. Further complexity could be added if disparate cellular populations in the tissue microenvironment are taken into account.

These considerations highlight the fundamental motivation of pharmacokinetic modeling, which is to provide quantitative metrics of tissue function that are useful in practice. While such metrics ideally represent a physiological process as accurately as possible, the high complexity of biological systems will always require trade-offs to strike a balance between physiological accuracy and practical utility. The more parameters a pharmacokinetic model contains, the greater the difficulty in applying it to a given dataset due to both increased computational overhead and greater uncertainty in the derived model parameters. With this in mind, it is worth reviewing analysis methods — including those that are not model-based — to evaluate their practical utility in the context of the most widely used metabolic HP agent, [1-^{13}C]pyruvate.

Non Model-Based Metabolic Analysis

The simplest analysis method for a metabolic agent is a ratiometric approach. Unlike the HP perfusion agent described in the previous section, metabolic agents like HP pyruvate generate multiple chemical signals *in vivo*, and their relative amplitudes can be easily quantified. This method was shown in practice in section 3.3 for HP pyruvate measurements as the normalized lactate ratio (nLac). nLac was calculated for this application as the ratio of the time-integrated area under the curve (AUC) for lactate to the sum of pyruvate and lactate AUCs.

$$nLac = \frac{AUC_{lac}}{AUC_{pyr} + AUC_{lac}} \tag{4.14}$$

In many cases, alternate ratiometric analyses are performed by calculating the time-integrated ratio of lactate relative to pyruvate or relative to the sum of all HP ^{13}C signals. For experiments with very limited temporal and spatial resolution, these ratiometric approaches may be the only viable method of data quantification. Due to the simplicity of these precursor-product ratios in quantifying the activity of metabolic agents, they are used in some form in nearly all studies of HP pyruvate metabolism. Even when data is intended for more complex pharmacokinetic analysis, the calculation of HP signal ratios often serves as a first-pass evaluation for the purpose of obtaining preliminary descriptive statistics. If the effects of HP agent delivery to the compartment in which chemical conversion takes place are consistent, ratiometric quantities can be shown to be directly proportional to the apparent rate constants of chemical conversion obtained via pharmacokinetic modeling [117].

The AUC ratios described above quantify the relative lactate signal accumulated over time. Another class of non model-based methods for HP pyruvate data analysis depends on measurements made at the precise moment of peak lactate signal. The lactate signal amplitude at this moment of peak intensity — typically normalized to the pyruvate signal at the same time point — is often used as a non model-based quantity descriptive of chemical conversion. Such a peak normalized lactate metric derived from time-resolved imaging was employed in a recently published clinical study of prostate cancer and shown to correlate with Gleason score [79]. Alternatively, the time elapsed from onset of HP lactate signal to the moment of peak lactate intensity has been proposed for model-free analysis, and was shown to correlate well with pharmacokinetic analysis *in vitro* and in tumor models in rodents [118]. These maximum lactate analyses are generally extremely sensitive to the precise timing of data acquisition. In some cases, the start of the imaging acquisition is delayed relative to the injection time in order to attempt to acquire images with greater lactate SNR due to the lesser RF depletion of the HP pyruvate precursor before it can undergo metabolic conversion. In this context, bolus tracking of HP pyruvate using very low excitation angle RF pulses can help ensure efficient use of the HP magnetization and reproducible timing of lactate imaging [119–121]. However, when initiating imaging after the HP

bolus arrival the initial portion of the HP signal time curves is lost, which complicates the use of pharmacokinetic modeling approaches for these data. Even when sampling of the peak lactate signal is timed perfectly, the lactate signal may have very poor SNR due to either the experimental setup or the physiological state of the tissue of interest. These types of peak lactate metrics are therefore better suited for studies in which strong HP lactate signal is always present.

Pharmacokinetic Metabolic Modeling

While the non model-based methods described in the preceding paragraphs permit rapid and straightforward quantification of HP pyruvate metabolism, they are sensitive to differences in physiological state apart from true variation in enzymatic flux. For example, the same nLac value could be measured in tissue with high LDH activity and low uptake of pyruvate as in tissue with low LDH flux and high pyruvate uptake. In such situations, pharmacokinetic modeling of HP signals provides a method for distinguishing tissues on the basis of the shape of the HP pyruvate and lactate signal curves over time, differentiating the disparate effects of HP agent uptake and chemical conversion. The solutions to these pharmacokinetic models permit the calculation of HP pyruvate and lactate signals at any point in time, allowing the non model-based metrics described above to be derived even for datasets for which they cannot be calculated directly. The primary drawbacks of pharmacokinetic analysis relative to non model-based analyses are that it can entail a computationally intensive optimization process, and that it often requires manual user input that could lead to erroneous results (e.g. the definition of a VIF or of assumed model parameters).

A set of three pharmacokinetic models describing HP pyruvate uptake and conversion to lactate was introduced by Bankson, et al. in 2015, and evaluated in the context of constrained reconstruction of HP images for small animal models of cancer [11]. These models account for two chemical pools of HP magnetization representing pyruvate and lactate, with chemical interconversion described as a first order process. In all cases, the parameter k_{PL} is the forward rate constant of this chemical conversion and is nominally indicative of metabolic flux. Typically the reverse reaction rate,

k_{LP}, is assumed to be negligible, which is often a reasonable assumption given the low concentration of endogenous pyruvate in tissue relative to lactate. For the sake of generalizability, k_{LP} terms are included in the equations presented here. Losses of longitudinal HP magnetization for pyruvate and lactate occur continuously in time with individual relaxation time constants that are often given as estimated values and held constant during the data fitting process. The VIF driving signal evolution in these models is assumed to deliver only HP pyruvate (not HP lactate) to the imaging volume, and the observed HP lactate is therefore assumed to be the product of local metabolism. This assumption is consistent with measurements of HP pyruvate activity in whole blood [122] and with spin-echo measurement of HP labeling in small animal models [123], which indicate negligible vascular HP lactate signal.

In the following paragraphs each of these three models will be described. In the original presentation of these models, losses due to RF pulses were modeled as continuous M_z decay at a rate of $\frac{1-\cos\theta}{TR}$. However, in the equations below RF excitation effects are excluded since they can be modeled more accurately for spoiled gradient echo imaging as discrete losses with equations 4.10 and 4.12. Differential equations are provided for each model below, and account for the remaining effects occurring in the delay between RF pulses, as in equation 4.11 ($T_{RF} \leq t \leq T_{RF} + TR$, where T_{RF} denotes the moment at the end of the RF pulse).

One-Compartment Model In the simplest pharmacokinetic model, all pyruvate is assumed to be in direct exchange with lactate in a single spatial compartment. The differential equations describing inter-pulse evolution of HP longitudinal magnetization for this one-compartment model are

$$\frac{\partial \mathbf{P}}{\partial t} = -\left(k_{PL} + \frac{1}{T_{1,P}}\right)\mathbf{P} + k_{LP}\mathbf{L}$$
$$\frac{\partial \mathbf{L}}{\partial t} = k_{PL}\mathbf{P} - \left(k_{LP} + \frac{1}{T_{1,L}}\right)\mathbf{L}$$

(4.15)

where **P** and **L** denote pyruvate and lactate, respectively. With a single spatial compartment, there is no explicitly defined VIF in this model. For *in vivo* data, the pyruvate and lactate signal curves are typically fit with the observed pyruvate signal serv-
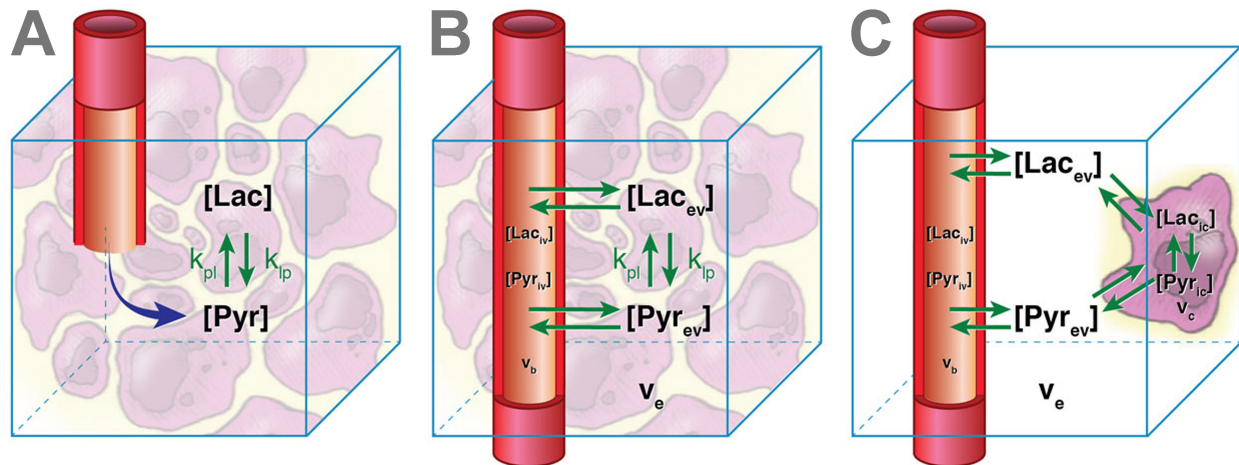
Figure 4.1: Candidate kinetic models to describe dynamic signal evolution of HP pyruvate and lactate in vivo. All models include two chemical pools and one spatial compartment (A), two spatial compartments (intravascular and extravascular) with exchange limited to extravascular region (B), or three spatial compartments (intravascular, extravascular/extracellular, and intracellular) with exchange restricted to the intracellular region (C).
Figure reprinted from James A Bankson, et al. Kinetic Modeling and Constrained Reconstruction of Hyperpolarized [1-13C]-Pyruvate Offers Improved Metabolic Imaging of Tumors. *Cancer Res* 2015; 75(22): 4708-15. doi:10.1158/0008-5472.CAN-15-0171. with permission from the American Academy for Cancer Research (License Number 4856260086289).

ing as the "effective VIF" driving the model. In this approach, the first row of equation 4.15 is disregarded since changes in **P** are not considered to occur due to chemical conversion and T_1 relaxation. Instead, the empirically measured HP pyruvate signal is assumed to reflect **P** and drive the production of HP lactate subject to k_{PL} and $T_{1,L}$. Some authors [124] refer to this type of analysis as "inputless fitting". For *in vitro* experiments, however, it is common for HP pyruvate to be injected rapidly into a cell suspension that is prepared in an enclosed chamber, e.g. a NMR tube. In such studies, the evolution of HP signals within a closed system can be modeled using the full set of differential equations 4.15.

Compared to a fully time-integrated lactate ratio, the k_{PL} derived from this model offers only marginal added benefits as a summary metric of metabolism. One such benefit is the ability to model relaxation losses of lactate, which are not accounted for systematically in non model-based metrics. The one-compartment k_{PL} is sensitive

to variations in pyruvate delivery to the site of metabolism much in the same way as nLac. If pyruvate is highly compartmentalized in tissue, for example due to slow transport across the capillary membranes, a one-compartment model may not be able to accurately represent the observed HP signal curves. Nevertheless, one-compartment modeling can be useful for *in vivo* HP experiments that provide dynamic spectroscopic information but lack the spatial resolution necessary to resolve signal arising from blood vessels and tissues (e.g. the slice-selective spectroscopy used in section 3.3). Due to the difficulty of measuring a VIF from the relatively large voxels typically used for clinical HP imaging, one-compartment modeling is the most widespread method for obtaining a k_{PL} value in human studies to date [107, 124–126].

Two-Compartment Model   The second model for HP pyruvate metabolism accounts for signals arising in vascular and extravascular spaces, similar to the two-compartment perfusion model derived in section 4.1. As in that case, signal evolution of the administered HP agent in the vascular compartment is described by the VIF ($\mathbf{P_b}$). If that perfusion model is expanded to include pyruvate and lactate pools with chemical exchange and T_1 losses occurring in the extravascular space, the following set of differential equations are derived.

$$
\begin{aligned}
\frac{\partial \mathbf{P_e}}{\partial t} &= -\left(\frac{k_{ve}}{v_e} + k_{PL} + \frac{1}{T_{1,P}}\right)\mathbf{P_e} + k_{LP}\mathbf{L_e} + \frac{k_{ve}}{v_e}\mathbf{P_b} \\
\frac{\partial \mathbf{L_e}}{\partial t} &= k_{PL}\mathbf{P_e} - \left(\frac{k_{ve}}{v_e} + k_{LP} + \frac{1}{T_{1,L}}\right)\mathbf{L_e}
\end{aligned}
\tag{4.16}
$$

This two-compartment model provides a more realistic depiction of the physiological process of HP agent delivery than the one-compartment model. However, if chemical conversion of HP pyruvate occurs only in the intracellular space the implicit assumption underlying this two-compartment model is that pyruvate transit across the plasma membrane is rapid. When a significant HP pyruvate concentration gradient is present between the extravascular/extracellular and intracellular spaces, this assumption is violated.

Three-Compartment Model The third model presented by Bankson, et al. accounts for HP pyruvate and lactate within three spatial compartments corresponding to the vascular, extravascular/extracellular and intracellular spaces. Chemical exchange of HP agent occurs only in the intracellular compartment, resulting in the following set of differential equations.

$$\frac{\partial \mathbf{P_{ee}}}{\partial t} = -\left(\frac{k_{ve}}{v_{ee}} + \frac{k_{ec}}{v_{ee}} + \frac{1}{T_{1,P}}\right)\mathbf{P_{ee}} + \frac{k_{ec}}{v_{ee}}\mathbf{P_{ic}} + \frac{k_{ve}}{v_{ee}}\mathbf{P_{b}}$$

$$\frac{\partial \mathbf{L_{ee}}}{\partial t} = -\left(\frac{k_{ve}}{v_{ee}} + \frac{k_{ec}}{v_{ee}} + \frac{1}{T_{1,L}}\right)\mathbf{L_{ee}} + \frac{k_{ec}}{v_{ee}}\mathbf{L_{ic}}$$

$$\frac{\partial \mathbf{P_{ic}}}{\partial t} = \frac{k_{ec}}{v_{ic}}\mathbf{P_{ee}} - \left(\frac{k_{ec}}{v_{ic}} + k_{PL} + \frac{1}{T_{1,P}}\right)\mathbf{P_{ic}} + k_{LP}\mathbf{L_{ic}}$$

$$\frac{\partial \mathbf{L_{ic}}}{\partial t} = \frac{k_{ec}}{v_{ic}}\mathbf{L_{ee}} + k_{PL}\mathbf{P_{ic}} - \left(\frac{k_{ec}}{v_{ic}} + k_{LP} + \frac{1}{T_{1,L}}\right)\mathbf{L_{ic}}$$

(4.17)

Here the subscripts $_{ee}$ and $_{ic}$ indicate extravascular/extracellular and intracellular signals or volume fractions, respectively. As in equation 4.16, k_{ve} denotes the rate of capillary transport, while the additional volume transfer coefficient, k_{ec}, describes the rate of HP agent transport across the cellular membrane.

When applying these models to *in vivo* imaging data for estimation of k_{PL} (where k_{LP} is assumed to be negligible), the one-, two- and three-compartment models require some combination of joint estimation or prior assumption for 1, 5 and 7 additional physiological parameters, respectively. Given this added complexity, the capability of established ^{1}H MRI methods to inform the quantitative analysis of HP ^{13}C MRI data is an important consideration. For example, anatomical and angiographic imaging can provide guidance on the spatial localization of HP signals and on the estimation of VIFs, while DCE and diffusion weighted imaging could provide spatially resolved estimation of tissue volume fractions and volume transfer rates. HP pyruvate imaging therefore provides a metabolic measurement that is particularly well suited as an addition to multiparametric MRI examinations that are being conducted with increasing frequency in diagnosing and staging pathologies of the brain [127], prostate [128], liver [129], kidney [130] and breast [131], as well as other organs.

The utility of a given quantitative analysis approach in HP MRI is very depen-

dent on the HP acquisition methods used, the biology of interest and the availability of prior information to inform this analysis. In the constrained reconstruction approach implemented by Bankson, et al. a HP pyruvate VIF was measured from the left ventricle of the rodent heart and image reconstruction was constrained to map HP signals to voxels containing tissue as visualized in anatomic ^{1}H imaging. Comparing the three pharmacokinetic models through these imaging methods, Bankson et al. demonstrated that the two-compartment model provided the optimal balance of quantitative accuracy and model complexity [11]. In a more recent study, Larson, et al. evaluated several lactate quantification approaches in the context of clinical HP MRI of the prostate using a variable excitation angle dynamic compressed sensing imaging method [124]. This study compared a simple ratiometric analysis, a time to peak lactate metric, the "inputless fitting" one-compartment k_{PL} described above (4.2), and k_{PL} from an extended one-compartment model that includes an unobserved VIF driving accumulation of HP pyruvate in the imaging volume. Unlike the multi-compartment models described here, this extended one-compartment model allows for only unidirectional flux of HP pyruvate from the VIF into the imaging voxel. In this application three VIF parameters describing the time of HP agent arrival, duration of the VIF and rate constant of HP pyruvate transfer from the unobserved VIF to the single modeled compartment were fit, with the prior assumption of a fixed VIF shape. Assessing these analysis methods for their clinical data and in numerical simulation, the authors found that the time to peak lactate performed very poorly at the SNRs observed *in vivo*. Additionally, both the ratiometric lactate measurement and the "inputless fitting" k_{PL} were more reproducible than the extended one-compartment k_{PL} that was obtained with joint estimation of VIF parameters.

Overall, quantification and modeling of HP MRI data remains a very active area of research, and results of these analyses must always be considered in the context of the specific biological and technical factors for a given study. Recent data reported in preclinical HP pyruvate imaging of colon and breast cancer [132] and in clinical imaging of the prostate [79] indicate that HP lactate production positively correlates with the expression of the MCT proteins responsible for plasma membrane transport. These

observations suggest that the cellular uptake of pyruvate is an important factor determining the evolution of HP signals *in vivo*, however the rate of such transport is only accounted for systematically in more complex kinetic modeling approaches that are difficult to implement in practice. Additionally, *in vitro* experiments have demonstrated that T_1 relaxation of carboxyl ^{13}C signals occurs much more rapidly in the cytosol than in the extracellular space [133]. While these studies and others are indicative of effects impacting the apparent chemical exchange rate of pyruvate and lactate *in vivo*, further work is required to quantitatively evaluate the impacts of plasma membrane transport and shorter intracellular T_1 relaxation time constants on k_{PL} values obtained through specific pharmacokinetic models.

4.3   Numerical Simulations of HP Perfusion Imaging

Pharmacokinetic models of HP agent behavior *in vivo* allow for both the quantitative analysis of experimental data and the numerical simulation of these experiments. In the latter application, synthetic HP signal curves are generated for a set of model and acquisition parameters, and the model is subsequently fit to this synthetic data with the addition of random noise. By repeating this curve fitting process with fresh noise multiple times, the accuracy and reproducibility of different sets of acquisition parameters can be compared for any set of physiological model parameters. These simulation experiments can therefore guide the selection of optimal imaging strategies by sampling the overall pharmacokinetic model and acquisition parameter space in a much more complete fashion than is possible through empirical experimentation. Additionally, by applying intentional errors to parameters that are assumed to be known in the curve fitting process, the sensitivity of the pharmacokinetic model to such inaccuracies may be systematically evaluated [101].

Numerical simulations of HP urea signal evolution were performed using the pharmacokinetic model derived in section 4.1. In these simulations, a conventional spoiled gradient-echo imaging approach was compared to two alternative approaches described in the following subsections. The ranges of acquisition parameter, standardized peak
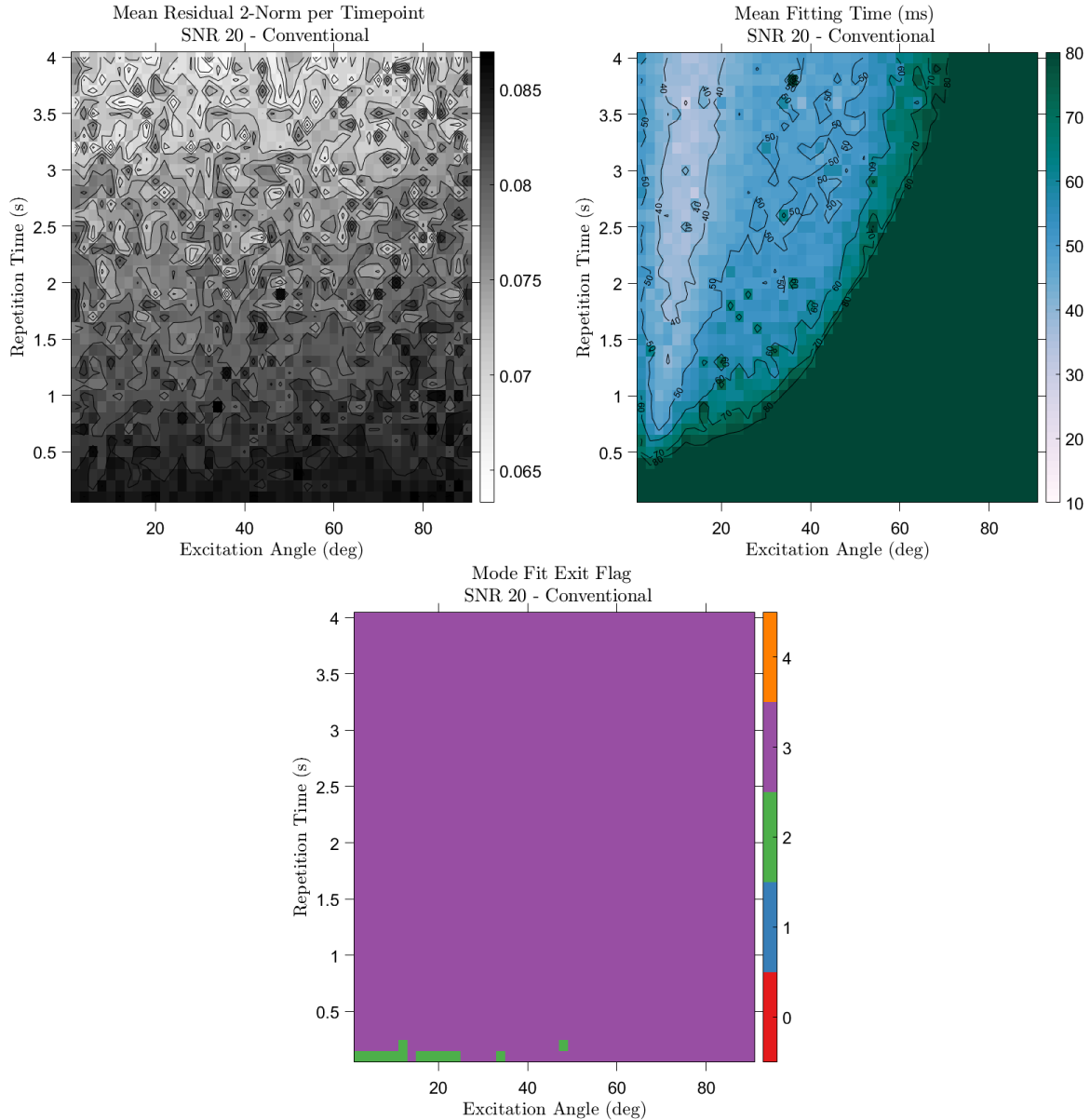
Figure 4.2: Least-squares curve fitting metrics for simulated HP perfusion imaging with conventional spoiled gradient-echo acquisitions. All curve fitting was performed in MATLAB using the `lsqcurvefit` function with a trust region reflective algorithm. The normalized 2-norm of the residuals provides a metric of the overall numerical accuracy of the fit. The exit flag indicates the termination condition of the fitting algorithm, with values of 2 and 3 indicating that the change in the fit parameters and in the residuals were less than a specified tolerance, respectively. For consistent simulation results, the optimization function should reach similar termination conditions indicative of the solver approaching a convergent solution, as shown here.

	TR (s)	θ (deg)	Peak SNR*	v_b	v_{ei}	k_{ve} (s^{-1})	T_1 (s)
Simulation Value	[0.1:0.1:4]	[2:2:90]	[5:5:50]	0.09	0.3	0.02	20

Table 4.1: Parameter ranges used for simulation of proposed HP urea acquisition methods are shown. Values in square brackets indicate ranges tested, using MATLAB notation (low : increment : high). Parameter values for k_{ve} and v_b correspond to those observed in two-compartment modeling of HP pyruvate [101], while the T_1 corresponds to the apparent *in vivo* relaxation time for HP urea [82]. Tissue cellularity can vary tremendously in tumors and other organs, but an extravascular distribution volume fraction (v_{ei}) was chosen based on DCE-MRI results from small animal tumor models. The peak SNR value corresponds to the variance of added Gaussian noise that would result in that SNR for a TR of 2 s and θ of 20 deg. Note that this value does not translate to the specified peak SNR for other TR and θ values due to variations in HP signal amplitude, however it provides a consistent parameterization of noise across these simulations.

SNR, and ground-truth physiological parameter values tested are provided in table 4.1. A gamma-variate VIF shape corresponding to that previously measured from HP urea imaging in mice was used, with $\alpha = 0.8$ and $t_{max} = 8.1$ s (equation 4.2). Although many noise levels were assessed, in the figures summarizing these experiments only the results for the noise variance that corresponds to a peak SNR of 20 in a 2 s TR, 20 deg excitation angle conventional imaging experiment are shown. At each combination of parameter values, fitting of synthetic signal curves was repeated 100 times with fresh noise using a nonlinear least-squares trust region reflective algorithm [134]. The accuracy of fitted pharmacokinetic model parameters was summarized as the mean error relative to the true values, and their reproducibility was assessed through the coefficient of variation. The figures in the following subsections comparing acquisition strategy performance on the basis of these numerical simulations present contour plots summarizing the mean relative error and coefficient of variation across the ranges of repetition times and excitation angles listed in table 4.1. Simulated acquisitions that result in better accuracy and reproducibility are always shown as lighter colors for each estimated physiological parameter.

Perfusion Imaging with Periodic Saturation

Large excitation angles are usually avoided in dynamic imaging of HP substrates to avoid saturating the non-renewable signal, however their careful use offer interesting possibilities particularly in the context of perfusion imaging. When a perfect 90 degree pulse is applied, the HP longitudinal magnetization in the imaging volume can be assumed to be fully expunged. If such a saturation pulse is applied at an appropriate time and location in the middle of a dynamic HP experiment, some HP signal will subsequently reperfuse the RF saturated tissue volume by vascular delivery. In the context of pharmacokinetic modeling of the HP signal, this greatly reduces the fundamental uncertainty which this analysis approach seeks to address — namely, the compartmentalization of the imaging agent *in vivo*.

We assessed a HP imaging technique in which 90 degree saturation pulses are used every 10 seconds in the dynamic imaging experiment, as depicted in figure 4.3. We refer to this method as "periodic saturation" and the contour plots that follow compare such a technique to the equivalent "conventional" spoiled gradient-echo imaging method with matching TR and excitation angle (at imaging time points not corresponding to the application of a saturation pulse).

From the results of these simulations, it is evident that the periodic application of saturation pulses primarily improves measurement of vascular volume (v_b, figure 4.5), at the expense of somewhat degraded performance in estimating capillary permeability (k_{ve}, figure 4.4) and particularly poor accuracy and reproducibility of the tissue distribution volume (v_{ei}, figure 4.6). In order to obtain estimates of k_{ve} and v_{ei} with reasonable accuracy and precision using the periodic saturation method, these simulations indicate that a narrow range of short repetition times and low excitation angles must be used. Depending on the capabilities of the MRI system on which the HP experiments are conducted, the use of such short TR values and low excitation angles may not be feasible due to gradient limitations or due to the SNR levels attainable with a given RF coil setup. Because of these practical considerations, it may not always be appropriate to assess the comparative performance of these imaging
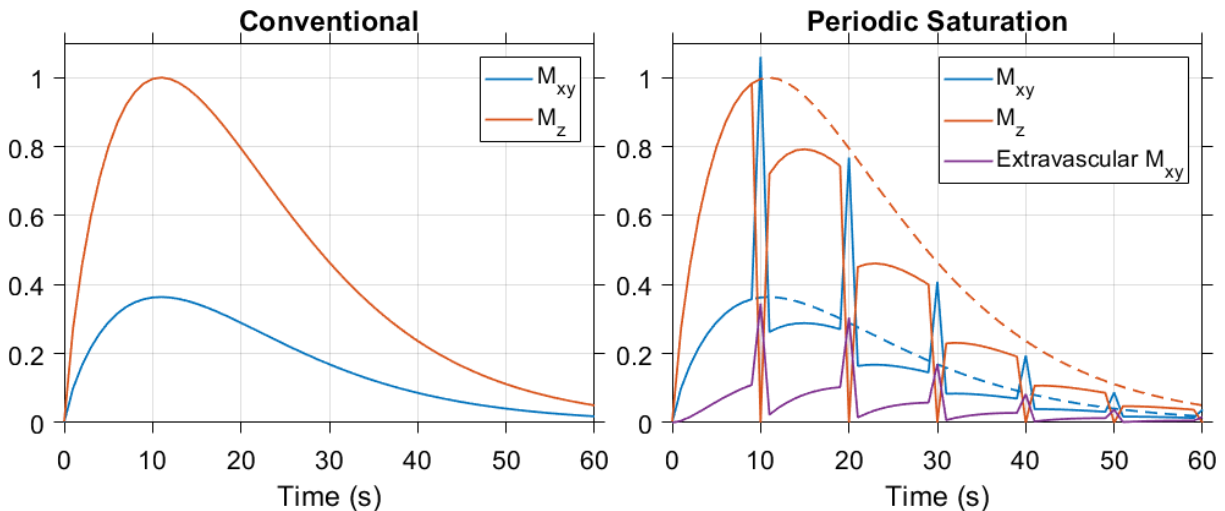
Figure 4.3: Simulated M_z and M_{xy} time curves are shown for HP urea imaging using conventional (left) and periodically saturated (right) spoiled gradient-echo imaging. Time curves of the conventional imaging method are plotted as dashed lines on the right. The application of 90 degree excitations every 10 seconds expunges HP magnetization in the extravascular space, allowing perfusion and permeability effects to be assessed multiple times in a single experiment through reperfusion of the HP agent. However, this comes at a cost as the overall HP signal is reduced significantly through the application of 90 degree pulses, as illustrated by these M_z and M_{xy} curves of the periodic saturation method relative to conventional imaging.

techniques on the basis of a single optimal set of acquisition parameters. In general, a more comprehensive comparison of the ranges of acquisition parameter values that provide accurate and reproducible results would be indicated to evaluate the utility of proposed imaging strategies in the face of these technical factors.

The results summarized in figures 4.4-4.6 agree with an intuitive interpretation of the periodic saturation method in the context of our two-compartment pharmacokinetic model. Through a 90 degree excitation that removes all previously accrued extravascular signal, the observed HP time intensity curves contain a greater proportion of vascular signal and therefore can provide less insight into the transit of HP agent into the tissue space. While these results may be true for the physiological parameters and specific model used in these simulations, the use of 90 degree pulses for dynamic HP imaging could prove useful in other contexts. When using modeling approaches that seek to quantify the rate of blood flow and vascular transit time in tissue (such as the modeling that is typically employed in DSC-MRI), the use of saturation pulses for
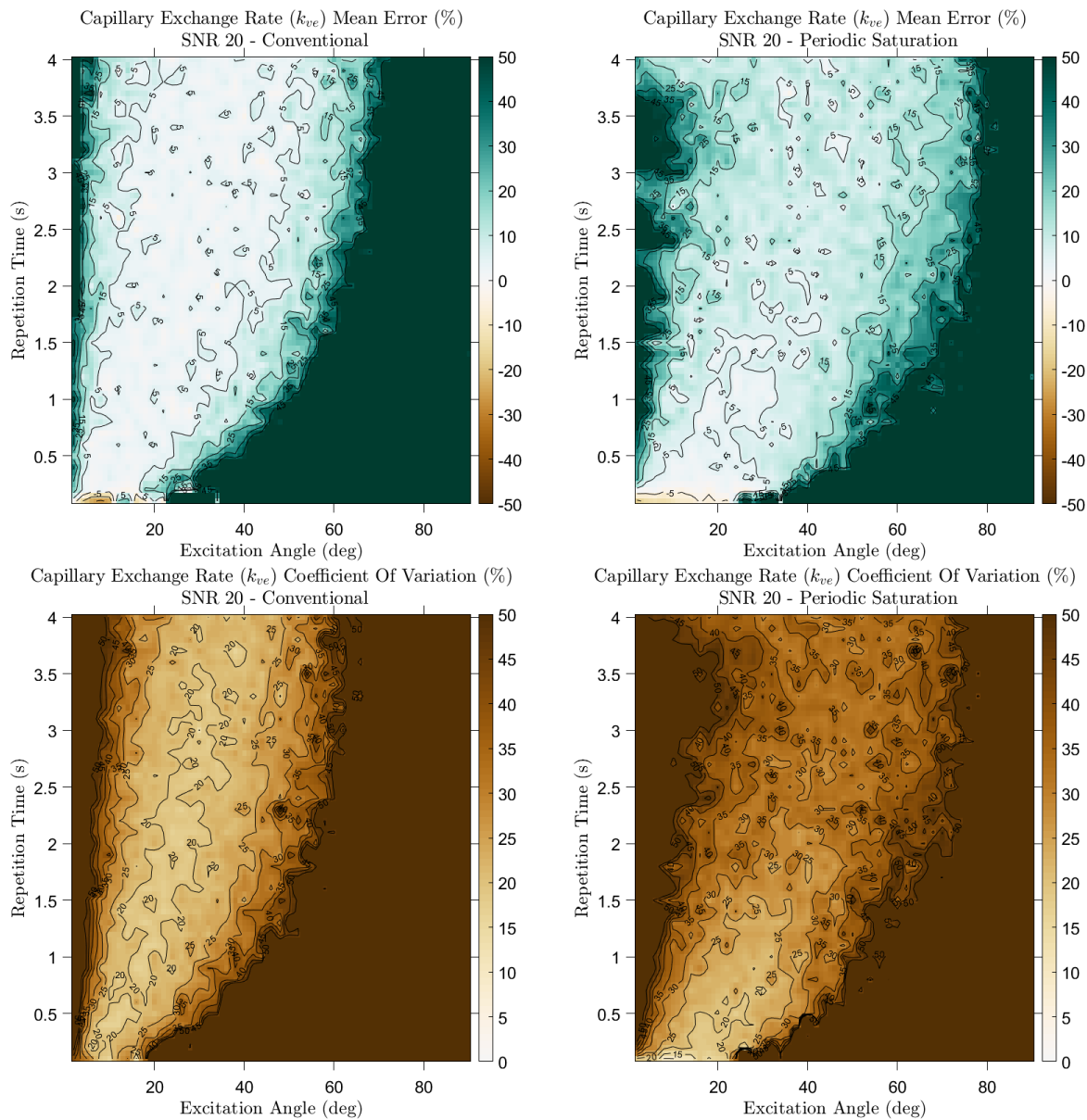
Figure 4.4: Accuracy and reproducibility plots of k_{ve} fits for conventional and periodically saturated acquisitions. Relative to the equivalent conventional metronomic acquisitions, the application of a 90 degree saturation pulse every 10 seconds generally tends to increase both the absolute mean error and the coefficient of variation for estimates of capillary permeability obtained through our pharmacokinetic model of HP perfusion agent signal evolution.
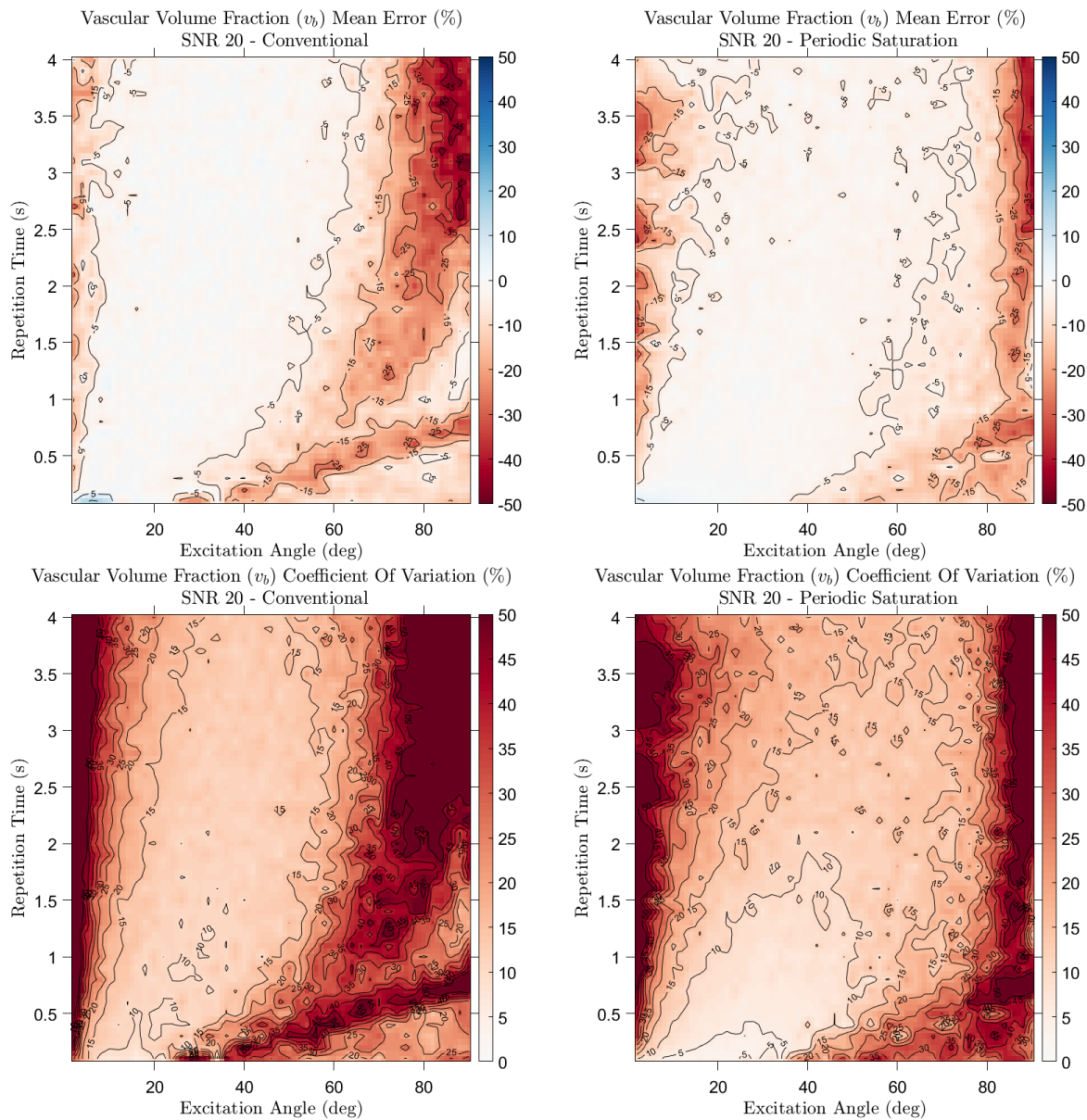
Figure 4.5: Accuracy and reproducibility plots of v_b fits for conventional and periodically saturated acquisitions. Relative to the equivalent conventional metronomic acquisitions, the application of a 90 degree saturation pulse every 10 seconds generally tends to decrease both the absolute mean error and the coefficient of variation for estimates of vascular volume obtained through our pharmacokinetic model of HP perfusion agent signal evolution.
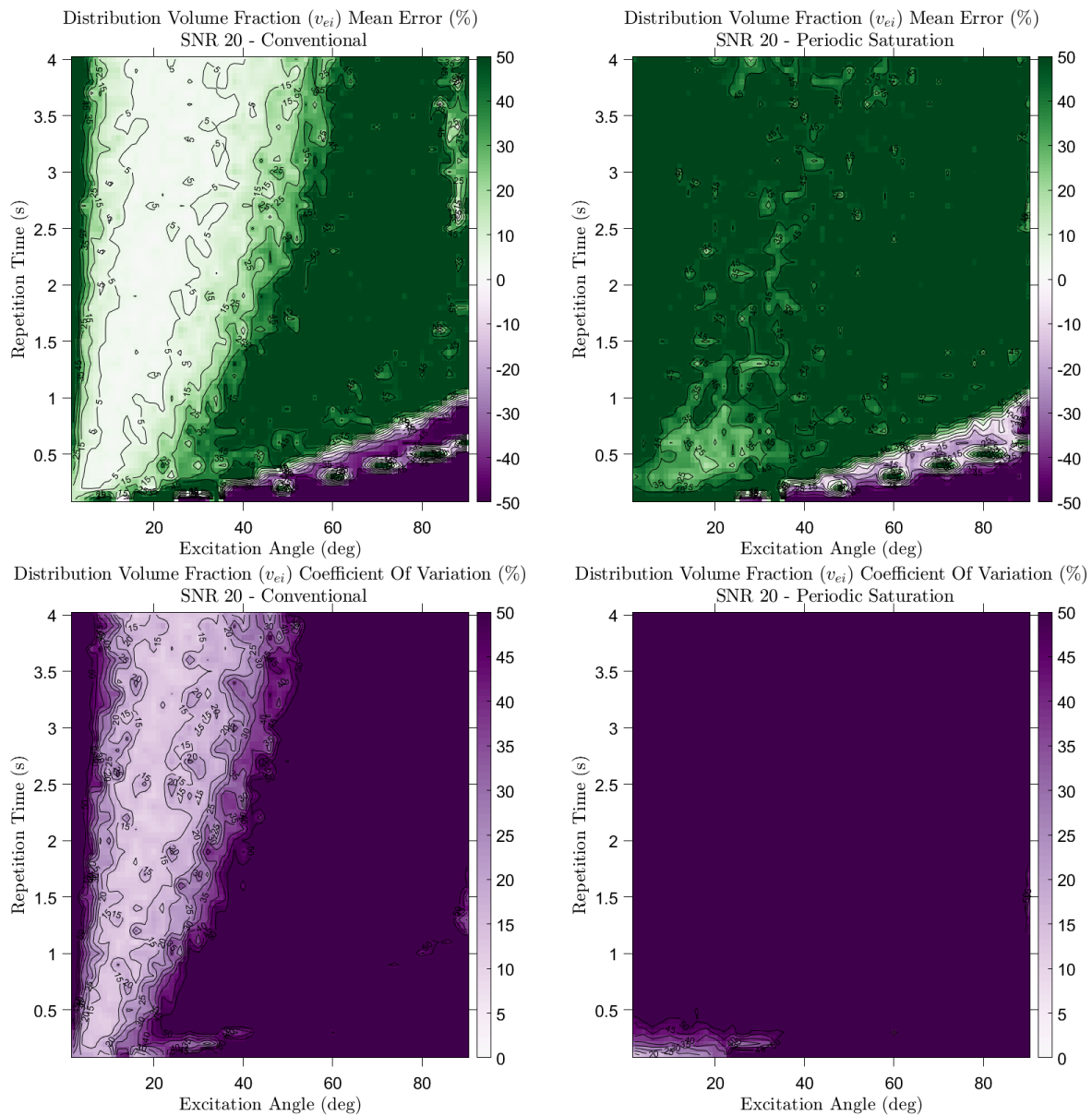
Figure 4.6: Accuracy and reproducibility plots of v_{ei} fits for conventional and periodically saturated acquisitions. Relative to the equivalent conventional metronomic acquisitions, the application of a 90 degree saturation pulse every 10 seconds *greatly* increases both the absolute mean error and the coefficient of variation for estimates of extravascular volume obtained through our pharmacokinetic model of HP perfusion agent signal evolution.

HP imaging can be of much greater benefit. In these cases, the retention of imaging agent outside of the vascular volume is not of interest and is in fact an impediment to kinetic modeling. The exclusive use of 90 degree pulses for dynamic HP imaging was proposed in the context of this type of perfusion modeling early in the development of HP MRI, and was referred to as "bolus differentiation" [135]. Additionally, the use of chemically selective pulses for saturating the biochemical products of metabolic HP agents has been proposed as a method for improving quantitative modeling of these substrates *in vivo* [136, 137].

In any case, extreme care must be taken when saturating HP signals *in vivo*. Imperfections in the calibration of RF power and slice profile effects will result in incomplete saturation that could negatively impact quantitative modeling. Slices should generally be positioned precisely to avoid depleting signal in organs and vessels (not of primary interest) containing a large proportion of the blood, such as the heart, liver, lungs or (for coronal and sagittal slices) the abdominal aorta. Because of these many technical difficulties that impact the application of saturation pulses to dynamic studies of HP agents, we chose not to further investigate this imaging approach *in vivo* for this work.

Perfusion Imaging with Interleaved Motion Suppression

The spatially dependent phase imparted by magnetic gradients can be used to encode not only position, but also motion. Isochromats that move during a gradient pulse accrue phase in proportion to their position, but at a rate that changes over time due to their change in position. These effects are used in several MRI techniques for encoding flow and diffusion. For the purpose of diffusion encoding, bipolar gradients are typically used to rewind positional phase in isochromats that are stationary, providing a signal in which mobile isochromats are selectively suppressed. Such diffusion encoding gradients are characterized by their b-value, which describes the exponential signal loss of isochromats due to their apparent diffusive motion during the bipolar gradient [138]. In this context, the MR signal as described in equation 4.12 can be

rewritten to account for the motion sensitizing gradient.

$$S_{MS}(t+TE) \propto M_{xy}(t+TE) \approx M_z(t)\sin(\theta)e^{-\frac{TE}{T_2^*}}e^{-bD_{app}} \qquad (4.18)$$

The gradient pulses used for encoding diffusion are traditionally applied in the same direction on opposite sides of a refocusing pulse for spin echo measurements, or (somewhat less traditionally) multiple pulses for stimulated echo measurements. These approaches have been used in various preclinical applications for HP imaging and spectroscopy to measure signal compartmentalization in tissue statically [123, 139], to quantify changes in the diffusion of HP urea in the liver due to fibrosis [140], and to separate intra- and extracellular HP signals for *in vitro* NMR [141].

The apparent diffusive motion sensitized by bipolar gradients encompasses effects other than true diffusive (i.e. Brownian) motion *in vivo*. In many tissues the random orientation of the microvasculature causes blood flow through this space to be indistinguishable from rapid diffusive motion [142]. This effect, known as intravoxel incoherent motion (IVIM), is particularly interesting for pharmacokinetic modeling of HP MRI since diffusion gradients can be used to selectively suppress signal from the vascular space. This approach has been used previously in preclinical HP studies to suppress blood signal in the chambers of the heart [143] and in large abdominal vessels [144]. Here, we will extend this approach to use bipolar motion sensitizing gradients in an interleaved fashion for every other repetition of the dynamic HP imaging experiment, as shown in figure 4.7. Compared to the conventional spoiled gradient-echo imaging method, simulation of these effects requires us to account for apparent diffusion rates in the vascular and extravascular compartments separately.

$$S_{MS}(t) \propto M_{xy,b} + M_{xy,e} = \sin(\theta)e^{-\frac{TE}{T_2^*}}\left(M_{z,b}(t)e^{-bD_b} + M_{z,e}(t)e^{-bD_e}\right) \qquad (4.19)$$

In the simulations summarized in figures 4.8-4.10, the apparent diffusion coefficient describing exponential signal loss in the vascular compartment was assumed to be 30 times the corresponding diffusion coefficient in the interstitial space. This factor is based on the apparent diffusion coefficients measured in human abdominal ^{1}H IVIM imaging [145]. A value of 0.75 x 10^{-3} mm^2/s was chosen for this apparent
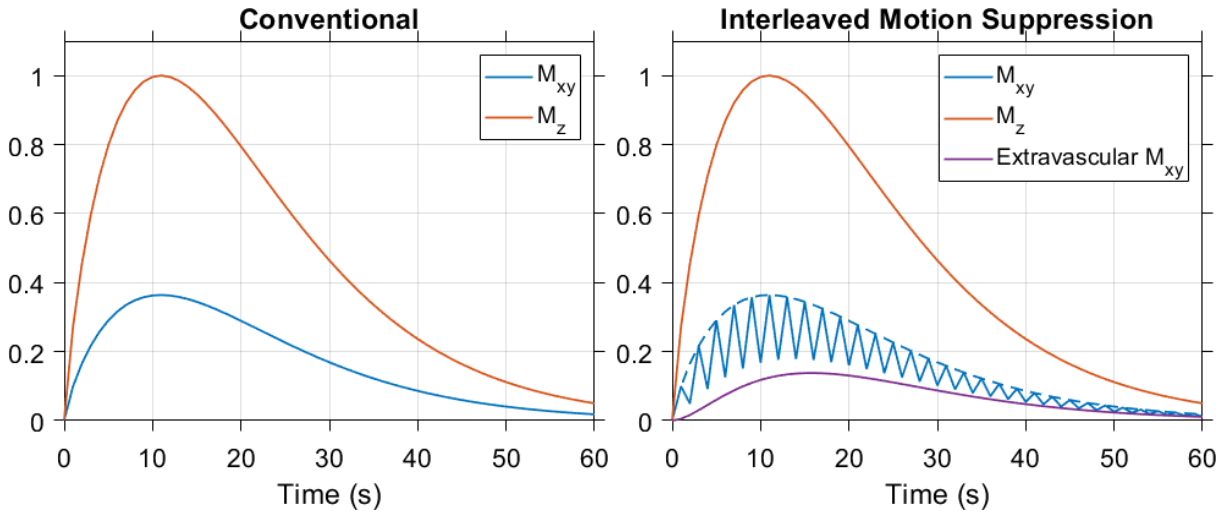
Figure 4.7: Simulated M_z and M_{xy} time curves are shown for HP urea imaging using conventional (left) and interleaved motion suppressed (right) spoiled gradient-echo imaging. The M_{xy} time curve of the conventional imaging method is plotted as a dashed line on the right. The application of diffusion gradients every other time point reduces signal predominantly from vascular compartment.

diffusion coefficient in the extravascular/extracellular space, based on previously reported diffusion measurement of HP urea in the healthy rat liver [140]. A b-value of 30 s/mm^2 and duration of 11 ms was modeled for the motion sensitizing gradient, roughly matching the diffusion weighting and duration of the gradient waveform used for mouse imaging described in the following section.

These numerical simulations suggest that the selective suppression of moving signals provides substantial benefits in the context of our two-compartment model of HP perfusion agent imaging. Unlike RF saturation of the HP system, the use of gradient encoding has no effect on the finite longitudinal magnetization and therefore preserves imaging signal for interrogation at subsequent time points. The improvements in the accuracy and reproducibility of vascular volume measurement (v_b, figure 4.9) across a very wide range of acquisition repetition times and excitation angles are particularly striking. However superior performance in measuring capillary permeability (k_{ve}, figure 4.8) and tissue distribution volume (v_{ei}, figure 4.10) is also evident. The stark benefit for v_b measurement matches an intuitive interpretation of this acquisition strategy. Through the selective suppression of the vascular component of the HP
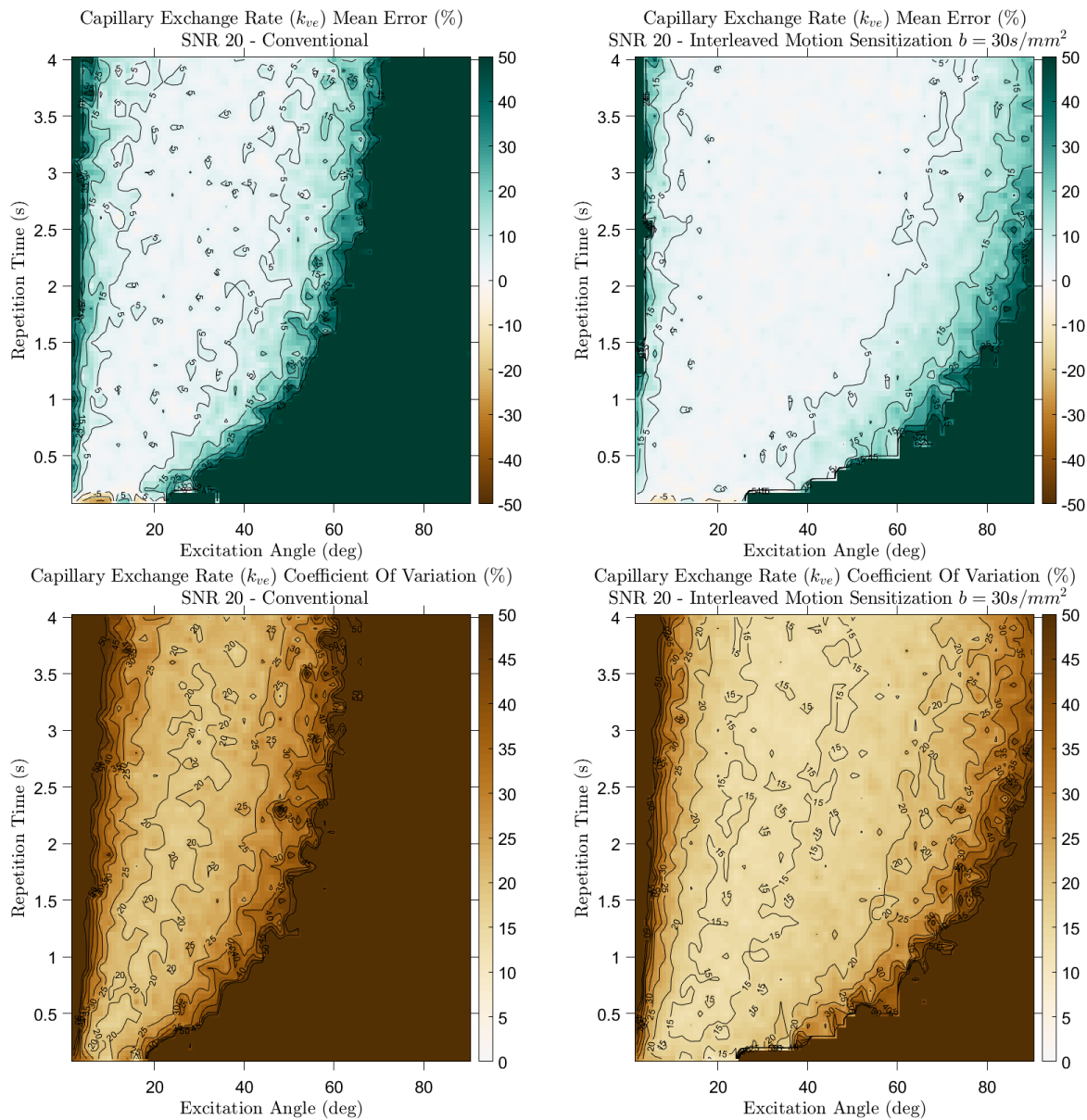
Figure 4.8: Accuracy and reproducibility plots of k_{ve} fits for conventional and interleaved motion suppressed acquisitions. Relative to the equivalent conventional metronomic acquisitions, the application of motion suppression gradients every other repetition generally tends to decrease both the absolute mean error and the coefficient of variation for estimates of capillary permeability obtained through our pharmacokinetic model of HP perfusion agent signal evolution.
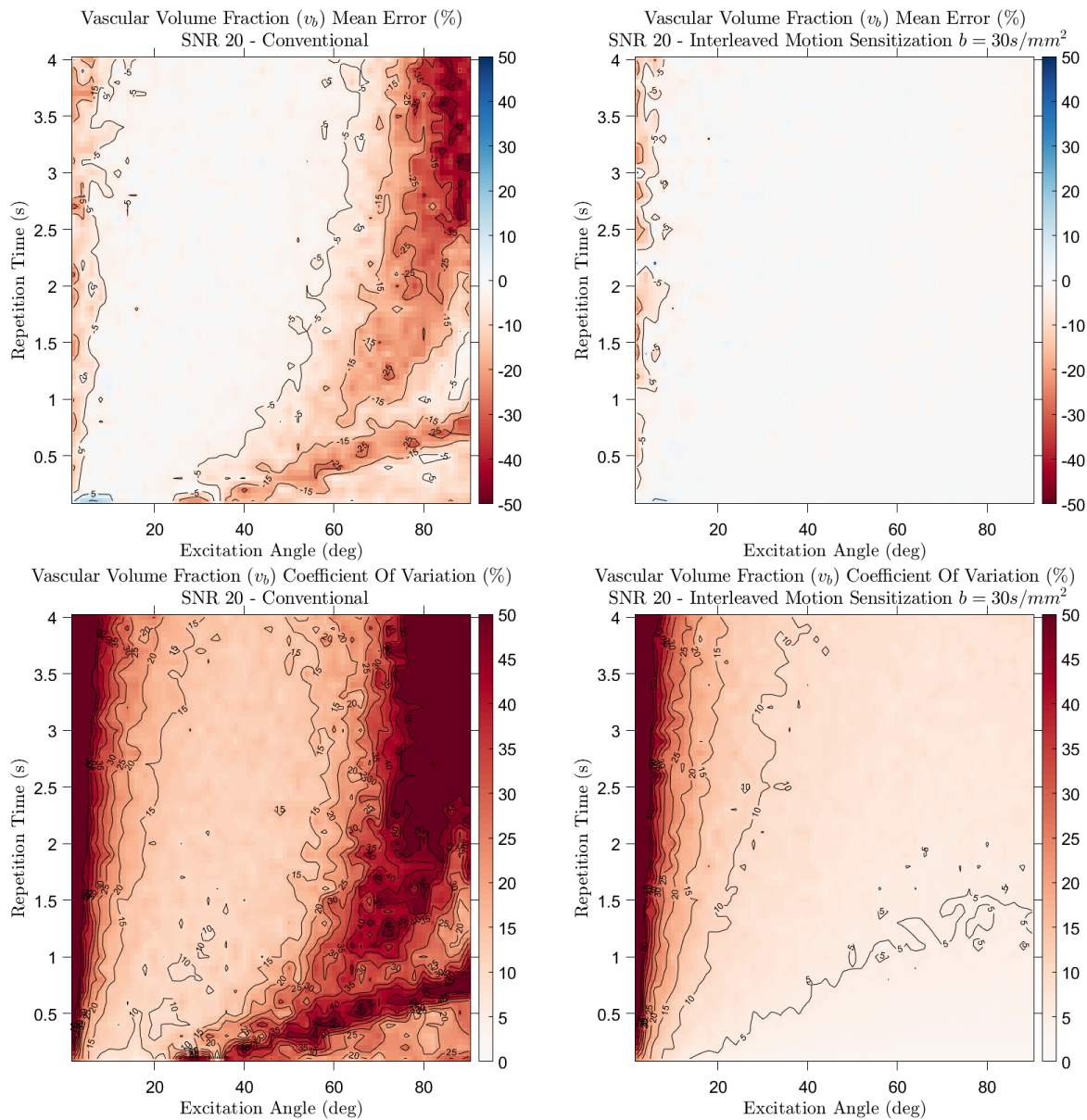
Figure 4.9: Accuracy and reproducibility plots of v_b fits for conventional and interleaved motion suppressed acquisitions. Relative to the equivalent conventional metronomic acquisitions, the application of motion suppression gradients every other repetition generally tends to decrease both the absolute mean error and the coefficient of variation for estimates of vascular volume obtained through our pharmacokinetic model of HP perfusion agent signal evolution.
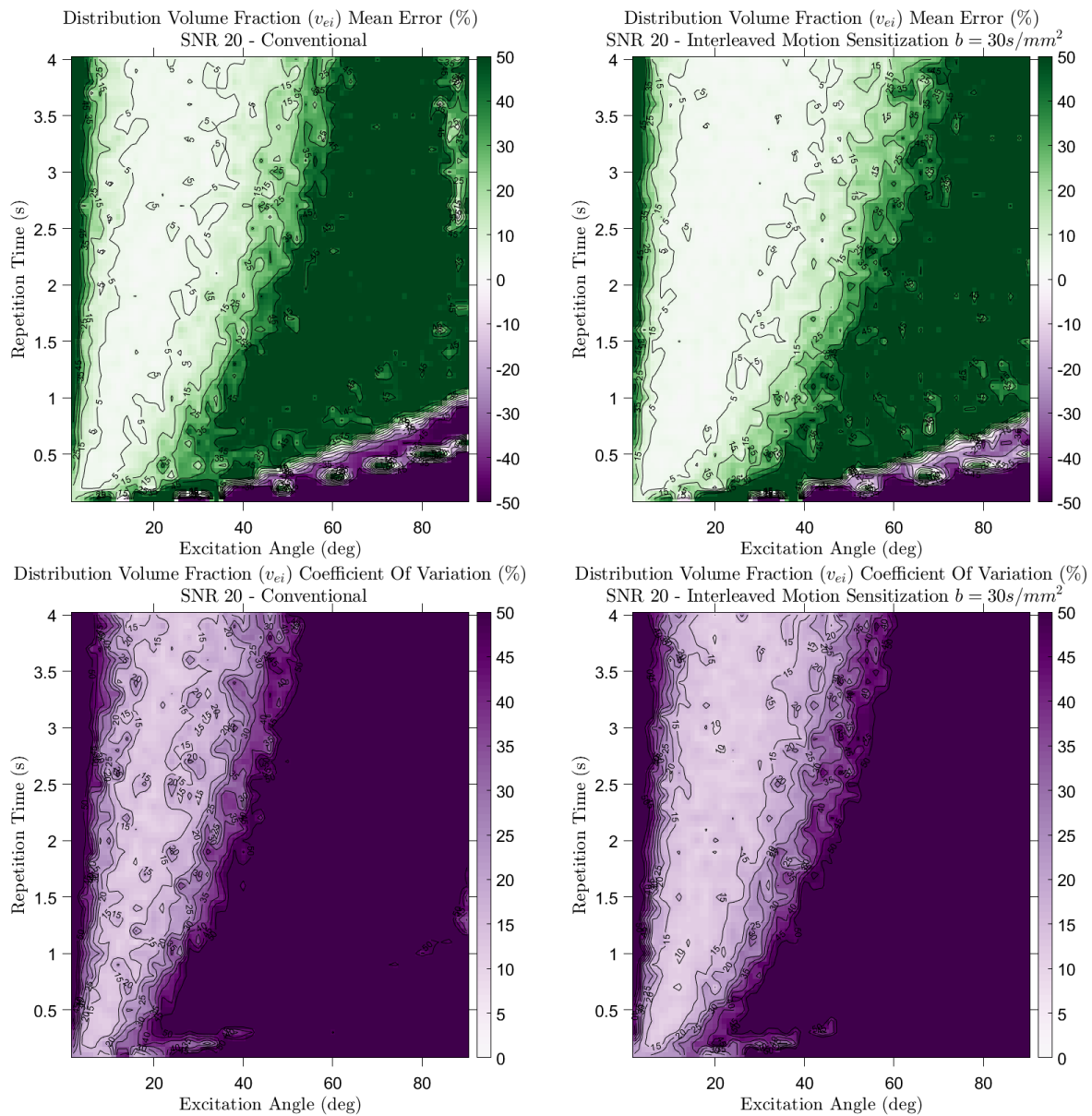
Figure 4.10: Accuracy and reproducibility plots of v_{ei} fits for conventional and interleaved motion suppressed acquisitions. Relative to the equivalent conventional metronomic acquisitions, the application of motion suppression gradients every other repetition generally tends to decrease both the absolute mean error and the coefficient of variation for estimates of extravascular volume obtained through our pharmacokinetic model of HP perfusion agent signal evolution.

signal represented in this volume, we are effectively measuring it more directly by negative contrast.

Just as in the case of the periodic saturation method, the results summarized in figures 4.8-4.10 should be considered in the context of the practical considerations of applying the interleaved motion suppressed imaging method. In general, the comparatively wider ranges of acquisition settings that provide accurate and reproducible measurement of the physiological model parameters could result in much more flexibility in setting up a dynamic HP urea imaging experiment on a given MRI system. However — unlike the conventional and periodic saturation imaging strategies — the simulations of the interleaved motion suppression strategy presented in this section were in many ways customized to the capabilities of our preclinical 7 T MRI system. Specifically, the simulated b-value and encoding time in dynamic gradient-echo imaging (30 s/mm^2 in 11 ms) requires high-power gradients to achieve for ^{13}C imaging, and would not be realizable on clinical MRI systems. One method for attaining sufficiently large b-values for suppression of flowing HP signals on clinical hardware is through the use of double spin-echo imaging [146], however kinetic simulation and modeling of this imaging approach would also require consideration of the effects of refocusing pulses on the HP magnetization.

Lastly, it should be noted that all of the numerical simulation results in this section are derived from the ground-truth physiological parameters outlined in table 4.1. These specific values were chosen as representative based on previous measurements in small animals. However, there is tremendous variation in the actual quantities these physiological parameters represent in tissue, and evaluations of the proposed HP urea imaging strategies across the wide ranges of values possible *in vivo* quickly become very computationally expensive. There may therefore be many circumstances in which the conclusions drawn from figures 4.4-4.6 and 4.8-4.10 fail to reflect the actual utility of *in vivo* HP urea imaging using the proposed strategies.

4.4   *In Vivo* ^{13}C Urea Imaging Experiments

While the simulation results illustrated in figures 4.8-4.10 make a strong claim for the benefit of using motion suppression gradients to improve measurement of HP agent uptake, the use of these gradient waveforms in the fashion described here has not been demonstrated *in vivo*. Therefore, we chose to test the feasibility of this imaging approach in small animal experiments. The proposed interleaved motion suppressed imaging method was applied to small animal HP urea imaging of thyroid tumors and healthy livers.

When implemented in practice, this motion suppression strategy is sensitive to the direction of the diffusion encoding gradient. As illustrated in figure 4.11, applying bipolar gradients in two directions simultaneously results in a rotation of the direction along which motion is suppressed. If isotropic suppression of diffusive motion is desired, the gradients sensitizing to motion in each direction must be offset in time.
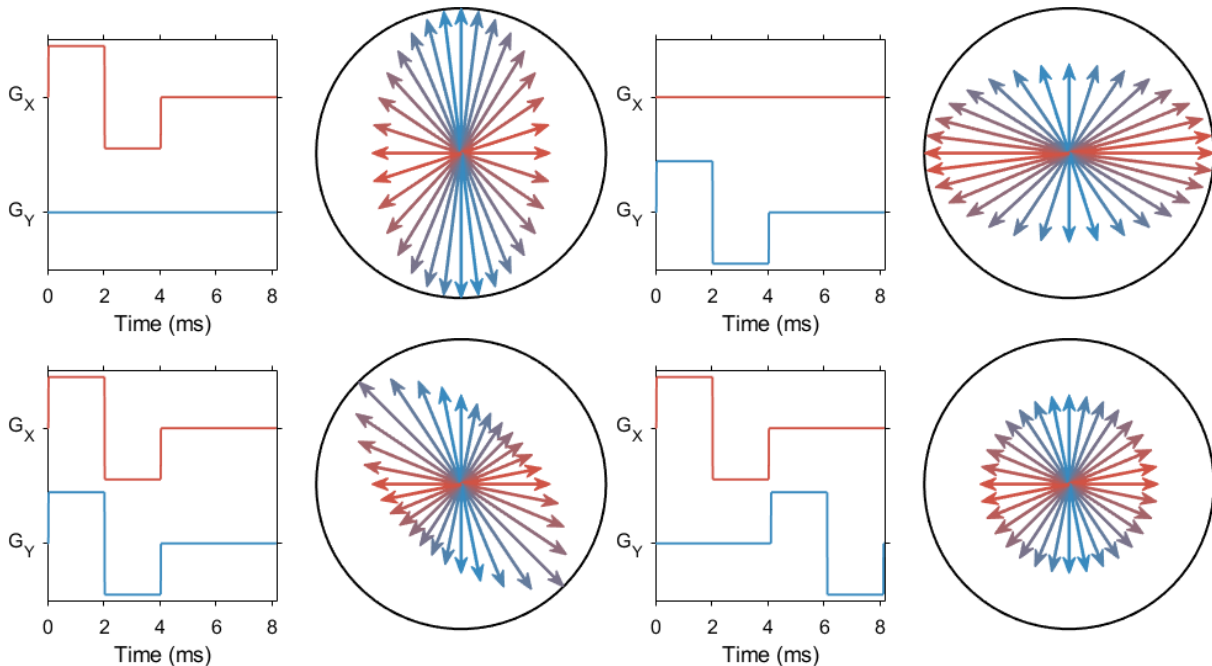
Figure 4.11: Sensitivity of motion suppression to gradient direction

In the context of diffusion imaging, the amplitude of a magnetic gradient over time defines a trajectory in q-space, which describes the spatial distribution of diffusion displacement sensitization [147]. The calculation of q-values in three dimensional

space is identical to the quantification of k-space, the only difference being that the gradient is used to encode diffusive molecular motion rather than spatial frequency.

$$\vec{q}(t) = \gamma \int_0^t \vec{G}(\tau)d\tau = \begin{bmatrix} q_x & q_y & q_z \end{bmatrix} \tag{4.20}$$

In this multi-dimensional context, the b-value describing the weight of diffusion encoding is a tensor quantity.

$$\bar{B}(t) = \int_0^t \vec{q}(\tau)^T \vec{q}(\tau)d\tau = \begin{bmatrix} b_{xx} & b_{xy} & b_{xz} \\ b_{yx} & b_{yy} & b_{yz} \\ b_{zx} & b_{zy} & b_{zz} \end{bmatrix} \tag{4.21}$$

Individual elements of the b-matrix denote the magnitude of motion sensitization in that direction, with the off-diagonal elements describing sensitivity to motion that is correlated in two directions. Note that through this calculation, b-values can be seen to be proportional to γ^2. This is an important consideration in the use of motion sensitizing gradients for ^{13}C MRI. Since the gyromagnetic ratio of ^{13}C is approximately 1/4 of ^{1}H, diffusion gradients designed for ^{1}H imaging will only provide around 1/16 the b-value in ^{13}C imaging.

For nearly isotropic motion sensitization in our small animal studies, we designed preparation gradients consisting of three bipolar pulses applied to each direction. Sinusoidal bipolar gradients were used to reduce the impact of eddy current effects from fast gradient switching. As a compromise between total preparation gradient duration and isotropic encoding, the sinusoidal bipolar gradient pulses are offset in time relative to one another with a 90 degree phase offset (1/4 the duration of each individual sinusoidal pulse). The single b-value reported for each preparation gradient is the unique value in the diagonal elements of the b-tensor (equation 4.21), and therefore do not account for sensitivity to motion correlated in two-directions. These three-dimensional motion sensitization gradients were played out between HP signal excitation and readout for single-shot EPI-encoded spoiled gradient-echo imaging using the pulse sequence described in chapter 5.

Orthotopic Thyroid Tumor

HP urea imaging was performed on a mouse bearing an orthotopic thyroid tumor using the interleaved motion suppression method. The preparation gradient applied at every other repetition is shown in figure 4.12. It has a total duration of 11 ms, an effective isotropic b-value of 28 s/mm^2 and a first gradient moment in each direction of 0.37 s/mm. A 4 x 4 cm^2 FOV flyback EPI trajectory was used to spatially encode a 16 x 16 image matrix with an echo time of 18.54 ms. A 20 degree pulse was applied with a 1 cm axial slice width and a 1 s repetition time, and an 11 ms delay between excitation and readout occurred in repetitions without motion suppression to provide consistent T_2^* decay in the dynamically acquired images. 200 µL of 100 mM HP ^{13}C urea was produced using a HyperSense DNP system and injected via tail vein manually, with the acquisition starting at the moment of dissolution and continuing through the observable lifetime of the HP signal *in vivo*. Anesthesia was induced and maintained through 2-4% isoflurane delivered via nose cone.

Separate time-averaged images of HP urea in this mouse are shown for the time points acquired with and without motion suppression in figure 4.13, along with a normalized time intensity curve for the ROI outlining the thyroid tumor. As shown in the image acquired without motion suppression, intense vascular signals originating from major blood vessels in the neck obscured the ability to assess the signal from the neighboring tumor. The application of diffusion preparation gradients suppressed these strong vascular signals, resulting in more uniform HP urea signal within the tumor and decreased signal intensities for the tumor ROI. At certain time points of this dynamic imaging experiment, the motion suppressed signal in the tumor ROI dropped below the baseline level present prior to the HP urea injection. While the precise reason for this non-physical level of signal reduction cannot be determined from these data, we suspect that it was due to bulk respiratory motion occurring during the application of preparation and readout gradients. Since the preparation gradients are designed to sensitize imaging signal to microscopic motion, such macroscopic respiratory motion would have a large effect on these HP images. Additionally, due to the

Figure 4.12: The diffusion preparation gradient waveform that was used for inter-leaved motion suppressed imaging of HP urea in a mouse model of orthotopic thyroid cancer. The gradient waveform is 11 ms in duration with a maximum amplitude of 640 mT/m. At the end of this preparation period, a first gradient moment of 0.37 s/mm and b-value of 28 s/mm^2 is imparted for ^{13}C in each principal direction.

significant partial volume averaging within the tumor ROI, the signal reduction effect observed in this animal corresponds to a suppression of more than just the microvascular signal within capillaries that is modeled in equation 4.18. Because of both these artifactual signal reductions and partial volume effects, we chose not to fit a kinetic model to these data. However, these observations informed our imaging methods when applying interleaved motion suppression to HP urea imaging of the rat liver.
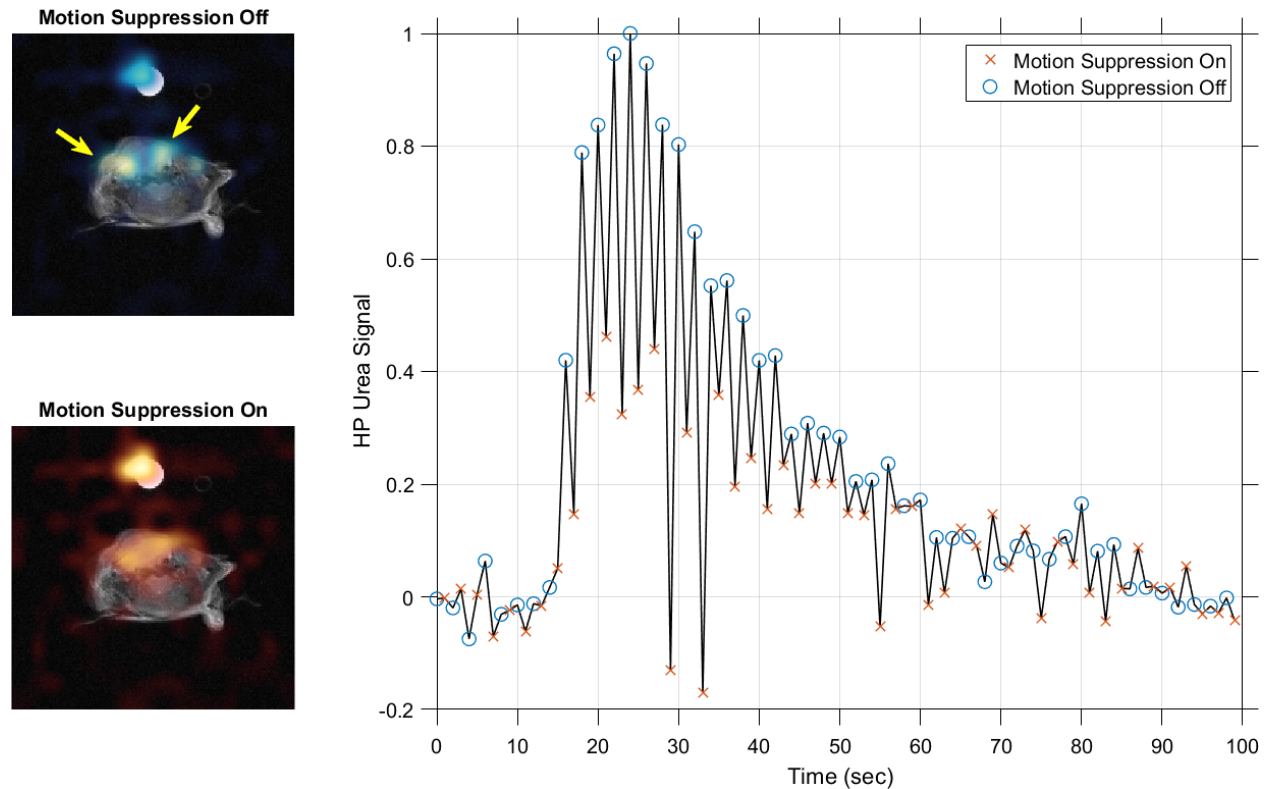
Figure 4.13: HP ^{13}C urea imaging of orthotopic thyroid tumor using interleaved motion suppression gradients. In the time-averaged images shown here, the application of motion suppression gradients eliminates the strong HP signals arising from large blood vessels in the neck (yellow arrows), resulting in a more uniform HP signal in the tumor. When the intensity of HP signal from a ROI containing the tumor (including partial volume contribution from blood vessels) is plotted over time, the effect of vascular signal dephasing is evident.

Normal Rat Liver

Dynamic HP urea imaging with and without interleaved motion suppression was also performed of the livers of healthy Sprague-Dawley rats. Three rats were imaged with the conventional spoiled gradient-echo method (without interleaved motion encoding) and the minimum achievable TE of 11.9 ms was used for these scans. One of these animals was rescanned at a later date using the interleaved motion encoding method with a TE of 19.1 ms and using a 7.2 ms preparation gradient waveform with an effective isotropic b-value of 6.8 s/mm^2 and a first gradient moment in each direction of 0.15 s/mm. The diffusion preparation gradient waveform used in imaging this rat is shown in figure 4.14. Due to the high sensitivity to physiological motion observed when us-

ing motion sensitization in mice, both conventional and interleaved motion suppressed scans were performed with respiratory gating to ensure gradient encoding occurred when the liver was stationary. The effective repetition time therefore varied within and between dynamic HP scans due to variations in the rats' respiratory rates, however in most cases a repetition time of 2 to 3 s was maintained. An excitation angle of 30 degrees was used with a 1 cm axial slice width, followed by a symmetric EPI readout encoding a 6 x 6 cm^2 FOV and 24 x 24 image matrix. For the interleaved motion suppression scan, a 7.2 ms delay provided consistent T_2^* image weighting when the preparation gradient was absent. 100 mM HP [^{13}C,^{15}N$_2$]urea (Sigma Aldrich, St. Louis, MO) was produced using a HyperSense polarizer and 2.5 mL of this HP solution was injected over 20 s via a tail vein catheter using an infusion pump (PHD 2000, Harvard Apparatus, Holliston, MA).

Dynamic images of HP urea in the rat liver acquired with interleaved motion suppression are shown in figure 4.15. As in the mouse imaging shown in the previous subsection, a marked reduction in signal from the region of large blood vessels is observed for time points at which diffusion preparation is applied. In contrast to imaging of the mouse thyroid, this intense vascular signal is located in a region of the image distant from the tissue of interest which allows the effect of motion suppression gradients on the microvascular signal in the tissue voxel to be measured.

For each dynamic HP scan in rats, a VIF estimate was obtained by fitting equation 4.2 to the time intensity curve of a voxel displaying intense HP urea signal from a voxel in the region of the large hepatic blood vessels (e.g. the voxel highlighted in green in figure 4.15). For the interleaved motion suppressed scan, this VIF fit only considered time points without motion sensitization. A separate artifact-free voxel representing normal parenchyma in the anterior liver near the ^{13}C receive surface coil was selected for fitting using the two-compartment perfusion model (e.g. the voxel highlighted in purple in figure 4.15). The estimated VIF was scaled relative to the tissue time intensity curve based on its position in the modeled B_1 profile of the ^{13}C receive surface coil, which is shown in figure 4.16. Fitting of the two compartment perfusion model to the tissue time intensity curve acquired with the conventional imaging method was
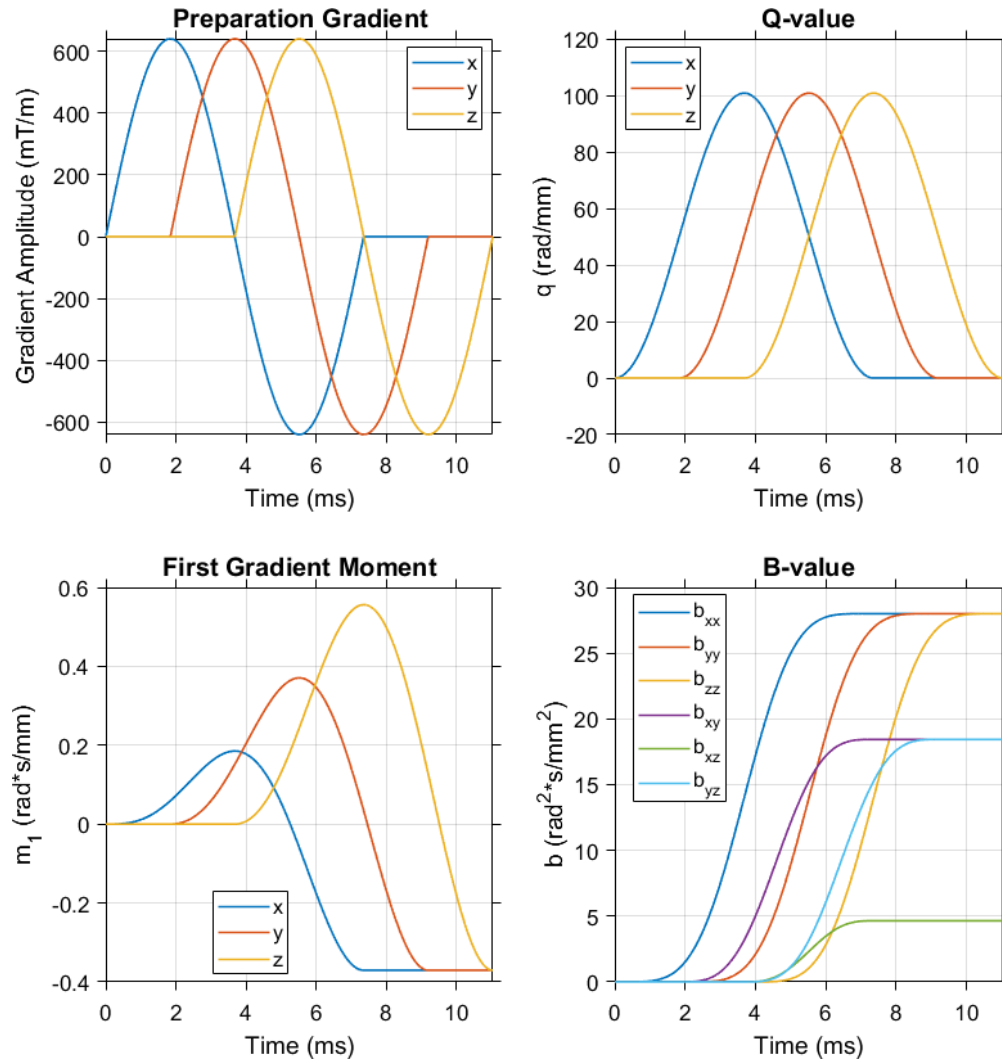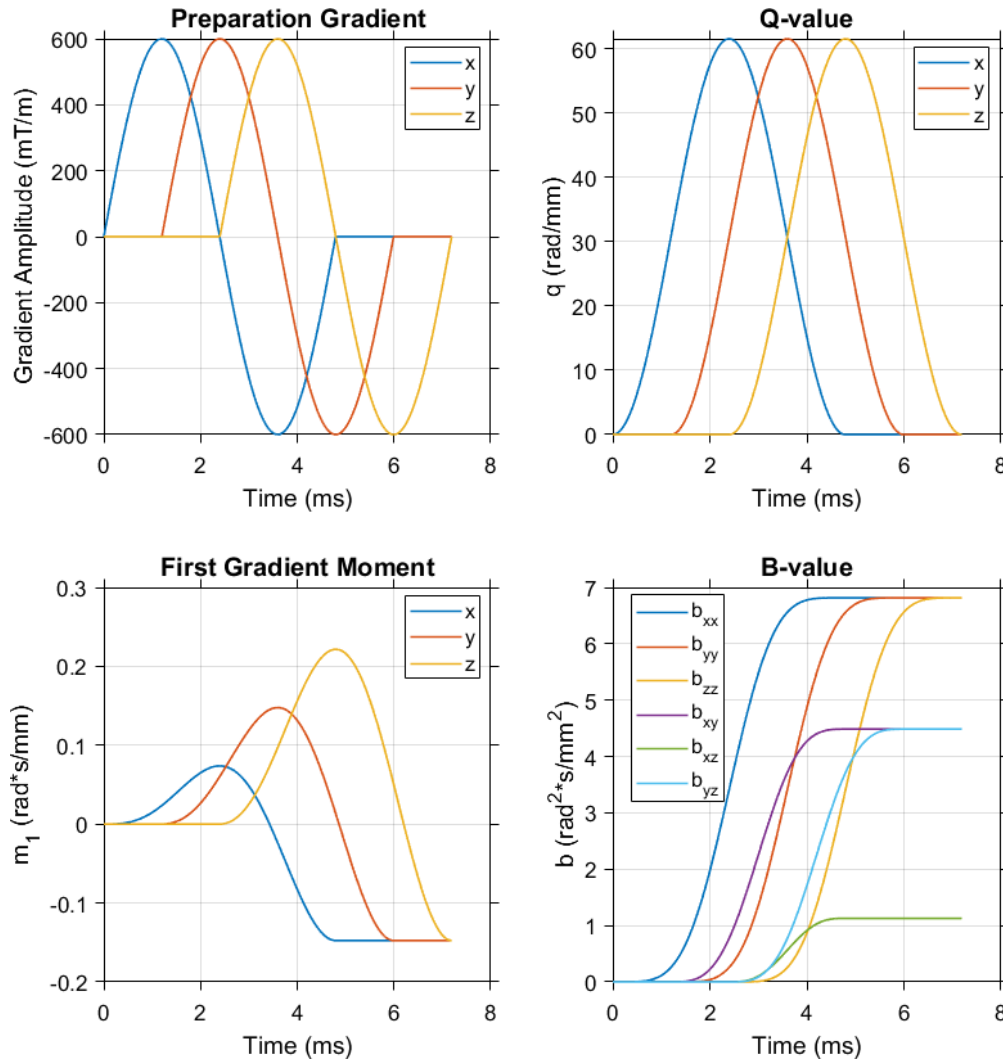
Figure 4.14: The diffusion preparation gradient waveform that was used for interleaved motion suppressed imaging of HP urea in the rat liver. The gradient waveform is 7.2 ms in duration with a maximum amplitude of 600 mT/m. At the end of this preparation period, a first gradient moment of 0.15 s/mm and b-value of 6.8 s/mm^2 is imparted for ^{13}C in each principal direction.

completed using equations 4.10-4.12 with k_{ve} and v_b as the two free parameters, and with the simplifying assumption of $v_e = 1 - v_b$ (i.e. $v_{ei} = 1$). Fitting of the time intensity curve acquired with interleaved motion suppression assumed that the preparation gradients fully eliminated vascular signal at the time points when they were applied.

When fitting the two-compartment model to tissue voxel time intensity curves selected from the three HP urea datasets acquired with conventional spoiled gradient-echo imaging, k_{ve} values of 0.016, 0.072 and 0.013 s^{-1}, and v_b values of 18.8, 37.3 and
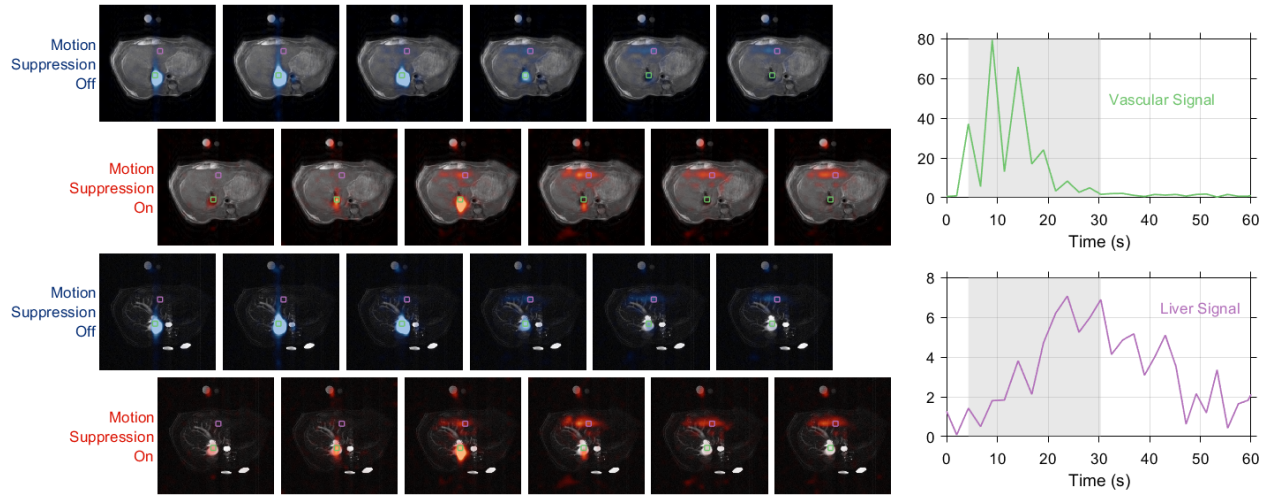
Figure 4.15: HP ^{13}C urea imaging of the healthy rat liver using interleaved motion suppression gradients. HP images are overlaid on both T_2-weighted anatomical (top) and time of flight angiographic images (below). Dynamic images acquired with motion suppression are shown in orange, while those without are blue. Note that ^{13}C image overlays are not corrected for the sensitivity profile of the receive surface coil. The effect of the preparation gradients is most pronounced for the voxels with intense vascular signals (green), however some suppression of the vascular signal is evident in the liver parenchyma (purple). The shaded region of the time intensity curves shown on the right indicate the twelve imaging time points depicted in the ^{13}C image overlays on the left.
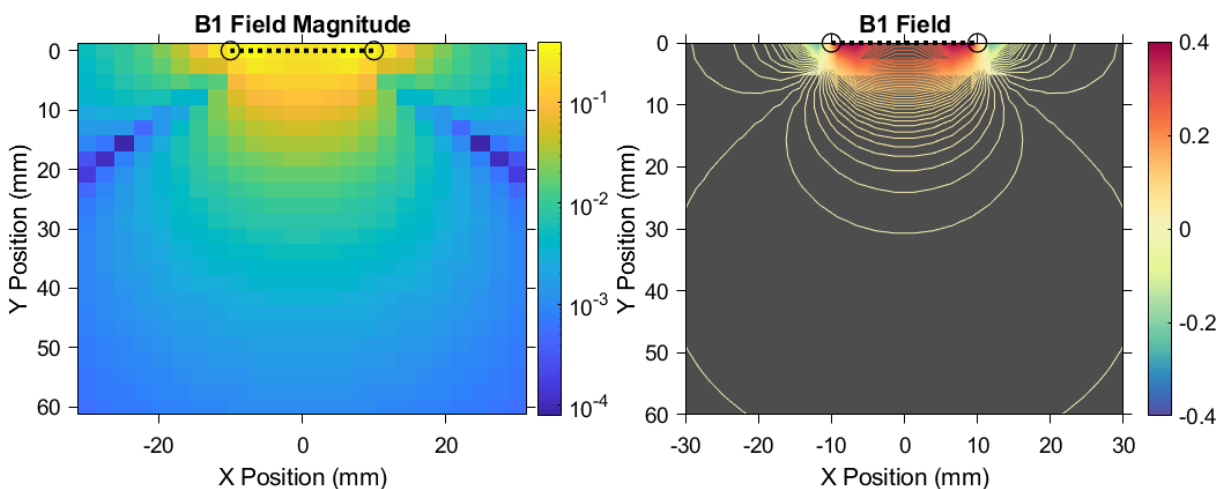
Figure 4.16: Relative B_1 profile of a 2 cm circular coil in a medium of uniform permittivity. Values shown in this figure were used to estimate the positional dependence of VIF scaling relative to the HP urea signal measured in liver tissue for the purpose of fitting a pharmacokinetic model to the observed HP time intensity curves.
Adapted from a script obtained from the MATLAB file exchange [148].

35.4% were obtained. Lower k_{ve} and v_b values of 0.012 s^{-1} and 18.3%, respectively, were measured for the hepatic tissue voxel interrogated with interleaved motion suppressed imaging. Without a greater sample size no firm conclusions can be drawn from these data, however it is instructive to consider these values in the context of previously reported measurements of these physiological quantities. Measurements of the permeability of hepatic capillaries to an agent with the biochemical properties of urea are not readily available, however mean K^{trans} values of 0.003 min^{-1} (5 $\times$ 10^{-5} s^{-1}) have been measured in the normal liver parenchyma in DCE-MRI of rabbits using extended Tofts modeling of clinical gadolinium chelate contrast agent uptake [149]. This capillary transfer rate of gadolinium agents is three orders of magnitude smaller than the values derived from our modeling of HP urea images, which could result from the smaller molecular size of urea and its much greater mobility in liver tissue. The hepatic blood volume fraction of normal liver tissue has been measured in many different ways, with a very wide range of values reported in the literature. The suggested reference range of the normal hepatic blood volume fraction in humans for radionuclide dosimetry is 18 to 30% [150], and imaging measurement of this quantity in humans through PET detection of inhaled C^{15}O has demonstrated regional values of 18 to 22% in normal livers (assuming a tissue density of 1 g/mL) [151]. Local tissue blood volume fractions of normal liver ranging from 28 to 31% in rabbits [152] and 11 to 18% in rats [153] have been reported using MRI measurements of macromolecular gadolinium agents. In this context, the lower v_b (18.3%) measured from our HP urea images acquired with interleaved diffusion preparation is in better agreement with published values than the blood volumes estimated from conventional spoiled gradient-echo imaging.

If microvascular signal is efficiently suppressed at the interleaved time points of the animal scanned with diffusion preparation, a lower capillary exchange rate and hepatic blood volume could generally be expected from this measurement when compared to conventional spoiled gradient-echo imaging. The velocity of blood varies greatly throughout the vascular tree, and this variation is particularly significant in the liver. A large portion ($\approx$25%) of the cardiac output is delivered to the liver through both ar-

terial and venous sources, and the hepatic capillaries have a wider diameter and are more permeable than capillaries in most other tissues [71]. Two-compartment modeling of HP agent delivery to the hepatic interstitium is therefore a very simplified representation. Signal in slow-moving capillary blood and in the extravascular space may be indistinguishable in modeling of conventional imaging data, which could be interpreted as more rapid transfer of HP agent into the extravascular compartment. This overestimation of k_{ve} for a given VIF and tissue time intensity curve could in turn result in underestimation of v_e (i.e. overestimation of v_b, particularly when assuming $v_{ei} = 1$) to scale the modeled extravascular signal in a manner that matches the observed data. In modeling of images acquired with interleaved suppression of vascular signals, the improved discrimination of true extravascular signal would be expected to reduce this overestimation of k_{ve} and v_b, however more *in vivo* data will be necessary to confirm this interpretation of our preliminary results. Note that in the numerical simulations outlined in section 4.3, these effects would not be observed since the time intensity curves were generated using the same kinetic model that was used for data fitting.

Further extension of dynamic HP imaging with motion suppression to kinetic modeling of *in vivo* data will require further research. Since the diffusion gradients impart negative contrast, the utility of this method depends strongly on the HP image SNR attainable without any suppression of moving signals, so a more robust evaluation of the effect of noise on analysis of these imaging data is called for. Unlike the somewhat simple accounting of flow effects in our simulations, the rates and directions of blood flow in tissue cannot be fully described as a uniform and isotropic diffusive motion that is accounted for via a single exponential signal weighting factor. However, as in any model-based analysis of *in vivo* data, these motion suppression effects only need to be represented with sufficient complexity to provide robust measurements that are sensitive to the physiological processes of interest. More experimentation will be necessary to define the appropriate levels of diffusion weighting when applying this method to specific *in vivo* applications. Overall, our results demonstrate the great potential of this technique to provide added insight into the physiological context of HP signals.

4.5 Conclusion

In this chapter, we have reviewed existing methods and introduced new strategies for quantitative analysis of HP MRI data with a specific focus on pharmacokinetic modeling of HP urea. A two-compartment kinetic model of HP urea signal evolution in tissue was derived from first principles and applied in numerical simulation of dynamic spoiled gradient-echo imaging. These simulations evaluated the relative performance of HP urea imaging using a conventional imaging method and two alternative dynamic imaging strategies that could provide additional insight into the physical compartmentalization of HP signals in tissue. Based on the results of these numerical simulations, the feasibility of one of these HP imaging strategies — which uses diffusion gradient encoding to preferentially suppress vascular signals — was evaluated *in vivo*.

These small animal experiments demonstrate the viability of our proposed method for interleaved motion encoding of dynamically sampled HP data. In both the mouse imaging illustrated in figure 4.13 and the rat liver imaging shown in figure 4.15, the application of our interleaved motion suppression method to HP urea imaging illustrates a marked reduction of strong vascular signals while preserving detectable signal from tissue. Notably, some signal suppression is observed even for the relatively slow rate of blood flow in the rat liver parenchyma when using preparation gradients that impart a much lower b-value than that used in mouse imaging. While data from only a single animal was analyzed through kinetic modeling, it is notable that the values derived from this HP imaging dataset provided a hepatic blood volume fraction that is in better agreement with published values than the blood volumes estimated from conventional spoiled gradient-echo imaging.

When extending this imaging approach to human and large animal imaging, similar microvascular flow suppression effects can be expected for similar b-values. Although blood flow occurs at slower velocities in larger animals, ^{1}H IVIM experiments have demonstrated that this is typically compensated by a proportional increase in the characteristic length of blood vessels resulting in microvascular flow suppression effects that are consistent across animals of varying size [154]. However, using even

the relatively low b-value employed here for rat liver imaging will be very difficult for dynamic gradient-echo ^{13}C imaging on clinical systems due to the limited gradient capabilities. As discussed at the end of section 4.3, the use of a double spin-echo imaging method could provide the additional encoding time necessary to impart b-values large enough to achieve the desired vascular dephasing effects on clinical MRI hardware. However, kinetic modeling of these data could be more complicated due to the inversion of HP magnetization by the refocusing pulses. In order to optimally exploit the vascular dephasing effect, future implementations of this HP imaging technique — on both preclinical and clinical MRI systems — could utilize numerically optimized diffusion gradient waveforms [155] and physiologically gate data acquisition so that images are acquired during systole, when blood velocities are at their maximum.

Overall, any quantitative analysis of HP MRI data must account for the evolution of signals in tissue due to substrate delivery, relaxation and utilization by the imaging sequence itself. Through numerical simulation, these effects can be evaluated to devise acquisition methods for optimal measurement of the specific physiological process of interest in a given HP imaging study.

Chapter 5

Hyperpolarized Chemical Shift Imaging

Imaging methods for hyperpolarized (HP) ^{13}C agents often must sample the evolution of multiple chemical shifts within a very brief timeframe, which is challenging using conventional imaging methods. Given the variety of HP agents available, flexibility in the choice of spatial and spectral encoding strategy is desirable.

Each HP agent produces a distinct set of chemical signals in tissue, requiring specialized MR methods to spectrally encode the corresponding chemical shifts that distinguish the biochemical fates of the HP ^{13}C labels. Imaging of these signals complicates the MR methods needed in HP experiments, as the sequence must encode 3 spatial dimensions in addition to chemical shift. Further technical complexity is introduced by the dynamic evolution of HP signals over time. As discussed in chapter 4, this temporal evolution is vital to quantitative modeling of HP substrate delivery and metabolism *in vivo*. Flexibility in the methods of spatial and spectral encoding is therefore critical when imaging HP agents, particularly for studies using novel HP preparations.

Various techniques for dynamic and single time point spectroscopic imaging of HP ^{13}C substrates have been developed. These include, among others, traditional phase-encoded CSI [68], echo-planar spectroscopic imaging (EPSI) [39], balanced steady-state imaging [156, 157], IDEAL [21, 22] and spectral-spatial excitations coupled with spiral [136], EPI [158] or EPSI readouts [159]. The IDEAL technique is appealing for HP MRSI since it constrains chemical shift encoding in a way that is optimized for the

specific set of chemical shifts that are known to be present in a given HP experiment [21]. However, there are limitations to the IDEAL method when the range of chemical shifts occur over a very wide range of frequencies. In these cases, limited slice gradient amplitude and RF bandwidth can result in large slice offsets for different chemical shifts. Additionally, the large excitation bandwidths necessary to cover a wide spectral range can require short RF pulses that exceed B_1 limitations. Alternatively, spectral-spatial RF pulses can accomplish the task of spectral encoding during excitation if the pulses are appropriately designed to excite only a single metabolite at a time [20]. This imaging strategy decouples encoding of k-space and chemical shift, greatly simplifying the HP imaging experiment and allowing excitation angle schemes that are tailored to the dynamic evolution of individual HP metabolites *in vivo* [160, 161]. However, design of these spectral-spatial pulses requires consideration of the specific gradient and RF capabilities of the MRI hardware on which they are to be implemented [159, 162]. Additionally, design of spectral-spatial pulses for selective excitation of individual metabolites within a wide range of chemical shifts is particularly difficult due to spectral aliasing and slice position shifts [90].

While multiple studies have quantitatively compared the performance of various HP imaging methods, published reports have provided such comparisons primarily for different spectroscopic imaging readouts on 3 T clinical MRI systems [106, 163]. Only one study has included a limited comparison of IDEAL spectroscopic imaging readouts to chemically selective excitations for HP pyruvate imaging in rodents [136]. In this report, differences in effective HP magnetization usage, sample polarization levels and rates of vascular delivery effects prevent these data from serving as a robust quantitative comparison of IDEAL and spectral-spatial imaging. On the GE clinical MRI platform that is most widely used for HP imaging, pulse sequences that can realize various encoding methods for spectroscopic ^{13}C imaging are provided by the vendor for systems equipped with multinuclear imaging capablities. In contrast, HP imaging on preclinical MRI systems typically requires the composition of custom pulse sequences by the end user, which is time consuming and introduces the possibility of errors due to the significant complexity inherent in dynamic chemical shift imaging

of HP substrates.

In this chapter, we will review and compare imaging methods for a typical HP [1-^{13}C]pyruvate experiment with chemical shift encoding through the frequency response either of the RF excitation pulse or of a multi-echo acquisition strategy (IDEAL). The pulse sequence that we have written to enable both of these forms of chemical shift imaging on our preclinical Bruker 7 T MRI system will be described, as well as quantitative numerical simulations and phantom experiments comparing the SNR performance of HP pyruvate and lactate imaging on this system with single band spectral-spatial excitation and IDEAL encoding. Lastly, we demonstrate the applicability of both of these imaging methods through dynamic HP imaging of pyruvate and lactate in a LDH phantom and in the murine kidney.

5.1   Imaging Instrumentation and Chemical Shifts

All imaging experiments were performed on a 7 T small animal MRI system (Biospec 70/30 USR, Bruker Biospin MRI, Billerica, MA) running ParaVision 6.0.1 and equipped with a 72 mm inner diameter ^{1}H/^{13}C volume resonator (Bruker Biospin MRI) and BGA-12SHP gradients capable of a maximum gradient of 660 mT/m and a maximum slew rate of 4570 T/m/s. Unless otherwise noted, a 20 mm diameter miniflex coil (Rapid MRI International, Columbus, OH) was used for ^{13}C signal reception with RF excitation from the volume resonator.

As described in section 2.4, SNR values in MR images require special consideration, particularly for low SNR magnitude images. In both numerical simulations and real imaging experiments, SNR values were calculated from magnitude image data and the standard deviation of an inverse Fourier transformed magnitude noise image, with correction for the Rayleigh distribution of magnitude noise (equation 2.17). In actual imaging experiments this noise image was obtained by acquiring a scan equivalent to the experimental scan but with negligible RF power [49]. In the special case of IDEAL imaging, this raw acquired noise was first processed through IDEAL decomposition in the same manner as the experimental imaging data. For display, ^{13}C images are

bilinearly interpolated to a resolution similar to the matching ^{1}H image data, typically with resampling factors of 8-16.

The numerical simulation and phantom experiments described in this chapter quantify the performance of different chemical shift encoding methods for a typical HP [1-^{13}C]pyruvate imaging experiment at 7 T, in which the chemical shifts listed in table 5.1 are present. Note that in our case, ^{13}C urea is present in the form of a phantom placed within the imaging volume for the purpose of calibrating the ^{13}C frequency and RF transmit power, however it could also occur as HP urea in the case of a multi-agent dissolution [164, 165].

Chemical Species	Pyruvate	Lactate	Pyruvate Hydrate	Urea	Alanine	Bicarbonate
Chemical Shift (ppm)	171	183.2	179.5	164	177	161
Frequency Offset at 7 T (Hz)	0	+921	+642	-566	+453	-755

Table 5.1: Chemical shifts present in a typical [1-^{13}C]pyruvate imaging experiment at 7 T.

5.2 Multi-Echo Chemical Shift Encoding (IDEAL)

For gradient echo imaging, the MR signal with a volume containing K chemical shifts can be modeled over time as the sum of K complex damped exponentials.

$$x(t) = \left(\sum_{k=1}^{K} \rho_k e^{\left(i2\pi\Delta f_k - R_2^* \right)t} \right) e^{i2\pi\psi(\vec{r})t} \tag{5.1}$$

Here, ρ_k is the relative complex amplitude of the signal arising from an individual chemical species, Δf_k is its chemical shift frequency offset (expressed in cyclic frequency, e.g. units of Hz), and R_2^* is the effective rate of spin-spin relaxation ($R_2^* = \frac{1}{T_2^*}$). The additional spatially-dependent phase shift $\psi(\vec{r})$ accounts for relative $\vec{B}_0$ field shift present in the imaging voxel (e.g. due to shimming or variations in material susceptibility). Assuming that these field inhomogeneities can be demodulated from the

measured imaging signals (e.g. by applying fieldmap corrections), the complex signal values for a sequence that captures N gradient echoes for K species can be written in matrix form as:

$$\vec{x} = \bar{A}\vec{\rho} = \begin{bmatrix} e^{\left(i2\pi\Delta f_1 - R_2^*\right)t_1} & \cdots & e^{\left(i2\pi\Delta f_K - R_2^*\right)t_1} \\ \vdots & \ddots & \vdots \\ e^{\left(i2\pi\Delta f_1 - R_2^*\right)t_N} & \cdots & e^{\left(i2\pi\Delta f_K - R_2^*\right)t_N} \end{bmatrix} \begin{bmatrix} \rho_1 \\ \vdots \\ \rho_K \end{bmatrix} \tag{5.2}$$

A least-squares estimate for $\vec{\rho}$ can be found using the Penrose-Moore pseudoinverse of $\bar{A}$ [21].

$$\vec{\rho} = \left(\bar{A}^H \bar{A}\right)^{-1} \bar{A}^H \vec{x} \tag{5.3}$$

Here ^{H} denotes the Hermitian transpose of a complex matrix. Note that at least K echoes are required to decompose K chemical shifts, but the acquisition of more echoes may improve noise performance in the decomposed images for individual resonances. The careful selection of echo times is critical for this approach to chemical shift encoding, since together with the known chemical shifts these echo times provide the basis for sampling the phase evolution of the aggregate signal. The prior knowledge of chemical shifts present should be used to select echo times for which the phase angles of the individual chemical shift signals are — at the very least — not static. In this situation, the condition number of $\bar{A}$ peaks and the system of equations described above are ill-posed.

This approach to chemical shift imaging is a generalization of the Dixon method for phase-sensitive separation of fat and water [166]. Throughout this work this type of chemical shift encoding will be referred to using the acronym IDEAL, which is short for iterative decomposition of chemical shifts with echo asymmetry and least squares estimation. Strictly speaking, IDEAL refers to a reconstruction approach in which the chemical shift images are estimated iteratively from multi-echo MRI data, usually with joint estimation of the fieldmap ($\psi(\vec{r})$). All applications of this imaging method shown here will directly solve for $\vec{\rho}$ using equation 5.3, which provides the theoretical SNR performance of IDEAL imaging in the absence of any B_0 inhomogeneity [167].

Selection of IDEAL Echo Times

The performance of IDEAL reconstruction for a given set of echo times and chemical shifts can be quantified through the condition number of $\bar{A}$ or through the effective number of signal averages (NSA) of individual chemical shifts [21]. While the condition number provides a summary metric of IDEAL performance for all resonances, it is often the case that specific ^{13}C chemical shifts are of interest while others may be present but optimizing the SNR of their corresponding images is not a priority. For example, in HP pyruvate imaging maximizing the SNR for products of *in vivo* metabolism such as lactate, alanine and bicarbonate is vital, whereas pyruvate-hydrate is often present from the moment of dissolution but is not metabolically active and provides little additional information [68]. The effective NSA can be used in such cases to assess noise performance for the specific chemical shifts of interest. This quantity is calculated as the reciprocal of the diagonal element of the covariance matrix of $\bar{A}$ for that resonance [21].

$$NSA_k = \frac{1}{\left(\left(\bar{A}^H \bar{A} \right)^{-1} \right)_{k,k}} \tag{5.4}$$

Without fieldmap demodulation, the application of IDEAL decomposition for a given set of chemical shifts is a linear transformation with a frequency response fully defined by the number of echoes used and their relative spacing in time [167]. The magnitude and phase response of a unit signal at a specific frequency can easily be evaluated through equation 5.3. From the standpoint of IDEAL decomposition, there is no requirement that the echoes be spaced evenly in time. However, equal echo spacing is most often used and can greatly simplify the pulse sequence used for data acquisition. In this work, uniform echo spacing is used.

In the context of HP [1-^{13}C]pyruvate imaging, it is instructive to consider situations in which some of the chemical shifts listed in table 5.1 are not accounted for in the IDEAL decomposition process. Bicarbonate, for example, may be difficult to reliably observe in some *in vivo* HP pyruvate studies, so there could be some theoretical benefit to disregarding this and other weak signals in the choice of echo spacing. In order to

evaluate these considerations systematically, five IDEAL experiments were simulated in which the numbers of echoes (4-8) acquired were two greater than the numbers of chemical shifts decomposed (2-6). Decomposed chemical shifts were added in each successive experiment in the order in which they are listed in table 5.1 (pyruvate, lactate, pyruvate hydrate, urea, alanine and bicarbonate), since this order typically corresponds to decreasing maximum signal magnitude in a preclinical HP pyruvate imaging experiment.

For each simulated IDEAL experiment, the condition number of the coefficient matrix ($\bar{A}$) and the NSA values for decomposed chemical shifts were calculated for echo spacings ranging from 1 µs to 1 ms at 1 µs increments. The shortest echo spacing in this range for which the condition number is minimized was used for evaluation of the frequency response. T_2^* decay was not simulated in these calculations ($R_2^* = 0$). The frequency response was calculated for each chemical shift as the magnitude and phase of the corresponding IDEAL decomposition output (ρ_k) for simulated time-domain input signals of unit magnitude with frequencies ranging from -1 kHz to +1 kHz at 1 Hz increments. In the magnitude and phase frequency response plots shown below in the lower panes of figures 5.1-5.5, the discrete offset frequencies of each chemical shift in table 5.1 are indicated as dashed vertical lines and a synthetic magnitude spectrum similar to that typically observed in slice-selective preclinical imaging of HP pyruvate is shown.

As figures 5.1-5.5 illustrate, the decomposition of additional chemical shifts using additional echoes results in modulations of the IDEAL frequency responses that map the added shifts to their own output with unit magnitude and zero phase, and that suppress the contribution of these signals in other outputs. For the IDEAL experiments simulated here, pyruvate and lactate are always decomposed since they are typically the HP signals of greatest interest in HP imaging of cancer. We chose to account for bicarbonate signal last since this resonance is typically the weakest product of HP pyruvate in small animal experiments. However, due to the spectral location of the bicarbonate signal relative to other chemical shifts, its magnitude is misregistered predominantly to lactate as additional shifts are added to the decomposition process.

Therefore if bicarbonate signal is present in IDEAL imaging data acquired using the encoding strategy shown in figures 5.3 or 5.4 it will produce a significant artifact in lactate images.

Figure 5.1: IDEAL imaging at 7 T with 4 echoes decomposing 2 chemical shifts: pyruvate and lactate. The frequency response for an echo spacing of 0.27 ms is shown as solid colored lines in the two lower plots. Note how pyruvate hydrate, alanine, urea and bicarbonate signals are mapped to the decomposed images with varying magnitudes and phases.
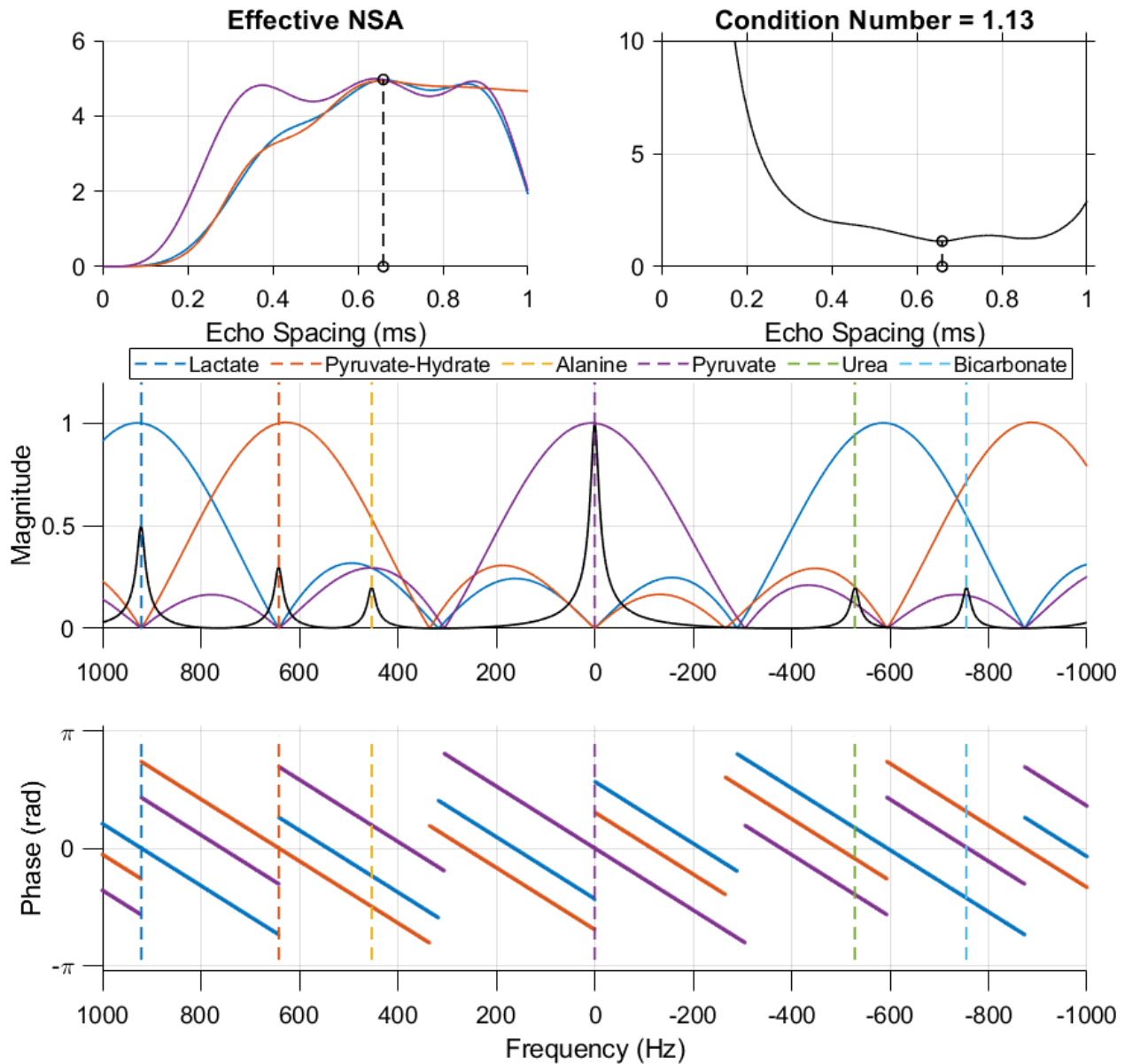
Figure 5.2: IDEAL imaging at 7 T with 5 echoes decomposing 3 chemical shifts: pyruvate, lactate and pyruvate hydrate. The frequency response for an echo spacing of 0.66 ms is shown as solid colored lines in the two lower plots. Note how alanine, urea and bicarbonate signals are mapped to the decomposed images with varying magnitudes and phases.
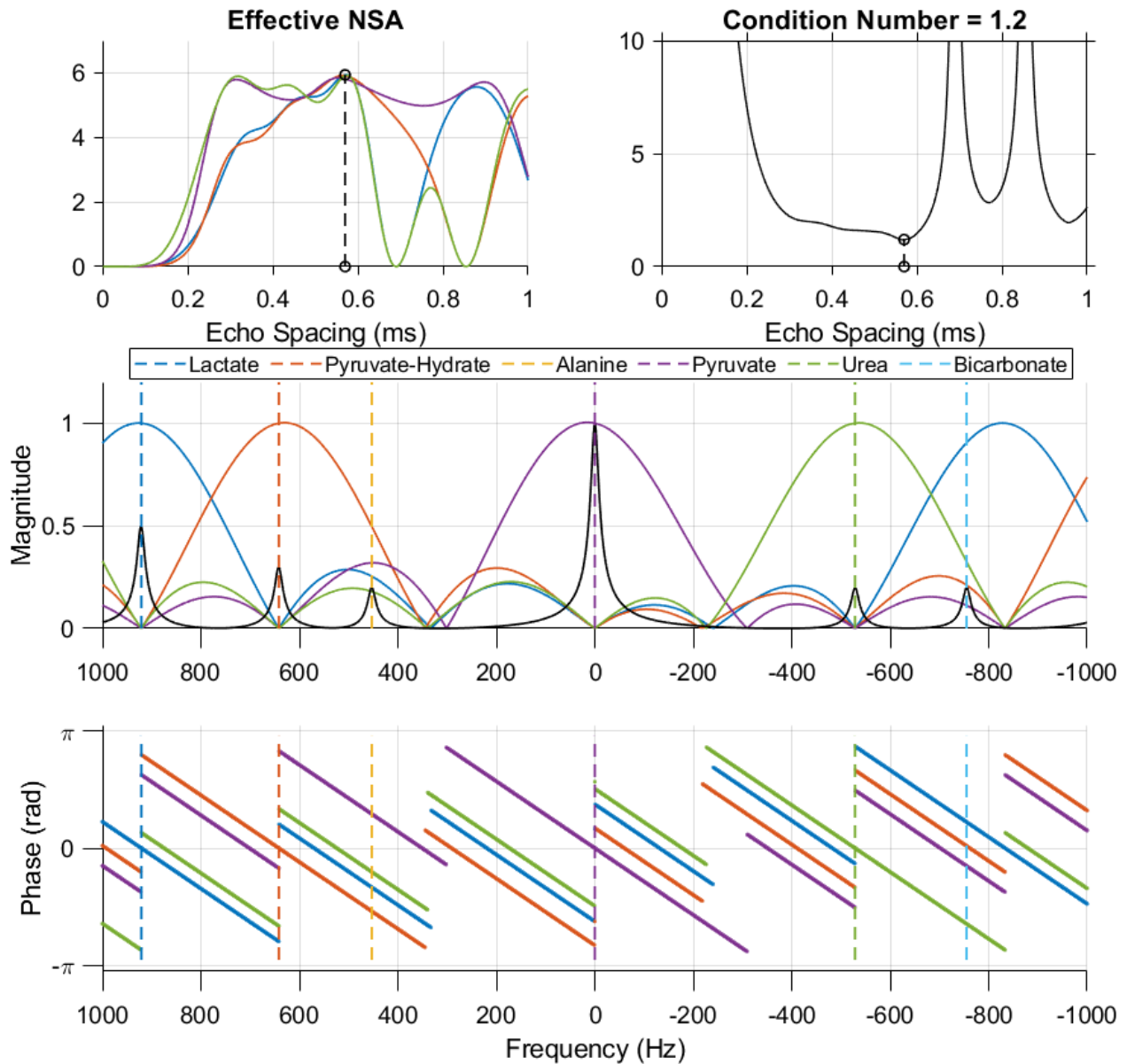
Figure 5.3: IDEAL imaging at 7 T with 6 echoes decomposing 4 chemical shifts: pyruvate, lactate, pyruvate hydrate and urea. The frequency response for an echo spacing of 0.57 ms is shown as solid colored lines in the two lower plots. Note how alanine and bicarbonate signals are mapped to the decomposed images with varying magnitudes and phases.
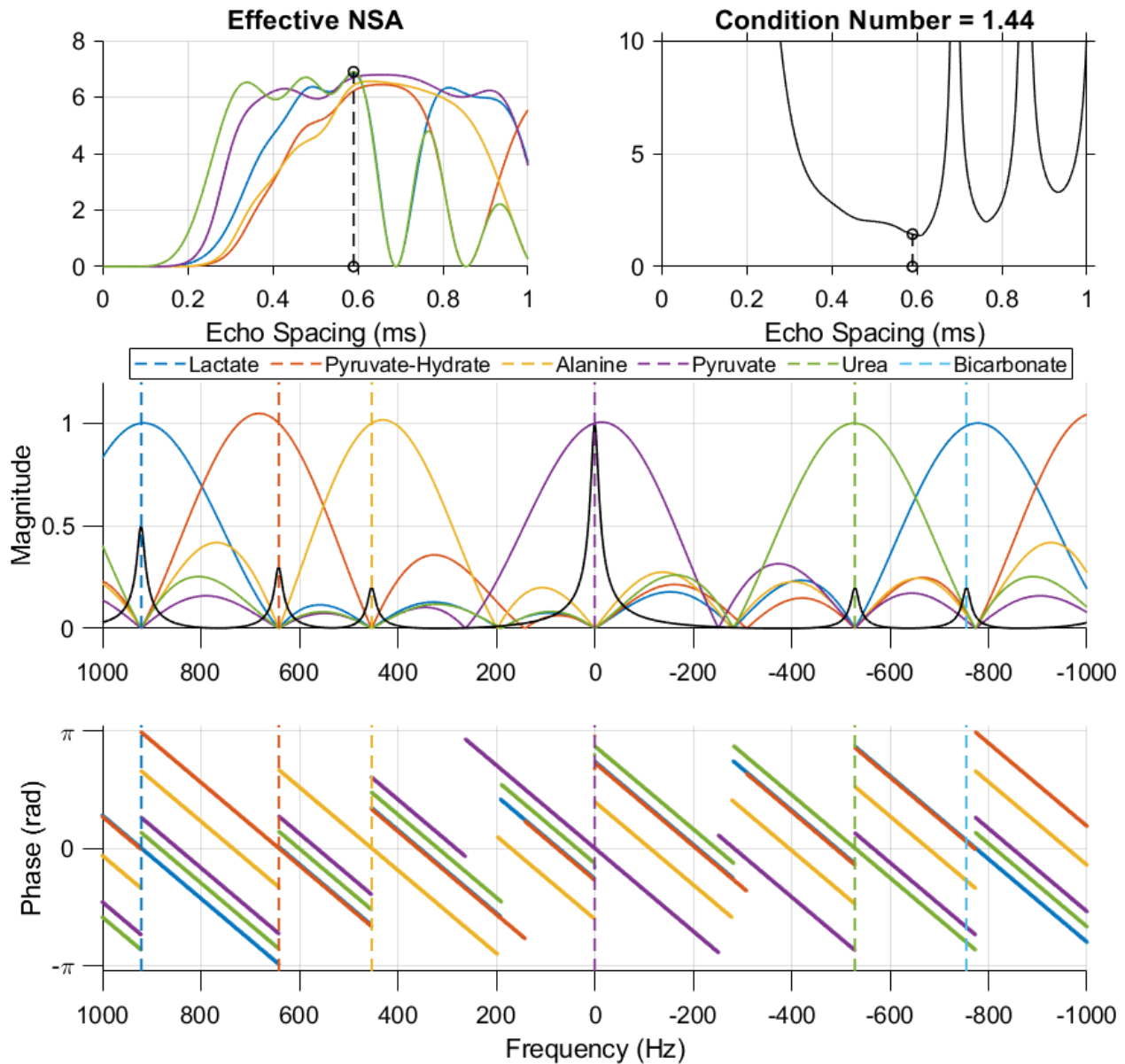
Figure 5.4: IDEAL imaging at 7 T with 7 echoes decomposing 5 chemical shifts: pyruvate, lactate, pyruvate hydrate, urea and alanine. The frequency response for an echo spacing of 0.59 ms is shown as solid colored lines in the two lower plots. Note how bicarbonate signal is mapped to the decomposed images, particularly lactate, with varying magnitudes and phases.
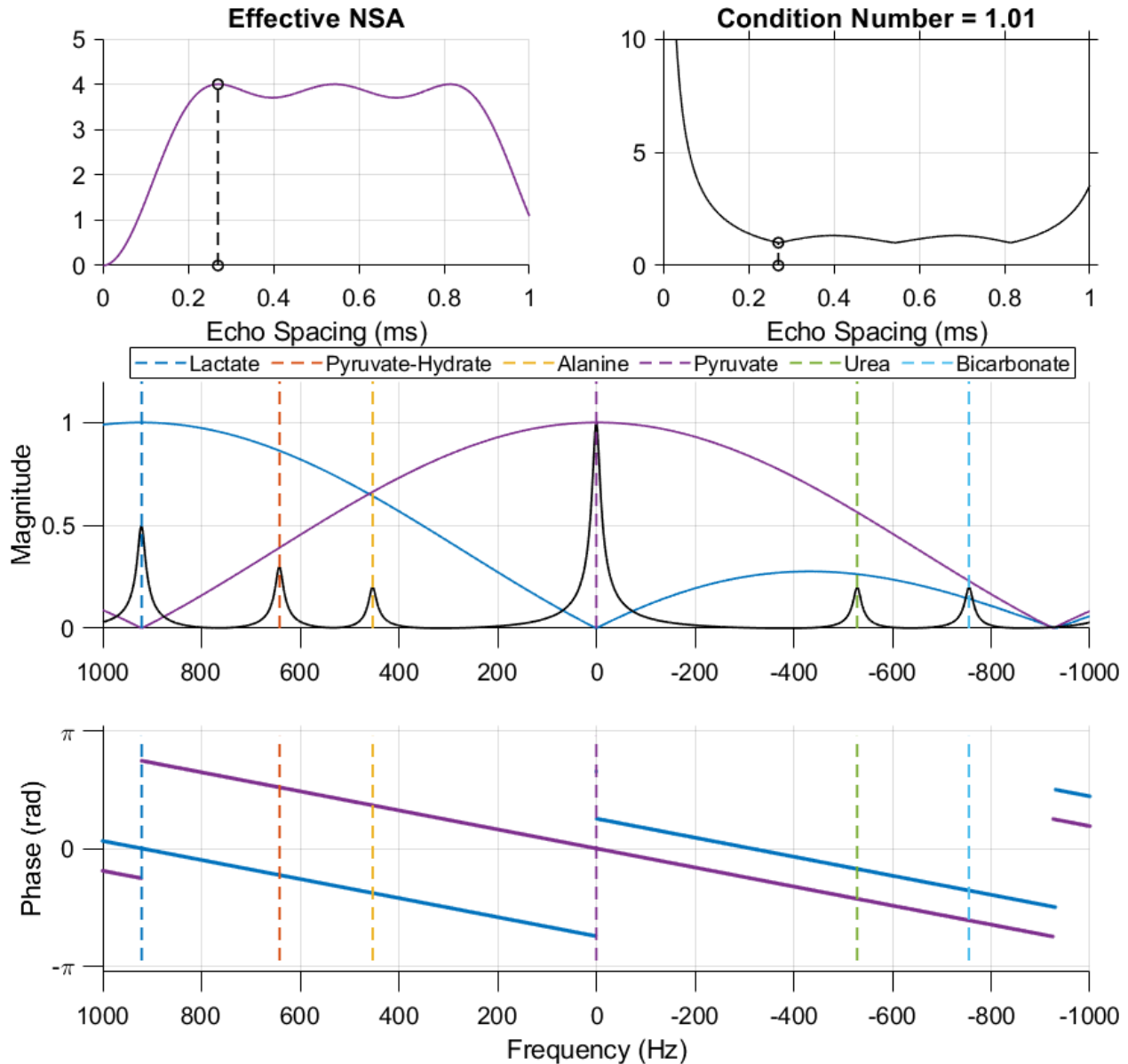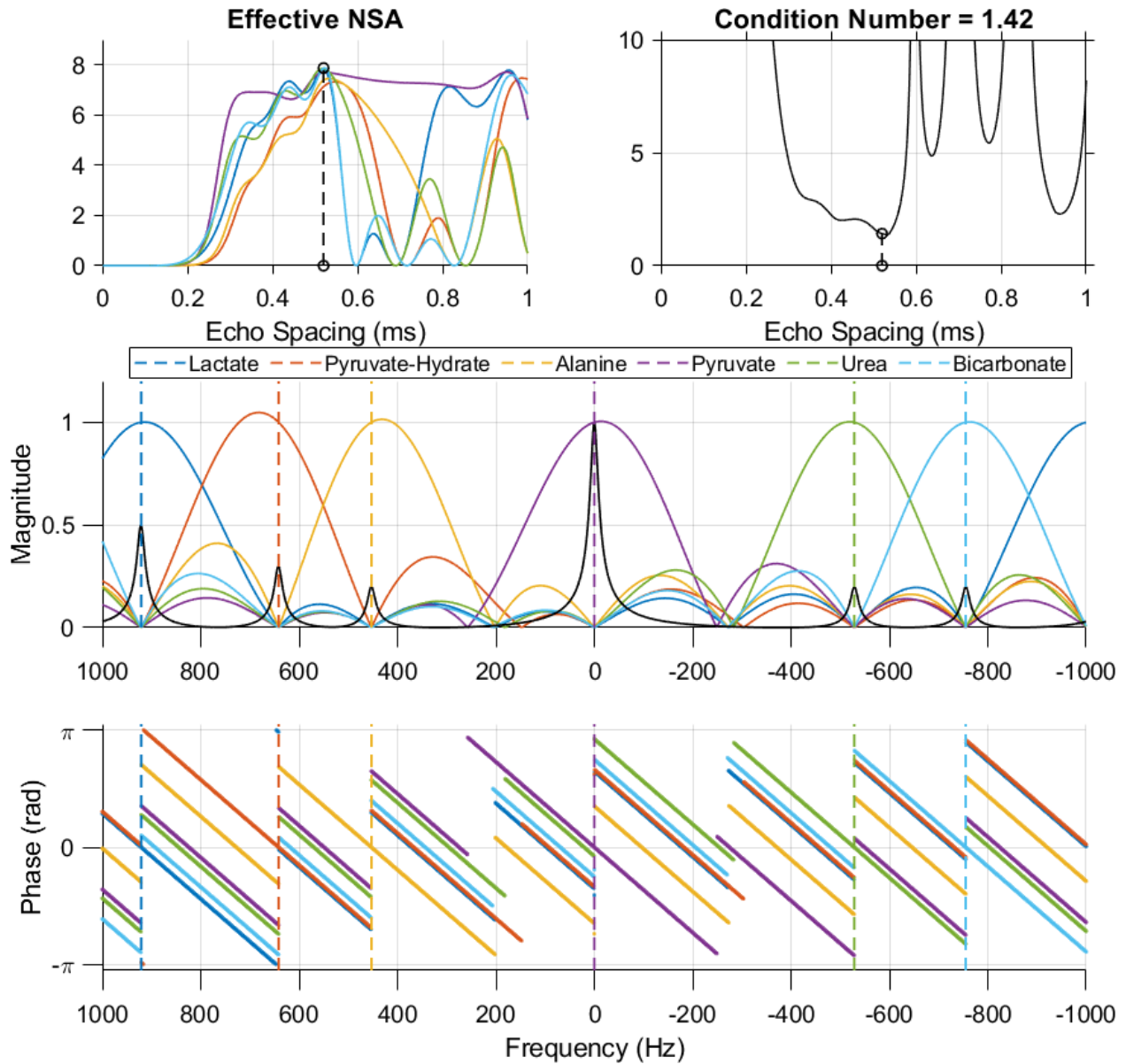
Figure 5.5: IDEAL imaging at 7 T with 8 echoes decomposing all 6 chemical shifts listed in table 5.1. The frequency response for an echo spacing of 0.52 ms is shown as solid colored lines in the two lower plots. Note how each resonance is properly mapped to the decomposed images with uniform magnitude and no phase shift.
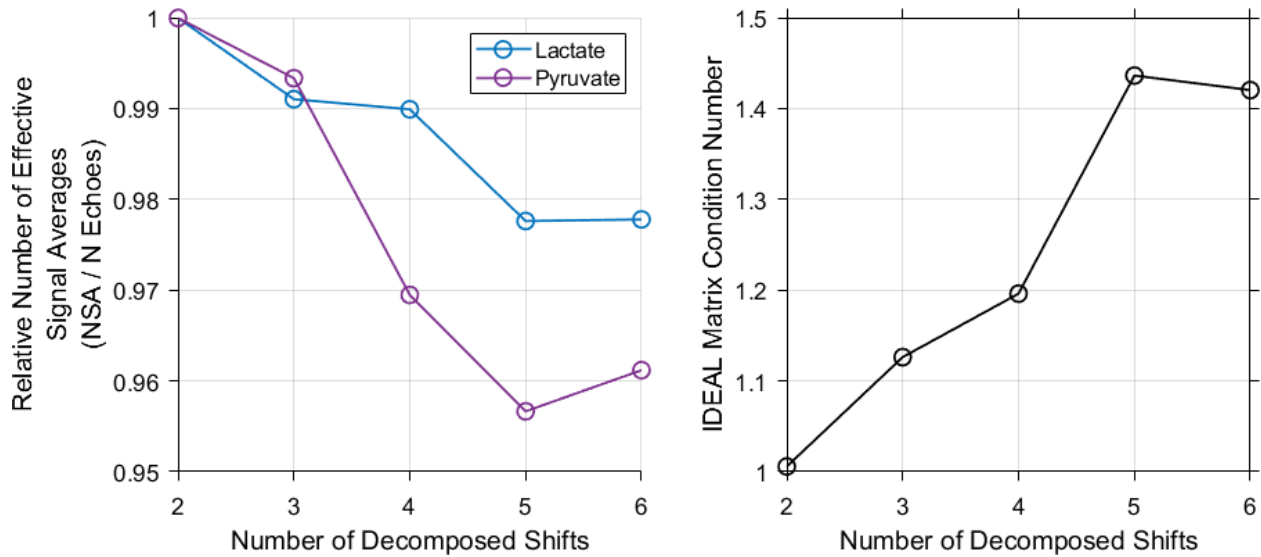
Figure 5.6: Effective number of signal averages and condition number for IDEAL imaging with 4-8 echoes and optimal echo spacing. A slight degradation in noise performance ($<5\%$) is seen with increasing number of echoes and chemical shifts, however this is most often necessary to prevent misregistrations of chemical signals in the images of interest. For clarity, the relative NSA is shown only for pyruvate and lactate, the two shifts most relevant to HP imaging in cancer that are decomposed in all simulations in figures 5.1-5.5.

The theoretical benefit of these IDEAL encoding strategies that account for fewer chemical shifts than may be present in HP imaging can be quantified by the effective NSA of the chemical shifts of primary interest (normalized to the number of echoes), and by the IDEAL matrix condition number. These quantities are summarized in figure 5.6, with the normalized effective NSA shown for pyruvate and lactate. While some very slight degradation in noise performance for pyruvate and lactate occurs for IDEAL encoding of additional chemical shifts, this change in SNR performance is very small for the optimal echo spacings illustrated in figures 5.1-5.5. For this very minor gain in SNR, decomposing fewer shifts using fewer echoes can result in the chemical misregistration of signals that are not accounted for in IDEAL decomposition, as described above for bicarbonate. Given the small differences in normalized effective NSA and IDEAL matrix condition number, the primary benefit of using any of the IDEAL encoding strategies decomposing fewer shifts (figures 5.1-5.4) would be the shorter overall image encoding time that can be realized in acquiring fewer echoes.

Pyruvate

	2	3	4	5	6
Lactate	0.02021%	0.03186%	0.02698%	0.03319%	0.02811%
Pyruvate-Hydrate	39.13%	0.04263%	0.043%	0.02843%	0.02734%
Alanine	66.28%	29.54%	31.96%	0.004318%	0.004402%
Pyruvate	100%	100%	100%	100%	100%
Urea	56.34%	12.11%	0.07089%	0.1226%	0.112%
Bicarbonate	23.01%	16.12%	11.21%	3.723%	0.009631%

Number of Decomposed Shifts

Lactate

	2	3	4	5	6
Lactate	100%	100%	100%	100%	100%
Pyruvate-Hydrate	86.29%	0.0825%	0.08024%	0.05734%	0.05731%
Alanine	64.25%	29.51%	25.37%	0.005433%	0.005246%
Pyruvate	6.246e-15%	1.57e-13%	1.928e-14%	3.168e-14%	4.918e-14%
Urea	26.28%	94.35%	0.1522%	0.1932%	0.1029%
Bicarbonate	14.32%	54.83%	90.48%	98.66%	0.02117%

Number of Decomposed Shifts

Figure 5.7: Heatmaps of individual chemical shift magnitude responses in IDEAL pyruvate and lactate output images for each input chemical shift listed in table 5.1. Each heatmap displays the percentage of each chemical shift magnitude that is passed through into decomposed pyruvate or lactate images by the IDEAL reconstruction using the optimal echo spacings shown in figures 5.1-5.5. For example, when 4 IDEAL echoes with the TE spacing shown in figure 5.1 are used for decomposition of only pyruvate and lactate, 39.1 and 86.3% of the pyruvate-hydrate signal magnitude present is mapped to the pyruvate and lactate output images, respectively. In addition being misregistered chemically, signals in the final IDEAL images originating from incorrect chemical shifts will be shifted spatially in a manner dependent on the method of spatial encoding, which can lead to severe image artifacts.

This chemical misregisration effect occurs to some degree in each output image, with contributions from each chemical shift that is not modeled in the IDEAL decomposition process. Figure 5.7 summarizes the percentage of each chemical shift magnitude that is mapped into the pyruvate and lactate IDEAL output images, as calculated from the magnitude frequency responses depicted in figures 5.1-5.5. Chemical signals that are mapped erroneously in this manner will also possess frequency shifts that result in spatial misregistrations dependent on the method of spatial encoding. While it may be feasible in certain situations to decompose fewer chemical shifts than may be present in a given HP pyruvate imaging experiment (e.g. using the four-shift IDEAL encoding depicted in figure 5.3 if alanine and bicarbonate are not of direct interest and can be expected to be virtually undetectable), doing so can result in artifacts in the IDEAL images due to these chemical and spatial misregistrations.

For these reasons, the IDEAL encoding strategy used throughout this chapter em-

ploys eight echoes to decompose all six chemical shifts listed in table 5.1. The echo spacing of this IDEAL strategy is 0.52 ms, which corresponds to the IDEAL experiment illustrated in figure 5.5.

5.3 Spectral-Spatial RF Pulses

Spectral-spatial pulses consist of multiple short RF pulses with consistent shape but variable amplitude applied synchronously with an oscillating slice selection gradient in order to perform excitation, saturation, refocusing or inversion of magnetization with a specific spatial and spectral profile. These pulses were first designed for selective ^{1}H imaging of water and fat [168], and the rapid acquisition of lipid-free imaging data remains the predominant application in clinical MRI (e.g. for blood oxygenation level dependent imaging). The flexibility in chemically selective excitation provided by spectral-spatial pulses has led to their use in ^{1}H [169] and ^{13}C [159] spectroscopic imaging. Compared to ^{1}H spectroscopy applications, design of spectral-spatial pulses for HP ^{13}C imaging is often easier due to the sparsity of chemical spectra and the lack of a significant macromolecular baseline. However, the creation of spectral-spatial pulses for ^{13}C imaging is still a challenging problem, particularly for HP preparations that probe multiple biochemical pathways *in vivo* [90] and for HP imaging on MRI systems with high magnetic fields and low gradient slew rate limits.

The first step of any spectral spatial pulse design problem is the selection of a balanced oscillating gradient shape. Although any shape may be employed, trapezoidal gradients are most often used with RF subpulses applied only during the constant amplitude gradient plateaus. In this case, the RF subpulse bandwidth and gradient amplitude specify the slice profile as in traditional slice selection. Similar to spatial image encoding, the gradient determines the excitation k-space trajectory. However, the slice gradient integral is evaluated inversely in time from the end of the slice rephasing gradient pulse to ensure $k_z = 0$ occurs at the center of each plateau [35].

$$k_z(t) = \gamma \int_{T_{end}}^{t} G_z(t')dt' \tag{5.5}$$

This equation describes the temporal phase evolution of isochromats due to their spatial position. Phase evolution due to chemical shift offset occurs linearly in time, and by periodic application of RF subpulses centered at $k_z = 0$ the spectral k-space is sampled. If the chemical shift dependent phase evolution is slow relative to the positional phase accumulation in each subpulse, the RF subpulses approximate discrete samples of spectral k-space. In this case, the individual subpulse amplitudes define a finite impulse response (FIR) filter that determines the spectral profile of the spectral-spatial pulse [170]. Given the desired frequency response, there are many methods for designing an optimal FIR filter. In this work, a publicly available MATLAB toolbox [171] for spectral-spatial pulse design was used that includes a specialized convex optimization FIR filter design algorithm [159]. The FIR filter design approach only provides an approximation of the pulse frequency response for the purpose of determining the individual RF subpulse amplitudes. Once these subpulse amplitudes are found, the spatial and spectral response of entire pulse can be evaluated more accurately via Bloch simulation.

The FIR filter can be visualized in the time domain as a broad RF envelope that modulates the amplitude of each subpulse, as shown for the Gaussian envelope in figure 5.8. The total time duration of this envelope (τ_2) is inversely proportional to the width of frequency passbands in the FIR filter frequency response. This frequency response is periodic with passband replicates occurring at the rate of subpulse sampling ($1/\tau_1$). More rapid subpulse sampling rates and greater total pulse durations are desirable for spectral-spatial pulses designed for selective imaging of individual chemical shifts, since these result in narrower and more isolated frequency passbands. However, the slew rate of the gradient system and the duration of individual RF subpulses needed to attain the desired spatial profile limit the minimum subpulse time separation. Additionally, the overall duration of spectral-spatial excitation pulses is limited in practice due to the finite lifetime of the signal it produces, as determined by the rate of spin-spin relaxation. Creation of spectral-spatial RF pulses is therefore a complicated design problem that must balance many competing effects to derive usable B_1 and gradient waveforms that impart acceptable magnetization response profiles in
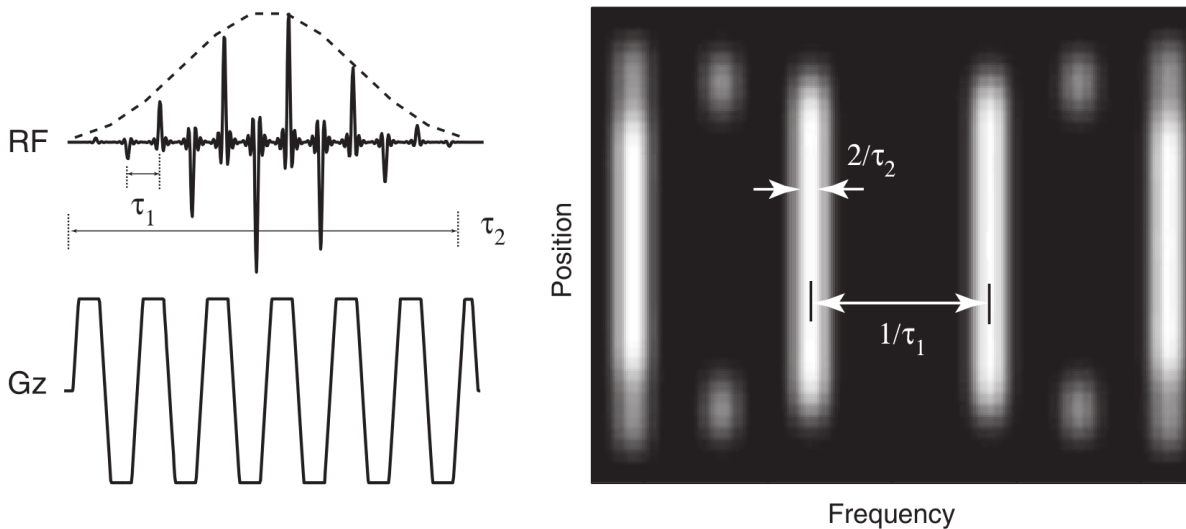
Figure 5.8: The relationship between spectral-spatial RF pulse frequency response and timing are demonstrated in this pulse designed for HP pyruvate imaging at 3 T. The RF and gradient waveforms (left) can be characterized by the time elapsed between subpulses (τ_1) and the total pulse duration (τ_2). The primary passbands possess a spatial profile determined by the subpulse shape and gradient amplitude, and a frequency profile determined by the envelope of the RF pulse. The passband frequency width is inversely proportional to the overall pulse duration. For the Gaussian envelope chosen for this pulse (dashed line), the spectral FWHM is $2/\tau_2$. The periodicity in time of the RF subpulses and gradient result in passband replicates occurring in the pulse frequency response with a separation of $1/\tau_1$.
Figure reprinted from Angus Z. Lau, et al. Spectral-spatial excitation for rapid imaging of DNP compounds. *NMR Biomed* 2011; 24: 988-996. doi:10.1002/nbm.1743. with permission from John Wiley and Sons (License Number 4873230896286).

space and frequency.

The spectral-spatial RF pulse used in this work was designed for selective HP imaging of [1-^{13}C]pyruvate and lactate at 7 T using the spectral spatial RF pulse design MATLAB package written by Adam Kerr and Peder Larson [159, 171, 172]. A flyback trapezoidal gradient was chosen with RF subpulses applied only during the unipolar gradient plateaus. This configuration entails a greater minimum subpulse separation than symmetric oscillating gradients (e.g. figure 5.8), however flyback gradients are less sensitive both to deviations in k_z from timing errors and eddy currents [35], and to uncompensated phase accumulation of moving isochromats [173]. The RF subpulses excite a 1 cm slice with a time-bandwidth factor of 3.5. For HP ^{13}C imaging
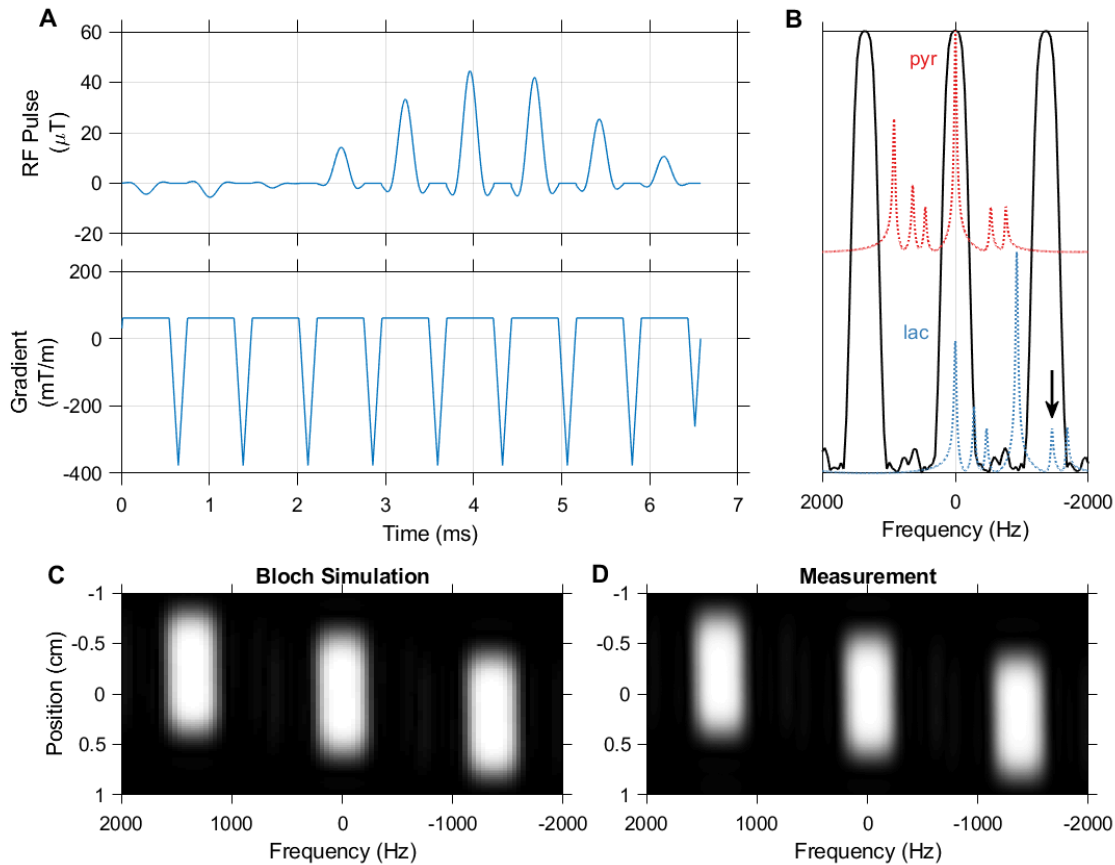
Figure 5.9: The spectral-spatial pulse used in this work was designed for selective imaging of pyruvate and lactate at 7 T with a 1 cm slice thickness and flyback gradient using a publicly available spectral spatial RF pulse design package (https://github.com/LarsonLab/Spectral-Spatial-RF-Pulse-Design) [171]. The RF excitation waveform (A) consists of 9 subpulses and has a total duration of 6.6 ms. The real RF B_1 magnitude shown corresponds to a 90 degree excitation, and may be scaled down to achieve lower excitation angles in HP experiments. A 420 Hz passband and 930 Hz stopband allow selective imaging of pyruvate and lactate at 7 T (B). ^{13}C urea at -1680 Hz (arrow) falls within a passband replicate when the MRI center frequency is set to lactate, but can be pre-saturated when using this pulse for dynamic imaging. Bloch simulation of the transverse magnetization response to this pulse (C) agrees with measurement in a relaxed water phantom (D).

the excitation of empty spectral regions may be permitted, however for this design we chose to specify a desired frequency response with sufficiently wide passband separation to minimize excitation of other chemical shifts when imaging pyruvate and lactate. The FIR design specifications included a single passband of at least 1 ppm width (75.5 Hz) separated from its frequency replicates by at least 12.3 ppm (930 Hz). With these specifications, a flyback gradient with a period of 0.74 ms was used, resulting in a passband replicate spacing of approximately 1350 Hz. As illustrated in figure 5.9, this spectral response allows selective imaging of pyruvate without significant excitation of the remaining chemical shifts listed in table 5.1. However, when the primary passband is centered on lactate significant excitation of ^{13}C urea occurs. For our purposes this urea signal is present in a thermally polarized phantom placed in the imaging volume for calibration of ^{13}C center frequency and RF transmit power, and the urea can be saturated using a separate spectrally selective RF pulse shortly before spectral-spatial excitation of lactate. The spatial and frequency response of this spectral-spatial RF pulse was validated by measuring one-dimensional spatial readouts along the slice direction in a gadolinium-doped water phantom with varying offsets between transmission and reception frequency. The spatial axis in this ^{1}H measured spectral-spatial profile was corrected by multiplying it by the ratio of ^{1}H to ^{13}C gyromagnetic ratios for comparison with the ^{13}C design Bloch simulation.

The spectral-spatial RF pulse used throughout this chapter was designed with a nominal excitation angle of 90 degrees, and the RF and gradient waveforms are exported to a plain text format that allows them to be imported into our custom pulse sequence (as described below). This sequence scales the B_1 waveform to provide any specified excitation angle <90 degrees. In order to realize spatial slice shifts, the B_1 phase of a spectral-spatial pulse must be modulated as a function of k_z [35].

$$B_1(t, \Delta z) = e^{i2\pi k_z(t)\Delta z} B_1(t, \Delta z = 0) \tag{5.6}$$

It is not possible to apply this non-linear phase modulation to our spectral-spatial RF waveforms directly on our MRI system. Instead, fixed spatial offsets (e.g. for multislice imaging) are realized by applying the phase modulation described in equation 5.6 to

the B_1 waveform before exporting it from MATLAB. The spectral-spatial pulse used in this chapter had no spatial shift, and great care was taken to position the imaging subject at the MRI system isocenter.

5.4 Sequence Design and Implementation

The vendor gradient-echo (FLASH) imaging method from ParaVision 6.0.1 was modified to permit gradient waveforms of arbitrary shape defined in plain text files to be played out during three sequence segments for excitation, preparation and readout. Gradient waveforms are stored in plain-text files with amplitude in units of mT/m and the dwell time of each point determined by the gradient timing resolution of the system (8 µs). The use of these custom gradient waveforms permit the use of spectral-spatial pulses (which are otherwise unavailable on this imaging platform), as well as more time-efficient imaging readouts.

Tools for single-shot flyback and symmetric EPI waveform design and image reconstruction were written in MATLAB R2017a. The EPI waveforms designed with our method are fully rewound and traverse in minimum time the k-space trajectory determined by the requested FOV, image matrix and readout bandwidth for the specified gyromagnetic ratio and gradient specifications (timing resolution, maximum amplitude and slew rate). Apart from the EPI encoding simulations described in the following subsection, all image data presented in this chapter were acquired or simulated using the flyback EPI trajectory shown in figure 5.10.

For selective imaging of individual chemical shifts, both the excitation angle and center frequency of each excitation can be set individually. The acquisition duration may also optionally be extended beyond the length of the single-shot imaging readout. As illustrated in figure 5.11, this extended readout can allow the measurement of a residual FID if T_2^* is sufficiently long. When the residual FID SNR is sufficiently high and represents a single chemical resonance, it is used to inform the reconstruction of the preceding imaging readout by correcting for the k-space data for the observed off-resonance chemical shift. Since the resonant frequencies of HP signals can be esti-
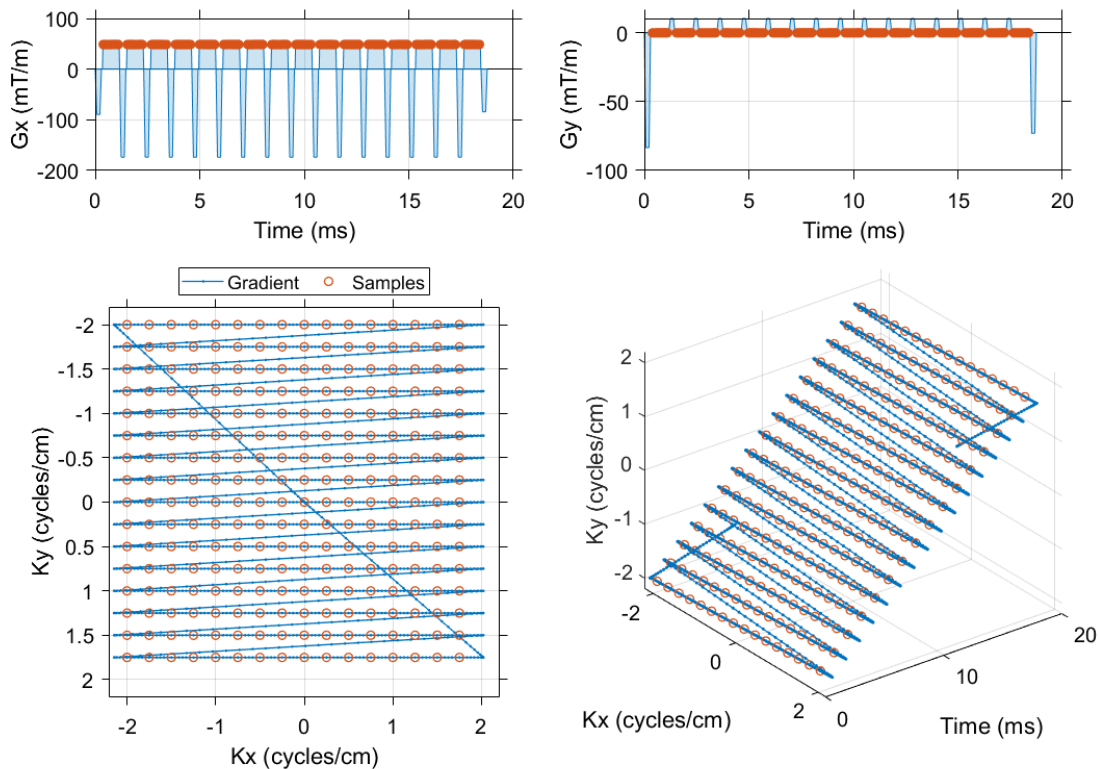
Figure 5.10: This single shot flyback EPI trajectory is used throughout this chapter, including in comparisons of spectral encoding strategies for imaging of [1-^{13}C]pyruvate and associated metabolites. This readout is designed for a 16 x 16 matrix, 4 cm field of view and 20.833 kHz readout bandwidth (48 µs dwell time). The center of k-space is sampled 9.984 ms into the gradient waveform, which has a total duration of 18.76 ms and an echo spacing of 1.152 ms (868 Hz phase bandwidth).

mated but not precisely known before their measurement, this off-resonance correction addresses the common issue of slight frequency offsets in HP imaging with spectrally selective imaging of individual chemical shifts. An alternative method available in our pulse sequence uses separate slice-selective broadband excitations (green pulses in figure 5.12) prior to each set of imaging acquisitions to measure the chemical shift offsets [22, 174]. However, unlike the residual FID measurement shown in figure 5.11, the acquisition of independent slice spectra entails additional RF depletion of the HP magnetization. These slice-selective broadband spectra are therefore used mainly for determination of precise HP chemical shift offsets in IDEAL experiments.

An optional variable TE delay between excitation and readout allows this sequence
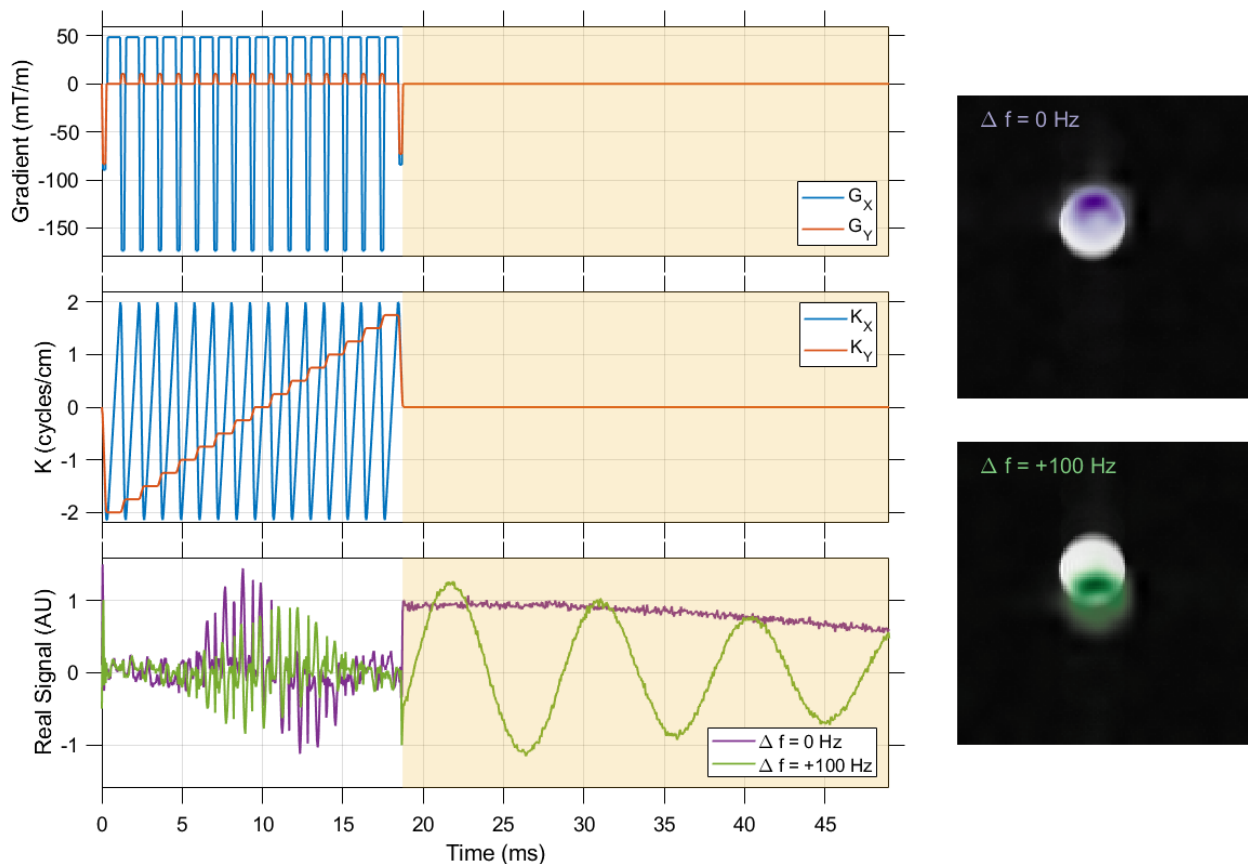
Figure 5.11: Single-shot imaging trajectories used in this work are fully rewound, permitting acquisition of a residual FID after image readout. If this residual FID is detectable following an imaging readout of a single chemical shift (e.g. when using a spectrally selective RF excitation), it may be used as a navigator to correct any off-resonance shift in the preceding k-space data prior to reconstruction.

to be used for IDEAL encoding [22]. In order to permit IDEAL image acquisition with flexible echo delays, each snapshot imaging readout follows a separate excitation pulse. As in selective excitation mode, the excitation angle of each individual pulse may be specified independently. The inter-pulse delay may be minimized to limit HP signal evolution within a single set of IDEAL echoes, and the delay between subsequent sets of IDEAL echoes may be set separately to control dynamic sampling of HP signal evolution.

All code for the imaging method, experiment design and image reconstruction are publicly available online (https://github.com/mda-mrsl/PV6-HPMR). Images are reconstructed from EPI data by 2D iDFT of plateau-sampled points. In IDEAL image re-
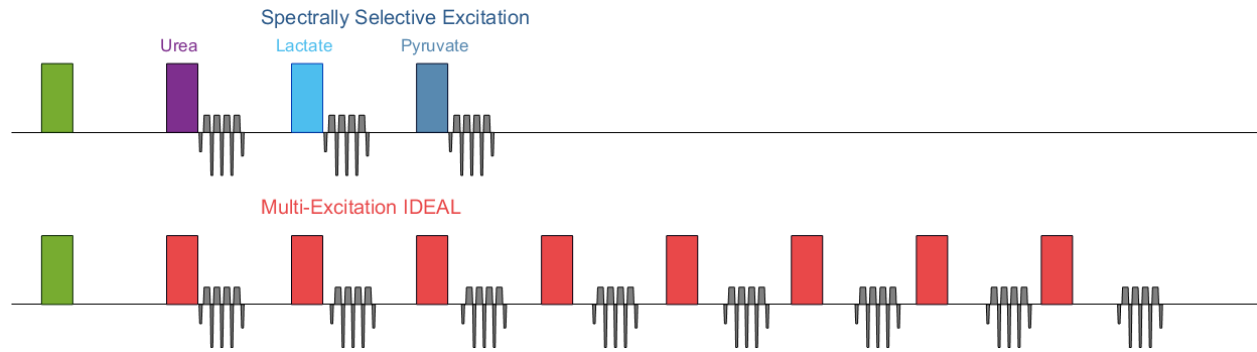
Figure 5.12: Simplified pulse sequence diagrams are shown here for a single time point in dynamic experiments using spectrally selective RF pulses (top) and multi-excitation IDEAL (bottom) for HP imaging of pyruvate and lactate. In both imaging techniques, a slice-selective spectrum may optionally be acquired before ^{13}C imaging at each timepoint using a broadband excitation (green pulse). For spectrally selective imaging, a saturation pulse (purple) may be applied to urea (or any other frequency) to prevent this signal from appearing in the HP images.

construction, 2D iDFT is preceded by multiplication of raw k-space data with the pseudoinverse of the coefficient matrix of phases accumulated by the decomposed chemical shifts at the specified TEs (equation 5.3), with off-resonance correction [22, 175]. All 6 chemical shifts listed in table 5.1 are modeled as individual discrete peaks in this decomposition. All multi-excitation IDEAL experiments were conducted with short inter-pulse delays to minimize T_1 recovery or decay.

Numerical Simulation of EPI Encoding

Numerical simulations were conducted to evaluate the performance of snapshot ^{13}C EPI encoding strategies. The relative SNR of flyback and symmetric EPI readouts for a range of acquisition dwell times and T_2^* relaxation time constants was calculated as [25]:

$$SNR_{Rel} = \sqrt{t_{dwell}} e^{\left(\frac{TE}{T_2^*}\right)} \tag{5.7}$$

These numerical simulations were conducted for gradient system limitations corresponding both to the preclinical 7 T MRI used throughout this work (maximum amplitude of 660 mT/m, maximum slew rate of 4570 T/m/s, gradient timing resolution of 8 µs) and to a clinical 3 T MRI (Discovery MR750, GE Healthcare, Waukesha, WI; maximum amplitude of 50 mT/m, maximum slew rate of 200 T/m/s, gradient timing

resolution of 4 µs). While the pulse sequence described above is not available on this clinical MRI system, a very similar sequence allows these snapshot EPI trajectories to be used on that scanner when multi-nuclear imaging capabilities are available. For the preclinical 7 T system, a single FOV and matrix size of 4 cm and 16 x 16 was used in these simulations, since these are typical for mouse imaging. For the clinical 3 T MRI, a typical human brain imaging FOV and matrix size of 24 cm and 24 x 24 was used [78, 97, 107, 176]. For each dwell time and T_2^* value simulated, a Shepp-Logan phantom was also digitally reconstructed with signal apodization and the normalized root mean square error (NRMSE) of the resulting image was calculated to quantify T_2^* blurring effects.

The results of these simulations are shown in figure 5.13 for trajectories representative of murine imaging at 7 T and in figure 5.14 for human head imaging at 3 T. These contour plots demonstrate that the choice of readout bandwidth must always balance SNR performance and error introduced by T_2^* decay during the encoding time. As illustrated in the point spread function shown in figure 5.15, this error imparted by signal apodization arises primarily from image blurring along the direction encoded more slowly with blipped gradient pulses (k_y). Compared to the results for our preclinical 7 T MRI, the same general trends in relative SNR and NRMSE are evident for the clinical 3 T system. However, the less powerful gradients and larger encoded matrix necessary for imaging of the human head result in a steeper decrease in SNR and increase in NRMSE with increasing readout dwell time. For a given dwell time and T_2^* value on either MRI system, symmetric EPI always utilizes the encoding time more efficiently than flyback EPI. Therefore the relative SNR is always higher and NRMSE is always lower for a symmetric trajectory than for a flyback trajectory designed with the same parameters. For the 3 T MRI, a greater benefit in the theoretical SNR is evident for symmetric EPI trajectories than on the preclinical system. This is a result of the lower gradient slew rate limit on the clinical system, which necessitates longer flyback gradient pulses. For well-shimmed small animal imaging at 7 T, we have typically observed a T_2^* value of around 20 ms. The results in figure 5.13 show that at this T_2^* value, a symmetric trajectory with 48 µs dwell time provides a 13.8% increase in

Figure 5.13: Numerical simulations demonstrate the relative SNR and NRMSE performance of single-shot EPI trajectories with flyback and symmetric readout gradients for ^{13}C imaging on a 7 T preclinical MRI system using a 4 cm FOV and 16 x 16 matrix. Minimum error occurs at short readout dwell times (maximum sampling bandwidth) due to reduced T_2^* decay during image encoding. However, the choice of dwell time represents a compromise between image accuracy and SNR.

SNR and 20.4% decrease in NRMSE compared to the equivalent flyback readout.

It should be noted, however, that these simulations account only for the effects of T_2^* decay and readout bandwidth. Despite the theoretical benefit shown for symmetric EPI, we chose to utilize the flyback EPI trajectory illustrated in figure 5.10 throughout this chapter due to the relative ease and simplicity flyback trajectories provide in reconstruction of artifact-free images. In particular, symmetric EPI often suffers from phase inconsistencies between readouts on the positive and negative lobes of the bipolar gradient, resulting in characteristic N/2 ghosts. A variety of methods are used to correct these phase inconsistencies and minimize or eliminate these ghosts, but most
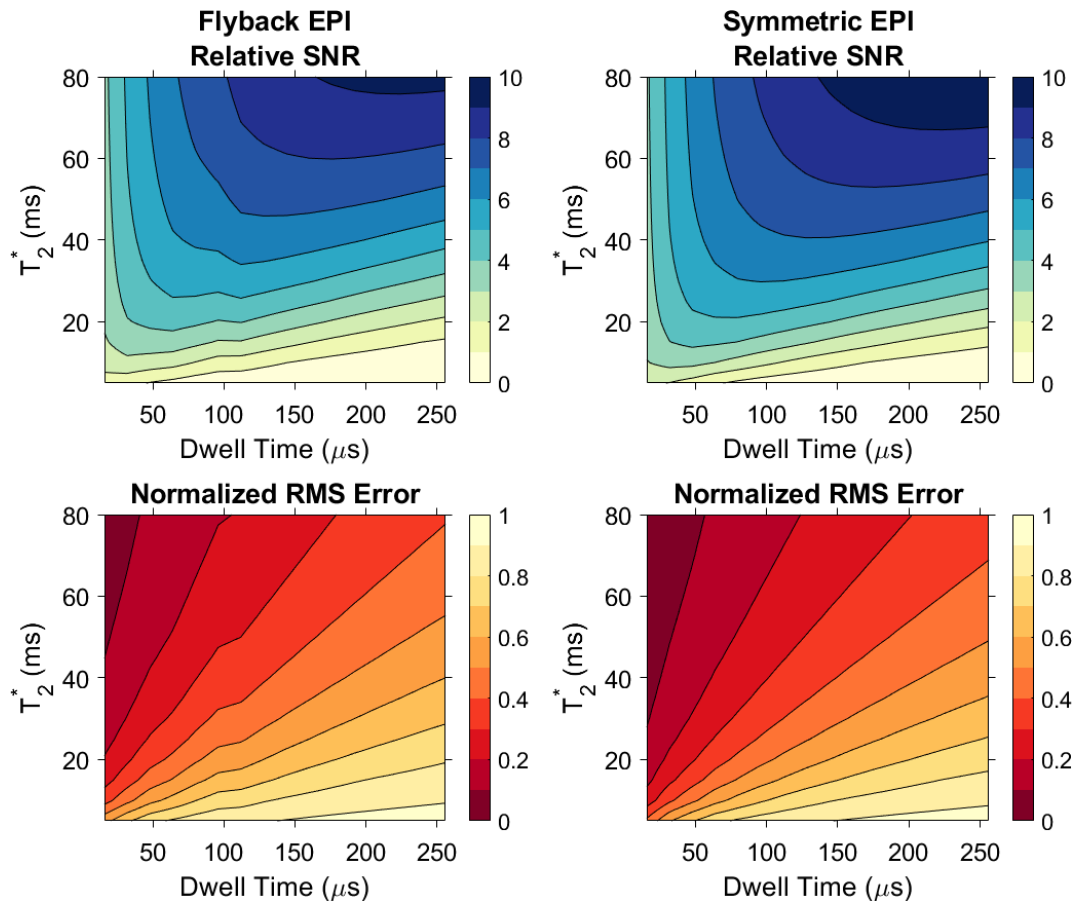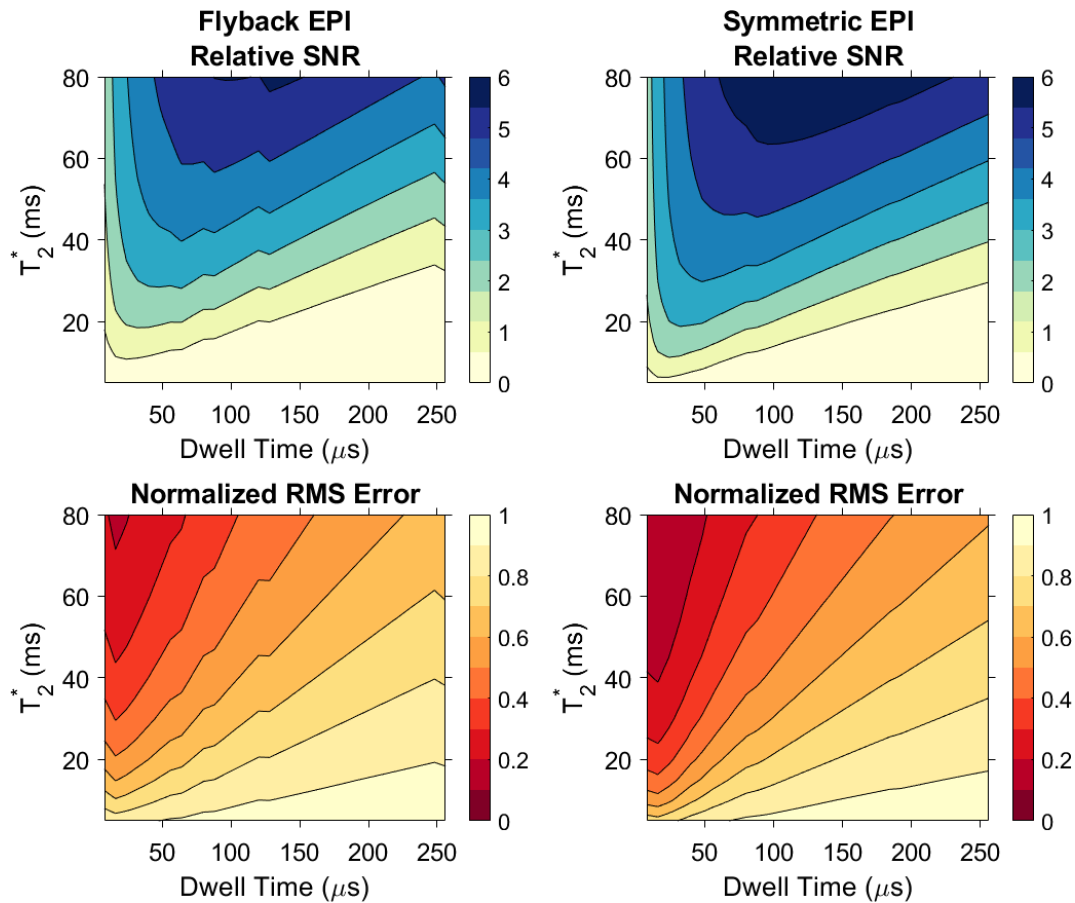
Figure 5.14: Numerical simulations demonstrate the relative SNR and NRMSE performance of single-shot EPI trajectories with flyback and symmetric readout gradients for ^{13}C imaging on a 3 T clinical MRI system using a 24 cm FOV and 24 x 24 matrix. These EPI trajectories were not implemented on the clinical MRI system for this work, but are presented to demonstrate the impact of larger matrix sizes and less powerful gradients.

often this is done through the acquisition of a separate reference scan that measures the signal phase evolution during the symmetric readout gradient without gradient blips applied in the orthogonal direction [177]. In HP imaging, the use of such reference scans is problematic as it must either use up a portion of the finite HP magnetization during its limited lifetime or be estimated from ^{1}H data acquired with an identical gradient trajectory [178]. For reconstruction of symmetrically encoded ^{13}C EPI data in our sequence, we have included an automated implementation of Buonocore's phase correction algorithm for N/2 ghost correction, which does not require a reference scan [179]. This algorithm estimates phase correction coefficients directly
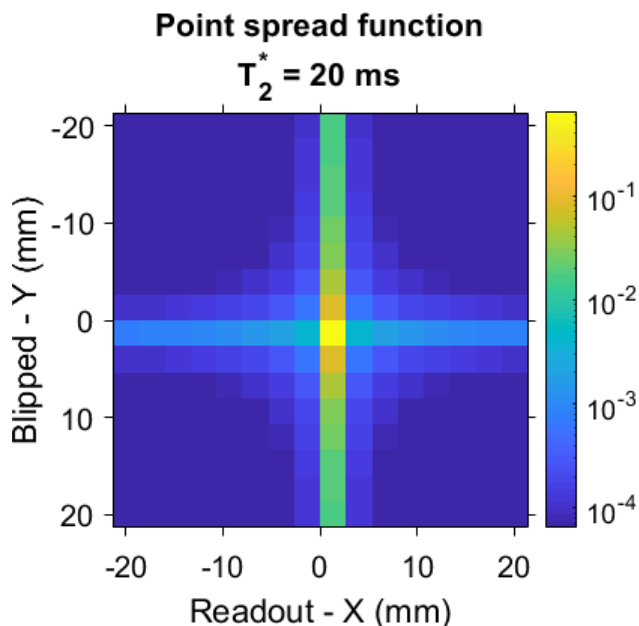
Figure 5.15: The point-spread function of the flyback EPI trajectory shown in figure 5.10 depicts image blurring predominantly in the blipped (k_y) direction due to T_2^* decay. This point-spread function was generated for a T_2^* of 20 ms, which corresponds to a well-shimmed *in vivo* experiment at 7 T. Note that color is scaled logarithmically to illustrate the much less significant blurring effect along the readout (k_x) direction.

from the image data and has been applied to HP ^{13}C imaging previously [180]. As an example, the rat liver HP ^{13}C urea images shown in section 4.4 were encoded with symmetric EPI readouts and reconstructed using this referenceless ghost correction algorithm.

5.5 Comparison of Spectral Excitation and IDEAL Encoding

The two methods for dynamic chemical shift encoding enabled in our imaging sequence, single-band spectral-spatial excitation [20] and IDEAL encoding [21], were both applied to HP pyruvate imaging within a few years of the initial reports demonstrating the ability of this agent to resolve metabolism *in vivo* [68–70]. To this day, both methods are still among the most widely used imaging strategies for time-resolved HP imaging of pyruvate and other metabolic agents. Although there are significantly different considerations in implementing these two chemical shift encoding methods for a particular HP experiment on a specific MRI system, they are both unique among

HP MRSI strategies in that they perform chemical shift encoding in a manner that is decoupled from the method of spatial encoding. It is therefore notable that to date — despite multiple studies comparing acquisition strategies for metabolic HP MRI [106, 163] — a direct quantitative comparison of spectral-spatial excitation and IDEAL encoding that fully accounts for the different HP magnetization usage between these methods has not been reported in the literature.

In this section, we will compare the single-band spectral-spatial excitation and IDEAL imaging methods designed for preclinical imaging of HP pyruvate and lactate at 7 T in terms their SNR performance in numerical simulations and phantom experiments. A fair comparison of HP image SNR for these two methods must properly account for the fraction of longitudinal magnetization depleted by each method. If proper RF calibration can be assumed and slice profile imperfections are neglected, a spectrally selective excitation simply reduces the longitudinal magnetization for the excited chemical shift by a factor of $\cos\theta$. However, the multiple broadband excitations applied in quick succession for IDEAL encoding will each experience a progressively smaller longitudinal magnetic moment due to the effects of preceeding excitations. Therefore, we devised a variable excitation angle scheme for multi-excitation IDEAL experiments to provide a constant signal amplitude across echoes and deplete the longitudinal magnetization to a fraction specified by the desired effective excitation angle, neglecting T_1 effects [181]. Individual excitation angles (θ_i) were calculated from a specified effective excitation angle (Θ) imparted by a series of N pulses as:

$$\theta_i = \sin^{-1}\left(\frac{\sin\Theta}{\sqrt{N}M_{z,i-1}}\right) = \sin^{-1}\left(\frac{\sin\Theta}{\sqrt{N}\prod_{j=0}^{i-1}\cos\theta_j}\right) \tag{5.8}$$

In this equation, M_z denotes the relative longitudinal magnetization present after each pulse, normalized to an initial value of 1 prior to the first pulse ($\theta_{j=0} = 0$).

This effective excitation angle describes the overall effect of the series of eight excitations used for IDEAL imaging in a single value that is comparable to the excitation angle of an individual single-band spectral-spatial pulse. It is very important to note that the variable excitation angle scheme described here is different from the variable excitation angle strategies typically used in HP MRI. Most often, these strategies

modulate the excitation angles over the imaging time points of a dynamic experiment to attempt to more reliably observe products of metabolism, accounting for RF losses, T_1 decay, perfusion and metabolic conversion [160, 161]. The variable excitation angle scheme outlined in equation 5.8 accounts only for the effects of prior RF losses within a train of pulses applied so rapidly that other effects are negligible.

Numerical Simulation of Chemical Shift Encoding

In numerical simulations comparing spectral-spatial pulses and multi-excitation IDEAL encoding, raw k-space data for a field strength of 7 T were synthesized for a numerical phantom consisting of ^{13}C urea and the five chemical shifts most commonly observed for *in vivo* imaging of [1-^{13}C]pyruvate (table 5.1). The layout of this numerical phantom is shown in figure 5.16 (center row), with each shift having a real magnitude of 1. For spectrally-selective excitations, a perfect single-band excitation profile was assumed for the target metabolite. IDEAL data were synthesized by summation of complex k-space data for all metabolites at eight echo times with the echo spacing chosen to optimize the performance of this method for these chemical shifts at 7 T (0.52 ms). The precise TEs for each spectral encoding technique matched those used in the phantom experiments described below. Simulations were conducted for a range of effective excitation angles and T_2^* time constants, and repeated 100 times for each variance of complex zero-mean Gaussian noise in k-space.

Thermal Phantom Simulation of Chemical Shift Encoding

^{13}C urea doped with gadolinium was imaged using both chemical shift encoding strategies with various effective excitation angles. A single 10 mm NMR tube containing the urea solution was imaged in the center of the 4 x 4 cm^2 FOV using the flyback EPI trajectory shown in figure 5.10 for spatial ^{13}C encoding (16 x 16 matrix, 20.833 kHz readout bandwidth, 868 Hz phase bandwidth). To simulate chemical shift encoding, either the 1 cm flyback spectral-spatial RF pulse designed for selective imaging of pyruvate and lactate was used (figure 5.9), or IDEAL imaging was performed by acquiring eight time-shifted readouts (figure 5.5). In the IDEAL scans a 1.6 ms (5000

Hz) Shinnar Le-Roux (SLR) calculated RF excitation with 1 cm slice width was used. The first TE for IDEAL imaging was 11.5 ms and the TE for spectral-spatial excitation images was 14 ms, with each of these TEs corresponding to the minimum possible value. In both experiments, imaging data were collected for effective excitation angles ranging from 10 to 90 degrees in 10 degree increments. At each effective excitation angle, data acquisition was repeated eight times with a 10 second repetition time to allow full spin-lattice recovery of the ^{13}C signal. (For this phantom, the ^{13}C urea T_1 was measured to be approximately 1.6 s in a saturation recovery experiment.)

The results of both numerical and phantom simulations are summarized in figure 5.16. Nearly identical theoretical SNR performance is seen with these two chemical shift encoding strategies for HP imaging. At very large T_2^* values spectrally selective excitations provide a slight improvement in SNR over IDEAL as measured by the mean SNR in simulation, however at no set of simulation parameters were the SNRs of these two chemical shift encoding methods separated by more than one standard deviation about their respective means. Under the conditions of a typical preclinical HP imaging experiment, which is often conducted through dynamic imaging at low excitation angles to observe substrate uptake and metabolic conversion, no significant difference in SNR performance between spectrally selective excitations and IDEAL decomposition was observed in numerical simulations.

Images of the thermally polarized ^{13}C urea phantom are shown in the bottom row of figure 5.16, with the mean phantom SNR plotted as a function of effective excitation angle alongside numerical simulation data in the top left plot. These phantom images showed ^{13}C signal only for the on-resonance decomposed IDEAL chemical shift offset. Both chemical shift encoding methods show the expected sinusoidal trend in image SNR with increasing excitation angle, and these phantom data are congruent with the numerical simulation results for a T_2^* of 20 ms and k-space noise variance of 0.09. At an effective excitation angle of 20 degrees, the ^{13}C images shown in the bottom row of figure 5.16 exhibit SNRs of 8.6 ± 0.47 and 8.7 ± 0.50 (mean $\pm$ standard deviation) for spectral-spatial excitation and multi-excitation IDEAL encoding, respectively.

At each effective excitation angle used in phantom experiments, the eight measured
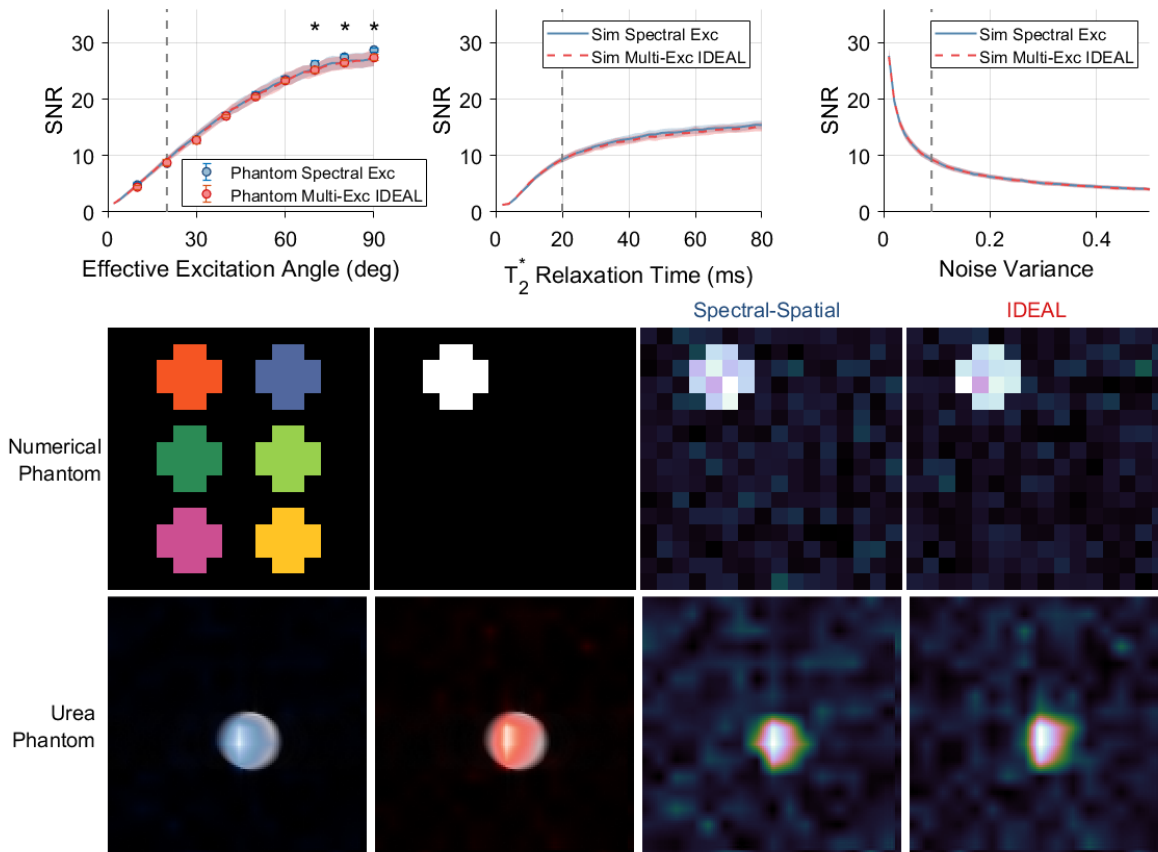
Figure 5.16: Single-band spectral-spatial excitation and multi-excitation IDEAL imaging provide equivalent SNR performance for HP pyruvate and lactate imaging at 7 T. The mean output SNRs for a single metabolite is summarized as a function of numerical simulation parameters in the plots in the upper row, with lines and shaded regions denoting one standard deviation about the mean. Vertical dashed lines indicate the value of each parameter used when plotting other parameters and displaying representative images of the numerical phantom (center row). Images from a thermal ^{13}C phantom corresponding to 20 degree effective excitations are shown in the bottom row, alone and as overlays on ^1H images. SNR values were measured in eight repetitions of this phantom imaging experiment at various effective excitation angles, and are plotted with numerical simulation results in the upper left. Phantom data show a significantly lower SNR for IDEAL at effective excitation angles ≥ 70 degrees (* $p < 0.05$, two-sample t-test), however the effect size is minuscule and not practically meaningful.

SNR values for each encoding method were compared using the two-sided two-sample t-test assuming equal variances. At a significance level of 5%, this analysis demonstrates that the SNR obtained through multi-excitation IDEAL imaging is lower than that of spectral-spatial imaging for effective excitation angles of 70 degrees or greater. This result could be attributed to multiple causes, including slight errors in RF power calibration or RF saturation effects that vary along the slice profile [182]. In any case, this effect is very unlikely to impact the decision of whether to use IDEAL for HP imaging in practice. Since a SNR difference is only observed at large effective excitation angles that are rarely used in HP imaging, and since the magnitude of this difference is quite small (<5%), we conclude that both numerical and phantom simulation results demonstrate that the SNR performance of spectral-spatial and IDEAL imaging are effectively equivalent for HP pyruvate and lactate imaging on our preclinical MRI system.

5.6 Validation of HP Imaging Methods

The suitability of both chemical shift encoding methods for imaging of HP pyruvate and lactate were evaluated in a LDH enzyme phantom and *in vivo* imaging of the murine kidney. The LDH phantom provides a controlled environment in which the localization of HP signals can be predicted *a priori*, while mouse kidney imaging entails the greater complexities of HP imaging in a living system.

LDH Phantom Experiment

The spatial fidelity of IDEAL and single-band spectral spatial excitations was tested in phantom experiments using lactate dehydrogenase (LDH) to catalyze the conversion of pyruvate to lactate [183]. The phantom consisted of a 50 mL conical tube containing doped water into which two 2 mL cryovials were inserted. One cryovial was prefilled with 1 mL of a solution containing 40 U/mL LDH (Worthington Biochemical, Lakewood, NJ) and 10 mM NADH (Sigma Aldrich, St. Louis, MO) dissolved in 0.2 M pH 7.6 TRIS buffer (Sigma Aldrich, St. Louis, MO). The other cryovial was prefilled with

1 mL of the TRIS buffer solution. 1 mL of 20 mM HP pyruvate produced using an HyperSense Polarizer (Oxford Instruments, Abingdon, England) was injected manually into both cryovials simultaneously after the start of each dynamic acquisition, resulting in a final concentration of 20 U/mL LDH, 5 mM NADH and 10 mM pyruvate in the vial containing LDH solution.

A 5 mm NMR tube containing concentrated doped ^{13}C urea was placed adjacent to the LDH phantom for calibrating the ^{13}C frequency and RF transmit power. Because of the strong HP ^{13}C signal observable with this phantom, the 72 mm ^{1}H/^{13}C volume resonator was used for both ^{13}C signal excitation and reception. HP images were acquired for 90 repetitions with a 2 second TR to sample dynamics of pyruvate delivery and conversion to lactate. At the start of each repetition, a 5 degree excitation was applied using the same RF pulse shape and slice gradient as IDEAL imaging to acquire a FID (1.6 ms, 5 kHz SLR calculated pulse). These slice spectra were averaged over time to determine the precise frequencies of pyruvate, lactate, pyruvate-hydrate and urea in IDEAL decomposition and for off-resonance correction of imaging data. Neglecting these 5 degree FID excitations, the effective excitation angle on pyruvate and lactate for both encoding methods was 20 degrees. For spectral-spatial excitations, a Gaussian saturation pulse (6.58 ms, 417 Hz) was applied at the urea frequency without slice localization just before lactate imaging. A ^{1}H RARE image was acquired after the HP ^{13}C scan with the same FOV and slice position to demonstrate the spatial context of ^{13}C images. HP ^{13}C imaging experiments were conducted once for each chemical shift encoding method, cleaning and replacing the LDH phantom inbetween experiments.

Images from this LDH phantom study demonstrate that both chemical shift imaging strategies evaluated in this work can be used for selective imaging the HP pyruvate and lactate. As shown in figure 5.17, similar HP imaging signal trends are seen in images acquired with spatial-spectral excitations and multi-excitation IDEAL. In these experiments, strong HP pyruvate signal is evident in both vials of our phantom, with lactate production observed only in the vial preloaded with the LDH enzyme and NADH cofactor. While the absolute SNR of LDH phantom images acquired with spectral-spatial excitations is greater than in IDEAL images, it would not be appro-
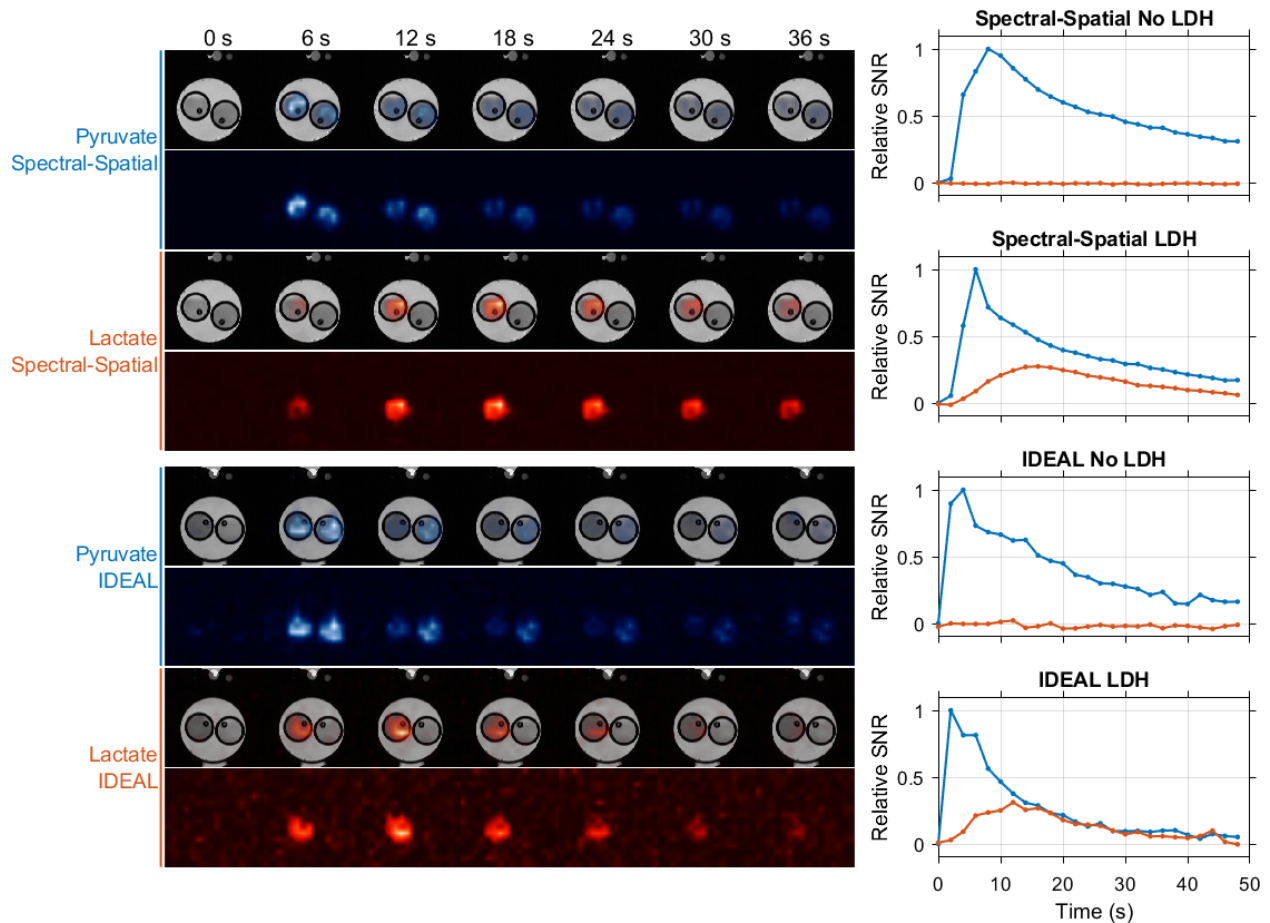
Figure 5.17: The spatial fidelity of both chemical shift imaging methods used in this work was evaluated in LDH enzyme phantom experiments. In these experiments only the vials seen on the left side of these images were preloaded with LDH and NADH, which catalyzed production of lactate when HP pyruvate was injected simultaneously into both vials. HP signal is plotted over time for a voxel at the center of each vial, showing similar substrate delivery and conversion trends for spectrally selective excitations and multi-excitation IDEAL imaging, with lactate signal confined to the vial containing LDH.

priate to attempt a quantitative comparison of these data (N = 1). Variations in the absolute pyruvate polarization fraction between dissolutions and in both the rate and precise amount of pyruvate delivery by manual injection preclude the conclusion that there is any difference in SNR for these two encoding methods in equivalent HP experiments. Nonetheless, these results demonstrate that both chemical shift imaging methods provide spatial fidelity appropriate for small animal imaging when used with the single-shot flyback EPI trajectory used in this work.

Mouse Kidney Experiment

Two healthy BALB/c mice were imaged using identical sequence methods to those described above for the LDH phantom experiment, with additional higher-order shimming applied to the isocentric 1 cm slice prior to HP imaging. The 20 mm ^{13}C receive surface coil was placed carefully over the left kidney on the posterior side of the animal and its positioning relative to internal anatomy and magnet isocenter was verified through ^{1}H imaging. The dynamic HP imaging sequences were initiated at the moment of dissolution, acquiring HP pyruvate and lactate images for the full lifetime of the HP signals *in vivo* following manual injection of 200 µL of 80 mM HP pyruvate via tail vein catheter. Each animal's respiration was monitored continuously and anesthesia was effected and maintained using 2-4% isoflurane delivered via nose cone.

Figure 5.18 depicts the slice positions, time-averaged HP pyruvate and lactate images, and HP signal time courses for selective voxels from each experiment. As expected, images from both encoding strategies show a very intense pyruvate signal from the voxel containing large blood vessels in the center of the abdominal cavity such as the inferior vena cava and abdominal aorta. Weaker HP pyruvate signal is observed for the voxel containing kidney parenchyma. The delay and dispersion of the pyruvate bolus as it passes through smaller blood vessels cause the signal from this voxel to reach a peak at later time points and persist longer than pyruvate within the vascular voxel. HP lactate signal is seen primarily within the kidneys, following delivery of pyruvate to this tissue.

In contrast to the LDH phantom imaging shown in figure 5.17, IDEAL imaging
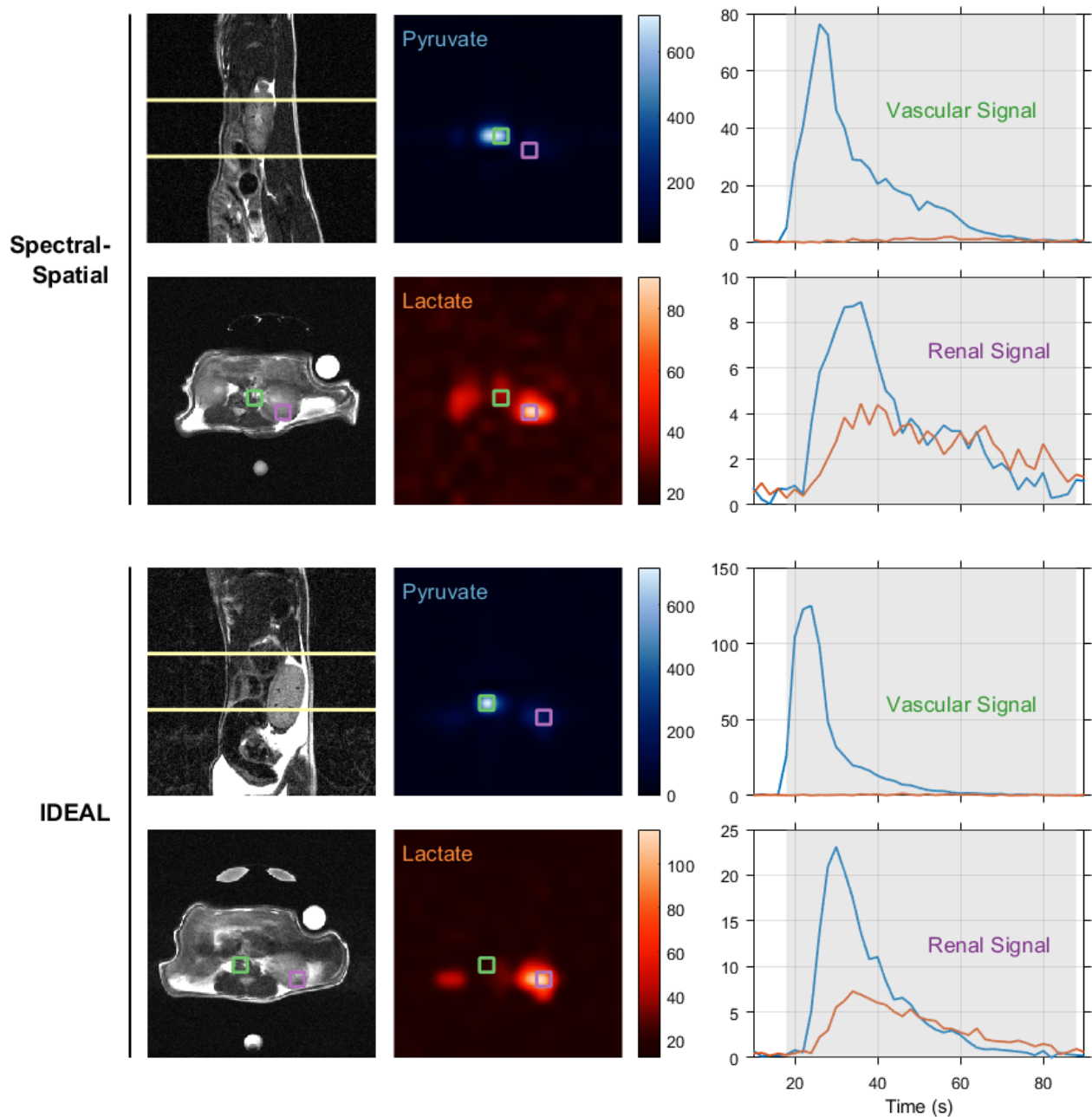
Figure 5.18: Renal pyruvate uptake and metabolism were imaged in healthy BALB/c mice using spectral-spatial excitation (upper panels) and multi-excitation IDEAL (lower panels). HP images in the central panel are bilinearly interpolated to the resolution of the axial proton images (lower left) and summed over time, with native resolution voxels containing a large blood vessel and kidney parenchyma outlined in green and purple, respectively. The HP signals for these vascular and renal voxels are plotted over time on the right, and the shaded portion of these plots indicate the time points summed in the HP images. All images depict a 4 x 4 cm^2 FOV.

provides greater SNR than spectral-spatial excitation in these animal experiments. However, no definitive conclusions can be drawn from these data (N = 1) on the relative performance of the two encoding methods, for all of the reasons described above in the context of the LDH phantom experiment as well as the additional variability inherent to metabolic HP imaging in living systems. While this mouse study lacks statistical power, it clearly demonstrates the capacity of our imaging methods to resolve real-time metabolism *in vivo*.

5.7 Conclusion

We have developed an imaging method for preclinical HP ^{13}C imaging and quantitatively compared the imaging approaches enabled in this pulse program. In comparing the two spectral encoding strategies written into this imaging method, multi-excitation IDEAL and spectrally selective excitations, we found in numerical simulations that both provide equivalent performance for HP imaging when the same amount of longitudinal magnetization is depleted. In phantom experiments we demonstrate the spatial fidelity of the image encoding strategies enabled by our method in a system that recreates the primary enzymatic reactions this imaging technique seeks to quantify *in vivo*. We further demonstrate the suitability of our specific methods to imaging HP pyruvate and lactate in small animals through experiments demonstrating uptake and metabolism in the murine kidney.

MRI scan parameters must be set carefully to provide optimal performance for a given experiment. This is particularly important for HP MRI due to the non-renewable nature of the imaging signal and the relatively low amplitude of signals produced via metabolic conversion in vivo. Quantitative evaluation of methods for encoding position and chemical shift is therefore critical for HP MRI. Previous work by Durst, et al. compared various chemical shift readout methods for HP ^{13}C imaging on a clinical 3 T system in extensive simulation, phantom and animal experiments [106]. While this study included a thorough comparison of traditional CSI, EPSI and IDEAL imaging using spiral readouts, spectrally selective excitations were not considered as an

option for encoding chemical shift nor was EPI used for spatial encoding. A separate study by Schulte, et al. focused on the evaluation of spectral-spatial excitation imaging at 3 T with a 15 degree excitation angle on pyruvate and saturation of downstream metabolites [136]. This study included a SNR comparison of this specific spectral-spatial imaging strategy to IDEAL encoding with seven 10 degree excitations in a rat tumor model. For the four animals imaged, greater mean peak SNR was observed for pyruvate using IDEAL compared to spectral-spatial imaging. The opposite result was seen for lactate and other downstream metabolites, where 90 degree spectral-spatial excitations provided superior SNR than IDEAL imaging. These results are consistent with ours, since the effective excitation angle for all metabolites in their method of IDEAL imaging ($\approx$26 degrees) is greater than the 15 degree spectral-spatial excitation angle applied to pyruvate, but much lower than the 90 degree spectral-spatial excitation angle applied to downstream metabolites. Additionally, due to differences in physiology, HP sample polarization and magnetization usage, these data provide only a very limited comparison of IDEAL and spectral-spatial imaging. Our results provide a robust quantitative evaluation of these alternative encoding techniques for preclinical imaging at 7 T.

The simulation and phantom experiments presented here demonstrate the relative performance of these imaging techniques on our preclinical 7 T MRI system. Different results could be expected if the same imaging methods were evaluated on a system operating at another field strength, or with different gradient capabilities and RF coils. Due to the variety of imaging applications possible with HP ^{13}C agents, we can make no general recommendations for use a specific imaging technique. The methods presented here can be adapted to evaluate the ^{13}C imaging techniques available in a given experiment to compare their performance on the specific hardware that is to be used.

In comparing single-band spectral-spatial excitations to multi-excitation IDEAL for spectral encoding, there are several practical distinctions that are worth noting. The longer total chemical shift encoding time required in IDEAL increases the chance of artifacts from physiological motion in these images. Depending on the organ of interest,

these motion effects can be mitigated by physiological gating of the image acquisition [184], however this gating can place strict limitations on the ability to dynamically measure HP signal evolution. For spectral-spatial imaging, reliable signal excitation depends on proper setting of the frequency offset so that the chemical shift of interest falls in the passband of the pulse's frequency response. If set incorrectly, the chemical shift may occur at the edge of the passband and experience a reduced excitation angle, or outside of the passband and not be detectable. This can be particularly problematic for HP imaging with narrowband pulses since this frequency offset must be set before the signals of interest are present. For IDEAL encoding, the wide bandwidth of the RF pulse used is typically sufficient to consistently excite all chemical shifts present, however the constant excitation gradient will impart positional shifts in the slice direction that vary across chemical shift offsets [185]. This effect can become significant when using IDEAL with thick slices [107] and when decomposing images for chemical shifts separated by large frequency offsets. Lastly, it should also be noted that the two chemical shift encoding strategies used here are not mutually exclusive. Multi-band excitation pulses can easily be used to control the chemical content of signals encoded with IDEAL [184] or other spectroscopic readouts such as EPSI [159]. This combination of chemical shift encoding in both excitation and readout provides methodological flexibility that is very useful in studies of novel HP preparations [90].

In conclusion, our imaging method provides flexibility in the choice of encoding methods for position and chemical shift and is readily adaptable for use in various hyperpolarized imaging experiments. We have made the source code for this method and for the reconstruction of images acquired with the techniques presented in this work available online (https://github.com/mda-mrsl/PV6-HPMR). Readers who conduct hyperpolarized and other specialized imaging experiments on Bruker MRI systems are invited to adapt this method for their needs.

Chapter 6

Hyperpolarized [2-^{13}C]Dihydroxyacetone

[2-^{13}C]Dihydroxyacetone (DHA) is a relatively new HP agent that has been applied primarily in studies of hepatic metabolism. As discussed briefly in section 3.2, *ex vivo* studies of perfused mouse livers [91] and *in vivo* measurements of hepatic activity in rats [92] have demonstrated that many of the products of HP DHA metabolism are sensitive to acute changes in nutritional state. When introduced to the liver through the blood, HP DHA is quickly taken up by hepatocytes and can provide non-invasive measurements of chemical flux through glyceroneogenic, glycolytic and gluconeogenic metabolism. In addition to these previously reported biochemical products, a chemical signal produced from HP DHA *in vivo* was preliminarily identified as a product of ketogenic metabolism in the course of the experiments outlined in this chapter.

In this chapter we will review the rationale for measuring the hepatic metabolism of HP DHA in the context of liver disease and present our studies investigating DHA metabolism in the healthy rat liver via MR spectroscopy and imaging.

6.1   Metabolic Liver Disease

The liver is arguably the most biochemically complex organ in the mammalian body. Apart from the liver's many vital roles in synthesizing bile, cholesterol, and albumin; in storing vitamins and minerals; and in breaking down drugs and alcohol, this organ also performs irreplaceable functions in the systemic metabolism of proteins, carbo-

hydrates and lipids [71].

In the fed state, hepatocytes take up glucose and other monosaccharides and convert them into glycogen for storage or into fatty acids. Within hepatocytes these fatty acids, which are also derived partly from uptake of dietary lipids, have three main biochemical fates [186]. They may be oxidized to produce acetyl-CoA that provides cellular fuel via the TCA cycle, or combined with glycerol to form triglycerides that are subsequently either condensed into intracellular lipid droplets or packaged into specific lipoproteins for export and delivery to peripheral tissues. Notably, hepatocytes are the primary site of *de novo* synthesis of lipids and fatty acids in the mammalian body. Adipose tissue can also generate lipids from carbohydrate sources, but additionally uptakes fatty acids from circulating lipoproteins.

In the fasted state, hepatocytes alter their metabolism of carbohydrates and lipids to support systemic metabolic requirements. Glycogen stores are broken down and glucose is exported. As glycogen stores become depleted, the liver and most other organs (apart from the brain) rely less on the oxidation of carbohydrates and more on fatty acids to meet their energetic needs. These fatty acids are supplied primarily by break down and mobilization of triglycerides stored in adipose tissue, but hepatocytes may also utilize the triglycerides stored within intracellular lipid droplets for their metabolic fuel. The glycerol liberated from the breakdown of triglycerides in adipocytes and hepatocytes is used in the liver for gluconeogenesis, yielding glucose that is exported.

Hepatocytes also utilize several other carbon sources to support gluconeogensis, including circulating pyruvate, lactate, and alanine, all of which must be converted to the TCA cycle metabolite oxaloacetate for gluconeogenesis. In prolonged fasts and uncontrolled metabolic diseases, the gluconeogenic depletion of oxaloacetate in hepatocytes prevents the acetyl-CoA produced by fatty acid oxidation from entering the TCA cycle and providing cellular fuel. The resulting accumulation of acetyl residues in hepatocytes is handled by condensing them in a series of reactions to form acetoacetate, which frees the CoA needed to oxidize fatty acids. Acetoacetate may spontaneously form acetone by non-enzymatic decarboxylation, and also rapidly interconverts en-

zymatically with β-hydroxybutyrate (βHB). These three metabolites are the primary products of ketogenic metabolism and are known collectively as ketone bodies.

The conversion of acetoacetate to βHB occurs via the reaction catalyzed by the enzyme βHB dehydrogenase, which restores NAD^+ from NADH as in the reaction catalyzed by LDH. Ketone bodies are highly mobile in tissue, and the mitochondria in hepatocytes do not contain enzymes necessary for ketolysis, the process of utilizing these metabolites as cellular fuel [187]. These ketone bodies are therefore exported by the liver, primarily under fasted conditions in which they are a vital cellular fuel source for the brain, which cannot utilize circulating fatty acids due to their inability to cross the blood-brain barrier. However, even in the liver of healthy fed mammals, ketogenic flux is essential in providing substrates for anabolic pathways such as cholesterol synthesis, and plays a very important role in preventing the build-up of reactive oxygen species from oxidative metabolism [188].

Hepatic metabolism through glycolytic, gluconeogenic, glyceroneogenic and ketogenic pathways is dysregulated in many common diseases. Recent studies have shown that hepatocellular carcinomas can gain the capacity to utilize ketone bodies as cellular fuel, and this re-activation of ketolysis correlates with higher rates of mortality in patients [189]. Non-alcoholic fatty liver disease (NAFLD) is a very common metabolic disorder associated with obesity and diabetes. By some estimates, as much as 40% of adults in the United States have NAFLD, with a yearly economic burden greater than $100 billion [190]. Most individuals with NAFLD are asymptomatic and exhibit only hepatic steatosis, the accumulation of triglyceride droplets in hepatocytes that does not impair liver function. However, in a some individuals this condition progresses to non-alcoholic steatohepatitis (NASH), in which inflammation and fibrosis of the liver progressively diminish hepatic function. NASH can further lead to cirrhosis and the development of hepatocellular carcinoma. NASH is predicted to become more prevalent in coming years, supplanting viral hepatitis as the leading indication for liver transplant [191].

The metabolic mechanisms underlying the progression of NAFLD are currently not well understood. While comorbidities such as obesity and diabetes are associated

with progression and worse outcomes, the biochemical etiology of NAFLD is complex and variable in different individuals [192]. Recent work has demonstrated that disruption of glycerol metabolism [193] and of mitochondrial ketogenesis [194, 195] are important in the development and progression of NAFLD in patients. However, the lack of methods for directly assessing these metabolic processes non-invasively is a significant barrier to the formulation of treatments that target the biochemical origins of NAFLD development and progression. Currently, no pharmacological treatment exists for managing NAFLD and therapies typically seek to manage comorbidities through lifestyle changes (i.e. diet and exercise) [196]. The gold-standard method for diagnosis and staging of NAFLD is liver biopsy, however this is a very invasive surgical procedure that is not suitable for monitoring disease progression [197]. Non-invasive imaging can quantify hepatic fat content via MRI or tissue stiffness via elastographic MRI or ultrasound, but these methods are sensitive to the outcomes of NAFLD progression (steatosis and fibrosis) and not the underlying biochemical causes.

In this context, the simultaneous measurement of flux through glycolytic, gluconeogenic and glyceroneogenic metabolism that HP DHA has been shown to provide has tremendous potential to elucidate the mechanisms of NAFLD progression, which would be instrumental in devising improved methods for non-invasively staging and for therapeutically managing this very common disease.

6.2 Hyperpolarized [2-¹³C]Dihydroxyacetone Spectroscopy

Previously identified metabolic products of HP DHA are shown in figure 6.1. DHA is rapidly taken up from circulation by hepatocytes, however the precise cellular transporters responsible for bringing DHA into the cytosol are not known. Once in the cell, DHA is phosphorylated to dihydroxyacetone phosphate (DHAP), which is an important glycolytic intermediate that is rapidly and reversibly isomerized into glyceraldehyde-3-phosphate (GA3P) by the enzyme triose phosphate isomerase. DHAP may also be reduced to form glycerol-3-phosphate (G3P) in an enzymatic reaction in which NADH is oxidized. Conversion of DHAP to GA3P introduces the ¹³C label to glycolytic and
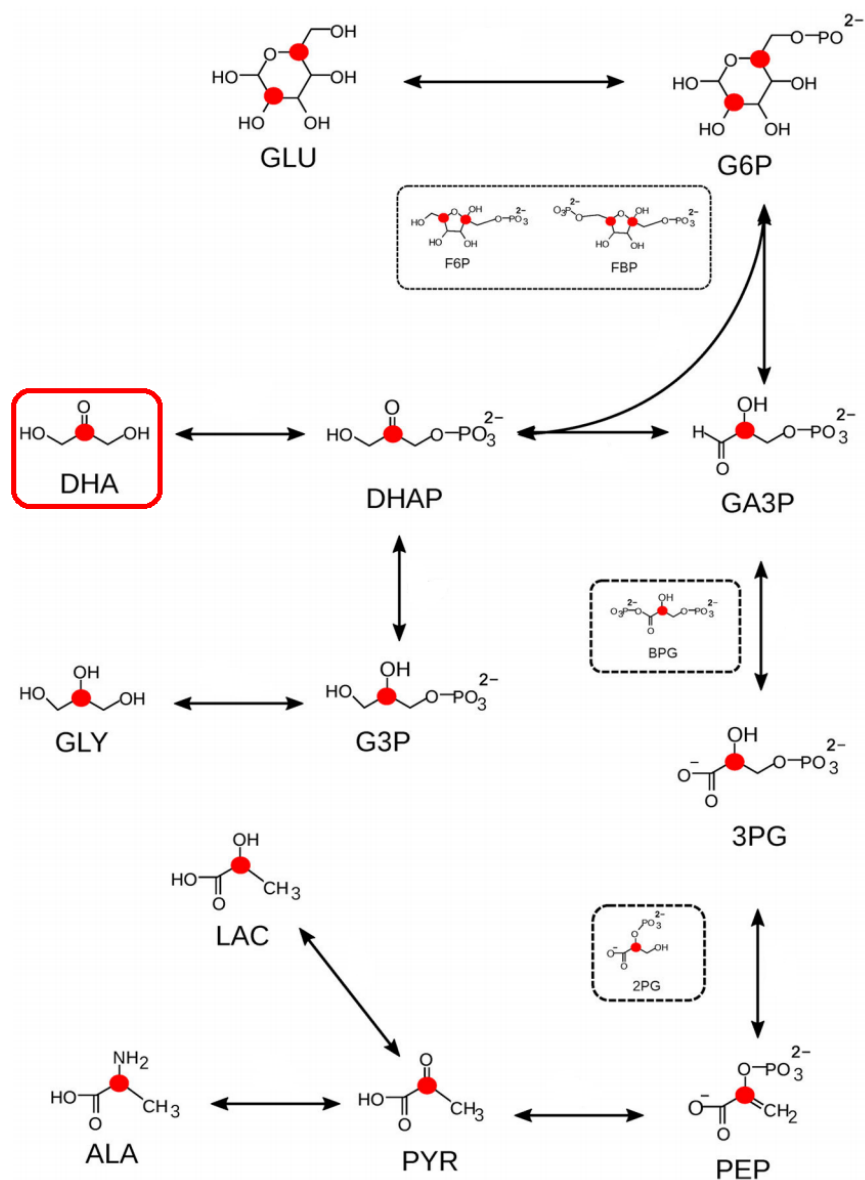
Figure 6.1: Previously reported chemical endpoints observed following HP DHA infusion in the isolated mouse liver are shown in this diagram. Colored circles indicate sites of ^{13}C enrichment, and the DHA precursor is highlighted by a red box. DHA undergoes rapid cellular uptake and phosphorylation to form DHAP, which then quickly enters glyceroneogenic, gluconeogenic and glycolytic pathways. The real-time and simultaneous measurement of chemical flux through multiple biochemical pathways provides broad insight into the metabolic state of the liver.

Figure adapted with permission from Alexander Kirpich, et al. Kinetic Analysis of Hepatic Metabolism Using Hyperpolarized Dihydroxyacetone. *J Chem Inf Model* 2019; 59(1): 605-14. doi:10.1021/acs.jcim.8b00745. Copyright © 2019 American Chemical Society.

gluconeogenic pathways, while reduction to G3P probes the pathway responsible for glycerol synthesis.

While the many chemical endpoints of HP DHA illustrated in figure 6.1 are observable *ex vivo* in perfused livers scanned on high-resolution NMR systems, relatively few of these signals are measurable *in vivo*. In particular, the products of the initial chemical transformations of HP DHA in the cell are observable, but are unfortunately not very well-resolved through *in vivo* MR spectroscopy. The ^{13}C chemical shift of DHAP is not distinguishable from the HP DHA precursor [91]. Without heteronuclear decoupling, the GA3P and G3P signals occur as overlapping doublets due to covalent bonding of the HP ^{13}C nuclide to ^{1}H. While proton decoupling can be used to improve the separability and detectability of G3P and GA3P [198], we did not have the capability to utilize this method on our preclinical MRI system for the experiments presented in this chapter. The only chemical end points previously reported from HP DHA *in vivo* are G3P, GA3P and phosphoenolpyruvate (PEP). In contrast to G3P and GA3P, PEP appears as a well-resolved singlet signal. In the very limited reports of *in vivo* HP DHA metabolism currently published, PEP and G3P were shown to be produced with greater intensity in liver tissue than in the kidneys [90]. In a separate study, both PEP and G3P signals were demonstrated to decrease by approximately 50% in the liver ten minutes following infusion of fructose, and this effect was attributed to depletion of ATP and changes in the overall concentration of these glycolytic intermediates in hepatocytes [92].

DHA Preparation and Dissolution

In all of the experiments discussed in this chapter, the dDNP solution was prepared by dissolving [2-^{13}C]dihydroxyacetone dimer (99% isotopic enrichment, Sigma Aldrich Isotec, Miamisburg, OH) at a concentration of 8 M in a 2:1 (by volume) solution of water:DMSO, with the addition of OX063 trityl radical (Oxford Instruments, Abingdon, UK) at a concentration of 15 mM and gadoteridol (ProHance, Bracco Diagnostics, Monroe Township, NJ) at a concentration of 1 mM. HP samples were produced by inserting 40 µL of this solution in a HyperSense system and polarizing for at least 60
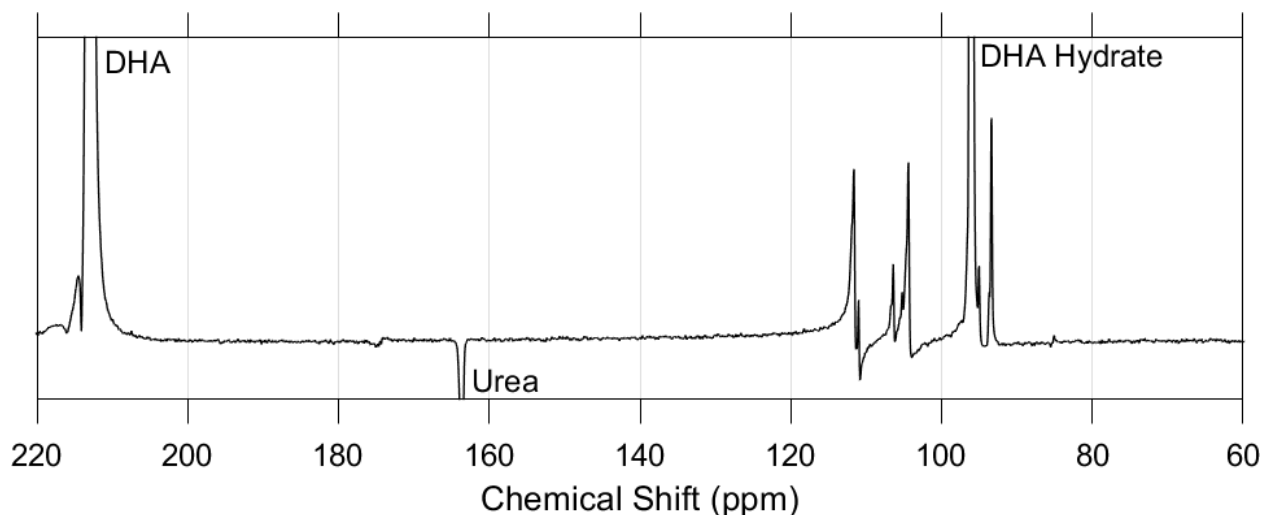
Figure 6.2: Time-averaged dynamic spectroscopy of a syringe containing the HP DHA dissolution depicts several unidentified trace ^{13}C chemical signals. The labeled resonances correspond to HP DHA (212.7 ppm), DHA hydrate (95.7 ppm) and an external urea phantom (164 ppm, inverted peak). Apart from DHA hydrate, signals in the frequency range from 92 to 114 ppm represent unidentified ^{13}C chemical environments, and were observed at similar SNR as products of DHA metabolism *in vivo* 6.4.

minutes prior to dissolution with 4 mL of phosphate buffered saline, resulting in a 80 mM HP DHA solution.

Figure 6.2 depicts the ^{13}C spectrum of a syringe containing this HP DHA solution, acquired using the same dynamic spectroscopy method that is described below for rat experiments. The labeled signals in this figure correspond to HP DHA, DHA hydrate and a thermally polarized ^{13}C urea phantom signal that was used to calibrate the MRI system center frequency and ^{13}C transmit power. Several signals are present in the 92 to 114 ppm frequency range that correspond to unidentified ^{13}C chemical environments. One putative source of these unidentified signals is the intermediate forms present in the self-dimerization reaction that DHA can undergo in solution [199], however they could also correspond to trace ^{13}C impurities present in the DHA sample from the manufacturing process. Chemical assignment of these signals by NMR is difficult since they are not readily detectable in thermally polarized samples, and their precise identification is beyond the scope of this work. In the ^{13}C spectra of the bare DHA dissolution, these unidentified peaks occur with amplitudes around 1% of the HP DHA peak. In the *in vivo* spectra shown in the following subsection,

they appear with approximately the same amplitude relative to DHA as the products of cellular metabolism.

In Vivo HP DHA Spectroscopy

In vivo spectroscopy and imaging of HP DHA have to date been performed only in a few small animal experiments on clinical 3 T MRI systems. In the first use of this agent at 7 T, we collected dynamic spectroscopic data from the rat liver to identify the chemical signals that presented sufficient signal for imaging on our preclinical MRI system. Three healthy fed female Sprague-Dawley rats (approximately 14 weeks old, 260 g) were scanned using dynamic pulse-acquire ^{13}C spectroscopy during intravenous infusion of HP DHA. Animals were anesthetized using 2-4% isoflurane delivered via nose cone and imaged on the same setup described in section 5.1. By placing the 20 mm ^{13}C receive surface coil on the rat's upper abdomen, the effective spatial profile of
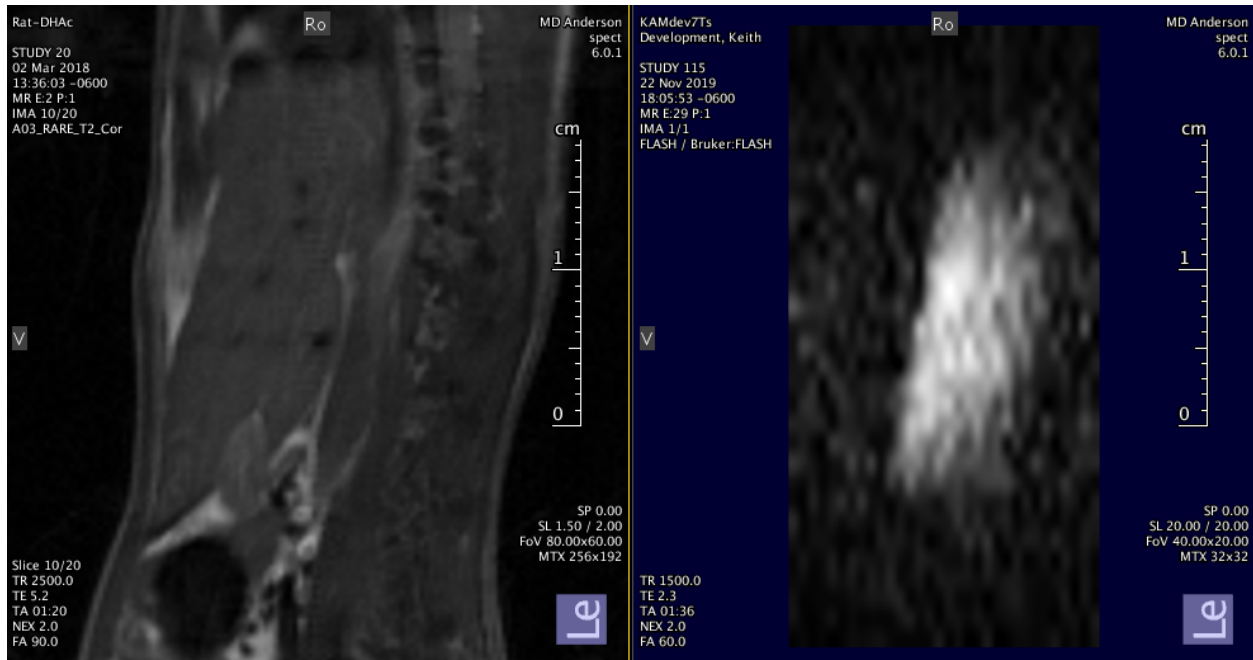
Figure 6.3: Without gradient localization of the excitation pulse, the effective spatial sensitivity profile of ^{13}C images and spectra in this chapter is equivalent to the sensitivity profile of the reception coil. This figure displays that sensitivity profile as measured in a ^{13}C urea phantom of much greater length than the surface coil (right). The effective slice profile matches the position of the rat liver, as shown in a T_2-weighted sagittal image (left).

these ^{13}C measurements was equivalent to this coil's receive sensitivity profile, as illustrated in figure 6.3. This surface coil was positioned carefully on the upper anterior abdomen, and its position relative to internal anatomy was verified in ^{1}H imaging prior to acquiring HP DHA spectra. A doped ^{13}C urea phantom was placed on the receive surface coil for calibration of the MRI system ^{13}C center frequency and RF transmit power, which was delivered via a volume resonator. Approximately 3.5 mL of 80 mM HP DHA ($\approx$ 98 mg/kg), produced as described above, was manually injected via tail vein. The injection was administered rapidly to hydrodynamically enhance delivery of the agent to the liver [200, 201]. A ^{13}C pulse-acquire dynamic spectroscopy scan with a TR of 3 s was initiated at the same moment as the start of the manual DHA injection. A 30 degree, 70 μs (18.3 kHz) hard pulse was used for excitation, followed by a 18.9 kHz, 4096 point spectral readout. Spectra were reconstructed in MATLAB with 15 Hz line broadening, using custom-written tools for phase and baseline correction.

The HP DHA spectra from each rat are shown in figure 6.4, averaged over the first twelve time points. The unidentified resonances present in the HP DHA dissolution itself (92-114 ppm) occur with similar amplitudes as the products of DHA metabolism *in vivo*. The previously reported resonances of PEP, GA3P and G3P were observed in each animal, along with some natural abundance ^{13}C labeling of endogenous fatty acids. Three previously unreported chemical signals were consistently observed at approximately 173, 174 and 181 ppm. Through correlative 2D NMR, we have tentatively identified the last of these signals as the ketone body, [1-^{13}C]β-hydroxybutyrate. The observation of products of ketogenic metabolism has never been reported from HP DHA, nor from any HP agent that enters cellular metabolism as a glycolytic intermediate. If this observation is confirmed, it would be particularly notable that βHB was reproducibly observed in the livers of healthy fed rats, for which ketogenic flux would be expected to be much less significant than in the fasted state. Excluding membrane transport, the molecule carrying the ^{13}C label must undergo at least twelve enzymatic reactions in the cytosol and mitochondrion for HP βHB to be produced from DHA, so its observation within seconds in these dynamic HP DHA experiments would be remarkable.
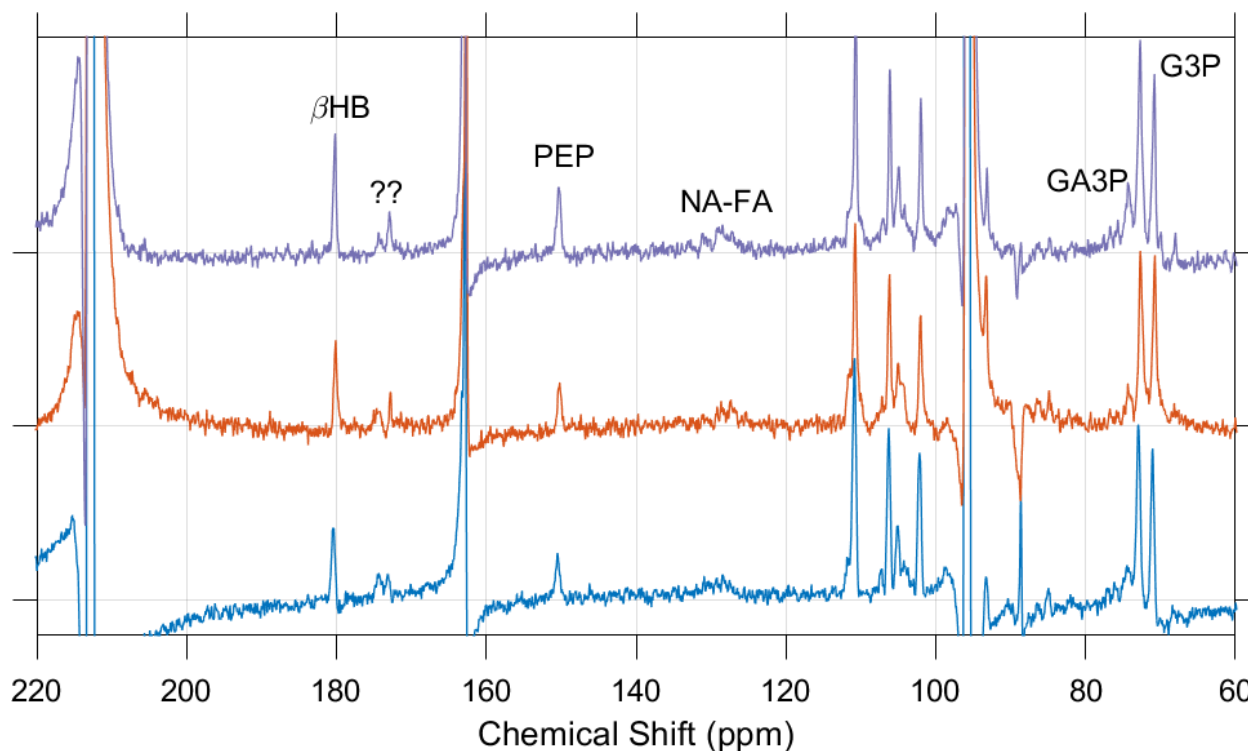
Figure 6.4: Time-averaged spectra of *in vivo* HP DHA metabolism in three normal fed rats demonstrate reproducible hepatic flux of the HP label into PEP, G3P, GA3P and a chemical environment preliminary identified as βHB. Apart from these metabolites and the DHA, hydrate, external urea and impurity signals shown in figure 6.2, HP labeling was apparent in two relatively weak peaks at approximately 173 and 174 ppm. These signals have not yet been definitively assigned. Other very weak HP signals observed in some cases correspond to [2-^{13}C]lactate (69 ppm) and [2-^{13}C]pyruvate (206 ppm), however they are not illustrated in this figure. Thermally polarized ^{13}C signal from natural abundance fatty acids (NA-FA) is detectable in multiple broad peaks around 130 ppm.

The time intensity curves of HP DHA metabolites are shown for a single rat in figure 6.5, along with simple precursor-product ratiometric quantifications of each metabolite in all three rats. With this very limited sample size, no definitive conclusions may be drawn from these data. However, it is notable that the two metabolites produced through the fewest enzymatic reactions of the DHA precursor molecule reach a maximum intensity prior to the peak of the HP DHA bolus, which could indicate saturation of rate-limiting transporters or enzymes. The putative βHB signal persists after its peak longer than the other metabolites, which is consistent with the inability of the hepatocyte to catabolize the ketone bodies it produces and with the
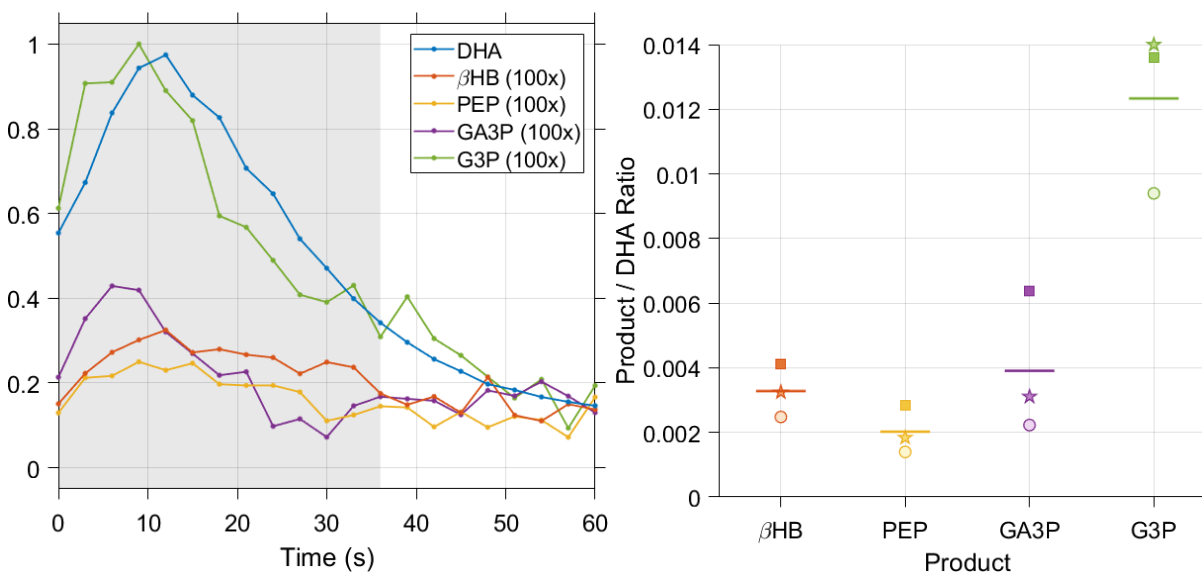
Figure 6.5: HP DHA metabolite time intensity curves and product / precursor ratios demonstrate rapid hepatic uptake and metabolism. The shaded region of the time intensity plot denotes the time points that were summed in calculation of the product / DHA ratios (and in the time-averaged spectra shown in figure 6.4). Note that quantifications of GA3P and G3P in this figure correspond to integrals of one peak of these doublet signals, and were multiplied by 2 for the data shown in this figure.

very high mobility of these molecules in tissue. The ratiometric quantification of each metabolite shown in figure 6.5 illustrate fairly good reproducibility between animals. Relative to one another, the roughly 1:2 amplitude ratio of PEP and GA3P signals in these *in vivo* data are in agreement with previous reports of HP DHA metabolism *ex vivo* in perfused rodent livers [91].

6.3 Hyperpolarized [2-^{13}C]Dihydroxyacetone Imaging

Imaging of the metabolic products of HP DHA is difficult due in part to the wide spectral range of these signals, which spans more than 150 ppm (>11 kHz at 7 T). Slice selection and spectroscopic readout encoding of chemical shifts with such a wide range of frequencies is extraordinarily challenging. Using the non-localized broadband excitation method and receiving ^{13}C signal from liver tissue through the precisely positioned surface coil as described in the previous subsection obviates the need for slice selection, however the high complexity of the spectra shown in figure 6.4 makes it very

difficult to simultaneously encode spatial and spectral information during signal read-out. For the same spectral resolution shown in these *in vivo* spectra, traditional CSI readouts of >200 ms duration are necessary, with repeated excitation to separately encode spatial frequencies. EPSI can be used to accelerate the simultaneous encoding of frequency and position, however this generally comes at the expense of degraded spectral resolution.

Prior work imaging HP DHA metabolites has only demonstrated the feasibility of doing so at 3 T, where the metabolic signals occur over a significantly narrower frequency range. While the reduced spectral width makes broadband slice-selective excitation and spectroscopic readout easier at 3 T, a drawback of conducting DHA experiments at lower field strengths is the reduced separation of metabolites of interest relative to one another. In particular, the GA3P signal often becomes indistinguishable in tissue from the larger and overlapping G3P signal at this field strength. Only two HP DHA imaging experiments have been reported in the literature to date. In one study, narrowband excitation and IDEAL encoding were used only for imaging of the DHA hydrate singlet and G3P doublet in the rat liver, covering a spectral range of roughly 20 ppm [174]. The other study utilized specialized multiband spectral-spatial excitations designed primarily for selective excitation of PEP and G3P [90], with accelerated encoding of the high spectral bandwidth using compressed sensing EPSI [202]. These imaging methods would require significant revision for use on our 7 T MRI system, and would still overlook the resonance we have identified as βHB that we were particularly interested in imaging.

In Vivo HP DHA Imaging

In order to demonstrate the feasibility of imaging HP DHA metabolites at 7 T, we chose to adapt the imaging sequence we developed in chapter 5 for single time point imaging. The same hardware setup described above for *in vivo* DHA spectroscopy was used, with narrowband chemically selective excitations and spatial encoding only in the axial plane during signal readout. Without gradient localization during RF excitation, the effective slice profile of these images in the rostral-caudal direction is

equivalent to the spatial sensitivity profile of the ^{13}C receive surface coil, shown in figure 6.3. A 300 Hz (9.13 ms) Gaussian excitation pulse was used to minimize off-resonance effects, and the center frequency of the scanner was iterated through the resonant frequencies of DHA, DHA hydrate, G3P, PEP, βHB and an external urea phantom. The scan was started approximately 10 seconds after injection in order to acquire images at the moment of maximum HP signal, as determined from dynamic ^{13}C pulse-acquire spectroscopy performed in the same animal approximately 24 hours before the imaging experiment. For snapshot imaging of these fairly weak metabolic signals, 90 degree excitation angles were applied to maximize image SNR and the minimum possible time elapsing between excitations was used. The imaged chemical shifts, and their corresponding spectral excitation frequencies, were determined based on their observability in this prior spectroscopic measurement as depicted in figure 6.6. Using this method, selective excitation of individual chemical shifts is performed for all imaging bands except for G3P and GA3P, which occur as overlapping doublets in the same excitation band.

The animal preparation and injection protocol for this imaging experiment was identical to that described above for dynamic DHA spectroscopy. A 6 x 6 cm^2 flyback EPI readout with a 24 x 24 imaging matrix was designed using the tools outlined in chapter 5 and used for in-plane spatial encoding of each chemically selective excitation band. This EPI trajectory sampled the center of k-space at a TE of 17.8 ms, and had a total duration of 23.95 ms, a readout bandwidth of 31.25 kHz and an echo spacing of 0.992 ms. The raw k-space data were filtered with a 2D Hann window prior to iDFT. For display and registration with ^{1}H images, ^{13}C images were bilinearly interpolated to a 192 x 192 image matrix.

^{13}C images for each of the six excitation bands illustrated in figure 6.6 are shown in figure 6.7, overlaid on anatomical ^{1}H FLASH images acquired during the same HP imaging study. The DHA, DHA hydrate and βHB excitation frequency bands depict imaging signals localized to the region of large hepatic blood vessels, illustrating the rapid uptake and metabolism of DHA *in vivo*. Imaging of the external ^{13}C urea phantom depicts the spatial fidelity of our encoding methods for singlet signals.
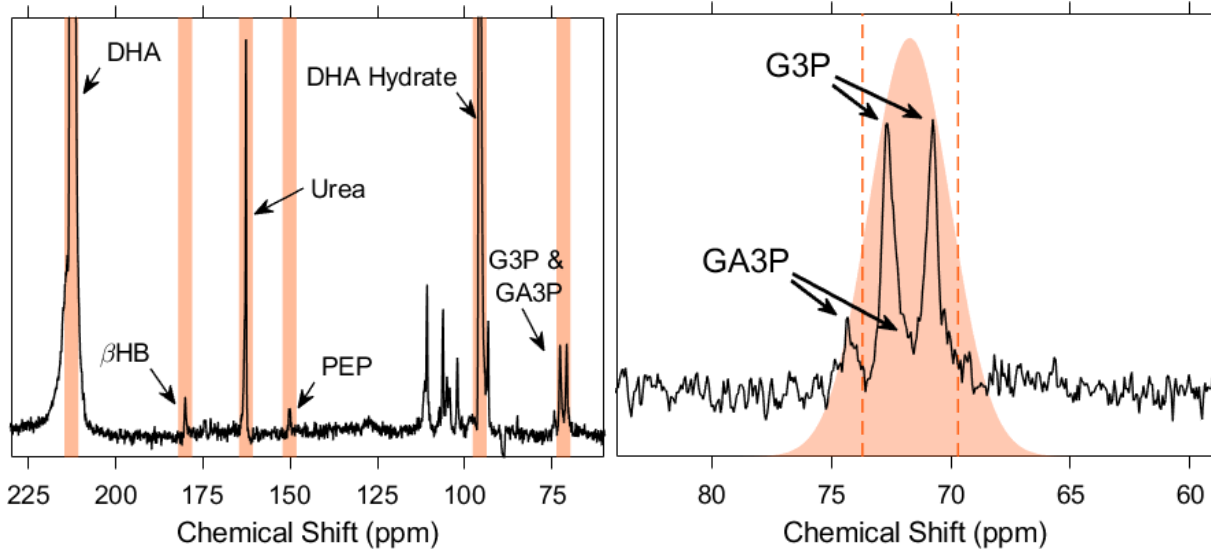
Figure 6.6: Excitation bands used for imaging of HP DHA metabolites were determined from pulse-acquire spectroscopy acquired in the imaged rats approximately 24 hours prior to the imaging experiment. The use of a 300 Hz Gaussian pulse provides excellent spectral isolation for selective imaging of all chemical shifts except for G3P and GA3P, which occur as overlapping doublets within a single excitation band (right). This excitation band frequency offset was centered on the larger G3P doublet ($J_{CH} \approx$ 144 Hz), and the multiple peaks in this excitation band appear in the EPI-encoded images as signals shifted along the low-bandwidth (phase blipped) direction.

As demonstrated in dynamic DHA spectroscopy, PEP was consistently the weakest of these metabolic signals in tissue. In this animal, the PEP signal did not have sufficient SNR for reliable imaging. The multiple overlapping peaks of G3P and GA3P lead to spatial shifts of these imaging signals relative to the center frequency of this excitation band. For the G3P doublet ($J_{CH} \approx$ 144 Hz) that was centered in this excitation band, the low phase bandwidth of the flyback EPI readout results in two ^{13}C signals with a spatial shift of approximately ± 7.4 mm in the anterior-posterior direction. As shown in figure 6.6, one peak of the GA3P doublet occurs close to the center of this Gaussian excitation band, which we believe corresponds to the third imaging signal occurring nearer to the large hepatic blood vessels in this image. Future work will address the misregistration of imaging signals in this excitation band, which could be corrected with slight modification of our imaging sequence through IDEAL encoding.
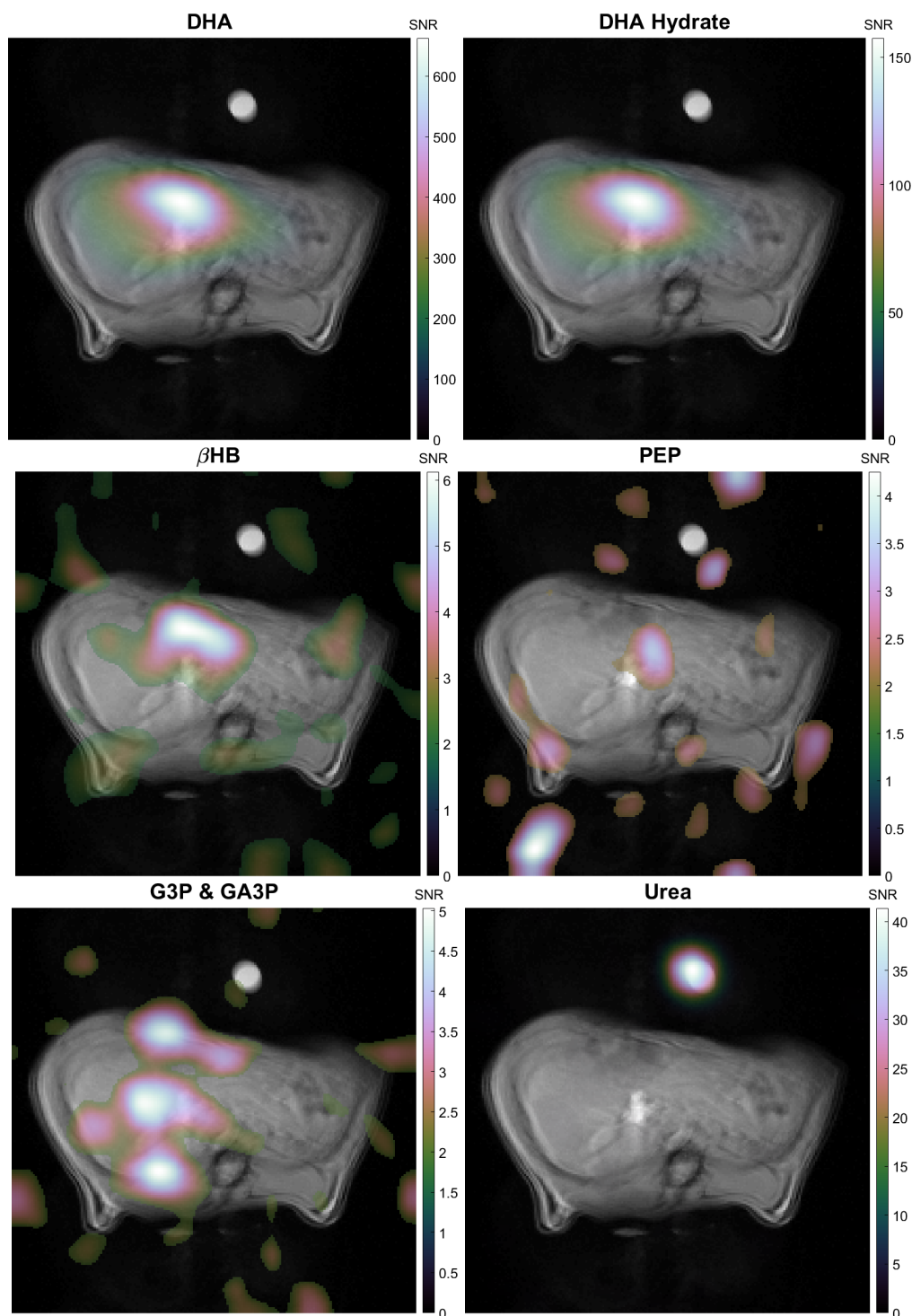
Figure 6.7: *In vivo* images of HP DHA metabolites in the rat liver are shown overlaid on an anatomical ^{1}H FLASH image. PEP signal in this animal was too weak to reliably image, however the DHA, hydrate and putative βHB signals demonstrate localization to regions of large hepatic blood vessels. Due to the multiple overlapping G3P and GA3P signals, spatial misregistrations are apparent in this imaging band. Imaging of the external urea phantom illustrates the spatial fidelity of our encoding method in the absence of these peak splitting effects.

6.4 Conclusion

In this chapter, we have demonstrated the feasibility of *in vivo* spectroscopy and imaging of HP DHA at 7 T. In contrast to prior *in vivo* studies using this agent at 3 T, our spectra depict more reliable measurement of GA3P, with quantifications of this metabolite that are in agreement with *ex vivo* high-resolution NMR experiments. Additionally, in the course of these experiments a previously unreported chemical signal was preliminary identified as a product of ketogenic metabolism, which would be a very significant result. Together with the non-invasive measurement of glycolytic, gluconeogenic and glycerol metabolism HP DHA provides, our experiments illustrate the tremendous potential of this agent to elucidate the mechanisms underlying the development and progression of very common metabolic diseases with great personal and societal impact.

The imaging results presented in this chapter constitute the first ever images of HP DHA at 7T, and the first ever imaging of the signal we have identified as βHB. The imaging method we have developed illustrates the adaptability of the HP imaging pulse sequence described in chapter 5, and with appropriate excitation bandwidths can easily encoding individual DHA metabolite chemical shift images at any field strength. In future work, we will refine this imaging method by adding ^{1}H decoupling and expanded chemical shift encoding capabilities to better resolve G3P and GA3P imaging signals. Further work will also be needed to determine the optimal methods for quantification of HP DHA data. In these our results, simple ratiometric analyses are employed, however it may be necessary in some cases to account for vascular delivery and variable rates of chemical exchange and T_1 relaxation in more complex pharmacokinetic modeling methods [203]. Lastly, studies measuring the metabolism of HP DHA in preclinical models of metabolic liver disease are needed to definitively demonstrate the direct impact this agent can have on our understanding of these conditions. In the context of these preclincal experiments, some independent verification of the isotopic enrichment of the biochemical endpoints of interest — for example via *ex vivo* NMR or mass spectrometry — may be necessary to validate these imaging measurements.

Chapter 7

Conclusion and Future Work

Hyperpolarized ^{13}C spectroscopy and imaging permits measurements of metabolic and physiological processes in living systems in ways not possible through conventional imaging methods. This technology is poised to make a more direct impact on clinical practice in coming years, with research trials assessing the value of this emerging molecular imaging modality in human diseases currently underway [9, 10].

The work presented in this dissertation reflects an investigation of several issues that are of profound importance in HP MRI. The development of specialized imaging protocols, such as the methods created for our preclinical MRI system in chapter 5, is a crucial step that must precede any successful HP MRI study. The acquisition strategy realized by a given imaging protocol should be evaluated carefully to ensure it utilizes the non-renewable HP magnetization efficiently and provides the greatest possible opportunity of observing and quantifying the physiological processes of interest. As demonstrated in the numerical simulations presented in chapter 4, this evaluation should consider in a holistic way the effects of the acquisition strategy on the anticipated physiological evolution of the HP signal in living systems. Lastly, we have shown in chapter 6 that novel HP agents hold tremendous value, allowing direct *in vivo* measurement of metabolic processes that are currently not completely understood.

7.1 Conclusions

Several significant findings and advancements have been presented throughout this dissertation.

We have demonstrated in section 3.3 that measurement of HP [1-^{13}C]pyruvate metabolism detects the effects of pharmacological treatment in a mouse model of glioma. Notably, HP pyruvate spectroscopy resolves these metabolic effects within *30 minutes* of animals receiving an *orally administered therapy*. The observation of treatment effects *in vivo* on this short of a time frame has — to our knowledge — never before been made with HP MRI. This study therefore evinces the tremendous value HP MRI can provide in evaluating therapeutic efficacy, which is of profound consequence for the individualized management of cancer and many other diseases.

Quantification of HP MRI data can be very challenging due to the transient nature of the imaging signal. In the brief lifetime of HP signals in a typical imaging experiment, a large but not directly quantifiable fraction of these signals arises from blood vessels rather than the tissue spaces that are of primary interest. Optimal methods for analyzing HP imaging data that account for these vascular delivery effects have not yet been established. In chapter 4, we presented methods for quantifying these signals that account for the effects of HP agent delivery *in vivo*. Through numerical simulation, we demonstrated the benefits of innovative imaging strategies designed to provide added insight into the compartmentalization of HP agents in tissue. One such approach to dynamic HP imaging utilizes preparatory gradients to sensitize the HP signal to motion *in vivo*, yielding measurements more specific to the extravascular signals that are typically of primary interest. The feasibility of this imaging strategy was illustrated through HP experiments in rodents.

Even without the utilization of new encoding strategies, imaging of HP agents is an extraordinarily difficult task that requires very specialized pulse sequences. In chapter 5, we presented the pulse sequence we have created for preclinical imaging of HP agents, which provides a high degree of flexibility in the dynamic encoding of chemical shift images. We have made this sequence available to the scientific community

to help alleviate the challenges of utilizing HP MRI in preclinical experimentation. Through phantom measurements and numerical simulations, we quantitatively compared the SNR performance of two chemical shift encoding strategies enabled by our sequence, spectral-spatial RF pulses and multi-excitation IDEAL imaging, in the context of a typical HP [1-^{13}C]pyruvate experiment at 7 T. This comparison, which had to our knowledge never before been made, demonstrated the conditions under which consistent SNR performance can be attained and highlighted the relative advantages and drawbacks of each chemical shift encoding method.

The full potential of HP imaging and spectroscopy encompasses chemical agents that have not yet been developed or are just starting to be investigated in living systems. In chapter 6, we investigated the activity of one such novel HP agent, [2-^{13}C]dihydroxyacetone, via *in vivo* spectroscopy and imaging of the rat liver. Through our collaborative work on DHA, a previously unreported chemical signal was preliminarily identified as a product of ketogenic metabolism. The application of HP DHA *in vivo* presents considerable technical challenges, and imaging of the diverse metabolic signals DHA produces has been shown only through proof of concept rodent studies at 3 T. By adapting the imaging sequence introduced in chapter 5, we have demonstrated a new method for DHA imaging that can more easily encode individual images of the many biochemical endpoints at any field strength. The direct measurement of disparate metabolic fluxes HP DHA provides offers rare insight into hepatic metabolism that can greatly improve our fundamental understanding of disorders with significant societal and personal impact such as diabetes, non-alcoholic fatty liver disease and cancer.

7.2 Future Work

The background discussions and new studies presented in this dissertation must necessarily represent a limited picture of a rapidly evolving new imaging modality. Significant advancements will continue to be made in the application of HP agents for imaging and spectroscopy of living systems. Currently, HP MRI in the clinic is per-

formed only in the context of clinical trials without direct impact on patient care. Improvements in accuracy and reproducibility of quantitative biomarkers derived from HP imaging data will be vital in establishing the value of HP MRI for clinical use. For this purpose, continued refinement of imaging hardware, pulse sequences and data analysis methods will be necessary.

Quantitative evaluation of HP imaging performance must account for signal variations due to agent delivery, relaxation and utilization by the imaging method itself to derive values that are meaningful in a specific biological context. Further evaluation of methods for quantifying HP MRI data that account for the specific biological and technical factors in preclinical and clinical imaging studies is needed to define the value of this emerging molecular imaging technology. The new method for sensitizing HP imaging signals to diffusive motion that we have shown to be feasible in rodent imaging will need further evaluation to confirm the benefit of this imaging strategy in other situations. Additionally, the quantitative measures of vascular delivery provided by this HP imaging strategy should be compared more directly to other more established techniques for measuring these effects, such as ^{1}H DCE and IVIM imaging. All HP imaging in this work was modeled and acquired with spoiled gradient-echo imaging, for which the effects of RF excitation on finite HP magnetization is relatively simple to model. For use on clinical MRI hardware, many of the imaging techniques developed here will need to be adapted to use more complex spin-echo imaging methods which will require both significant revision of the pulse sequence and of the methods for data analysis.

The development and application of new HP agents brings both novel biological insights and additional technical challenges for HP MRI. Through adaptation of our preclinical imaging method, we have demonstrated that imaging of HP DHA can provide broad insight into hepatic metabolism non-invasively. Further application of our spectroscopic and imaging methods for this agent in preclinical studies assessing normal and abnormal metabolism will be needed to demonstrate the capacity of HP DHA to provide the direct measurements of biochemical processes underlying the development and progression of specific metabolic diseases.

In the foreseeable future, we plan to build upon the many compelling results outlined in this document. Through refinement of the pharmacokinetic modeling and data acquisition infrastructure we have developed, optimal methods of HP data acquisition and analysis will be identified. This process must be done in a holistic and synergistic fashion, with full consideration of the specific biology of interest and the imaging methods available for a given study. By expanding the capabilities of HP MRI sequences, new analysis methods are made possible that can fulfill the tremendous potential of HP MRI for clinical and research applications.

Bibliography

[1]D. Hanahan and R. A. Weinberg, "The hallmarks of cancer," Cell **100**, 57–70 (2000).

[2]R. L. Siegel, K. D. Miller, and A. Jemal, "Cancer statistics, 2020," CA: A Cancer Journal for Clinicians **70**, 7–30 (2020).

[3]D. Hanahan and R. Weinberg, "Hallmarks of cancer: the next generation," Cell **144**, 646–674 (2011).

[4]R. Weinberg, *The biology of cancer* (Garland Science, New York, 2007).

[5]F. S. Collins and H. Varmus, "A new initiative on precision medicine," New England Journal of Medicine **372**, 793–795 (2015).

[6]E. Eisenhauer, P. Therasse, J. Bogaerts, L. Schwartz, D. Sargent, R. Ford, J. Dancey, S. Arbuck, S. Gwyther, M. Mooney, L. Rubinstein, L. Shankar, L. Dodd, R. Kaplan, D. Lacombe, and J. Verweij, "New response evaluation criteria in solid tumours: revised RECIST guideline (version 1.1)," European Journal of Cancer **45**, 228–247 (2009).

[7]A. R. Padhani and K. A. Miles, "Multiparametric imaging of tumor response to therapy," Radiology **256**, 348–364 (2010).

[8]J. Kurhanewicz, D. B. Vigneron, K. Brindle, E. Y. Chekmenev, A. Comment, C. H. Cunningham, R. J. Deberardinis, G. G. Green, M. O. Leach, S. S. Rajan, R. R. Rizi, B. D. Ross, W. S. Warren, and C. R. Malloy, "Analysis of cancer metabolism by imaging hyperpolarized nuclei: prospects for translation to clinical research," Neoplasia **13**, 81–97 (2011).

[9]J. Kurhanewicz, D. B. Vigneron, J. H. Ardenkjaer-Larsen, J. A. Bankson, K. Brindle, C. H. Cunningham, F. A. Gallagher, K. R. Keshari, A. Kjaer, C. Laustsen, D. A. Mankoff, M. E. Merritt, S. J. Nelson, J. M. Pauly, P. Lee, S. Ronen, D. J. Tyler, S. S. Rajan, D. M. Spielman, L. Wald, X. Zhang, C. R. Malloy, and R. Rizi, "Hyperpolarized (13)c mri: path to clinical translation in oncology," Neoplasia **21**, 1–16 (2019).

[10]Z. J. Wang, M. A. Ohliger, P. E. Z. Larson, J. W. Gordon, R. A. Bok, J. Slater, J. E. Villanueva-Meyer, C. P. Hess, J. Kurhanewicz, and D. B. Vigneron, "Hyperpolarized (13)c mri: state of the art and future directions," Radiology **291**, 273–284 (2019).

[11]J. A. Bankson, C. M. Walker, M. S. Ramirez, W. Stefan, D. Fuentes, M. E. Merritt, J. Lee, V. C. Sandulache, Y. Chen, L. Phan, P. C. Chou, A. Rao, S. C. Yeung, M. H. Lee, D. Schellingerhout, C. A. Conrad, C. Malloy, A. D. Sherry, S. Y. Lai, and J. D. Hazle, "Kinetic modeling and constrained reconstruction of hyperpolarized [1-13c]-pyruvate offers improved metabolic imaging of tumors," Cancer Res **75**, 4708–17 (2015).

[12]C. M. Walker, Y. Chen, S. Y. Lai, and J. A. Bankson, "A novel perfused bloch-McConnell simulator for analyzing the accuracy of dynamic hyperpolarized MRS," Medical Physics **43**, 854–864 (2016).

[13]R. Aggarwal, D. B. Vigneron, and J. Kurhanewicz, "Hyperpolarized 1-[13 c]-pyruvate magnetic resonance imaging detects an early metabolic response to androgen ablation therapy in prostate cancer," European Urology **72**, 1028–1029 (2017).

[14]S. E. Day, M. I. Kettunen, M. K. Cherukuri, J. B. Mitchell, M. J. Lizak, H. D. Morris, S. Matsumoto, A. P. Koretsky, and K. M. Brindle, "Detecting response of rat c6 glioma tumors to radiotherapy using hyperpolarized [1- 13c]pyruvate and 13c magnetic resonance spectroscopic imaging," Magn Reson Med **65**, 557–63 (2011).

[15]S. Hu, A. Balakrishnan, R. A. Bok, B. Anderton, P. E. Larson, S. J. Nelson, J. Kurhanewicz, D. B. Vigneron, and A. Goga, "13c-pyruvate imaging reveals alterations in glycolysis that precede c-myc-induced tumor formation and regression," Cell Metab **14**, 131–42 (2011).

[16]I. Park, R. Bok, T. Ozawa, J. J. Phillips, C. D. James, D. B. Vigneron, S. M. Ronen, and S. J. Nelson, "Detection of early response to temozolomide treatment in brain tumors using hyperpolarized 13c mr metabolic imaging," J Magn Reson Imaging **33**, 1284–90 (2011).

[17]J. M. Park, L. D. Recht, S. Josan, M. Merchant, T. Jang, Y. F. Yen, R. E. Hurd, D. M. Spielman, and D. Mayer, "Metabolic response of glioma to dichloroacetate measured in vivo by hyperpolarized (13)c magnetic resonance spectroscopic imaging," Neuro Oncol **15**, 433–41 (2013).

[18]M. Radoul, M. M. Chaumeil, P. Eriksson, A. S. Wang, J. J. Phillips, and S. M. Ronen, "Mr studies of glioblastoma models treated with dual pi3k/mtor inhibitor and temozolomide:metabolic changes are associated with enhanced survival," Mol Cancer Ther **15**, 1113–22 (2016).

[19] M. Radoul, C. Najac, P. Viswanath, J. Mukherjee, M. Kelly, A. M. Gillespie, M. M. Chaumeil, P. Eriksson, R. Delos Santos, R. O. Pieper, and S. M. Ronen, "Hdac inhibition in glioblastoma monitored by hyperpolarized (13) c mrsi," NMR Biomed **32**, e4044 (2019).

[20] C. H. Cunningham, A. P. Chen, M. Lustig, B. A. Hargreaves, J. Lupo, D. Xu, J. Kurhanewicz, R. E. Hurd, J. M. Pauly, S. J. Nelson, and D. B. Vigneron, "Pulse sequence for dynamic volumetric imaging of hyperpolarized metabolic products," J Magn Reson **193**, 139–46 (2008).

[21] S. B. Reeder, J. H. Brittain, T. M. Grist, and Y. F. Yen, "Least-squares chemical shift separation for (13)c metabolic imaging," J Magn Reson Imaging **26**, 1145–52 (2007).

[22] F. Wiesinger, E. Weidl, M. I. Menzel, M. A. Janich, O. Khegai, S. J. Glaser, A. Haase, M. Schwaiger, and R. F. Schulte, "Ideal spiral csi for dynamic metabolic mr imaging of hyperpolarized [1-13c]pyruvate," Magn Reson Med **68**, 8–16 (2012).

[23] J. Larmor, "On the theory of the magnetic influence on spectra; and on the radiation from moving ions," Phil Mag **Series 5, 44 (271)**, 503–512 (1897).

[24] I. Rabi, "Space quantization in a gyrating magnetic field," Phys Rev **51**, 652–4 (1937).

[25] E. Haacke, R. Brown, M. Thompson, and R. Venkatesan, *Magnetic resonance imaging physical principles and sequence design* (John Wiley & Sons, 1999).

[26] F. Bloch, W. Hansen, and M. Packard, "Nuclear induction," Phys Rev **69**, 127 (1946).

[27] E. Purcell, H. Torrey, and P. RV, "Resonance absorption by nuclear moments in a solid," Phys Rev **69**, 37–38 (1946).

[28] M. L. Hirsch, N. Kalechofsky, A. Belzer, M. Rosay, and J. G. Kempf, "Brute-force hyperpolarization for NMR and MRI," Journal of the American Chemical Society **137**, 8428–8434 (2015).

[29] T. Walker and W. Happer, "Spin-exchange optical pumping of noble-gas nuclei," Rev. Mod. Phys. **69**, 629 (1997).

[30] F. W. Hersman, I. C. Ruset, S. Ketel, I. Muradian, S. D. Covrig, J. Distelbrink, W. Porter, D. Watt, J. Ketel, J. Brackett, A. Hope, and S. Patz, "Large production system for hyperpolarized 129xe for human lung imaging studies," Acad Radiol **15**, 683–92 (2008).

[31] J. Natterer and J. Bargon, "Parahydrogen induced polarization," Progress in Nuclear Magnetic Resonance Spectroscopy **31**, 293–315 (1997).

[32] W. Iali, P. J. Rayner, and S. B. Duckett, "Using para hydrogen to hyperpolarize amines, amides, carboxylic acids, alcohols, phosphates, and carbonates," Sci Adv **4**, eaao6250 (2018).

[33] A. Overhauser, "Polarization of nuclei in metals," Phys Rev **92**, 411–415 (1953).

[34] F. Bloch, "Nuclear induction," Phys Rev **70**, 460–474 (1946).

[35] M. Bernstein, K. King, and X. Zhou, *Handbook of mri pulse sequences* (Elsevier, 2004).

[36] N. Bloembergen, E. Purcell, and R. Pound, "Relaxation effects in nuclear magnetic resonance absorption," Phys Rev **73**, 679 (1948).

[37] J. Facelli, D. Grant, and J. Michl, "Carbon-13 shielding tensors: experimental and theoretical determination," Acc Chem Res **20**, 152–158 (1987).

[38] E. Hahn, "Spin echoes," Phys Rev **80**, 580–594 (1950).

[39] C. H. Cunningham, A. P. Chen, M. J. Albers, J. Kurhanewicz, R. E. Hurd, Y. F. Yen, J. M. Pauly, S. J. Nelson, and D. B. Vigneron, "Double spin-echo sequence for rapid spectroscopic imaging of hyperpolarized 13c," J Magn Reson **187**, 357–62 (2007).

[40] H. C. Torrey, "Bloch equations with diffusion terms," Physical Review **104**, 563–565 (1956).

[41] H. M. McConnell, "Reaction rates by nuclear magnetic resonance," The Journal of Chemical Physics **28**, 430–431 (1958).

[42] W. Proctor and F. Yu, "The dependence of a nuclear magnetic resonance frequency upon chemical compound," Phys Rev **77**, 717 (1950).

[43] "Nmr nomenclature. nuclear spin properties and conventions for chemical shifts (iupac recommendations 2001)," **24** (2002).

[44] R. Bracewell, *The fourier transform and its applications*, Third (McGraw-Hill, 2000).

[45] R. R. Ernst and W. A. Anderson, "Application of fourier transform spectroscopy to magnetic resonance," **37**, 93–102 (1966).

[46] D. Hoult and P. Lauterbur, "The sensitivity of the zeugmatographic experiment involving human samples," J Magn Reson **34**, 425–433 (1979).

[47] W. A. Edelstein, P. A. Bottomley, and L. M. Pfeifer, "A signal-to-noise calibration procedure for nmr imaging systems," Med Phys **11**, 180–5 (1984).

[48] R. M. Henkelman, "Measurement of signal intensities in the presence of noise in mr images," Med Phys **12**, 232–3 (1985).

[49]*Determination of signal-to-noise ratio (snr) in diagnostic magnetic resonance imaging*, tech. rep. MS 1-2008 (R2014) (NEMA, 2008).

[50]H. Gudbjartsson and S. Patz, "The rician distribution of noisy mri data," **34**, 910–914 (1995).

[51]P. Lauterbur, "Image formation by induced local interaction; examples employing nuclear magnetic resonance," Nature **242**, 190–191 (1973).

[52]P. Mansfield and P. K. Grannell, "Nmr 'diffraction' in solids?" **6**, L422–L426 (1973).

[53]A. Kumar, D. Welti, and R. Ernst, "Nmr fourier zeugmatography," J Magn Reson **18**, 69–83 (1975).

[54]J. Ma, F. W. Wehrli, H. K. Song, and S. N. Hwang, "A single-scan imaging technique for measurement of the relative concentrations of fat and water protons and their transverse relaxation times," **125**, 92–101 (1997).

[55]R. Damadian, "Tumor detection by nuclear magnetic resonance," Science **171**, 1151–3 (1971).

[56]J. H. Ardenkjaer-Larsen, B. Fridlund, A. Gram, G. Hansson, L. Hansson, M. H. Lerche, R. Servin, M. Thaning, and K. Golman, "Increase in signal-to-noise ratio of $> 10,000$ times in liquid-state nmr," Proc Natl Acad Sci U S A **100**, 10158–63 (2003).

[57]F. Mentink-Vigier, Ü. Akbey, Y. Hovav, S. Vega, H. Oschkinat, and A. Feintuch, "Fast passage dynamic nuclear polarization on rotating solids," Journal of Magnetic Resonance **224**, 13–21 (2012).

[58]H. R. Ward and R. G. Lawler, "Nuclear magnetic resonance emission and enhanced absorption in rapid organometallic reactions," Journal of the American Chemical Society **89**, 5518–5519 (1967).

[59]T. Carver and C. Slichter, "Experimental verification of the overhauser nuclear polarization effect," Phys Rev **102**, 957–980 (1956).

[60]J. H. Ardenkjaer-Larsen, S. Macholl, and H. Jóhannesson, "Dynamic nuclear polarization with trityls at 1.2 k," Applied Magnetic Resonance **34**, 509–522 (2008).

[61]H. Jóhannesson, S. Macholl, and J. H. Ardenkjaer-Larsen, "Dynamic nuclear polarization of [1-13c]pyruvic acid at 4.6 tesla," Journal of Magnetic Resonance **197**, 167–175 (2009).

[62]L. Lumata, M. E. Merritt, C. R. Malloy, A. D. Sherry, and Z. Kovacs, "Impact of gd3+ on DNP of [1-13c]pyruvate doped with trityl OX063, BDPA, or 4-oxo-TEMPO," The Journal of Physical Chemistry A **116**, 5129–5138 (2012).

[63] J. H. Ardenkjaer-Larsen, A. M. Leach, N. Clarke, J. Urbahn, D. Anderson, and T. W. Skloss, "Dynamic nuclear polarization polarizer for sterile use intent," NMR in Biomedicine **24**, 927–932 (2011).

[64] J. H. Ardenkjaer-Larsen, "On the present and future of dissolution-DNP," Journal of Magnetic Resonance **264**, 3–12 (2016).

[65] S. R. Cherry, J. A. Sorenson, and M. E. (of California School of Medicine) Phelps, *Physics in nuclear medicine* (Elsevier Health Sciences, Apr. 10, 2012), 544 pp.

[66] M. A. Janich, M. I. Menzel, F. Wiesinger, E. Weidl, O. Khegai, J. H. Ardenkjaer-Larsen, S. J. Glaser, A. Haase, R. F. Schulte, and M. Schwaiger, "Effects of pyruvate dose on in vivo metabolism and quantification of hyperpolarized 13 c spectra," NMR in Biomedicine **25**, 142–151 (2011).

[67] A. Cho, R. Eskandari, V. Z. Miloushev, and K. R. Keshari, "A non-synthetic approach to extending the lifetime of hyperpolarized molecules using d2o solvation," J Magn Reson **295**, 57–62 (2018).

[68] K. Golman, R. in 't Zandt, and M. Thaning, "Real-time metabolic imaging," Proc Natl Acad Sci U S A **103**, 11270–5 (2006).

[69] K. Golman and J. S. Petersson, "Metabolic imaging and other applications of hyperpolarized 13c1," Acad Radiol **13**, 932–42 (2006).

[70] K. Golman, R. I. Zandt, M. Lerche, R. Pehrson, and J. H. Ardenkjaer-Larsen, "Metabolic imaging by hyperpolarized 13c magnetic resonance imaging for in vivo tumor diagnosis," Cancer Res **66**, 10855–60 (2006).

[71] E. Marieb, *Human anatomy & physiology* (Pearson, Boston, 2013).

[72] S. Hui, J. M. Ghergurovich, R. J. Morscher, C. Jang, X. Teng, W. Lu, L. A. Esparza, T. Reya, L. Zhan, J. Y. Guo, E. White, and J. D. Rabinowitz, "Glucose feeds the TCA cycle via circulating lactate," Nature **551**, 115–118 (2017).

[73] M. G. V. Heiden, L. C. Cantley, and C. B. Thompson, "Understanding the warburg effect: the metabolic requirements of cell proliferation," Science **324**, 1029–1033 (2009).

[74] O. Warburg, "On the origin of cancer cells," Science **123**, 309–314 (1956).

[75] A. Luengo, D. Y. Gui, and M. G. V. Heiden, "Targeting metabolism for cancer therapy," Cell Chemical Biology **24**, 1161–1180 (2017).

[76] K. A. Michel, R. Zieliński, C. M. Walker, L. L. Roux, W. Priebe, J. A. Bankson, and D. Schellingerhout, "Hyperpolarized pyruvate MR spectroscopy depicts glycolytic inhibition in a mouse model of glioma," Radiology **293**, 168–173 (2019).

[77]S. J. Nelson, J. Kurhanewicz, D. B. Vigneron, P. E. Z. Larson, A. L. Harzstark, M. Ferrone, M. van Criekinge, J. W. Chang, R. Bok, I. Park, G. Reed, L. Carvajal, E. J. Small, P. Munster, V. K. Weinberg, J. H. Ardenkjaer-Larsen, A. P. Chen, R. E. Hurd, L.-I. Odegardstuen, F. J. Robb, J. Tropp, and J. A. Murray, "Metabolic imaging of patients with prostate cancer using hyperpolarized [1-13c]pyruvate," Science Translational Medicine **5**, 198ra108–198ra108 (2013).

[78]I. Park, P. E. Z. Larson, J. W. Gordon, L. Carvajal, H. Y. Chen, R. Bok, M. Van Criekinge, M. Ferrone, J. B. Slater, D. Xu, J. Kurhanewicz, D. B. Vigneron, S. Chang, and S. J. Nelson, "Development of methods and feasibility of using hyperpolarized carbon-13 imaging data for evaluating brain metabolism in patient studies," Magn Reson Med **80**, 864–873 (2018).

[79]K. L. Granlund, S. S. Tee, H. A. Vargas, S. K. Lyashchenko, E. Reznik, S. Fine, V. Laudone, J. A. Eastham, K. A. Touijer, V. E. Reuter, M. Gonen, R. E. Sosa, D. Nicholson, Y. W. Guo, A. P. Chen, J. Tropp, F. Robb, H. Hricak, and K. R. Keshari, "Hyperpolarized mri of human prostate cancer reveals increased lactate with tumor grade driven by monocarboxylate transporter 1," Cell Metab (2019).

[80]M. Peeters, "Urea breath test: a diagnostic tool in the management of helicobacter pylori-related gastrointestinal diseases," Acta Gastroenterol Belg **61**, 331–5 (1998).

[81]R. F. Reeder and R. E. Harbaugh, "Administration of intravenous urea and normal saline for the treatment of hyponatremia in neurosurgical patients," Journal of Neurosurgery **70**, 201–206 (1989).

[82]K. Golman, J. H. Ardenkjaer-Larsen, J. S. Petersson, S. Mansson, and I. Leunbach, "Molecular imaging with endogenous substances," Proceedings of the National Academy of Sciences **100**, 10435–10439 (2003).

[83]C. Ø. Mariager, P. M. Nielsen, H. Qi, M. Schroeder, L. B. Bertelsen, and C. Laustsen, "Can hyperpolarized 13 c-urea be used to assess glomerular filtration rate? a retrospective study," Tomography **3**, 146–152 (2017).

[84]C. von Morze, R. A. Bok, G. D. Reed, J. H. Ardenkjaer-Larsen, J. Kurhanewicz, and D. B. Vigneron, "Simultaneous multiagent hyperpolarized13c perfusion imaging, Multiagent hp13c perfusion mri," **72**, 1599–1609 (2014).

[85]J. M. Park, S. Josan, T. Grafendorfer, Y.-F. Yen, R. E. Hurd, D. M. Spielman, and D. Mayer, "Measuring mitochondrial metabolism in rat brainin vivousing MR spectroscopy of hyperpolarized [2-13c]pyruvate," NMR in Biomedicine **26**, 1197–1203 (2013).

[86]S. Josan, R. Hurd, J. M. Park, Y.-F. Yen, R. Watkins, A. Pfefferbaum, D. Spielman, and D. Mayer, "Dynamic metabolic imaging of hyperpolarized [2-13 c]pyruvate using spiral chemical shift imaging with alternating spectral band excitation," Magnetic Resonance in Medicine **71**, 2051–2058 (2013).

[87]B. T. Chung, H.-Y. Chen, J. Gordon, D. Mammoli, R. Sriram, A. W. Autry, L. M. L. Page, M. M. Chaumeil, P. Shin, J. Slater, C. T. Tan, C. Suszczynski, S. Chang, Y. Li, R. A. Bok, S. M. Ronen, P. E. Larson, J. Kurhanewicz, and D. B. Vigneron, "First hyperpolarized [2-13c]pyruvate MR studies of human brain metabolism," Journal of Magnetic Resonance **309**, 106617 (2019).

[88]F. A. Gallagher, M. I. Kettunen, D. E. Hu, P. R. Jensen, R. I. Zandt, M. Karlsson, A. Gisselsson, S. K. Nelson, T. H. Witney, S. E. Bohndiek, G. Hansson, T. Peitersen, M. H. Lerche, and K. M. Brindle, "Production of hyperpolarized [1,4-13c2]malate from [1,4-13c2]fumarate is a marker of cell necrosis and treatment response in tumors," Proc Natl Acad Sci U S A **106**, 19801–6 (2009).

[89]S. E. Bohndiek, M. I. Kettunen, D.-e. Hu, and K. M. Brindle, "Hyperpolarized 13c spectroscopy detects early changes in tumor vasculature and metabolism after VEGF neutralization," Cancer Research **72**, 854–864 (2012).

[90]I. Marco-Rius, P. Cao, C. von Morze, M. Merritt, K. X. Moreno, G. Y. Chang, M. A. Ohliger, D. Pearce, J. Kurhanewicz, P. E. Larson, and D. B. Vigneron, "Multiband spectral-spatial rf excitation for hyperpolarized [2-(13) c]dihydroxyacetone (13) c-mr metabolism studies," Magn Reson Med **77**, 1419–1428 (2017).

[91]K. X. Moreno, S. Satapati, R. J. DeBerardinis, S. C. Burgess, C. R. Malloy, and M. E. Merritt, "Real-time detection of hepatic gluconeogenic and glycogenolytic states using hyperpolarized [2-13c]dihydroxyacetone," J Biol Chem **289**, 35859–67 (2014).

[92]I. Marco-Rius, C. von Morze, R. Sriram, P. Cao, G. Y. Chang, E. Milshteyn, R. A. Bok, M. A. Ohliger, D. Pearce, J. Kurhanewicz, P. E. Larson, D. B. Vigneron, and M. Merritt, "Monitoring acute metabolic changes in the liver and kidneys induced by fructose and glucose using hyperpolarized [2-(13) c]dihydroxyacetone," Magn Reson Med **77**, 65–73 (2017).

[93]A. Omuro and L. M. DeAngelis, "Glioblastoma and other malignant gliomas a clinical review," Jama-Journal of the American Medical Association **310**, 1842–1850 (2013).

[94]M. Koshy, J. L. Villano, T. A. Dolecek, A. Howard, U. Mahmood, S. J. Chmura, R. R. Weichselbaum, and B. J. McCarthy, "Improved survival time trends for glioblastoma using the seer 17 population-based registries," J Neurooncol **107**, 207–12 (2012).

[95] M. Sanzey, S. A. Abdul Rahim, A. Oudin, A. Dirkse, T. Kaoma, L. Vallar, C. Herold-Mende, R. Bjerkvig, A. Golebiewska, and S. P. Niclou, "Comprehensive analysis of glycolytic enzymes as therapeutic targets in the treatment of glioblastoma," PLoS One **10**, e0123544 (2015).

[96] M. M. Chaumeil, T. Ozawa, I. Park, K. Scott, C. D. James, S. J. Nelson, and S. M. Ronen, "Hyperpolarized 13c mr spectroscopic imaging can be used to monitor everolimus treatment in vivo in an orthotopic rodent model of glioblastoma," Neuroimage **59**, 193–201 (2012).

[97] V. Z. Miloushev, K. L. Granlund, R. Boltyanskiy, S. K. Lyashchenko, L. M. DeAngelis, I. K. Mellinghoff, C. W. Brennan, V. Tabar, T. J. Yang, A. I. Holodny, R. E. Sosa, Y. W. Guo, A. P. Chen, J. Tropp, F. Robb, and K. R. Keshari, "Metabolic imaging of the human brain with hyperpolarized (13)c pyruvate demonstrates (13)c lactate production in brain tumor patients," Cancer Res **78**, 3755–3760 (2018).

[98] S. Lal, M. Lacroix, P. Tofilon, G. N. Fuller, R. Sawaya, and F. F. Lang, "An implantable guide-screw system for brain tumor studies in small animals," J Neurosurg **92**, 326–33 (2000).

[99] W. Priebe, R. Zielinski, I. Fokt, E. Felix, V. Radjendirane, J. Arumugam, M. Khuong, M. Krasinski, and S. Skora, "Exth-07: design and evaluation of wp1122, an inhibitor of glycolysis with increased cns uptake," in Neuro-oncology, Vol. 20, Supp 6 (Nov. 2018), p. vi86.

[100] A. T. Feldman and D. Wolfe, "Tissue processing and hematoxylin and eosin staining," Methods Mol Biol **1180**, 31–43 (2014).

[101] C. Y. Sun, C. M. Walker, K. A. Michel, A. M. Venkatesan, S. Y. Lai, and J. A. Bankson, "Influence of parameter accuracy on pharmacokinetic analysis of hyperpolarized pyruvate," Magn Reson Med **79**, 3239–3248 (2018).

[102] S. Daniele, E. Zappelli, and C. Martini, "Trazodone regulates neurotrophic/growth factors, mitogen-activated protein kinases and lactate release in human primary astrocytes," J Neuroinflammation **12**, 225 (2015).

[103] H. Di, X. Zhang, Y. Guo, Y. Shi, C. Fang, Y. Yuan, J. Wang, C. Shang, W. Guo, and C. Li, "Silencing ldha inhibits proliferation, induces apoptosis and increases chemosensitivity to temozolomide in glioma cells," Oncol Lett **15**, 5131–5136 (2018).

[104] S. Maraka, M. D. Groves, A. G. Mammoser, I. Melguizo-Gavilanes, C. A. Conrad, I. W. Tremont-Lukats, M. E. Loghin, B. J. O'Brien, V. K. Puduvalli, E. P. Sulman, K. R. Hess, K. D. Aldape, M. R. Gilbert, J. F. de Groot, W. K. Alfred Yung, and M. Penas-Prado, "Phase 1 lead-in to a phase 2 factorial study of temozolomide plus

memantine, mefloquine, and metformin as postradiation adjuvant therapy for newly diagnosed glioblastoma," Cancer (2018).

[105] H. M. De Feyter, K. L. Behar, Z. A. Corbin, R. K. Fulbright, P. B. Brown, S. McIntyre, T. W. Nixon, D. L. Rothman, and R. A. de Graaf, "Deuterium metabolic imaging (dmi) for mri-based 3d mapping of metabolism in vivo," Sci Adv **4**, eaat7314 (2018).

[106] M. Durst, U. Koellisch, A. Frank, G. Rancan, C. V. Gringeri, V. Karas, F. Wiesinger, M. I. Menzel, M. Schwaiger, A. Haase, and R. F. Schulte, "Comparison of acquisition schemes for hyperpolarised (1)(3)c imaging," NMR Biomed **28**, 715–25 (2015).

[107] J. T. Grist, M. A. McLean, F. Riemer, R. F. Schulte, S. S. Deen, F. Zaccagna, R. Woitek, C. J. Daniels, J. D. Kaggie, T. Matys, I. Patterson, R. Slough, A. B. Gill, A. Chhabra, R. Eichenberger, M. C. Laurent, A. Comment, J. H. Gillard, A. J. Coles, D. J. Tyler, I. Wilkinson, B. Basu, D. J. Lomas, M. J. Graves, K. M. Brindle, and F. A. Gallagher, "Quantifying normal human brain metabolism using hyperpolarized [1-(13)c]pyruvate and magnetic resonance imaging," Neuroimage **189**, 171–179 (2019).

[108] S. Reynolds, S. Metcalf, E. J. Cochrane, R. C. Collins, S. Jones, M. N. J. Paley, and G. M. Tozer, "Direct arterial injection of hyperpolarized 13 c-labeled substrates into rat tumors for rapid mr detection of metabolism with minimal substrate dilution," Magn Reson Med **78**, 2116–2126 (2017).

[109] D. R, "The derivation of the gamma-variate relationship for tracer dilution curves," Journal of nuclear medicine : official publication, Society of Nuclear Medicine **24** (1983).

[110] M. T. Madsen, "A simplified formulation of the gamma variate function," **37**, 1597–1600 (1992).

[111] S. M. Kazan, S. Reynolds, A. Kennerley, E. Wholey, J. E. Bluff, J. Berwick, V. J. Cunningham, M. N. Paley, and G. M. Tozer, "Kinetic modeling of hyperpolarized13c pyruvate metabolism in tumors using a measured arterial input function," Magnetic Resonance in Medicine **70**, 943–953 (2012).

[112] R. J. Gillies, P. A. Schomack, T. W. Secomb, and N. Raghunand, "Causes and effects of heterogeneous perfusion in tumors," Neoplasia **1**, 197–207 (1999).

[113] D. M. McDonald and P. Baluk, "Significance of blood vessel leakiness in cancer," (2002).

[114] P. S. Tofts, "Modeling tracer kinetics in dynamic gd-DTPA MR imaging," Journal of Magnetic Resonance Imaging **7**, 91–101 (1997).

[115] R. I. Macey, "Transport of water and urea in red blood cells," American Journal of Physiology-Cell Physiology **246**, C195–C203 (1984).

[116]C. K. Garcia, J. L. Goldstein, R. K. Pathak, R. G. Anderson, and M. S. Brown, "Molecular characterization of a membrane transporter for lactate, pyruvate, and other monocarboxylates: implications for the cori cycle," Cell **76**, 865–873 (1994).

[117]D. K. Hill, M. R. Orton, E. Mariotti, J. K. R. Boult, R. Panek, M. Jafar, H. G. Parkes, Y. Jamin, M. F. Miniotis, N. M. S. Al-Saffar, M. Beloueche-Babari, S. P. Robinson, M. O. Leach, Y.-L. Chung, and T. R. Eykyn, "Model free approach to kinetic analysis of real-time hyperpolarized 13c magnetic resonance spectroscopy data," PLoS ONE **8**, edited by T. F. Bathen, e71996 (2013).

[118]C. J. Daniels, M. A. McLean, R. F. Schulte, F. J. Robb, A. B. Gill, N. McGlashan, M. J. Graves, M. Schwaiger, D. J. Lomas, K. M. Brindle, and F. A. Gallagher, "A comparison of quantitative methods for clinical imaging with hyperpolarized 13 c-pyruvate," NMR in Biomedicine **29**, 387–399 (2016).

[119]M. Durst, U. Koellisch, C. Gringeri, M. A. Janich, G. Rancan, A. Frank, F. Wiesinger, M. I. Menzel, A. Haase, and R. F. Schulte, "Bolus tracking for improved metabolic imaging of hyperpolarised compounds," Journal of Magnetic Resonance **243**, 40–46 (2014).

[120]S. Tang, W. Jiang, H.-Y. Chen, R. Bok, D. B. Vigneron, and P. E. Z. Larson, "A 2drf pulse sequence for bolus tracking in hyperpolarized13cimaging," Magnetic Resonance in Medicine **74**, 506–512 (2014).

[121]S. Tang, E. Milshteyn, G. Reed, J. Gordon, R. Bok, X. Zhu, Z. Zhu, D. B. Vigneron, and P. E. Z. Larson, "A regional bolus tracking and real-time b1 calibration method for hyperpolarized (13) c mri," Magn Reson Med **81**, 839–851 (2019).

[122]I. Marco-Rius, M. C. D. Tayler, M. I. Kettunen, T. J. Larkin, K. N. Timm, E. M. Serrao, T. B. Rodrigues, G. Pileio, J. H. Ardenkjaer-Larsen, M. H. Levitt, and K. M. Brindle, "Hyperpolarized singlet lifetimes of pyruvate in human blood and in the mouse," NMR in Biomedicine **26**, 1696–1704 (2013).

[123]M. I. Kettunen, B. W. C. Kennedy, D.-e. Hu, and K. M. Brindle, "Spin echo measurements of the extravasation and tumor cell uptake of hyperpolarized [1-13 c]lactate and [1-13 c]pyruvate," Magnetic Resonance in Medicine **70**, 1200–1209 (2012).

[124]P. E. Z. Larson, H. Y. Chen, J. W. Gordon, N. Korn, J. Maidens, M. Arcak, S. Tang, M. Criekinge, L. Carvajal, D. Mammoli, R. Bok, R. Aggarwal, M. Ferrone, J. B. Slater, S. J. Nelson, J. Kurhanewicz, and D. B. Vigneron, "Investigation of analysis methods for hyperpolarized 13c-pyruvate metabolic mri in prostate cancer patients," NMR Biomed **31**, e3997 (2018).

[125] J. C. Crane, J. W. Gordon, H.-Y. Chen, A. W. Autry, Y. Li, M. P. Olson, J. Kurhanewicz, D. B. Vigneron, P. E. Larson, and D. Xu, "Hyperpolarized 13 c MRI data acquisition and analysis in prostate and brain at university of california, san francisco," NMR in Biomedicine, e4280 (2020).

[126] F. A. Gallagher, R. Woitek, M. A. McLean, A. B. Gill, R. M. Garcia, E. Provenzano, F. Riemer, J. Kaggie, A. Chhabra, S. Ursprung, J. T. Grist, C. J. Daniels, F. Zaccagna, M.-C. Laurent, M. Locke, S. Hilborne, A. Frary, T. Torheim, C. Boursnell, A. Schiller, I. Patterson, R. Slough, B. Carmo, J. Kane, H. Biggs, E. Harrison, S. S. Deen, A. Patterson, T. Lanz, Z. Kingsbury, M. Ross, B. Basu, R. Baird, D. J. Lomas, E. Sala, J. Wason, O. M. Rueda, S.-F. Chin, I. B. Wilkinson, M. J. Graves, J. E. Abraham, F. J. Gilbert, C. Caldas, and K. M. Brindle, "Imaging breast cancer using hyperpolarized carbon-13 MRI," Proceedings of the National Academy of Sciences **117**, 2092–2098 (2020).

[127] O. Wu, R. M. Dijkhuizen, and A. G. Sorensen, "Multiparametric magnetic resonance imaging of brain disorders," Topics in Magnetic Resonance Imaging **21**, 129–138 (2010).

[128] A. Stabile, F. Giganti, A. B. Rosenkrantz, S. S. Taneja, G. Villeirs, I. S. Gill, C. Allen, M. Emberton, C. M. Moore, and V. Kasivisvanathan, "Multiparametric MRI for prostate cancer diagnosis: current status and future directions," Nature Reviews Urology **17**, 41–61 (2019).

[129] R. Banerjee, M. Pavlides, E. M. Tunnicliffe, S. K. Piechnik, N. Sarania, R. Philips, J. D. Collier, J. C. Booth, J. E. Schneider, L. M. Wang, D. W. Delaney, K. A. Fleming, M. D. Robson, E. Barnes, and S. Neubauer, "Multiparametric magnetic resonance for the non-invasive diagnosis of liver disease," Journal of Hepatology **60**, 69–77 (2014).

[130] E. F. Cox, C. E. Buchanan, C. R. Bradley, B. Prestwich, H. Mahmoud, M. Taal, N. M. Selby, and S. T. Francis, "Multiparametric renal magnetic resonance imaging: validation, interventions, and alterations in chronic kidney disease," Frontiers in Physiology **8** (2017).

[131] M. A. Marino, T. Helbich, P. Baltzer, and K. Pinker-Domenig, "Multiparametric MRI of the breast: a review," Journal of Magnetic Resonance Imaging **47**, 301–315 (2017).

[132] R. L. Hesketh, J. Wang, A. J. Wright, D. Y. Lewis, A. E. Denton, R. Grenfell, J. L. Miller, R. Bielik, M. Gehrung, M. Fala, S. Ros, B. Xie, D.-e. Hu, and K. M. Brindle, "Magnetic resonance imaging is more sensitive than PET for detecting treatment-induced cell death–dependent changes in glycolysis," Cancer Research **79**, 3557–3569 (2019).

[133]M. Karlsson, P. R. Jensen, J. H. Ardenkjaer-Larsen, and M. H. Lerche, "Difference between extra- and intracellular t 1 values of carboxylic acids affects the quantitative analysis of cellular kinetics by hyperpolarized NMR," Angewandte Chemie International Edition **55**, 13567–13570 (2016).

[134]M. A. Branch, T. F. Coleman, and Y. Li, "A subspace, interior, and conjugate gradient method for large-scale bound-constrained minimization problems," SIAM Journal on Scientific Computing **21**, 1–23 (1999).

[135]E. Johansson, L. Olsson, S. Månsson, J. Petersson, K. Golman, F. Ståhlberg, and R. Wirestam, "Perfusion assessment with bolus differentiation: a technique applicable to hyperpolarized tracers," Magnetic Resonance in Medicine **52**, 1043–1051 (2004).

[136]R. F. Schulte, J. I. Sperl, E. Weidl, M. I. Menzel, M. A. Janich, O. Khegai, M. Durst, J. H. Ardenkjaer-Larsen, S. J. Glaser, A. Haase, M. Schwaiger, and F. Wiesinger, "Saturation-recovery metabolic-exchange rate imaging with hyperpolarized [1-13c] pyruvate using spectral-spatial excitation," Magn Reson Med **69**, 1209–16 (2013).

[137]T. Harris, S. Uppala, N. Lev-Cohain, Y. Adler-Levy, D. Shaul, A. Nardi-Schreiber, G. Sapir, A. Azar, A. Gamliel, J. Sosna, J. M. Gomori, and R. Katz-Brull, "Hyperpolarized product selective saturating-excitations for determination of changes in metabolic reaction rates in real-time," NMR in Biomedicine **33** (2019).

[138]E. O. Stejskal and J. E. Tanner, "Spin diffusion measurements: spin echoes in the presence of a time-dependent field gradient," The Journal of Chemical Physics **42**, 288–292 (1965).

[139]P. E. Larson, R. E. Hurd, A. B. Kerr, J. M. Pauly, R. A. Bok, J. Kurhanewicz, and D. B. Vigneron, "Perfusion and diffusion sensitive 13c stimulated-echo MRSI for metabolic imaging of cancer," Magnetic Resonance Imaging **31**, 635–642 (2013).

[140]I. Marco-Rius, J. W. Gordon, A. N. Mattis, R. Bok, R. Delos Santos, S. Sukumar, P. E. Z. Larson, D. B. Vigneron, and M. A. Ohliger, "Diffusion-weighted imaging of hyperpolarized [(13) c]urea in mouse liver," J Magn Reson Imaging **47**, 141–151 (2018).

[141]B. L. Koelsch, R. Sriram, K. R. Keshari, C. L. Swisher, M. V. Criekinge, S. Sukumar, D. B. Vigneron, Z. J. Wang, P. E. Larson, and J. Kurhanewicz, "Separation of extra- and intracellular metabolites using hyperpolarized 13c diffusion weighted MR," Journal of Magnetic Resonance **270**, 115–123 (2016).

[142]D. L. Bihan and R. Turner, "The capillary network: a link between ivim and classical perfusion," Magnetic Resonance in Medicine **27**, 171–178 (1992).

[143] A. Z. Lau, J. J. Miller, M. D. Robson, and D. J. Tyler, "Cardiac perfusion imaging using hyperpolarized 13 c urea using flow sensitizing gradients," Magnetic Resonance in Medicine **75**, 1474–1483 (2015).

[144] J. W. Gordon, D. J. Niles, E. B. Adamson, K. M. Johnson, and S. B. Fain, "Application of flow sensitive gradients for improved measures of metabolism using hyperpolarized (13) c mri," Magn Reson Med **75**, 1242–8 (2016).

[145] A. Lemke, F. B. Laun, D. Simon, B. Stieltjes, and L. R. Schad, "An in vivo verification of the intravoxel incoherent motion effect in diffusion-weighted imaging of the abdomen," Magnetic Resonance in Medicine **64**, 1580–1585 (2010).

[146] H. Y. Chen, J. W. Gordon, R. A. Bok, P. Cao, C. von Morze, M. van Criekinge, E. Milshteyn, L. Carvajal, R. E. Hurd, J. Kurhanewicz, D. B. Vigneron, and P. E. Z. Larson, "Pulse sequence considerations for quantification of pyruvate-to-lactate conversion kpl in hyperpolarized (13) c imaging," NMR Biomed **32**, e4052 (2019).

[147] C.-F. Westin, H. Knutsson, O. Pasternak, F. Szczepankiewicz, E. Özarslan, D. van Westen, C. Mattisson, M. Bogren, L. J. O'Donnell, M. Kubicki, D. Topgaard, and M. Nilsson, "Q-space trajectory imaging for multidimensional diffusion MRI of the human brain," NeuroImage **135**, 345–362 (2016).

[148] S. Rao, *Magnetic field of a Circular current loop using Biot Savart's Law. Retrieved June 10, 2020.* 2020.

[149] Y. Zhang, H. Liu, W. Xiao, L. Zhu, N. Wang, X. He, Z. Jiang, and B. Guan, "Quantitative dynamic contrast-enhanced magnetic resonance imaging in a VX2 rabbit liver tumour model using different gadolinium-based contrast agents: comparison of DCE-MRI quantitative results between magnevist and eovist," BJR|case reports **3**, 20160099 (2017).

[150] R. W. Leggett and L. R. Williams, "Suggested reference values for regional blood volumes in humans," Health Physics **60**, 139–154 (1991).

[151] H. Taniguchi, M. Masuyama, H. Koyama, A. Oguro, and T. Takahashi, "Quantitative measurement of human tissue hepatic blood volume by c15o inhalation with positron-emission tomography," Liver **16**, 258–262 (2008).

[152] J. Blustajn, C.-A. Cuenod, O. Clement, N. Siauve, V. Vuillemin-Bodaghi, and G. Frija, "Measurement of liver blood volume using a macromolecular MRI contrast agent at equilibrium," Magnetic Resonance Imaging **15**, 415–421 (1997).

[153] C. Schwarzbauer, J. Syha, and A. Haase, "Quantification of regional blood volumes by rapidT1 mapping," Magnetic Resonance in Medicine **29**, 709–712 (1993).

[154] D. L. Bihan, "What can we see with IVIM MRI?" NeuroImage **187**, 56–67 (2019).

[155] J. Sjölund, F. Szczepankiewicz, M. Nilsson, D. Topgaard, C.-F. Westin, and H. Knutsson, "Constrained optimization of gradient waveforms for generalized diffusion encoding," Journal of Magnetic Resonance **261**, 157–168 (2015).

[156] J. Leupold, S. Mansson, J. S. Petersson, J. Hennig, and O. Wieben, "Fast multiecho balanced ssfp metabolite mapping of (1)h and hyperpolarized (13)c compounds," Magma **22**, 251–6 (2009).

[157] E. Milshteyn, C. von Morze, J. W. Gordon, Z. Zhu, P. E. Z. Larson, and D. B. Vigneron, "High spatiotemporal resolution bssfp imaging of hyperpolarized [1-(13)c]pyruvate and [1-(13)c]lactate with spectral suppression of alanine and pyruvate-hydrate," Magn Reson Med **80**, 1048–1060 (2018).

[158] A. Z. Lau, A. P. Chen, R. E. Hurd, and C. H. Cunningham, "Spectral-spatial excitation for rapid imaging of DNP compounds," NMR in Biomedicine **24**, 988–996 (2011).

[159] P. E. Larson, A. B. Kerr, A. P. Chen, M. S. Lustig, M. L. Zierhut, S. Hu, C. H. Cunningham, J. M. Pauly, J. Kurhanewicz, and D. B. Vigneron, "Multiband excitation pulses for hyperpolarized 13c dynamic chemical-shift imaging," J Magn Reson **194**, 121–7 (2008).

[160] Y. Xing, G. D. Reed, J. M. Pauly, A. B. Kerr, and P. E. Larson, "Optimal variable flip angle schemes for dynamic acquisition of exchanging hyperpolarized substrates," Journal of Magnetic Resonance **234**, 75–81 (2013).

[161] C. M. Walker, D. Fuentes, P. E. Larson, V. Kundra, D. B. Vigneron, and J. A. Bankson, "Effects of excitation angle strategy on quantitative analysis of hyperpolarized pyruvate," Magnetic Resonance in Medicine **81**, 3754–3762 (2019).

[162] R. F. Schulte and F. Wiesinger, "Direct design of 2d RF pulses using matrix inversion," Journal of Magnetic Resonance **235**, 115–120 (2013).

[163] Y. F. Yen, S. J. Kohler, A. P. Chen, J. Tropp, R. Bok, J. Wolber, M. J. Albers, K. A. Gram, M. L. Zierhut, I. Park, V. Zhang, S. Hu, S. J. Nelson, D. B. Vigneron, J. Kurhanewicz, H. A. Dirven, and R. E. Hurd, "Imaging considerations for in vivo 13c metabolic mapping using hyperpolarized 13c-pyruvate," Magn Reson Med **62**, 1–10 (2009).

[164] D. M. Wilson, K. R. Keshari, P. E. Larson, A. P. Chen, S. Hu, M. Van Criekinge, R. Bok, S. J. Nelson, J. M. Macdonald, D. B. Vigneron, and J. Kurhanewicz, "Multicompound polarization by dnp allows simultaneous assessment of multiple enzymatic activities in vivo," J Magn Reson **205**, 141–7 (2010).

[165] H. Y. Chen, P. E. Z. Larson, R. A. Bok, C. von Morze, R. Sriram, R. Delos Santos, J. Delos Santos, J. W. Gordon, N. Bahrami, M. Ferrone, J. Kurhanewicz, and D. B. Vigneron, "Assessing prostate cancer aggressiveness with hyperpolarized dual-agent 3d dynamic imaging of metabolism and perfusion," Cancer Res **77**, 3207–3216 (2017).

[166] S. B. Reeder, Z. Wen, H. Yu, A. R. Pineda, G. E. Gold, M. Markl, and N. J. Pelc, "Multicoil dixon chemical species separation with an iterative least-squares estimation method," Magnetic Resonance in Medicine **51**, 35–45 (2003).

[167] E. K. Brodsky, V. V. Chebrolu, W. F. Block, and S. B. Reeder, "Frequency response of multipoint chemical shift-based spectral decomposition," J Magn Reson Imaging **32**, 943–52 (2010).

[168] C. H. Meyer, J. M. Pauly, A. Macovskiand, and D. G. Nishimura, "Simultaneous spatial and spectral selective excitation," Magnetic Resonance in Medicine **15**, 287–304 (1990).

[169] D. Spielman, C. Meyer, A. Macovski, and D. Enzmann, "1h spectroscopic imaging using a spectral-spatial excitation pulse," Magnetic Resonance in Medicine **18**, 269–279 (1991).

[170] Y. Zur, "Design of improved spectral-spatial pulses for routine clinical use," Magnetic Resonance in Medicine **43**, 410–420 (2000).

[171] P. Larson, E. Milshteyn, J. Gordon, X. Zhu, D. Korenchan, J. Maidens, H. Chen, and H. Shang, *Hyperpolarized-MRI-toolbox. Retrieved July 30 2019.* (2020).

[172] A. Kerr, P. E. Larson, M. Lustig, C. H. Cunningham, A. P. Chen, D. B. Vigneron, and J. M. Pauly, "Multiband spectral-spatial design for high-field and hyperpolarized c-13 applications," in In proceedings of the 16th annual meeting of the ismrm (ISMRM, 2008), p. 226.

[173] J. O. Fredrickson, C. Meyer, and N. J. Pelc, "Flow effects in spectral spatial excitation," in In proceedings of the 5th meeting of the ismrm (ISMRM, 1997), p. 113.

[174] J.-x. Wang, M. E. Merritt, D. Sherry, and C. R. Malloy, "A general chemical shift decomposition method for hyperpolarized13c metabolite magnetic resonance imaging," Magnetic Resonance in Chemistry **54**, 665–673 (2016).

[175] E. K. Brodsky, J. H. Holmes, H. Yu, and S. B. Reeder, "Generalizedk-space decomposition with chemical shift correction for non-cartesian water-fat imaging," Magnetic Resonance in Medicine **59**, 1151–1164 (2008).

[176] J. W. Gordon, H. Y. Chen, A. Autry, I. Park, M. Van Criekinge, D. Mammoli, E. Milshteyn, R. Bok, D. Xu, Y. Li, R. Aggarwal, S. Chang, J. B. Slater, M. Ferrone, S. Nelson, J. Kurhanewicz, P. E. Z. Larson, and D. B. Vigneron, "Translation of carbon-13 epi for hyperpolarized mr molecular imaging of prostate and brain cancer patients," Magn Reson Med **81**, 2702–2709 (2019).

[177] S. B. Reeder, E. Atalar, B. D. Bolster, and E. R. McVeigh, "Quantification and reduction of ghosting artifacts in interleaved echo-planar imaging," Magnetic Resonance in Medicine **38**, 429–439 (1997).

[178] J. W. Gordon, D. B. Vigneron, and P. E. Larson, "Development of a symmetric echo planar imaging framework for clinical translation of rapid dynamic hyperpolarized (13) c imaging," Magn Reson Med **77**, 826–832 (2017).

[179] M. H. Buonocore and L. Gao, "Ghost artifact reduction for echo planar imaging using image phase correction," Magnetic Resonance in Medicine **38**, 89–100 (1997).

[180] J. Wang, A. J. Wright, R. L. Hesketh, D. E. Hu, and K. M. Brindle, "A referenceless nyquist ghost correction workflow for echo planar imaging of hyperpolarized [1-(13) c]pyruvate and [1-(13) c]lactate," NMR Biomed **31** (2018).

[181] K. Nagashima, "Optimum pulse flip angles for multi-scan acquisition of hyperpolarized nmr and mri," J Magn Reson **190**, 183–8 (2008).

[182] J. M. Wild, M. N. Paley, M. Viallon, W. G. Schreiber, E. J. van Beek, and P. D. Griffiths, "K-space filtering in 2d gradient-echo breath-hold hyperpolarized3he MRI: spatial resolution and signal-to-noise ratio considerations," Magnetic Resonance in Medicine **47**, 687–695 (2002).

[183] C. M. Walker, J. Lee, M. S. Ramirez, D. Schellingerhout, S. Millward, and J. A. Bankson, "A catalyzing phantom for reproducible dynamic conversion of hyperpolarized [1-13c]-pyruvate," PLoS One **8**, e71274 (2013).

[184] A. Sigfridsson, K. Weiss, L. Wissmann, J. Busch, M. Krajewski, M. Batel, G. Batsios, M. Ernst, and S. Kozerke, "Hybrid multiband excitation multiecho acquisition for hyperpolarized (13) c spectroscopic imaging," Magn Reson Med **73**, 1713–7 (2015).

[185] S. Yang, J. Lee, E. Joe, H. Lee, Y.-S. Choi, J. M. Park, D. Spielman, H.-T. Song, and D.-H. Kim, "Metabolite-selective hyperpolarized 13c imaging using extended chemical shift displacement at 9.4 t," Magnetic Resonance Imaging **34**, 535–540 (2016).

[186] M. Alves-Bezerra and D. E. Cohen, "Triglyceride metabolism in the liver," Compr Physiol **8**, 1–8 (2017).

[187] P. Puchalska and P. A. Crawford, "Multi-dimensional roles of ketone bodies in fuel metabolism, signaling, and therapeutics," Cell Metabolism **25**, 262–284 (2017).

[188] S. Li, H.-Y. Tan, N. Wang, Z.-J. Zhang, L. Lao, C.-W. Wong, and Y. Feng, "The role of oxidative stress and antioxidants in liver diseases," International Journal of Molecular Sciences **16**, 26087–26124 (2015).

[189] D. Huang, T. Li, L. Wang, L. Zhang, R. Yan, K. Li, S. Xing, G. Wu, L. Hu, W. Jia, S.-C. Lin, C. V. Dang, L. Song, P. Gao, and H. Zhang, "Hepatocellular carcinoma redirects to ketolysis for progression under nutrition deprivation stress," Cell Research **26**, 1112–1130 (2016).

[190] Z. Younossi, Q. M. Anstee, M. Marietti, T. Hardy, L. Henry, M. Eslam, J. George, and E. Bugianesi, "Global burden of NAFLD and NASH: trends, predictions, risk factors and prevention," Nature Reviews Gastroenterology & Hepatology **15**, 11–20 (2017).

[191] C. Estes, H. Razavi, R. Loomba, Z. Younossi, and A. J. Sanyal, "Modeling the epidemic of nonalcoholic fatty liver disease demonstrates an exponential increase in burden of disease," Hepatology **67**, 123–133 (2017).

[192] T. Marjot, A. Moolla, J. F. Cobbold, L. Hodson, and J. W. Tomlinson, "Nonalcoholic fatty liver disease in adults: current concepts in etiology, outcomes, and management," Endocrine Reviews **41**, 66–117 (2019).

[193] E. S. Jin, J. D. Browning, R. E. Murphy, and C. R. Malloy, "Fatty liver disrupts glycerol metabolism in gluconeogenic and lipogenic pathways in humans," Journal of Lipid Research **59**, 1685–1694 (2018).

[194] N. E. Sunny, F. Bril, and K. Cusi, "Mitochondrial adaptation in nonalcoholic fatty liver disease: novel mechanisms and treatment strategies," Trends in Endocrinology & Metabolism **28**, 250–260 (2017).

[195] J. A. Fletcher, S. Deja, S. Satapati, X. Fu, S. C. Burgess, and J. D. Browning, "Impaired ketogenesis and increased acetyl-CoA oxidation promote hyperglycemia in human fatty liver," JCI Insight **4** (2019).

[196] S. L. Friedman, B. A. Neuschwander-Tetri, M. Rinella, and A. J. Sanyal, "Mechanisms of NAFLD development and therapeutic strategies," Nature Medicine **24**, 908–922 (2018).

[197] E. Fitzpatrick, "Noninvasive biomarkers in non-alcoholic fatty liver disease: current status and a glimpse of the future," World Journal of Gastroenterology **20**, 10851 (2014).

[198]C. von Morze, J. Tropp, A. P. Chen, I. Marco-Rius, M. V. Criekinge, T. W. Skloss, D. Mammoli, J. Kurhanewicz, D. B. Vigneron, M. A. Ohliger, and M. E. Merritt, "Sensitivity enhancement for detection of hyperpolarized 13 c MRI probes with 1 h spin coupling introduced by enzymatic transformation in vivo," Magnetic Resonance in Medicine **80**, 36–41 (2017).

[199]A. Owens, "The kinetics of the dissociation of dihydroxyacetone dimer in aprotic media," MSc Thesis (University of Waikato, Hamilton, New Zealand, 2016).

[200]N. Kobayashi, M. Nishikawa, K. Hirata, and Y. Takakura, "Hydrodynamics-based procedure involves transient hyperpermeability in the hepatic cellular membrane: implication of a nonspecific process in efficient intracellular gene delivery," J Gene Med **6**, 584–92 (2004).

[201]T. Suda, X. Gao, D. B. Stolz, and D. Liu, "Structural impact of hydrodynamic injection on mouse liver," Gene Therapy **14**, 129–137 (2006).

[202]P. Cao, P. J. Shin, I. Park, C. Najac, I. Marco-Rius, D. B. Vigneron, S. J. Nelson, S. M. Ronen, and P. E. Z. Larson, "Accelerated high-bandwidth MR spectroscopic imaging using compressed sensing," Magnetic Resonance in Medicine **76**, 369–379 (2016).

[203]A. Kirpich, M. Ragavan, J. A. Bankson, L. M. McIntyre, and M. E. Merritt, "Kinetic analysis of hepatic metabolism using hyperpolarized dihydroxyacetone," Journal of Chemical Information and Modeling **59**, 605–614 (2019).

Vita

Keith Andrew Michel was born on December 8, 1988 in Union, Kentucky, the son of Kristina Jansson Michel and Gary Anthony Michel. After graduating in 2006 as salutatorian of his class at Covington Latin School in Covington, Kentucky, he matriculated at Rice University in Houston, Texas. He received the degree of Bachelors of Science in Bioengineering from Rice in May, 2010. In 2011, he began working as an Imaging Research Technician in the Small Animal Imaging Facility at MD Anderson Cancer Center. In August 2015 he entered the Medical Physics Ph.D. program in The University of Texas MD Anderson Cancer Center UTHealth Graduate School of Biomedical Sciences.

Current address:

1885 El Paseo Street

Houston, Texas 77054